The strength and mechanical behaviour of quartz slip interfaces: An experimental investigation

Kathryn Suzanne Hayward

August 2015

A thesis submitted for the degree of
Master of Philosophy
of The Australian National University

Australian
National
University

Declaration

The work in this thesis is my own except where otherwise stated.

Kathryn S. Hayward

“Process is more important than outcomes. When the outcome drives the process we will only ever go where we've already been. If the process drives the outcome we may not know where we're going, but we will know we want to be there."

-Bruce Mau

For my parents - thank you for everything

Abstract

An experimental study has been undertaken to explore the strength, mechanical behaviour and microstructural evolution of bare interfaces in quartz sandstone during slip. These experiments were designed to simulate fault processes with increasing depth in the continental crust. Two main aspects have been explored: (1) the effect of temperature and confining pressure on the behaviour and stability of favourably-oriented faults, and (2) the influence of reactivation angle on the mechanical behaviour and associated microstructural evolution of a fault zone. Experiments were conducted on Fontainebleau sandstone using a triaxial deformation apparatus, at normal stresses comparable to that in the continental seismogenic regime and over small slip displacements.

The first suite of experiments was conducted at temperatures of 400-927°C and confining pressures of 50-200MPa. Experiments reveal complex transitions in fault behaviour between stick-slip and stable sliding regimes. Mechanical results are coupled with microstructural analysis using multiple techniques (including high resolution FE-SEM, and FIB-TEM) that provide insights into fault surface processes down to the nano-scale. Significant findings include the identification of a partially amorphous layer formed during aseismic creep and the generation of pure-silica frictional melt (pseudotachylyte) during high temperature seismic slip events. The pseudotachylyte is recognisable by the formation drawn-out glass filaments and fractured glass patches on the fault surfaces, forming a discontinuous layer up to 2μm thick and covering 10-60% of the fault surface. At normal stresses > 200MPa, frictional melt develops within the first 50μm of rapid slip, correlating with changes in slip acceleration and velocity. High temperature hydrothermal treatment of melt-covered fault surfaces indicates that the pseudotachylyte has a short lifespan (<1 hour) in the presence of high temperature, reactive fluids.

The second suite of experiments explores reactivation of fault surfaces inclined between 25º and 70º to the maximum shortening direction, representing faults that vary from

optimally-oriented to severely-misoriented for failure. These faults have been reactivated in both dry and fluid-saturated conditions, using two different loading mechanisms. ‘Stress-driven failure’ involves increasing the axial load at constant rate until failure, whereas ‘fluid-driven failure’ is achieved by maintaining a constant axial load and increasing pore fluid pressure until slip occurs. While the initial reactivation of faults obeys frictional theory, continued reactivation is strongly influenced by the microstructural evolution of the fault surface, most notably through the development of frictional melt. Rapid-slip events form a locally-continuous layer of frictional melt in both the dry and water-saturated samples. The presence of pseudotachylyte increases fault cohesive strength through a process termed ‘melt-welding’. Melt-welded regions serve as a nucleation point for the development of off-fault damage and on the most unfavourably-oriented faults, cause lock-up and the failure of a new, more favourably-oriented fault.

This work provides new insights into the behaviour and microstructural development of fault surfaces during the early stages of seismic instability. These results have implications for the interpretation of slip processes in natural fault zones, and also more generally for understanding slip mechanics, weakening distances and coseismic fault strength within the continental seismogenic regime.

Acknowledgements

This thesis marks not only a milestone of academic learning but also, on more personal level, a change in career from working in the business sector to the beginnings of a journey into the earth sciences. Such a significant change cannot be achieved by one person alone and I am deeply grateful to all those that have contributed to this transformation.

My supervisor, Stephen Cox, is owed a special thank you, for not only for his role as supervisor, mentor and friend, but also for his courage in taking on a student with none of the requisite knowledge that most students possess when they enter their graduate studies. I consider it a privilege to have been guided by Stephen, and thank him for his patience, instruction, rigorous approach and for the inspiration that our many discussions have generated. I look forward to continuing to work with you into future, both on my PhD and beyond.

The first 15 months of this project was hampered by equipment issues as the deformation apparatus was resurrected from its experimental hiatus and a new digital data acquisition system was installed. Hayden Miller and the electronics and mechanical workshops are thanked for their wonderful technical support – often at very short notice. The rest of the rock physics group, including Mervyn Paterson, Ian Jackson, Emmanuel David, Christopher Cline, Yang Lee, Richard Skelton and Harri Kokkonen, are thanked for their assistance in the lab and also for the comradery and lively discussions over the past two years.

The knowledge and expertise of John Fitz Gerald has contributed significantly to the microstructural studies in this project and I greatly appreciate the time that John spent teaching me how to operate the TEM. I am grateful to Harri Kokkonen for his patience, humour and instruction on the finer points of sample preparation and for the preparation of a number of samples, especially during the final stages of the project. Further, I would like to thank members of the microscopy community at ANU, including Frank

Brink, Hua Chen, David Llewellyn and Felipe Kreme (Centre for Advance Microscopy), Lily Li and Mark Lockrey (Australian National Fabrication Facility) for the thorough training, assistance and interesting discussions about various aspects of electron microscopy and sample preparation.

I wish to thank Tim Senden, Michael Turner and Holger Averdunk from the department of Applied Mathematics at ANU for their assistance with the micro-computed X-ray tomography and subsequent data processing. Rhys Hawkins is thanked for his assistance with writing the Python scripts used for the thermal modelling.

A special thank you is also owed to Michelle Salmon for her encouragement, friendship and loan of, and assistance with the use of seismic equipment that is being used to better constrain slip duration. Bram Slagmolen, Perry Forsyth and Daniel Shaddock from the Department of Quantum Science are thanked for their wonderful help with the development of the laser interferometry system.

My thanks and gratitude also goes to the student body at RSES for the many discussions, laughs, and sharing the frustrations of failures when they occurred. A special thank you goes to Rhys, Shayne, Chris, Eleanor, Rachel, Marie, Johanna and Tanja.

Finally, to my parents, brother and family, who have encouraged and supported me in all aspects of life including the path that has led to this thesis and beyond - thank you.

Contents

Chapter 1

Introduction

Earthquakes are the result of shear mode failure of rock in a brittle regime. Most seismogenic ruptures in a continental setting occur in the upper 5-20km of the crust [*Sibson*, 1983], representing the zone of brittle failure and unstable frictional sliding that is, to a first order, governed by the empirical Coulomb failure criterion faulting. However, once slip nucleates, the behaviour of the fault is controlled by both dynamic weakening and strengthening mechanisms that either enhance or impede fault slip propagation. Despite having a crucial role in understanding fault rupture properties, including coseismic stress drop, energy radiation and heat production, dynamic fault strength remains a source of significant uncertainty in earthquake mechanics [*Di Toro et al.*, 2006a].

The propagation of seismic slip is generally ascribed to the activation of dynamic fault weakening mechanisms at high slip velocities, which result in a significant deviation in frictional values from typical laboratory-derived static friction estimates of between $0.6 < \mu_s < 0.85$ [*Byerlee*, 1978]. Rate- and state-dependent friction laws have been used to describe the evolution of dynamic friction values observed in small displacement experiments [*Dieterich*, 1978; *Ruina*, 1983; *Scholz*, 1998]. While useful for understanding a number of seismic observations, including aftershock occurrence and nucleation [*Marone*, 1998; *Scholz*, 2002], this model has a number of limitations in its application to large-scale slip processes owing to the experimental restrictions of small displacements and low slip velocities [*Paterson and Wong*, 2005 and ref. therein]. Importantly, rate- and state- dependent friction laws are empirical and do not incorporate the fundamental microstructural and material evolution of the slip surfaces [*Di Toro et al.*, 2006b]. Dynamic variations in pressure and temperature on the fault surface during high velocity slip cause changes in fault surface properties and microstructure, leading to transient, but potentially dramatic, reductions in fault strength.

The concept of dynamic fault weakening is supported by a number of observations from large earthquake ruptures, including: (1) unusually large stress drops associated with some earthquakes [*Malagnini et al.*, 2010], (2) the lack of a pronounced heat flow anomaly associated with some major active fault zones (e.g., San Andreas fault [*Brune et al.*, 1969; *Lachenbruch and Sass*, 1980]), (3) unusually large co-seismic slip displacements for some large earthquakes [*Rodgers and Little*, 2006; *Fujiwara et al.*, 2011], and (4) the high seismic radiation efficiency of some earthquakes [*Venkataraman and Kanamori*, 2004]. Possible mechanisms for dynamic weakening have been explored both experimentally and numerically over the past fifteen years, especially with the advent of the high velocity friction apparatus and a proliferation of experimental studies [e.g., *Hirose and Shimamoto*, 2005b; *Di Toro et al.*, 2006b; *Han et al.*, 2011; *Proctor et al.*, 2014]. Mechanisms such as thermal pressurisation [*Sibson*, 1973; *Wibberley and Shimamoto*, 2005; *Rempel and Rice*, 2006], silica gel lubrication [*Goldsby and Tullis*, 2002; *Di Toro et al.*, 2004; *Hayashi and Tsutsumi*, 2010; *Nakamura et al.*, 2012], dynamic activation / powder lubrication by gouge particles [*Han et al.*, 2010; *Reches and Lockner*, 2010; *Han et al.*, 2011; *Siman-Tov et al.*, 2013], flash heating [*Rice*, 2006; *Goldsby and Tullis*, 2011], elasto-hydrodynamic lubrication [*Brodsky and Kanamori*, 2001], thermal decomposition [*Han et al.*, 2007] and lubrication by frictional melting [*Hirose and Shimamoto*, 2005b; *Di Toro et al.*, 2006a] have been proposed to produce in significant dynamic weakening (dynamic frictional values approaching 0.1). However, of these mechanisms, the production of pseudotachylyte or quenched frictional melt is the only mechanism that is definitively identified within natural fault zones and is regarded as the only unequivocal evidence in the rock record of the occurrence of seismic slip [*Sibson*, 1975; *Kirkpatrick et al.*, 2009].

Despite having highlighted the structural, chemical and tribological effects that high velocity slip can have on rock interfaces, there are limitations in the extrapolation of the results of high velocity friction experiments to crustal earthquake processes. Due to apparatus and sample constraints, these experiments are typically performed dry, at low uniaxial normal stresses (< 120MPa) [*Proctor et al.*, 2014] and ambient temperatures, which are potentially unrealistic for crustal faulting conditions. To compensate for the low normal stresses, most experiments involve large displacements (> 0.5m) [e.g., *Goldsby and Tullis*, 2002; *Di Toro et al.*, 2004; *Hirose et al.*, 2012] using an imposed high (typically approaching seismic) slip velocity. Consequently many of the

microstructures associated with the initial stages of fault weakening are rapidly overprinted and the identified effects of transient strengthening and weakening cannot be explored in terms of their direct effect on the promotion and termination of slip. In the case of dynamic weakening by melt lubrication, high velocity friction experiments have shown complex behaviour including a marked strengthening at the onset of melting. However, it remains uncertain how this behaviour changes at high confining pressures and realistic normal stresses [*Fialko and Khazan*, 2005]; further experimental investigation is needed to explore whether the strengthening associated with the onset of melting is sufficient to impede, or even terminate, some seismic ruptures.

1.1 Frictional melting and the scarcity of pseudotachylytes on natural faults

Earthquakes are associated with a rapid release of energy that is either dispersed in the form of radiated seismic energy [*McGarr,* 1999] or adsorbed along the rupture zone through mechanical work in the form of fracturing [*Pittarello et al.,* 2008] and heat generation [*Sibson,* 1975]. A fundamental prerequisite for the generation of frictional melt is a high rate of mechanical work resulting in a rate of heat generation that exceeds the rate of heat dissipation [*Di Toro et al.,* 2011]. However, examination of exhumed natural fault zones suggests that the formation of pseudotachylyte is rare [*Sibson and Toy*, 2006; *Kirkpatrick et al.*, 2009]. This raises the possibility that frictional melting does not occur within all seismogenically active faults zones, or that pseudotachylyte forms at scales below standard microstructural observation (i.e. < 2μm), or that many pseudotachylytes are not preserved over geological timescales.

The feasibility of frictional melting occurring during moderate seismic slip events (~1m) is confirmed by theoretical modelling, provided that slip is localised within a zone less than approximately 10cm wide [*Cardwell et al.*, 1978]. Therefore the scarcity of pseudotachylyte in natural fault zones implies that, at least in part, other factors must suppress localised heating on the fault interface [*Bjornerud,* 2010]. These factors may include the activation of weakening mechanisms, the activation of mechanisms that adsorb an increased proportion of the mechanical work (e.g., dynamic pulverisation [*Reches and Dewers,* 2005]), or the existence of a more dispersed slip zone resulting in the distribution of mechanical work over a larger volume [*Spray,* 1995; *Kanamori and Rivera,* 2006]. High velocity experiments have shown both fault weakening and

significant energy expenditure through the formation of amorphous gels and the generation of nano-size gouge particles [*Fondriest et al.*, 2013]. However, whether these wear products act as a precursor or inhibitor of frictional melting, and their influence on the macroscopic behaviour and stability of faults at realistic effective normal stresses remains largely unknown.

Although gels have been experimentally produced on the slip surfaces of faults during slip approaching seismic slip velocities [*Hayashi and Tsutsumi*, 2010], amorphous material has also been produced at comparatively low slip velocities ($V<3\mu m.s^{-1}$) [*Yund et al.*, 1990; *Pec et al.*, 2012]. Accordingly, gel formation could potentially occur at any stage during the seismic cycle. Quartz and silica appear particularly susceptible to amorphisation processes [*Heaney*, 1994]. Intriguingly, despite quartz being a common mineral within fault zones in the continental crust, there are very few recorded examples of pure silica pseudotachylytes [*Bestmann et al.*, 2011]. Whether this is a result of the high melting temperature of quartz [*Navrotsky*, 1994], weakening due to the presence of fluids, or due to the propensity of quartz to form amorphous gels that weaken the fault prior to the onset of melting, needs to be explored experimentally at realistic crustal stress conditions. Most high-velocity experiments undertaken on quartz-rich rocks (e.g., quartzite, novaculite and chert) have tended to form gels rather than frictionally melting, although novaculite has been shown to produce a high viscosity melt after approximately 0.4-0.6m of slip at 12.5MPa applied normal stress [*Di Toro et al.*, 2006a].

The prevalence of fluids within most crustal fault zones is often cited as a reason for the scarcity of natural pseudotachylytes [*Sibson and Toy*, 2006]. It is thought that fault weakening processes such as thermal pressurization of fault fluids [*Sibson*, 1973] and elasto-hydrodynamic lubrication [*Brodsky and Kanamori*, 2001] potentially inhibit melt generation in water-saturated environments, leading to the view that frictional melt generation is largely limited to single slip events within low-porosity, dry crystalline host rocks [*Sibson and Toy*, 2006]. Technical limitations of high velocity rotary shear apparatus mean that it remains experimentally untested whether pseudotachylyte can be formed in water-saturated conditions or on a macroscopically porous slip interface.

1.2 Fault orientation and weakening mechanisms

The previous experimental work that has been discussed so far involves either uniaxial compression, direct shear arrangements or are 'Andersonian'- type faults that are approximately optimally-oriented for reactivation. However, there is compelling geological evidence for the existence and reactivation of unfavourably-oriented faults that are inherited from previous deformation [*Sibson*, 1985, 1990b]. To reactivate these faults, by definition, they must be either frictionally weak or influenced by high pore fluid pressures [*Sibson*, 1990b; *Cox*, 2010]. Few experimental works have considered the reactivation of unfavourably-oriented faults [*Jaeger*, 1959; *Handin*, 1969; *Mitchell et al.*, 2011], and even less work has been undertaken to investigate the influence of the high normal stresses on the microstructural evolution of the fault interface.

1.3 Research aims and thesis structure

From the preceding introductory discussion it is clear that a need exists for new experiments to span the experimental conditions between conventional low strain-rate rock shear failure experiments and high-velocity friction experiments undertaken on rotary-shear-type apparatus. This thesis combines (1) experimental work using the technical infrastructure of the Rock Physics Group at the Research School of Earth Sciences with (2) the novel application and use of high resolution imaging techniques to:

1. Explore the behaviour and stability of pre-existing sliding interfaces in a pure-quartz sandstone over a range temperature and pressure conditions.
2. Establish if there are identifiable differences in the slip velocities and acceleration of sliding instabilities during stick-slip behaviour at various pressure and temperature conditions and loading velocities.
3. Provide insights into precursory microstructures and phenomena associated with the early stages of seismic instability.
4. Explore the reactivation potential of faults that are unfavourably-oriented relative to the shortening direction to gain insights into mechanical behaviour and microstructural evolution associated with the reactivation of an inherited fault zone.

5. Examine the role of low-temperature fluids on the reactivation of unfavourably-oriented faults, including their effects on the development of slip-related microstructures.
6. Investigate the longevity of slip-related microstructures during the interseismic period in the presence of hydrothermal fluids.

This thesis uses small displacement (<1mm) deformation experiments on bare quartz sandstone sliding interfaces to provide new insights into the behaviour and microstructural development of the fault surface during the early stages of seismic instability. The experiments are undertaken at confining pressures that are comparable to those of seismogenic depths in the continental crust (up to 250MPa) and are performed using an internally-heated, triaxial gas-medium deformation apparatus. An essentially pure quartz sandstone is used as the sample material with specimens configured with pre-ground bare interfaces to simulate the growth and development of faults where slip is highly localised. Two types of experiments are undertaken: the first suite presented in Chapter 2, involves high temperature (400-927ºC) reactivation of approximately optimally-oriented fault surfaces; the second set of experiments (Chapter 3) are undertaken at room temperature on faults oriented at between 25-70º to the shortening direction, representing faults orientations that range from optimally-oriented to severely-misoriented for reactivation.

The role of low-temperature fluids in modifying slip mechanics and microstructural evolution is also explored in Chapter 3. In this chapter, faults are reactivated in both dry and fluid-saturated conditions. Failure is instigated in two ways: the first involves the increase of axial load at constant rate until failure (stress-driven failure) and is undertaken at either nominally dry or water-saturated conditions; the second method involves reactivation of the fault by maintaining a constant axial load and increasing pore fluid pressure until slip occurs (fluid-driven failure).

A major component of this thesis is the investigation of microstructures formed at the slip interface. One of the biggest challenges is to attempt to connect the macro-scale fault behaviour and empirically-derived friction laws with the micro-, nano- and even molecular-scale mechanisms occurring at the fault interface. The results presented in Chapters 2 and 3, use a number of imaging techniques including high resolution scanning electron microscopy (SEM) and cathodoluminescence (CL-SEM), focused ion

beam milling assisted transmission electron microscopy (FIB-TEM) and microcomputed X-ray tomography, to provide insights into slip processes and deformation mechanisms at a range of scales and in both two- and three-dimensions.

Finally, Chapter 4 draws together the mechanical and microstructrual data presented in earlier chapters to identify implications of the results to our understanding of earthquake source mechanics, fault behaviour and stability, and recognition of slip-related structures on natural faults. This chapter also includes a discussion of future reseach directions, both in terms of the current study and also more broadly.

Chapter 2

Frictional Melting on Experimental Quartz Fault Interfaces at Elevated Temperatures

1. Introduction

Pseudotachylyte, typically a dark coloured, vitreous rock associated with high strain rate deformation structures such as impact craters and faults zones, has long captured the interest of geologists [*MacCulloch*, 1819; *Holland*, 1900; *Shand*, 1916], with its existence in faults potentially providing an important indicator of the behaviour and strength of faults in non fluid-active environments at upper to mid-crustal conditions [*Sibson*, 1977; *Sibson and Toy*, 2006]. The origin and mechanism for pseudotachylyte generation has been the source of debate for a number of decades with some authors favouring a strict definition that pseudotachylyte arises from the frictional heating and melting of the fault surface [*Sibson*, 1975; *Maddock*, 1983; *Spray*, 1995, 2010; *Kirkpatrick and Rowe*, 2013], while others have adopted a broader definition that includes any amorphous matrix within the fault zone that displays similar physical characteristics to melt-origin pseudotachylyte (such as injection veins and flow textures) [*Wenk*, 1978; *Lin*, 1997; *Ozawa and Takizawa*, 2007; *Janssen et al.*, 2010; *Pec et al.*, 2012]. While the formation of different types of amorphous material within fault zones has been associated with fault weakening [e.g. *Goldsby and Tullis*, 2002; *Pec et al.*, 2012; *Proctor et al.*, 2014], the variation in the mechanisms and conditions of formation suggests that there could be significant differences in the interpretation of pseudotachylytes within the geological record. If a fault has generated a melt phase, this places important constraints on the conditions of rupture, the rate of mechanical work and the potential seismic energy dissipation, with melt-origin pseudotachylyte often being cited as an indicator of ancient seismic faulting [e.g. *Sibson*, 1975; *Di Toro et al.*, 2005]. In contrast if amorphisation is generated through mechanical, chemical or solid-

state processes, the conditions of fault rupture can be very different and potentially occur at sub-seismic slip rates [*Pec et al.*, 2012].

Our understanding of the processes involved in the development of fault weakening behaviour and pseudotachylite generation has progressed rapidly over the past 15 years with extensive experimentation, primarily on high velocity rotary shear apparatus [e.g. *Shimamoto and Tsutsumi*, 1994; *Di Toro et al.*, 2006a; *Proctor et al.*, 2014]. Many advances have been made in understanding high-velocity friction and dynamic fault weakening, with such behaviours being attributed to mechanisms such as flash heating of asperities [*Rempel*, 2006; *Goldsby and Tullis*, 2011], thermal pressurisation [*Sibson*, 1973; *Rice*, 2006], intense comminution [*Han et al.*, 2011], frictional melting [*Spray*, 1995; *Di Toro et al.*, 2006a; *Nielsen et al.*, 2008], and the formation of amorphous silica-gels [*Goldsby and Tullis*, 2002; *Di Toro et al.*, 2004; *Hayashi and Tsutsumi*, 2010; *Nakamura et al.*, 2012]. While the high velocity rotary shear apparatus allows exploration of velocities approaching seismic slip rate rates, the low normal stresses (< 97MPa [*Proctor et al.*, 2014]) and unrealistically high displacements (> 0.5m, but commonly between 20-100m [e.g. *Goldsby and Tullis*, 2002; *Di Toro et al.*, 2004; *Hirose and Shimamoto*, 2005b]) potentially place limitations on the extrapolation of the observed phenomena to crustal faulting conditions. Comparison of observations from high velocity shear experiments with those performed on a triaxial apparatus under high confining pressure can provide a point of correlation between the preliminary behaviours and microstructures marking the onset of dynamic weakening and fault rupture.

Quartz is one of the most prevalent minerals found in fault zones in the continental lithosphere, and as such is often used as a sample material in the experimental study of crustal deformation [*Paterson and Wong*, 2005 and references contained therein]. However, despite its abundance in fault zones and the frequent occurrence of pseudotachylytes in silica-rich rocks (such as granitoids) [e.g. *Otsuki and Monzawa*, 2003; *Di Toro et al.*, 2008], natural pure quartz pseudotachylytes are rare [*Lin*, 1994; *Bestmann et al.*, 2011]. Even in the laboratory setting, the experimental generation of quartz melt has proved difficult at all but the highest velocities [*Di Toro et al.*, 2004; *Di Toro et al.*, 2006b], with most experiments showing quartz as survivor clasts within a melt matrix [*Spray*, 2010; *Pec et al.*, 2012] or, in its pure form, forming amorphous gels [*Di Toro et al.*, 2004; *Hayashi and Tsutsumi*, 2010]. The ability of quartz to form a

hydrated amorphous gel during high velocity sliding alludes to some of the specific material properties of this mineral, including the ability to modify its crystal structure under different pressure-temperature conditions resulting in numerous polymorphs [*Heaney*, 1994] and, almost conversely, the ability to lose its long range crystal order to become amorphous at high pressure (when the rate of damage of the crystal lattice exceeds the rate of growth of the new stable crystalline phase) [*Winters et al.*, 1992; *Badro et al.*, 1998], during shear [*Yund et al.*, 1990; *Di Toro et al.*, 2004; *Nakamura et al.*, 2012] and at high temperature. In the current context of pseudotachylite generation, where stress and temperature states are extreme and dynamic, the ability of quartz to transition between phases and crystalline-amorphous states brings into question whether quartz pseudotachylytes are rare [*Sibson and Toy*, 2006], or whether the amorphous silica and glass are poorly preserved [*Kirkpatrick et al.*, 2009], reverting to a more stable crystalline form or being overprinted by such processes as hydrothermal alteration and recrystallization. The difficulty of experimentally producing a quartz melt may also simply be a consequence of experimental set-up with the majority of pseudotachylite research being undertaken at low normal stresses and ambient temperatures.

In this study, experiments undertaken in a triaxial apparatus are used to explore the physical and mechanical changes that slip induces on a fault interface in a simplified chemical environment consisting of an essentially pure quartz, single phase starting material. The exploration of small displacement slip events under realistic normal stresses provides insights into the transition of fault behaviour from both aseismic creep to seismic slip and from frictionally locked to rapid sliding following the development of fault instability. By capturing the microstructures formed early during slip, precursory phenomena can be isolated from the spectrum of behaviours associated with large displacements at high slip rates, such as the development a full coverage melt film or amorphous gel. Small displacement slip experiments also provide an opportunity to explore the long-standing controversy about the origin of amorphous material in slip interfaces. The use of optical and electron microscopy techniques to characterise the microstructure provides insights into mechanisms controlling fault behaviour at the macro-, micro-, and nanoscale. These analyses, supported by basic thermal modelling, allow exploration of the potential generation of frictional heat and whether flash heating

or localised melting can be correlated with the observed physical and mechanical phenomena.

2. Experimental method and analysis techniques

2.1 Experimental procedure and conditions

The experiments performed in this study are undertaken on pre-ground Fontainebleau sandstone fault interfaces that are in direct contact (i.e. there is no layer of simulated gouge material between the fault surfaces). Fontainebleau Sandstone is an approximately equigranular, almost pure quartz sandstone with grain size between approximately 200-250μm and a porosity between 6-8%. This sandstone has been consolidated by the formation of syntaxial overgrowths in a silica-supersaturated solution [*Thiry et al.*, 1998; *Haddad et al.*, 2006], resulting in a subhedral to euhedral grain shape. The quartz grains contain numerous fluid inclusions that are observed to occur both within the detrital grains or decorating healed intragranular fractures and overgrowth boundaries. The distribution of the fluid inclusions is heterogeneous making up between 0.01 – 0.1 vol. % of the crystalline material within sample, with an average inclusion size of ~1.1μm^3. The fluid inclusions contain multiple phases, with $H_2O_{(Liquid + Vapour)}$, $CO_{2\ (Liquid)}$ and small daughter crystals in a number of the locations but dominantly within the detrital grains indicating formation during petrogenesis. Given the coastal depositional environment and subsequent shallow burial of the Fontainebleau sandstone [*Thiry et al.*, 1998], it is assumed that most post-sedimentation fluid inclusions also contain at least some free water. The presence of water is supported by a small spike in the Raman spectra at 3420 (cm^{-1}), however the size of the inclusions are too small to allow a more robust spectral analysis.

Samples are prepared by finely grinding sandstone cores (ϕ=9.98mm) at an angle of 30º to the cylinder axis. The two fault blocks are ground to an overall length of 21mm then oven dried at 70°C for at least 48 hours prior to use. Specimens are loaded into a 0.25mm thick annealed copper sleeve and capped with split alumina spacers, which allow pore fluid access while isolating the sample from the rest of the assembly. The sleeve and pistons are then loaded into a thin-walled (~0.4mm), low-carbon mild steel jacket that allows the separation of the sample (and where applicable, the pore fluid) from the argon confining medium. To accurately determine the sample strength during

deformation, a correction for the strength contribution of the metal jacket assembly has been applied (refer to Appendix 2).

Experiments were undertaken in a Paterson internally heated, gas-medium, rock deformation apparatus that permits the independent control and measurement of temperature, confining pressure (P_c), pore fluid pressure (P_f), axial displacement rate and axial load [*Paterson*, 1970]. This device is considered a 'soft' apparatus, as it accumulates significant elastic strain during loading that can be imparted to a specimen during failure, resulting in significantly higher displacements and stress drops than could be achieved using a more rigid apparatus. The experiments were conducted over a range of temperatures from 500-927ºC, P_c between 50-200MPa and a nominal axial displacement rate between 0.36-0.72μms^{-1}. Data was recorded using a digital data acquisition system (National Instruments LabView 11.0) with a sampling frequency of 100Hz and recording frequency of 1Hz.

Increased constraints on slip duration and insights into seismic slip velocity and acceleration were explored through the installation of a seismometer and accelerometer at the top of the apparatus (Fig. 1). The seismometer used was a Lennartz LE-3D Lite three component 1Hz (short period) sensor from which data was sampled at 1000 samples per second using a LPR200 custom built recorder. The triaxial acceleration components were measured and recorded using a JoyWarrior24F14 accelerometer with USB interface and a data acquisition frequency of 100 samples per second. However, if it is assumed that a stick-slip event in the rock deformation apparatus simulates earthquake rupture then an upper bound on rupture velocity can be estimated by the shear wave velocity of the medium [*Johnson and Scholz*, 1976; *Scholz*, 2002]. The shear wave velocity of Fontainebleau sandstone is well established and the rupture velocity is estimated to be in the order of 3500m.s^{-1} [*Gomez et al.*, 2010]. This equates to a rupture time of 6μs, assuming a fault length of 1.7cm. The estimated rupture time is several orders of magnitude less than the sampling rate of the seismic instrumentation and therefore it is suggested the seismic data recorded during the experiments is not sufficient to provide absolute information about rupture propagation. However, the seismic data has been found to provide valuable qualitative data about the relative velocities and accelerations of the slip events for a subset of experiments in the current suite (refer to Appendix 4).

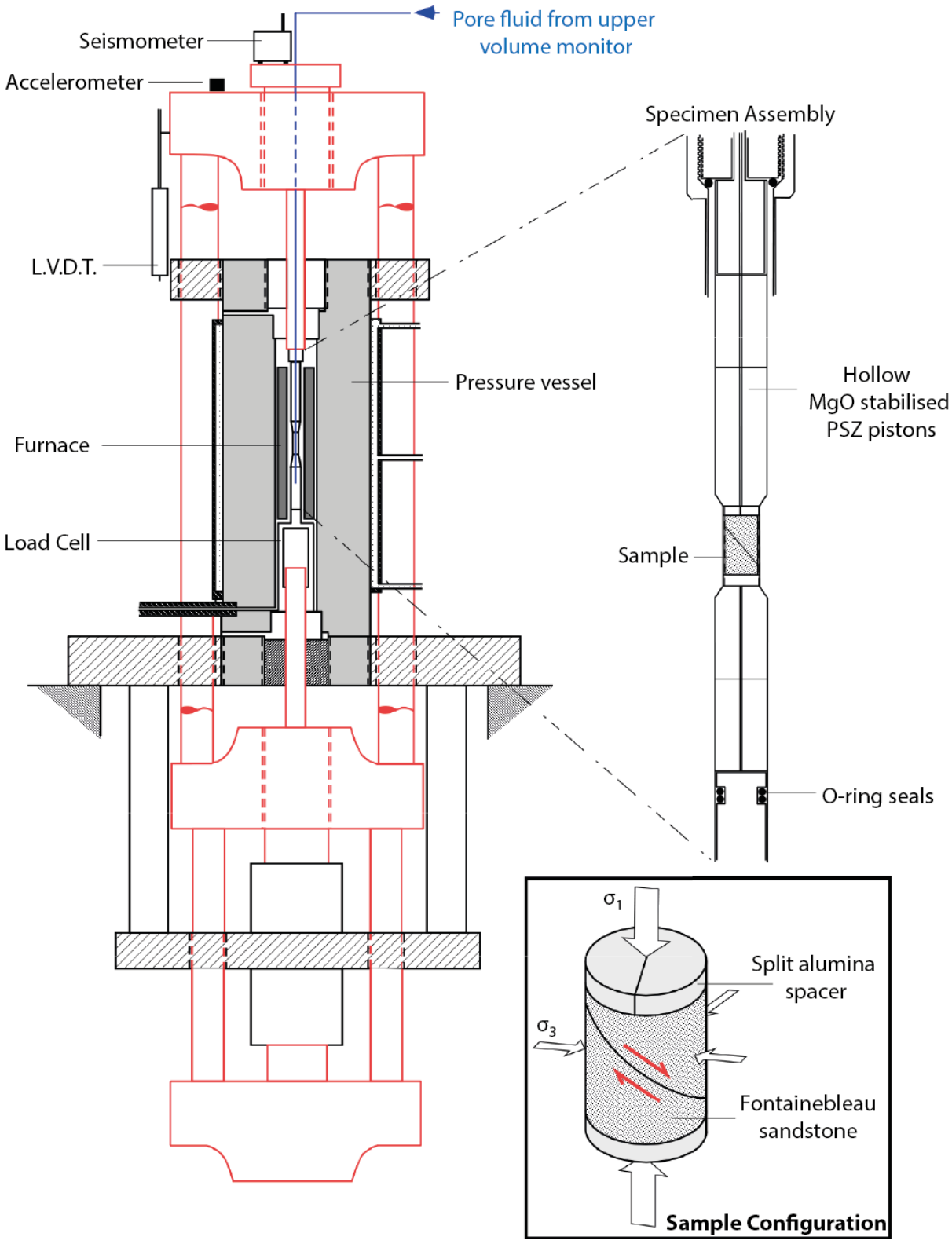

Figure 1: Schematic illustration of deformation apparatus and sample configuration
See text for details.

The longevity of the pseudotachylite in its vitreous form was explored by completing a number of experiments involving isostatic pressing of the slipped sample over a range of experimental conditions in both dry and hydrothermal conditions. To investigate the potential crystallisation of the melt in nominally dry conditions, the axial load was removed and the temperature set at 700º following a large stick-slip event for between 1- 6 hours. This temperature was chosen as it is comfortably within the stability field of β-quartz at the given confining pressures.

To explore the stability of the pseudotachylite in a hydrous environment, two experiments were performed where pore fluids were added following the melt-producing slip event. During these experiments, the axial load was removed following the slip event and the temperature and confining pressure were reduced to T = 25°C and $P_c \approx$ 40MPa. Deionized water pore fluid was then introduced via the upper hollow ceramic (MgO stabilized PSZ) pistons before the temperature and confining pressure were concurrently increased. Approximately 20 minutes prior to the desired conditions being attained, the pore fluid pressure was gradually increased until the hydrothermal isostatic pressing (HTIP) conditions of 500-900ºC, P_c=250MPa and P_f=150MPa were attained. The pore fluid was introduced in this way to ensure that a sufficient effective confining pressure was maintained to preserve the integrity of the assembly seals and to keep the reaction time between the pore fluids and pseudotachylyte constrained as much as possible to the HTIP period of 1 hour.

2.2 Microstructural analysis techniques

The morphology and structure of the slipped surfaces where investigated using a range of techniques including reflected light microscopy, scanning electron microscopy (SEM), transmission electron microscopy (TEM) and x-ray diffraction (XRD). To prepare the slip surfaces for optical and SEM analysis, the jacket and sleeve surrounding the experimental sample were dissolved in concentrated nitric acid. The two halves of the fault were retrieved and carefully rinsed in water, dried and mounted in a custom sample holder for examination by secondary electron SEM. To achieve the highest resolution during imaging whilst minimising charging, the fault surfaces were sputter coated with platinum.

During SEM imaging of the fault surfaces it became apparent that during the dissolution of the copper sleeve, copper nitrate precipitated onto the fault surfaces. The precipitate

was commonly observed to have a spherulitic texture suggesting rapid growth from a liquid, with many of the fine gouge particles serving as crystallisation nucleation points. Consequently, the sample preparation technique was modified to avoid sample – acid contact. For experiments undertaken at temperatures below approximately 700°C the iron jacket and copper sleeve were not bonded and the jacket and sleeve were individually peeled off with great care taken to prevent disturbance of the fault surfaces. For experiments undertaken at higher temperatures, the iron jacket was dissolved in nitric acid and then the inner copper sleeve was manually peeled from the sample.

Fault surface textures were analysed using the in-lens secondary electron (SE) detector of the high resolution Zeiss UltraPlus field emission SEM (FE-SEM). Working conditions of 3.0-5.0kV accelerating voltage, a 10μm objective aperture and a working distance between 3-5mm allowed an imaging resolution of less than 10nm.

Cross-sections from selected areas of the fault surface were prepared for analysis by transmission election microscope (TEM) using a Helios NanoLab 600 Dualbeam focused ion beam scanning electron microscope (FIB-SEM) at the Australian National Fabrication Facility, Canberra. Cross-section foils approximately 12-15μm long, 5μm deep and <100nm thick were milled using a Ga-ion beam before being removed from the sample and mounted on a carbon film TEM grid. TEM analysis was undertaken using a Philips CM300 TEM operating at 300kV accelerating voltage. The TEM foils prepared on the FIB were found to be very sensitive to electron beam damage so to minimise sample heating and damage the majority of TEM work was undertaken at low magnification (up to x15000) and low-intensity illumination (i.e. using a 50μm condenser aperture, 20μm objective aperture and condenser 1 aperture set to spot size 5). Energy dispersive spectroscopy (EDS) was undertaken using a Jeol 2100F field emission TEM, operating at 200kV accelerating voltage. SEM & TEM analysis was undertaken at the Centre for Advanced Microscopy, the Australian National University.

X-ray powder diffraction (XRD) analysis was used as a semi-quantitative tool to examine *in situ* the phases present on slipped fault surfaces. X-ray diffraction was carried out with a SIEMENS D501 Bragg-Brentano diffractometer equipped with a graphite monochromator and scintillation detector, using Cu $K\alpha$ radiation. Multiple pass scans were undertaken with a scan range between 2°-70° 2θ, at a step width of 0.02°, and with a scan speed of 0.33° per minute. The composition was then interpreted using

the SIEMENS software package Diffrac*plus* Eva 10 (2003) which uses the PDF-II database provided by the International Centre for Diffraction Data.

The use of Raman spectroscopy was also attempted to gain an understanding of the composition and structure of the fault wear products, but the laser beam intensity that was required to produce a signal was higher than the sample could support without damage.

3. Results

3.1 Mechanical behaviour

Thirty optimally oriented, high temperature (T=400-950°C), nominally dry bare interface fault experiments were completed over a range of confining pressures (P_c=50-200MPa) and axial displacement rates (a summary of which is provided in Appendix 4). The results reveal a surprisingly complex range of mechanical behaviours with a number of behavioural transitions (Fig. 2A) being observed with changes in temperature and confining pressure. Experiments were undertaken at regular intervals of temperature and confining pressure to better understand and bracket the observed transitions in behaviour.

Although the samples appear to maintain an essentially brittle, high-friction sliding behaviour, the samples deformed at temperatures from 400-600° are characterised by a poorly-defined but high yield point (nearly twice that of similar experiments undertaken at room temperature – refer to Chapter 3). The post-yield sliding behaviour consists of approximately 0.2mm of slip hardening followed by peak stress and a transition into slip weakening, but essentially stable sliding behaviour (Fig. 2A). In contrast, experiments undertaken between 650-927°C generally exhibit the same high yield point, but after varying displacements experience significant stick-slip events. The stick-slip phenomena is manifest by unsteady relative motion of the sliding surfaces and are evidenced by sudden drops in axial load. The audible click that accompanies the stick-slip event alludes to a rupture velocity approaching the speed of sound and a slip rate approaching seismic velocities. Estimations of the coefficient of dynamic friction (assuming the dynamic friction coefficient is given by the ratio of shear stress to normal stress at a given point) is in the order of 0.8 immediately prior to stick-slip events and

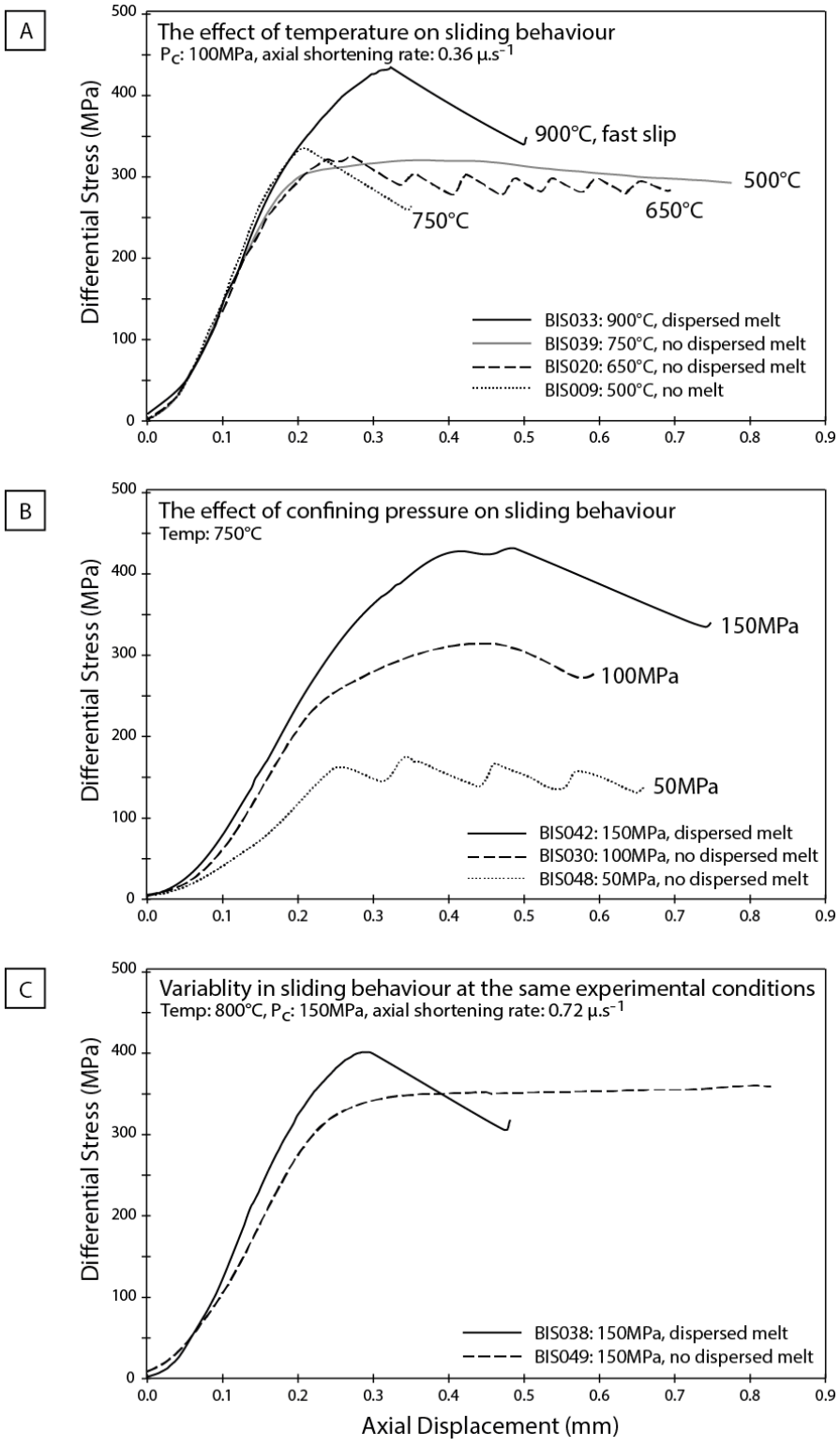

Figure 2: Representative mechanical behaviour of faults over a range of experimental conditions. Graphs show differential stress plotted as a function of axial displacement. (A) Effect of increasing temperature at equivalent confining pressures and nominal axial displacement rates. Fault behaviour is observed to transition from stable sliding, through low amplitude stick-slip to high amplitude, high displacement stick-slip at high temperatures. (B) Increasing magnitude of the stress drop and displacement associated with increasing confining pressures at constant temperatures. Note that melt is only produced during the slip event at the highest confining pressure (see section 3.2). (C) Variations in sliding behaviour at the same experimental conditions - possibly indicating a transition from a stick-slip back into a stable sliding regime at higher confining pressures.

averages ~0.7 during the lower temperature stable sliding experiments. These results are comparable to other frictional sliding experiments undertaken a slow slip rates (<0.1mm.s^{-1}) [*Byerlee*, 1978].

A comparison of experiments undertaken at comparable confining pressures reveals a systematic increase in shear strength (calculated from peak stress prior to the first stick-slip event, if relevant) with increasing temperature, from approximately 128MPa at 400°C to 161MPa at 927°C (Fig. 3A). Undertaking a least squares linear regression of the experimental data supports this observation with a positive correlation being observed between peak shear strength and temperature ($\frac{d\tau}{dT} = 0.061 \pm 0.025$MPa/°C including all data, and $\frac{d\tau}{dT} = 0.065 \pm 0.011$MPa/°C with outliers removed; uncertainty is reported at one standard deviation). However, this result is somewhat biased given the limited number of experiments performed at lower temperatures. The faults that exhibit stick-slip behaviour generally have a higher peak strength, although there are a couple of notable exceptions: first, BIS027 (P_c=100MPa T=800°C) was characterised by an anomalously low peak strength and experienced significant slip weakening prior to failure; and second, BIS026 (P_c=100MPa T=900°C) experienced an initial small stress drop (~12% of peak differential stress) prior to a second, much larger stick-slip event.

The seismometer and accelerometer were installed and used to record data on eight of the stick-slip experiments. Although, the sampling rate of the instrumentation potentially significantly under samples the fault rupture (see Section 2.1), systematic and consistent differences were observed between the different events. While no credence has been placed on the absolute values of the recorded data, the results of the experiments does show the existence of two distinct populations of data: the first has a higher apparent velocity and acceleration, while the second has a comparatively lower apparent velocity and acceleration (Fig. 3B). For ease of communication, these populations will be referred to as high-velocity slip and low-velocity slip events, respectively. The apparent velocity of the slip events displays a strong positive correlation with both net slip displacement (Fig. 3C) and the associated stress drop, with high-velocity slip events slipping further and resulting in larger stress drops than the low velocity experiments. Additional information showing preliminary results of a novel interferometry system designed and built for better constraining slip time is included in Appendix 1.

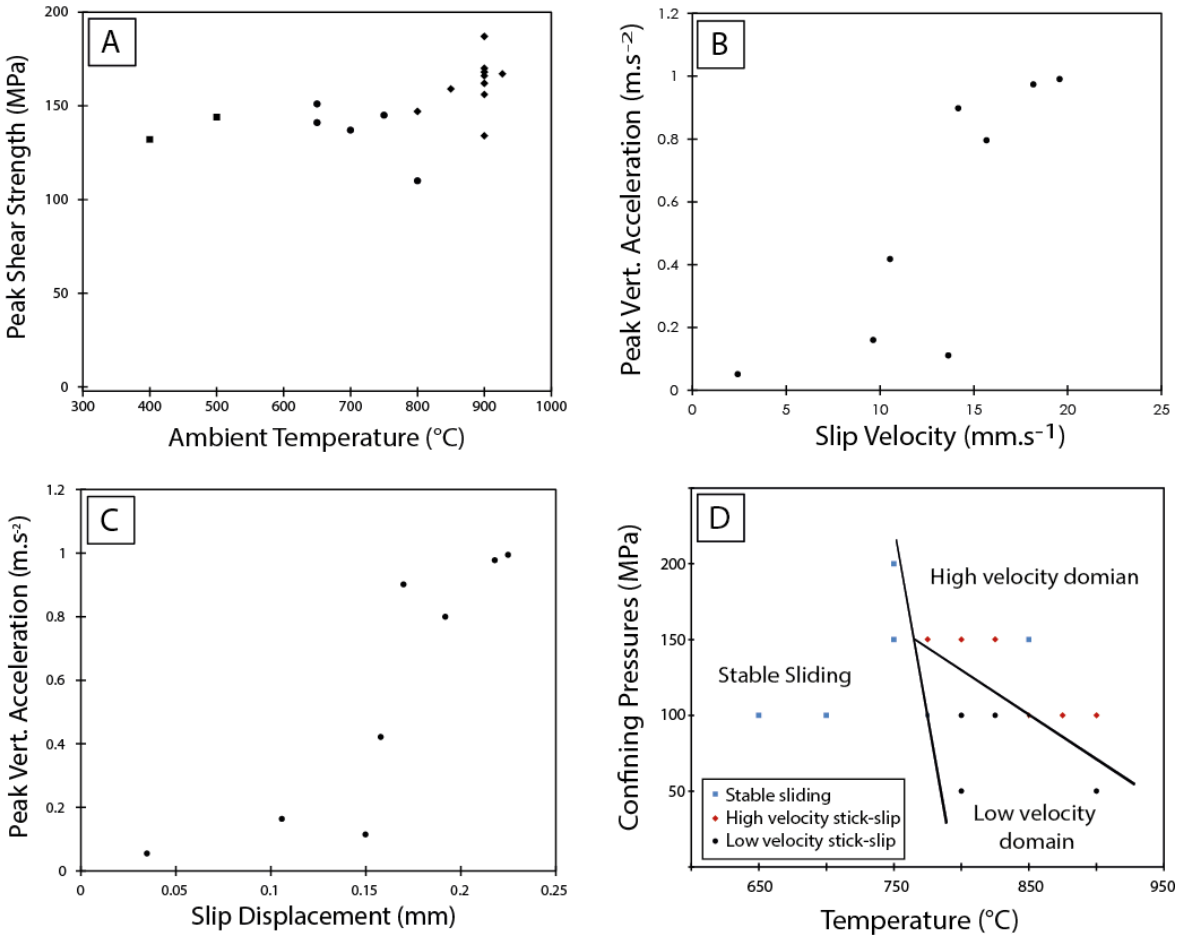

Figure 3: Relationship between experimental conditions and mechanical behaviour.
(A) Comparison of experiments at P_c=100MPa showing the relationship between increasing temperature and peak shear strength. (B) Relative peak vertical acceleration during the first stick-slip event is plotted against slip velocity showing the distinct difference between high apparent acceleration and velocity and low apparent acceleration and velocity. (C) Peak vertical acceleration is plotted as a function of slip displacement showing the strong correlation between high peak acceleration and large slip displacements. (D) Identification of regions of different sliding behaviours as a function of confining pressure and temperature. Note the occurrence of stable sliding at high confining pressures and temperatures.

Many experiments were halted after the first large stress drop to allow analysis of the microstructures developed during rapid slip. However, a number of experiments were also allowed to proceed until a total axial displacement of ~1mm was achieved. For these experiments it was observed that once the stick-slip behaviour developed, it continued, forming alternations between essentially elastic loading and rapid stress drops. For experiments in the low pressure - high temperature region associated with low velocity stick-slip, continued deformation is characterised by a general decrease in peak strength (prior to slip events) and a reduction in the amplitude of the stress drop (e.g., 650°, Fig. 2A), with stress drops in the order of 16% of peak differential stress. In comparison the experiments undertaken at higher temperatures (e.g., 900°, Fig. 2A) experience very large stress drops (in the order of 22% of peak differential stress), with

peak strength prior to subsequent stress drops increasing with continued displacement. Similar observations were made for experiments undertaken at comparatively high confining pressures (Fig. 2B), although the larger stress drops and higher displacement in this case may be partially associated with the increased stored elastic strain in the apparatus.

A number of experiments (notably BIS037 and BIS049) showed differences in sliding behaviour at the same experimental conditions (Fig 2C). It was found that in the temperature range from 650-800°C with increasing confining pressure, both stick-slip and stable sliding behaviours were activated, suggesting the possibility that a transition to stable-sliding behaviour may occur at higher confining pressures (Fig. 3D).

3.2 Optical and SEM microstructural analysis

3.2.1 Fault surfaces that have experienced stick-slip events

The most distinguishing microstructural feature of faults experiencing large displacement, high-velocity slip events, is the formation of reflective, striated areas distributed heterogeneously across the fault surfaces when viewed with a reflected light microscope. Examination of these textures using SE-SEM and TEM (see Section 3.3) reveals that between 10-60% of the fault surface is coated with an amorphous film. These coatings have two very distinct morphologies (Fig. 4): the first, and most easily recognisable, is a veneer of quenched melt or glass on the grain surfaces (with coated areas ranging in size from less than 1μm^2 to in excess of 200μm^2) and characteristically displaying numerous flow structures oriented approximately parallel to the direction of slip (Figs. 4D, 5 & 7). In the following description, where melt-flow textures are present the amorphous material is referred to as ‘melt’. The second type of amorphous layer occurs as fractured ‘patches’ (Figs. 4B, 6), recognisable by the lack of gouge particles and a distinctive, fractured surface that forms parallel to the slip interface (see Section 3.2.2). This layer is shown to have an amorphous structure, with a loss of long range order when analysed using TEM (see Section 3.3). However, while describing the results, where there are no visible melt flow textures present, the layer is referred to as ‘amorphous’ material, to reflect its potential origin through either thermal or mechanical amorphisation processes. The term ‘glass’ is used interchangeably in the description of both of these morphologies to describe material having an amorphous structure.

Compositional analysis (energy dispersive analysis of X-rays) of the melt layer by both SEM and TEM-EDS indicates that it is comprised essentially of pure silica with impurities being below limits of detection. The microstructure of the dispersed film is consistent with a highly viscous siliceous melt. There is limited evidence of lateral extrusion with melt patches forming lobate flow fronts and no evidence of flow into adjacent pores. Many regions are characterised by the formation of long ribbon-like glass filaments (see esp. Fig. 5), thought to be formed when melt adhered to the sliding surfaces is drawn apart during sliding, forming a toffee-like shear sense indicator. In some cases, the glass filaments have snapped while still soft, forming nanometre scale curls and folded pieces of glass (Fig. 5B & F). Other flow textures form striations ranging in length from a few microns to in excess of 150μm (Fig. 4A, 7A).

Occasional fracturing and removal of part of the melt surface during sample recovery, reveals that the thickness of the melt layer is between ~1-2μm (Fig. 5D). The surface of the melt is locally vesicular and SEM imaging indicates that gouge particles are rarely present in the melt. In particular, the striated upper surface of the melt is generally smooth and free of incorporated clasts. Where clasts (ranging in size from 20nm-1μm) are present, they are rounded; many have mantled tails of melt forming linear flow textures parallel to the slip direction (see arrows, Fig. 5E). Locally the melt layer has the appearance of a holey film with glass filaments being drawn off gouge particles (Fig. 5C).

The formation of a striated, dispersed film of melt is a microstructural feature limited to the high-velocity, large stick-slip events. In contrast the formation of the debris-free, fractured patches is a microstructure common to all faults that have experienced a stick-slip event (Fig. 6). However, such glass patches are not found on fault interfaces where the mechanical behaviour is typified by stable sliding. In the higher temperature and pressure experiments, it is thought that the fractured glass patches formed where melt has quenched between grain contacts, essentially bonding the interfaces. These areas subsequently have fractured parallel to the fault surface, forming smooth, debris-free patches. Fracturing could have occurred as a result of either thermal spalling or tensile failure of interfaces during experimental unloading and depressurisation. A number of the fractured patches also show a distinct change in topography between the welded contact and the flow-texture-dominated area. This change potentially represents

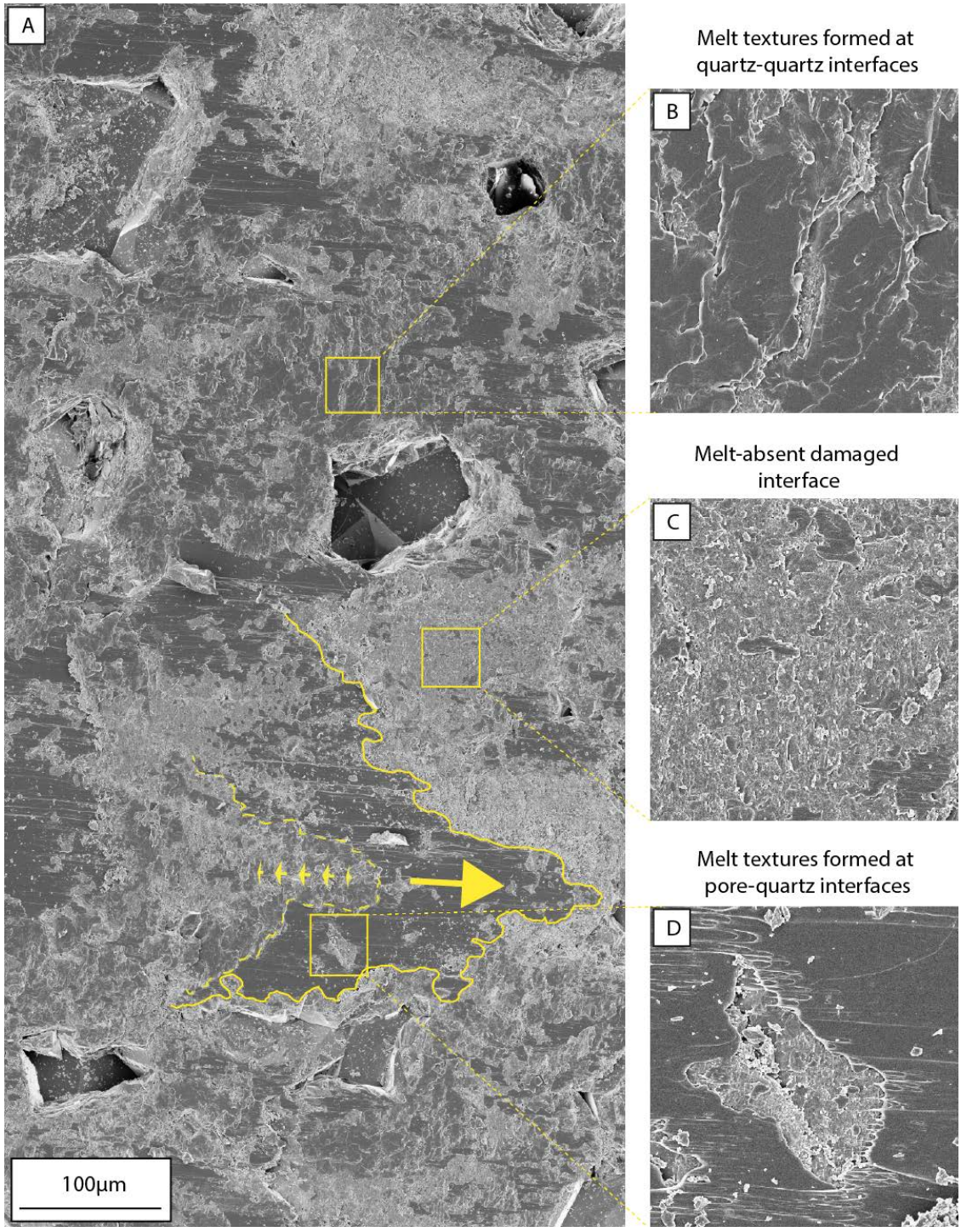

Figure 4: Overview of fault surface showing characteristic microstructures.
(A) Montage of SEM images showing an overview of the fault surface. The outline and displacement of an asperity has been shown from the formation of melt to its final location at the end of slip. Dashed outline and small arrows indicates the relative motion of the upper (removed) fault surface. Large solid arrow shows the relative direction of fault motion of the imaged fault surface. Typical images of the morphology of each of the main surface structures are shown in the insets on the right. (B) Fractured melt patches that are assumed to form at asperity contacts when sliding ceases. (C) Fractured and damaged slip surface – fractures are commonly seen to form perpendicular to the slip direction. Note that gouge is not particularly abundant. (D) Striated flow textures and formation of ribbon-like filaments formed during the slip of a melted asperity contact during rupture.

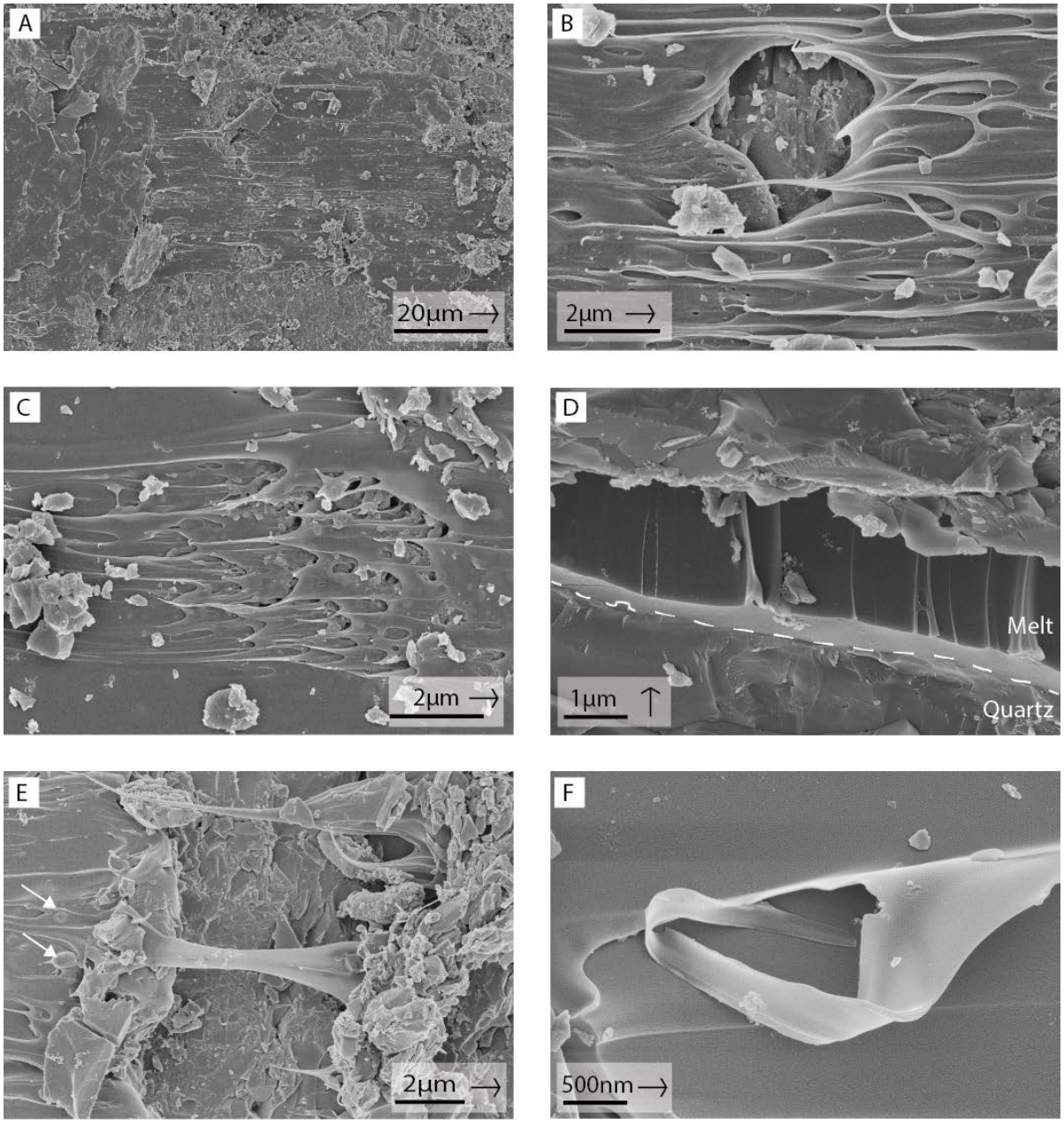

Figure 5: Melt structures on fault surfaces.
Secondary electron SEM images of melt structures on slip surface in BIS010, slipped at 900ºC, P_c=100MPa. Arrows indicate slip direction of the imaged fault block. (A) Overview of an area on the fault surface showing regions of melt (darker grey, lineated surfaces), the lighter-coloured, melt absent fractured fault surface and scattered gouge particles. (B) Detail of the ribbon-like glass filaments on the fault surface. Note the fractured substrate beneath the melt and the lack of significant wear products (gouge). (C) Drawn-out ribbon textures produced where melt has been sheared across a substrate of gouge. (D) Broken away section of melt provides a cross-sectional view of the melt layer. The dashed line indicates the melt-quartz boundary. (E) Drawn out ribbon of melt spanning the gap between surfaces that have separated during slip. Significant quantities of gouge particles have accumulated onto of the melt surface on the right of the image, whereas melt on the left shows the inclusion of clasts within the melt (indicated by white arrows). (F) Example of the delicate structures that are preserved on the fault surface. This image depicts a glass filament that has broken during slip and folded back on itself.

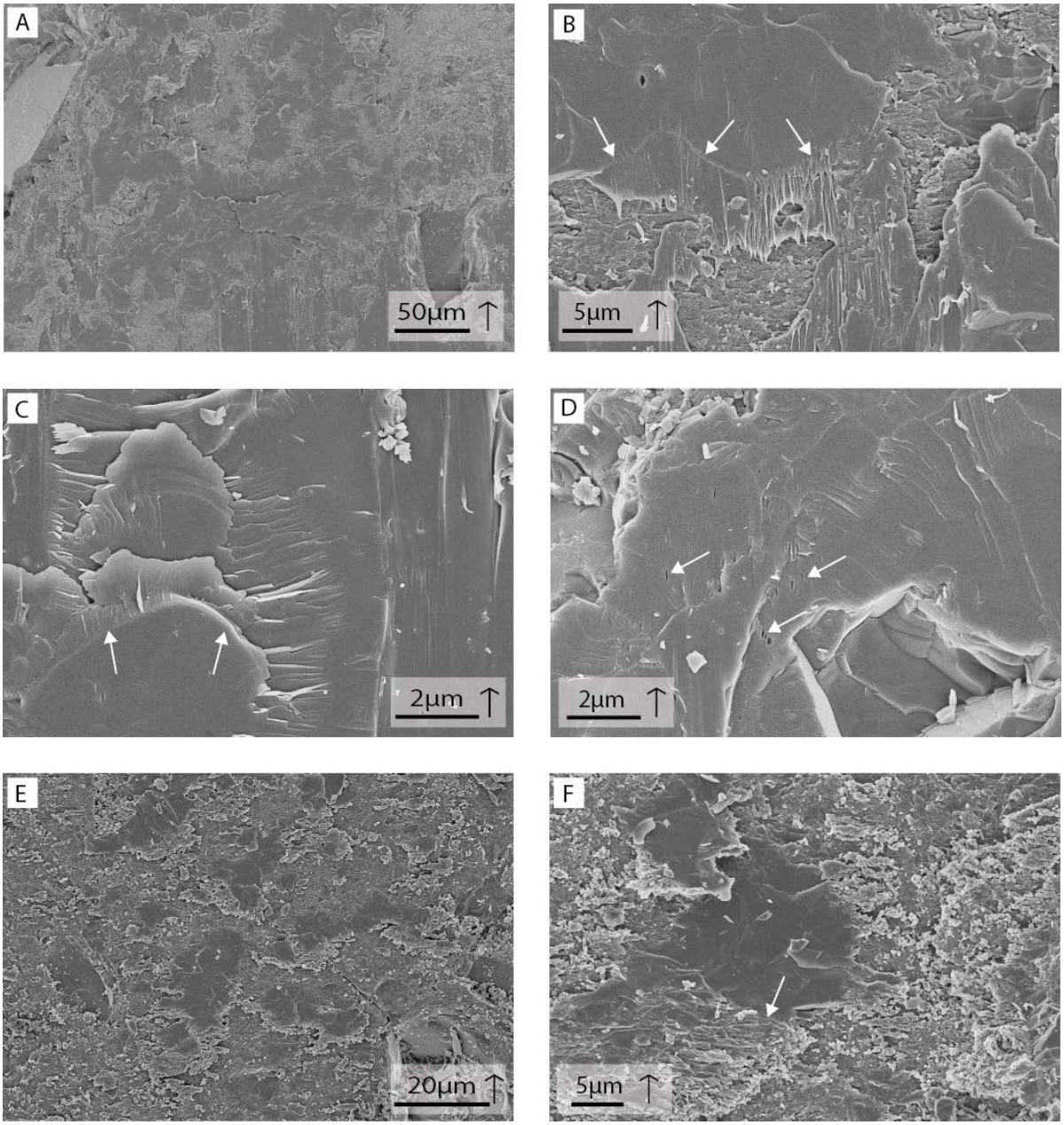

Figure 6: Fractured patches of amorphous material without flow structures.
SE-SEM images of microstructures on fault interfaces - arrows indicate direction of slip of the imaged surface. (A-C) Sample BIS043, overview and details of fault surface showing fractured, debris-free patches, recognisable by the smooth darker regions (A). The continuation of these patches into areas with melt (B) suggests that in the melt-producing experiments these patches are melt which has fractured after quenching. Some patches show what appears to be the outline where an asperity on the removed fault surface contacted melt (C) (see arrows). This suggests that these dark areas are melt that has welded to grain contacts at the cessation of slip. (D) BIS043, fractured melt patch showing elongate vesicles demonstrates melt flow within this melt patch (E) BIS041, fractured, debris-free patches on the surface of a fault that experienced a low velocity slip event. These patches are similar in morphology to those produced during high-velocity slip events where distributed melt is also present. TEM analysis of a patch from this sample has confirmed that the patches are amorphous. (F) BIS030, similar microstructures to (E) and also produced in a low-velocity slip event. Note the extensive brittle fracturing of areas of the patches, with closely spaced fractures forming perpendicular to the slip (see arrows).

the outline of the shape of the asperity or grain on the opposite surface (see arrows, Fig. 6B). Additionally, vesiculated regions within the fractured glass patches typically have vesicles elongate in the direction of slip, thus indicating viscous shear occurred within the melt (Fig. 6D). Glass patches formed during the small stress drop, low velocity slip events (Fig. 6E-F) have a similar habit to those of the high velocity slip events, although the ribbon-textured melt domains (i.e. glass filaments, flow textures etc.) are absent and there is no indication of viscous shear within the patches (e.g. elongate vesicles).

The preservation of delicate melt structures on the rupturing fault surface suggests that melt forms at asperity contacts and is then transported by the shearing surfaces to regions adjacent to pores. The formation and preservation of these melt flow structures provides unique insights into the timing relationships of slip and melt formation. Many of the striated melt-covered surfaces preserve continuous linear flow structures in excess of 150μm long, providing unequivocal evidence of continuous slip on a melted fault surface for the majority (~70%) of the displacement recorded during the rapid slip event (Fig. 7A).

The formation of evenly spaced fractures and indentation marks within the glass layer in close proximity to clasts (Figs. 7B-E) suggest the formation of chatter marks [cf. *Doblas*, 1998] and similarly provide insights into the timing of melt formation. These chatter marks display textures indicating varying degrees of melt viscosity at the time of formation, ranging from molten (Figs. 7B-C) to dominantly brittle (Fig. 7E). The interaction of clasts with less viscous melt (Figs. 7B-C) is commonly characterised by the formation of a ‘bow-wave’ of melt around the front of the clast, accretion of melt onto the clast and the development of a melt-imprinted trail. In comparison, the chatter marks produced on a more viscous surface (Fig. 7E) have left a trail of evenly spaced, semi-brittle fractures inclined in the direction of the clast movement and have an inferred depth and aperture of approximately 200nm. Some chatter marks exhibit both brittle and viscous deformation features (Fig. 7D) and may arise from variations in melt temperature and potential strain-rate dependence of melt deformation.

The presence of fractured remnants of glass filaments, melt textures within areas of accumulated gouge and the fragmentation of areas of quenched melt (e.g. Fig 8), suggests a complicated history of melting and quenching during a single slip event.

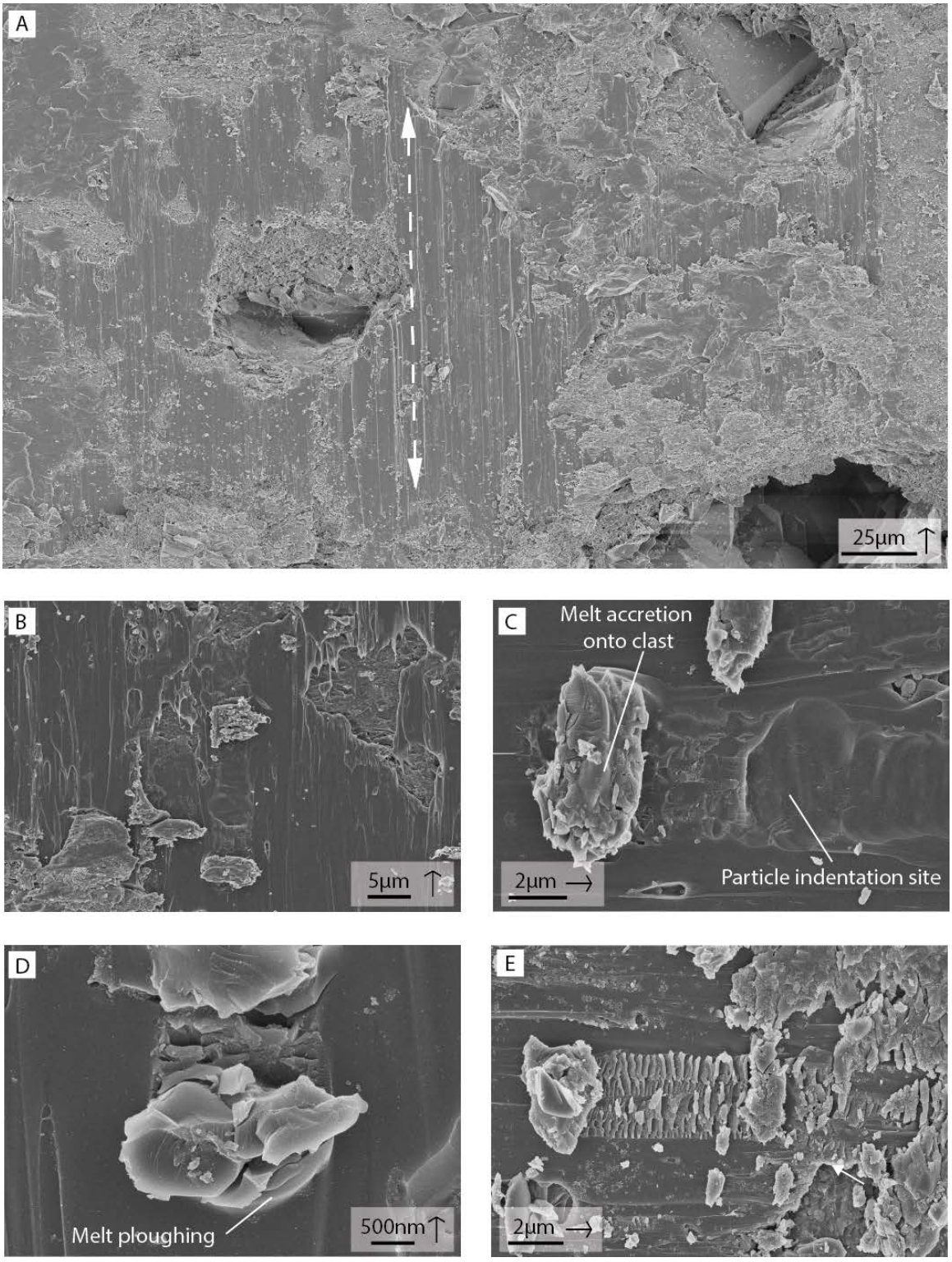

Figure 7: Microstructural insights into the timing relationships between production of melt and slip.
Arrows indicate direction of slip of the imaged surface. (A) BIS043 overview of fault surface showing continuous lineations in excess of 150µm long on the melt surface. (B-D) BIS033, indentation marks in the melt created by a gouge particles being rolled across a melt-covered surface. Note the imprinted trail in melt layer and the accretion of melt onto the clast in B & C. Note that figure C is a detail of B. Fig. D is a good example of the 'bow-wave' effect caused by clast ploughing into the soft surface. (E) BIS032, chatter marks characterised by rows of evenly-spaced, parallel fractures on a semi-quenched melt/glass surface.

Drawn out delicate ribbon-like filaments (diameters < 20nm) indicative of melt stretching, form within the extensively damaged and fractured zones associated with the production of gouge (see arrows, Figs. 8A-C). This raises the possibility that melting occurs locally late in the slip event, overprinting a previously damaged substrate. Significant heating between impinging gouge particles is thought to form these occasional areas of melt.

The quartz substrate in areas immediately adjacent to the melted regions is generally extensively damaged with closely spaced arrays of extension fractures forming orthogonal to the sliding direction and inclined at an acute angle to the slip surface, opposite to direction of motion of the fault block. That is, the fractures dip towards the direction of motion of the opposite fault block, making them a reliable shear sense indicator. These fractures could be the result of both thermal and mechanical processes arising from intense localised temperature gradients, coupled with the substantial dynamic stresses associated with fault slip (Figs. 4-7). The fractures are between 1-3μm in length and spaced between 200nm-1μm apart, forming an extensively damaged surface. Despite this fracturing many of these regions lack surficial wear products (e.g. Fig. 4C).

Where gouge is present on the fault surface, the particles appear to have developed initially as small slivers aligned parallel to the micro-cracks and perpendicular to the direction of slip, resulting in large areas of similarly oriented particles (Fig 8D-E). During subsequent slip many fragments are crushed and rotated, forming areas of irregularly oriented gouge particles ranging in size from <100nm-2μm (Fig. 8F). The volume of gouge on the fault surface positively correlates with increasing aseismic displacement prior to the fault rupture and rapid stress drop. The fault surfaces of experiments that have produced low-velocity slip events also show an increase in the abundance of fragments compared with the gouge produced in experiments where distributed melt is also formed.

3.2.2 Stable sliding of fault surfaces

In experiments where the mechanical behaviour is characterised by stable sliding, the microstructures of the fault interfaces are dominated by brittle deformation processes,

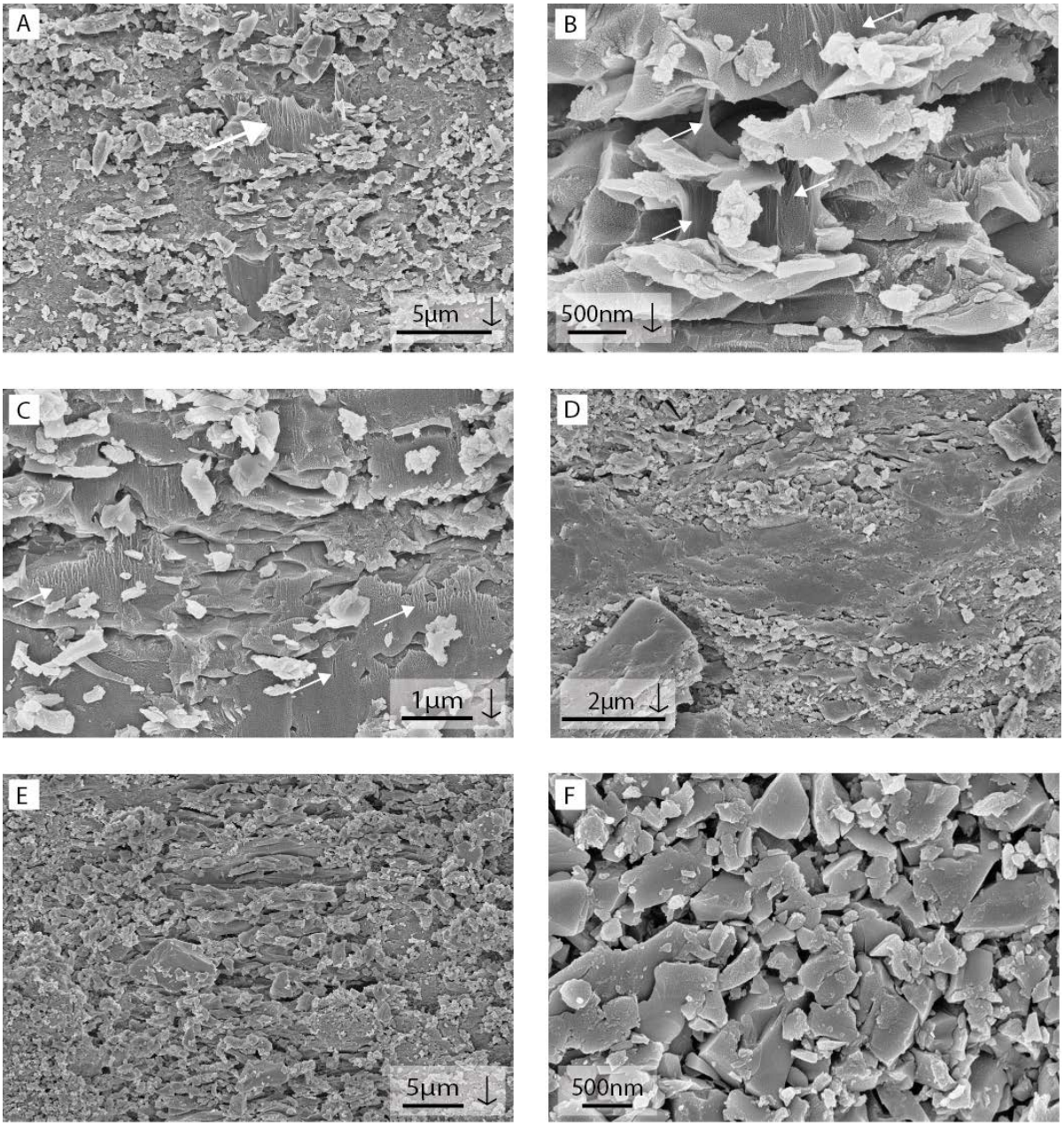

Figure 8: Microstructure of gouge and mechanisms for gouge production on fault surfaces.
SE-SEM images of microstructures on fault interfaces. Black arrows indicate direction of slip of the imaged surface. (A-C) BIS043, examples of melt textures in amongst the gouge particles – drawn out glass ribbons, delicate ribbon-like filaments (diameters < 20nm) as indicated by the white arrows. The surface of substrate in (C) has the morphology of melt (lobate edges, possible elongated vesicles, glass filaments) showing the melting of a previously slipped surface within the same slip event. Note the formation of fractures perpendicular to the slip direction and angular shape of the gouge particles. Images D, E, F are from melt absent interfaces. (D) BIS046, highly comminuted and compacted region. (E) BIS020, example of gouge production on the fault surface with the intense fracturing of the quartz substrate perpendicular to slip direction, forming somewhat aligned slivers of gouge. (F) BIS040, typical example of the size and shape of randomly oriented gouge particles on the fault surfaces. Particles range in size from <100nm-2µm.

with the copious generation of fragments. However, microscopic analysis identifies a range of phenomena that could be either precursory to the microstructures identified in the stick-slip experiments or associated with the development of amorphous material on the fault interface (Fig. 9). Cylindroidal structures present on the slip surface are elongate perpendicular to the direction of slip, and have a morphology indicative of formation as either agglomerated rolls of particles (Fig. 9A-B) or as a rolled film-like structure (see arrows, Fig. 9E). Flaky patches of densely packed, fine-grained material with an overall diameter between 10-25μm are also present on the fault surfaces (Figs. 9C-D and G-H). These structures differ from both the crystalline quartz substrate and the glass patches (formed during stick-slip events) described in Section 3.2.1. At the larger scale these smooth texture zones are characterised by lobate edges and surfaces decorated by slickenlines. Examination at higher magnification densely packed particles bound together in a possibly melt-like matrix (Fig. 9H). Many of these regions exhibit chatter marks similar to those observed on the partially quenched melt surfaces.

Although not unique to stable sliding experiments, a number of samples have 'negative crystals' (see arrow, Fig. 9F). These are interpreted to represent fluid inclusions in the starting quartz crystal that, during hot pressing and deformation, have re-equilibrated to the most stable surface energy state for the inclusion [*Van den Kerkhol and Hein*, 2001]. During SEM imaging the negative crystals are often localised or form on a linear trace, appearing to be generally sub-micron in size and having varyingly developed faceted surfaces. The best developed negative crystal shapes are present in the high temperature or long duration experiments, supporting the interpretation that the fluid inclusions have re-equilibrated during the experiment. These fluid inclusions potentially provide a fluid source for the formation of vesicles present in the melt layers of stick-slip experiments.

3.2.3 The effect of hydrothermal treatment after slip

Two experiments (BIS024 & BIS028) were subjected to hydrothermal isostatic pressing (HTIP) for a period of 1hr, at 900º and 500ºC respectively, after melt-producing slip events. Examination of the slip surfaces using reflected light microscopy reveals the partial to complete destruction of the melt-covered surface on both samples. Occasional fractured reflective regions, similar to the melt patches in the non-hydrothermally

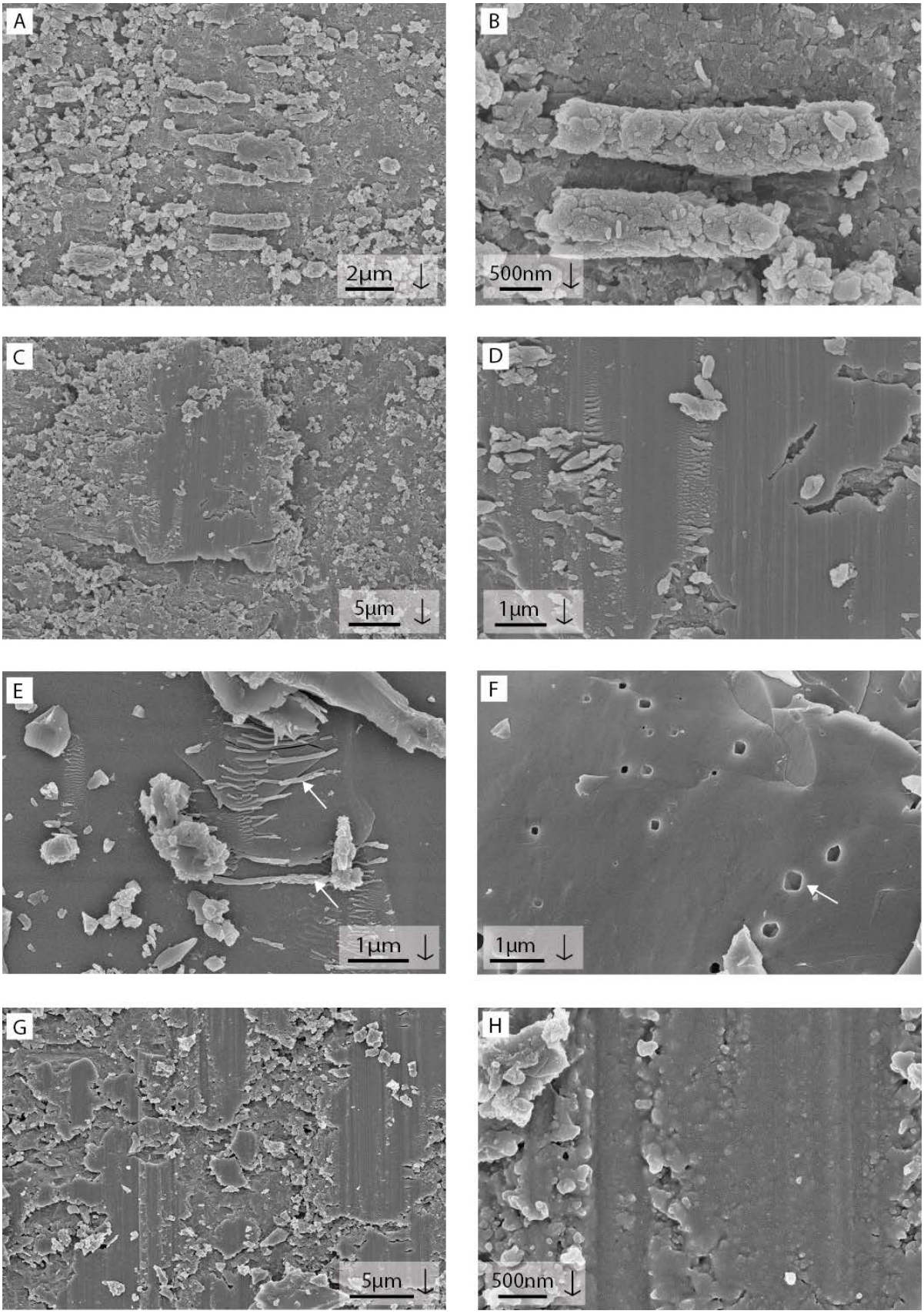

Figure 9: Microstructures from faults that did not experience stick-slip or did not produce visible melt.
For caption please see next page.

treated samples, suggest either residual areas of melt or zones of minimal topography formed by quartz precipitation. SE-SEM analysis of the fault surfaces (Fig. 10) also reveals a dramatic change in microstructure compared with the melt-related textures of an untreated sample. There is no distinguishable evidence of melt remaining on slip surface at the conclusion of either experiment, however on the high temperature HTIP sample some surfaces have developed stepped edges producing polyhedral faceted surfaces (Fig. 10A). The variability of the orientation of the stepped edges between grains suggests that these structures are crystallographically controlled.

Features on the fault surface of BIS028 (500°C HTIP) are more easily correlated with the microstructures in the dry slip experiments. Areas that could be melt-generation surfaces appear to be free of melt; remnants of fractures and slickensteps that are characteristic of the crystalline substrate form approximately linear features perpendicular to the slip direction (see arrows, Fig. 10C). However, these surfaces are also characterised by textures that are very different from the untreated samples. Lobate domains are interspersed with fine (< 1μm) rounded particles that commonly display euhedral faces (Figs. 10C-D). Lineations are parallel to the slip direction and are often recognised by changes in topography of the lobate domains. On the submicron scale many of small (<200nm) particles are observed to be embedded and almost enveloped in the smooth, but occasionally faceted surface (Fig. 10E). The rounding of edges and formation of euhedral surfaces on small grains, together with etching along fractured surfaces and the development of the stepped polyhedral faceted surfaces on the high temperature (900°C) sample, indicate the activation of dissolution-precipitation processes during the hydrothermal treatment. Further evidence of the activation of

Figure 9 continued.
SE-SEM images of microstructures on fault interfaces - arrows indicate direction of slip of the imaged surface. (A-D) Images from BIS048: (A-B) Overview and detail of cylindrical structures resulting from the agglomeration of particles during sliding. These roll-like structures occur on the slip surfaces and are perpendicular to the direction of slip. (C-D) Overview and detail of a lineated, possibly partially amorphous patch on the fault interface. These patches differ from the crystalline quartz, having lobate edges and surfaces lineated by slickenlines. Note also chatter marks similar to those observed on the partially quenched melt surfaces. The fractures associated with the formation of chatter marks are somewhat rounded, implying that they have formed in a soft, deformable material. (E) BIS020, roll-structures (see arrows) on the fault surface, with long axes perpendicular to slip direction. (F) BIS045, inclusions in the crystalline fault surface that have a 'negative crystal' shape (see arrow), representing the most stable surface energy state for the fluid inclusion. (G) BIS037, overview of lineated patches on the fault surface. (H) Detail of (G) showing numerous fine particles bound together in a melt-like matrix.

dissolution-precipitation process occurs on the nano-scale where grain interface structures are visible where gouge particles have been dislodged during sample preparation. The interface structures include ridge and plateau features [cf. *Cox and Paterson*, 1991] that have the semblance of silica precipitation locally surrounding flat bottomed interfacial pores (Fig. 10F, see arrows). More common, however, are the smooth faced dissolution pits or depressions caused by the impingement of grains during HTIP.

The finest fraction of the gouge particles are absent from the HTIP sample. This reflects the rapid dissolution of the fine particles due to their high solubility (Ostwald Ripening) [*Steefel and Van Cappellen*, 1990]. The changes in grainsize are very temperature dependent, with the largest changes being observed in the 900° HTIP sample, where the gouge particles <1000nm have been removed in contrast to the 500°C experiment in which particles <100nm are absent. Many of the remaining gouge particles have lost the angular appearance that is characteristic of gouge in the dry sliding experiments (Fig. 8F), instead becoming rounded and/or developing euhedral surfaces (Fig. 8E-F). The formation of small quantities of platy minerals is also noted. These possibly reflect a reaction between the pore fluid and copper jacket forming copper (II) oxide (CuO).

3.3 TEM analysis

Eight samples for TEM analysis were prepared using ion beam milling in a FIB-SEM. This method of producing TEM foils proved to be extremely useful for analysing cross sections of the fault zones and facilitating comparison of microstructures across a range of scales. The FIB milling process provides a 10-15μm long and 4-5μm wide cross section of a targeted feature on the fault surface, thus providing subsurface information about microstructures identified in the SEM (refer to Appendix 5). In the following section microstructural observations from the FIB sections are described.

3.3.1 High velocity stick-slip events

Five FIB foils were milled across fault surfaces that had produced high velocity stick-slip events. Low magnification bright-field TEM imaging reveals that an amorphous layer, ranging in thickness from approximately 0.3 to 1.7μm is present over the full length of all these sections adjacent to the slip surface (Figs. 11-15). The amorphous

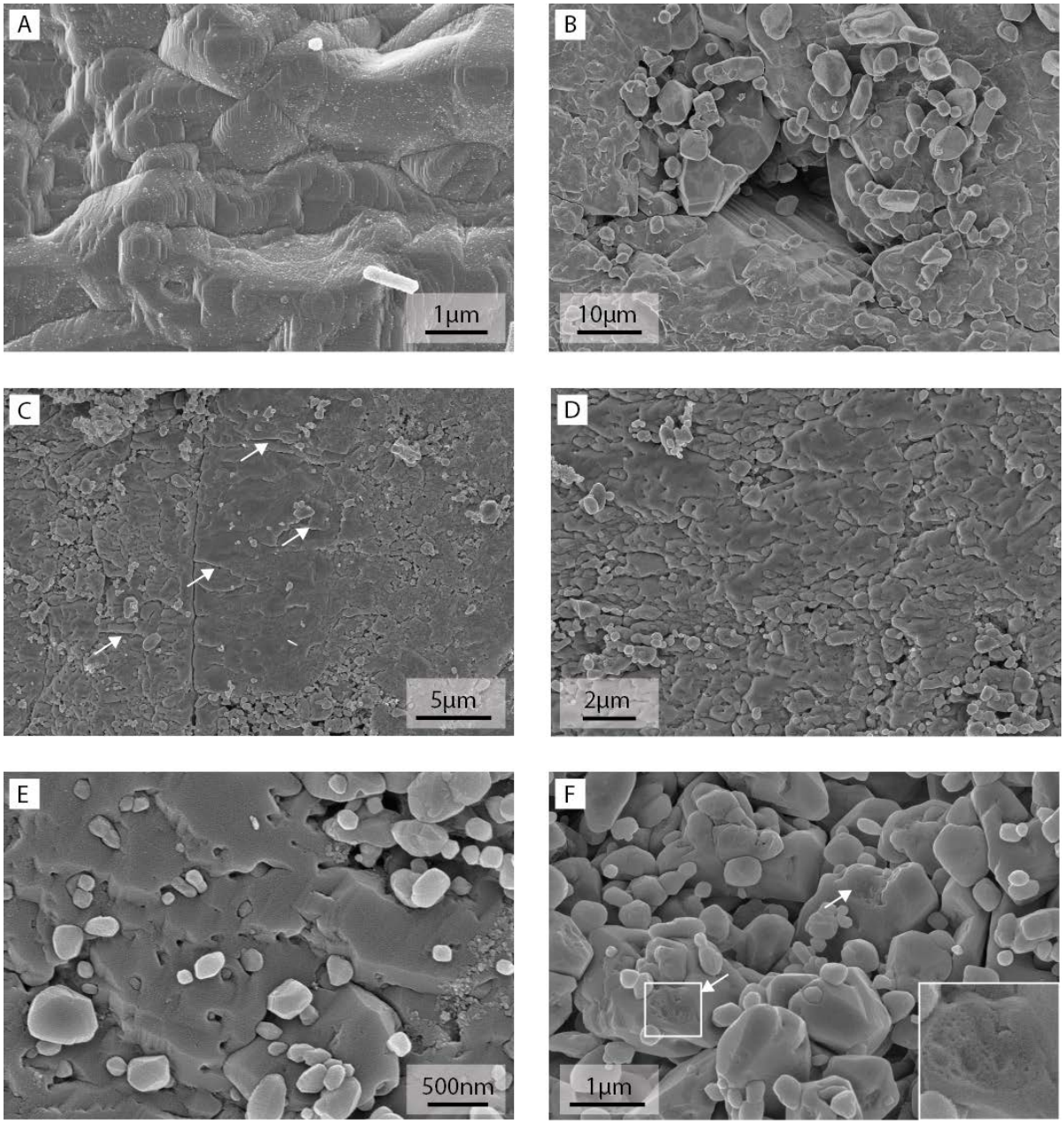

Figure 10: The effect of hydrothermal isostatic pressing on melt covered surfaces.
SE-SEM images of microstructures on fault surfaces. All images have a vertical slip direction. (A-B) BIS024: HTIP at 900°C for 1 hour. (A) Etched crystal on the fault surface. (B) Note the absence of the gouge fraction <1µm in diameter. Remaining larger grains are also more rounded when compared with the dry gouge particles (Fig 7). (C-F) BIS028: HTIP at 500°C for 1 hour. (C) Area assumed to be an originally melt-bearing surface prior to HTIP. Fractures formed perpendicular to the slip direction are exposed and etched. (D) Detail of HTIP surface showing domains of lobate textures. (E) Finest fraction of the gouge material is absent (grains <100nm). The grains have become much more rounded in comparison with samples that have not been HTIP and many of the grain surfaces are developing euhedral faces. Note that many of the smallest residual grains are almost enveloped by overgrowth of the underlying quartz (wall-rock) substrate. Fine grained material on the right hand side of the image is thought to be silica precipitated during quenching. (F) Rounded grains, euhedral faceted surfaces and ridge and plateau structures [cf. *Cox and Paterson*, 1991] on exposed surface of a grain-to-grain contact (see arrows and detail in inset) suggest activation of dissolution and precipitation processes.

material is recognised in bright-field mode by the absence of Bragg diffraction contours and its uniform, unchanging contrast. The amorphous structure was confirmed by selected area electron diffraction (SAED), which shows a broad diffuse ring around the central transmitted beam, reflecting the lack of long-range crystalline order within the sample (Fig. 11A and 13C). For samples BIS010 and BIS035 this amorphous layer corresponds to the striated quenched-melt film that is visible on the surface of samples during SEM analysis. The sections from sample BIS043 (Figs. 13 - 14), were milled in locations characterised by fractured, debris-free melt patches on the fault surface. FIB Section 4 (Fig. 14) was milled across the boundary between the fractured melt patch and a region exhibiting melt flow textures. The presence of the amorphous layer on this sample adds weight to the supposition outlined in the Section 3.2.1 that this area represents melt between two asperities, and that has fractured after quenching.

A number of the characteristic melt textures identified during SEM analysis have been captured in the FIB sections. Linear flow textures are preserved in the sample cut perpendicular to the slip direction, forming small v-shaped structures on the melt surface (identified by the white arrows in Fig. 11F). Small bubbles or vesicles are also preserved in the glass layer in FIB sections 2 & 4 (see white arrows in Fig 12B and Fig. 14A). During slip these bubbles elongate forming elliptical strain markers that are preserved as the melt quenches. The increase in axial ratio of the ellipses away from the crystal-melt interface indicates increasing strain towards the centre of the fault zone. The method of formation of the vesicles is uncertain, but could include processes such as vapour incorporated into melt due to decrepitation of fluid inclusions, or incorporation of air into the melt during slip (e.g. from air pockets trapped during the extrusion or propagation of the melt front through a porous, gouge dominated region).

In all samples, the portion of the melt layer closest to the fault core is homogenous in appearance and free of relict clasts of crystalline quartz; this is consistent with observations made during SEM analysis. Towards the melt-substrate boundary there are relatively small numbers of randomly oriented grains. These range in size from 10nm-1μm and either abut the crystalline substrate or are incorporated into the melt. The clasts are recognised in bright-field imaging by their changing intensity when viewed during

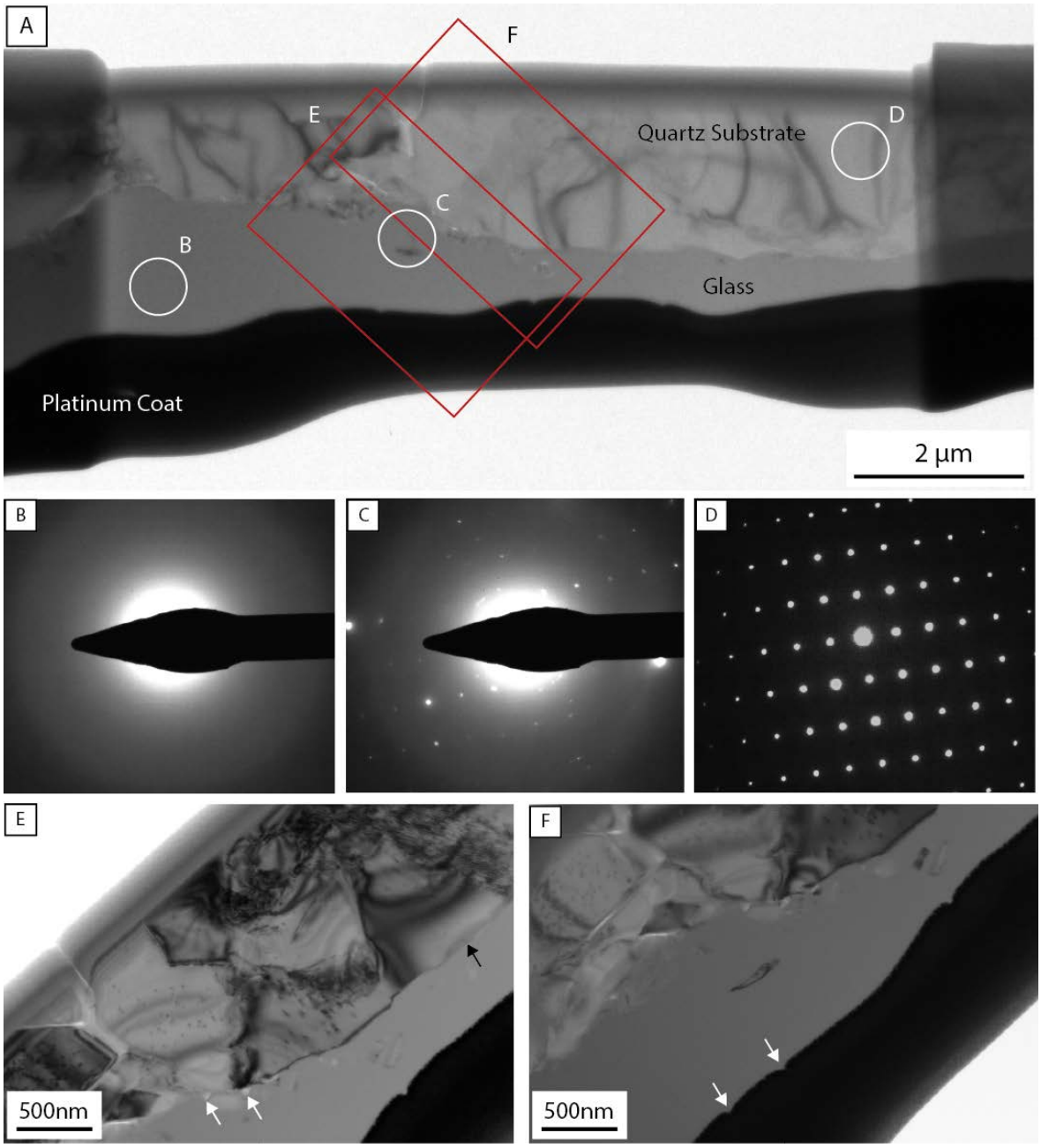

Figure 11: FIB Section 1, BIS010 – High velocity slip experiment cut perpendicular to the slip direction.
(A) Low magnification bright-field image of the FIB section. The location of the higher magnification images is indicated by the red rectangles and the circles indicate the locations where the diffraction patterns were collected. The black layer is a coating of platinum deposited prior to milling the section to protect the sample from ion beam damage. The melt film is the 0.5-2µm thick homogeneous layer of uniform contrast between the platinum and the crystalline substrate (recognisable by the Bragg contours). (B) The broad diffuse ring in diffraction pattern confirms the amorphous structure of the melt layer. (C) A number of small crystalline particles are present in close to the melt-substrate boundary – as shown by the diffraction spots. Note the clusters of diffraction spots forming an inner ring close to the transmitted beam showing the presence of multiple grains. (D) Diffraction pattern confirms the crystalline nature of the quartz substrate. (E) Triangular pores (indicated by the white arrows) are present on the junctions between melt, gouge particles, and the substrate. Note the very sharp melt-crystal boundary (indicated by the black arrow) that is <10nm wide. (F) Small gouge particles are very visible within the melt layer. Also note the flow structures that are preserved by the platinum at the surface of the melt (see arrows). Images (E) and (F) also exhibit beam damage which is evidenced by the spots on the crystalline areas

sample tilting with the objective aperture in place, signifying diffraction by crystalline material. The SAED pattern is characterised by diffraction spots in a broader band of diffuse electron intensity that is consistent with multiple crystalline grains in an amorphous matrix (Fig. 11C).

FIB Section 3, milled from BIS043, contains a larger number of clasts than the other sections, with many having angular shapes. A number of the larger clasts are laced by a network of melt-filled fractures (see arrows, Fig. 13C). The angularity of the crystalline fragments indicates that the clasts are gouge particles that have been incorporated into the melt. The angularity may indicate that grains have not significantly melted. In contrast, in Section 6 from BIS035 (Fig. 15C), a region within the amorphous layer contains very fine quartz crystals (diameter between ~5-50nm) that are rounded in appearance, possibly signifying incorporation by the melt prior to quenching. This sample was hot pressed under isostatic conditions for 6 hours at 700°C following slip. The lack of euhedral shapes implies that these crystals did not nucleate from the silica glass during hot pressing. The absence of devitrification textures such as spherulites shows that in dry experimental conditions, the melt is relatively stable over the time frame of the hot pressing.

The sharpness of the glass - quartz substrate boundary is notable (e.g., Fig.11 and Fig. 15), with many (see black arrow, Figure 11E) being less than 10nm wide. Such boundaries are consistent with observations made of melt-crystal interfaces during thermal induced melting [*Dell'Angelo and Tullis*, 1988].

Unlike many natural pseudotachylytes which, at a macroscopic level, have remarkably planar melt generation surfaces, all the samples show significant topography along the melt-crystal interface, with height variation ranging up to ~1μm, on sections cut parallel to fault slip. The interface morphology of FIB samples where an amorphous layer overlies the crystalline quartz substrate is controlled largely by the formation of arrays of extension fractures in the substrate; these are oriented at between ~30° and 90° to the slip surface in a direction opposite to the sense of motion of the imaged fault block (e.g., see arrows, Fig. 15B, F). The leading edge of the hanging wall of many of these fractures is fragmented and forms pockets of intensely fractured material with a similar orientation (Fig. 15B). The consistency of crystalline orientation among grains is

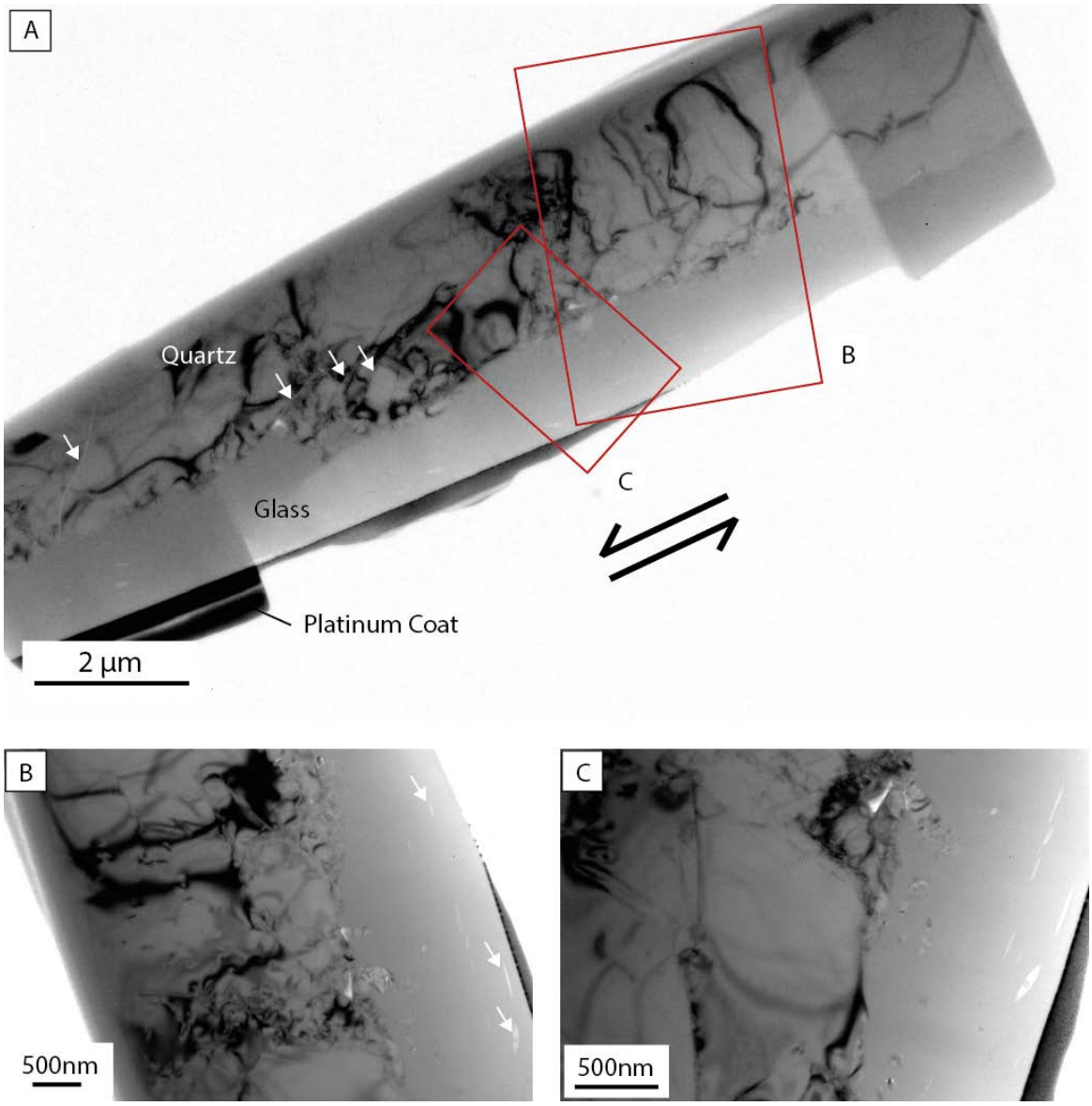

Figure 12: FIB Section 2, BIS010 – High velocity stick-slip event cut parallel to slip direction.
(A) Low magnification bright-field image of the FIB section. Arrows indicate the fault slip-sense and location of the higher magnification images are indicated by the red rectangles. The melt film is clearly visible as the homogeneous region of uniform contrast between the residue platinum layer and crystalline substrate (recognisable by the Bragg contours and variable contrast). Note the pores in the substrate that are identifiable by the bright/white areas. Numerous, possibly melt filled fractures extend from the fault surface down into the substrate, with their orientation consistent with shear sense (see arrows). (B) Numerous vesicles are present in the melt layer and have been elongated during fault slip (identified by arrows). Note the gouge particles along the melt/crystal boundary. (C) A number of gouge particles can be seen dispersed in the melt layer. Note the collection of gouge particles at the melt/substrate boundary in the upper portion of the image (recognisable by the variable contrast and higher porosity). An example of a sharp crystal/melt boundary can also be seen in the lower portion of the image.

determined in bright-field imaging by the similarity of electron intensity between different grains within an region when the objective aperture is in place. This and other similar fragmented material may be a source of gouge particles that become entrained within the melt.

The crystalline quartz substrate in all FIB sections is recognisable in bright-field TEM images by Bragg contours corresponding to highly variable image intensity. The differences in contrast between grains relates to variations in crystal orientation and/or to sample thickness. Holes, fluid inclusions and pores appear as light grey to white, corresponding to lower scattering of electrons resulting from the reduced thickness of crystalline quartz. The SAED patterns confirm the crystallinity of the quartz substrate (e.g., Fig. 11D). The microstructure of the quartz substrate is complex, with extensive fracturing and other deformation-related microstructures such as dislocations, subgrains, and healed micro-fractures (Figs. 11-15). These complexities reflect microstructures from both the current experimental deformation, and also from the previous deformation history of the clasts forming the Fontainebleau sandstone (refer to Appendix 3). However, for the purposes of this study the main focus is on the microstructures associated with amorphisation and the amorphous-crystalline interface, so only brief observations are made regarding the crystalline substrate.

A number of the FIB sections have numerous fractures that penetrate up to 2.5μm from the melt-quartz interface into the substrate, and contain amorphous material. For example, the melt-filled fracture (see black arrows, Fig. 14G) penetrates the substrate at approximately 90° to the slip surface and has a number of subsidiary melt-filled fractures branching off at a high angle to the main vein. However, in other locations determining if microcracks within the substrate contain melt can be very difficult in bright-field imaging due to factors such as fracture orientation and sample thickness. In some situations, dark-field mode TEM observations can be used to highlight the amorphous material by enhancing sensitivity to crystalline orientation. In Figure 15F, melt-filled microfractures have formed in the quartz near the glass-substrate boundary and are highlighted by their uniform higher intensity relative to the quartz substrate. These glass-filled veins are up to ~850nm in length, ~10-20nm wide and have a uniform orientation, dipping away from the direction of motion of the imaged fault block. The development of these veins at a high angle to σ_3 is consistent with the formation

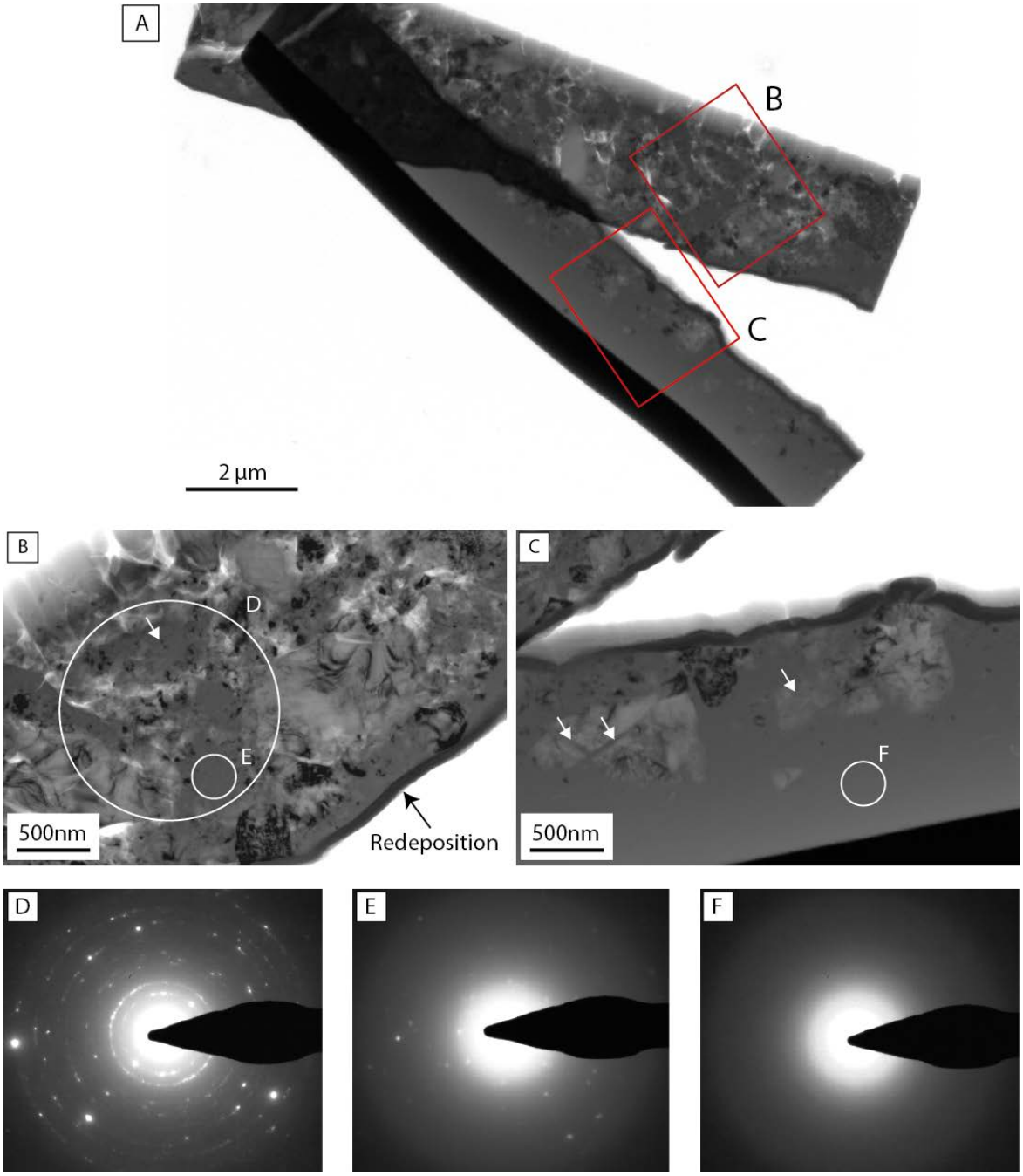

Figure 13: FIB Section 3, BIS043 – High velocity stick-slip experiment cut parallel to the slip direction on a fractured area with no visible melts textures.
During milling it was apparent that there was fracture or plane of weakness ~1.7µm beneath the surface of the sample. When the section was removed it separated along this fracture and became misaligned during placement on the carbon TEM grid. The approximately 100nm wide dark layer at the boundary of the two sections (see black arrow in image B) is thought to be the result of re-deposition of material during milling. (A) Low magnification bright-field image of the FIB section showing the location of the other higher magnification images. (B) The substrate in this sample is composed of a porous agglomeration of numerous particles - most likely accumulated gouge. Diffraction pattern collected at area D indicates the random orientation of grains within the substrate (identifiable by the formation of diffraction rings). The diffraction pattern collected at area E shows the presence of amorphous material within the substrate – indicated by the broad diffuse ring. This area also contains a number of small crystals as indicated by the diffraction spots. (C) Amorphous layer as shown by diffraction pattern F. Unlike the other samples, this amorphous layer contains a number of large (<1µm) clasts, some of which contain one or more melt filled factures (indicated by arrows).

as extension veins during fault slip.

Variable densities of dislocations are present within the crystalline substrate of the samples, as expected given the presence of undulose extinction in the starting material (see Appendix 3). Localised dislocation arrays are accompanied by a high density of fluid inclusions (see arrows, Fig 15E). These dislocations are interpreted to have developed along healed micro-cracks [cf. *Fitz Gerald et al.*, 1991] in the quartz prior to erosion and incorporation of clasts in the Fontainebleau sandstone, rather than during experimental deformation. However, the crystalline substrate of FIB Section 4 (Fig. 14) is characterised by the formation of parallel linear defects in the ~2μm adjacent to the melt interface. TEM analysis indicates that these structures are dislocation lines and their approximately straight orientation suggests that they are restricted to their glide planes, forming parallel to (0001).

Dark-field imaging of the crystalline substrate in areas where the dislocations have formed shows the presence of amorphous material within fractures (Fig. 14E,G). Brittle deformation of this region of the substrate also appears to be controlled by crystallographic orientation, with consistently oriented fractures assumed to be forming parallel to a plane (not identified) of weakness within the crystal. The morphology of the melt-substrate interface and the formation of gouge fragments within the melt layer are governed by the geometry of the defects, with melt invasion of these sites forming stacked blocks of similarly oriented crystals making up the gouge (Fig. 14D). The change in orientation of the upper 1-2 clasts (shown by a change in diffraction intensity relative the rest of the sequence) implies the beginning of rotation and entrainment of the clasts within the shearing melt layer.

The substrate of FIB Section 3 (Fig. 13) is not composed of large fractured grains, like the other samples, but rather, is an agglomeration of irregularly oriented grains (diameter from <100nm ~1.5μm) interspersed with melt and voids/pores. The irregular orientation of the grains is confirmed by the ring shaped SAED pattern (Fig.13D). In a number of locations within the substrate the nanocrystalline particles (grain diameter <100nm) are located within an amorphous matrix. In bright-field the nanocrystalline material is recognised by the small diffracting particles (see white arrow, Fig. 13B) embedded within a uniform grey glass matrix. SAED patterns confirm the dominance of

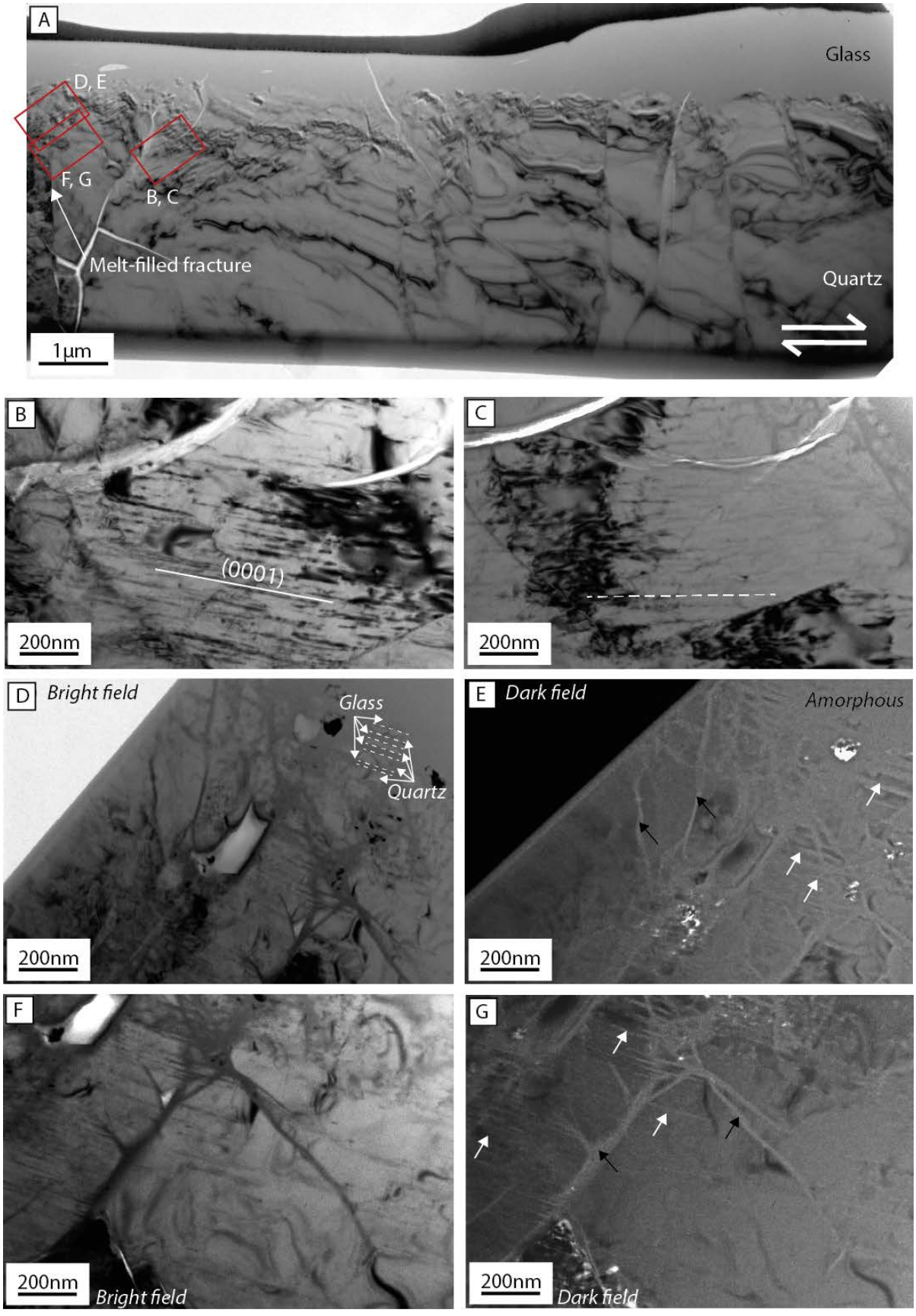

Figure 14: FIB Section 4, BIS043 – high velocity experiment cut parallel to slip direction on an boundary between striated melt textures and a fractured, debris free patch.
For caption please see next page.

amorphous material within area B (Fig. 13) and also weak crystalline spots. Porosity is variable within the substrate of this sample with higher porosity regions being located either adjacent to clasts or away from the glass-substrate boundary.

3.3.2 Low velocity stick-slip events

A FIB sample was milled into a fractured, debris-free patch on the surface of BIS041 (P_c = 50MPa, T = 900°, Fig. 16), which is a sample that experienced a small displacement (106μm) slip event. SEM analysis of the slip interface had shown no visible signs of melt flow textures, other than the fractured, glass-like debris-free patches (Fig. 6E). However, TEM of a cross section of the fault zone uncovers many of the first-order features that are present in the high slip velocity samples, including an approximately 600nm wide amorphous layer between the fault surface and the crystalline substrate. Compositional analysis of the amorphous material using TEM-EDS reveals that the material is essentially pure silica, with other detected elements being attributable to contamination associated with FIB sample preparation (such as gallium and platinum; for analysis locations see red dashed circles, Fig. 16).

Comparatively more clasts occur within the amorphous layer of this FIB section than occur in the high slip velocity samples described in Section 3.3.1, with clasts ranging in size between <10nm to 200nm. A number of the clasts exhibit textures indicative of

Figure 14 continued.
(A) Low magnification bright-field image of the FIB section. Location of the higher magnification images is indicated by the red rectangles and the arrows indicate the fault slip-sense. The melt film is clearly visible as the homogeneous region of uniform contrast between the protective platinum layer and crystalline substrate. This FIB section was milled on the boundary between a region showing striated melt textures and a fractured debris-free patch. The boundary between the two zones is recognisable only by the change in topography of the upper surface of the melt. Note the development of a linear texture within the crystalline substrate, especially on the upper left side of the sample and the formation of a large, approximately vertical melt filled fracture – recognisable by the change of contrast between the crystalline regions at the far left of image A. (B-C) Image of the dislocations formed parallel with (0001) of the quartz. Rotation of the image perpendicular to the basal plane shows the rotation of the linear structures (see relative differences in the angle of the white line), conclusively showing that these features are linear and not planar structures. (D-E) Bright-field and dark-field image of the same region highlighting the formation of possible amorphous material along fractures (black arrows) and possible fractures associated with dislocations (white arrows) within the sample substrate. Note the melt-invasion of the single crystal quartz causing the substrate boundary to have the appearance of stacked blocks (highlighted by dashed lines). The dark particles within this region indicate clasts that have rotated into a different orientation. (E) In the dark-field images the amorphous material is visually accentuated as the intermediate grey contrast between the dark, non-diffracting crystals and bright diffracting crystals. (F-G) Bright-field and dark-field images of a region adjacent to (D-E) but further away from the melt-substrate boundary. Again images show the possible presence of amorphous material along fractures at a depth of >1μm from the melt-substrate boundary.

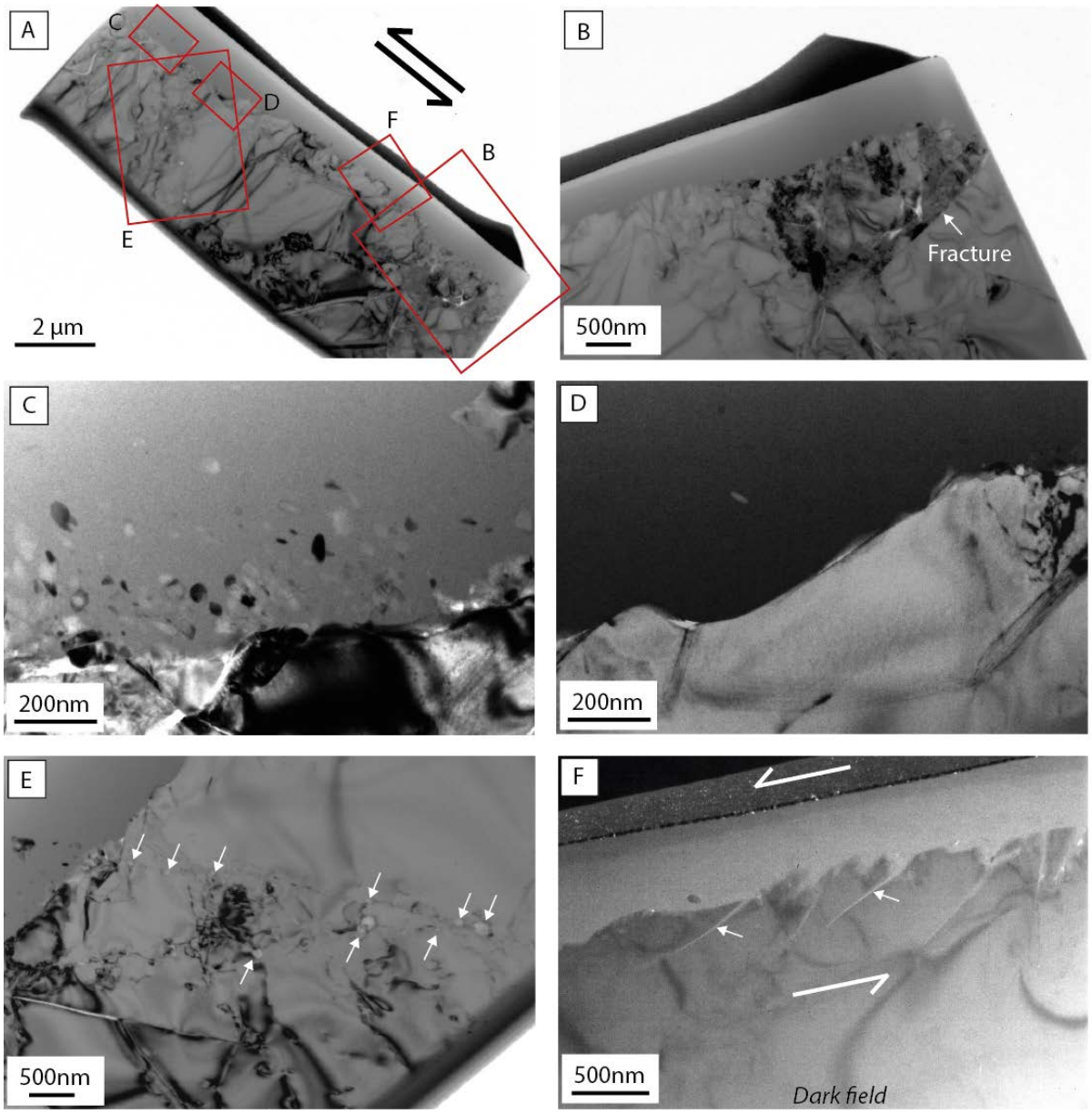

Figure 15: FIB Section 5, BIS035 from high velocity slip experiment cut parallel to slip direction and perpendicular to slip surface; hot-pressed for 6 hours following slip.
(A) Low magnification bright-field image of the FIB section with location of other images shown. Arrows indicate slip sense. The melt film is clearly visible as the homogeneous amorphous layer between the platinum and crystalline quartz substrate (recognisable by the Bragg contours and variable contrast). (B) The area of high contrast outlines a region of numerous fine particles – note the very similar crystallographic orientation of different regions of gouge particles (ascertained from the similarity of diffraction contrast). (C) Very fine crystalline grains (d=10-100nm) within the amorphous layer. Grains have rounded shapes suggesting melting of the outer faces of the gouge particles. (D) Sharp boundary between melt and the crystalline substrate (width of < 10nm). For this image the sample has been tilted so that the crystalline material diffracts less strongly than the amorphous material, thus making the contrast of the melt appear darker than quartz substrate. (E) Healed micro cracks within the quartz substrate. The locations of the micro cracks are identifiable by the dislocation arrays linking bands of fluid inclusions (see arrows). (F) Dark-field image highlighting melt filled fractures along a grain at the melt – substrate boundary.

partial melting, including embayed margins and the development of incipient melt veins within the entrained clast. In topographically lower regions of the amorphous-crystalline interface, a number of pockets of gouge remain, while in contrast, other regions of the interface are characterised by a sharp, debris-free boundary. In many locations within the amorphous layer, the crystalline gouge particles are irregularly distributed, whereas in other areas the clasts occur in clusters and form trails of particles approximately parallel with the melt-substrate boundary (see dashed lines, Fig. 16F). The absence of microstructures such as elongate vesicles or melt-flow textures indicating viscous flow suggests the possibility that these debris trails may not be a shear-related feature, but instead may represent features such as grain-size variation in the fault zone prior to melting.

Within the melt layer are a number of fractures oriented parallel to the melt formation surface (e.g., Fig. 16A, F). These fractures possibly form as a result of local tensile stresses within the glass layer during quenching, unloading or decompression. Intense fracturing is also observed in a clast at the slip interface, resulting in the formation of closely-spaced (<50nm) parallel fractures (see arrows, Fig. 16F) orientated at a high angle (~90º) to the slip surface, again suggesting possible crystallographic control. These fractures contain amorphous material as shown by the lack of contrast change during specimen tilting in bright-field mode; the presence of amorphous material could arise from either melt injection or from preferential melting along the fracture boundaries. Regardless, such fractures must have formed during slip activity.

3.3.2 Microstructures formed during stable sliding

A TEM foil was milled perpendicular to the slip surface and parallel to the slip direction of BIS037 (P_c = 150MPa, T = 800°, Fig. 17) in an area where densely-packed particles are bonded with a melt-like matrix, forming the lineated gouge patch identified during SEM imaging (Figs. 9G-H). TEM analysis reveals that the slip surface is remarkably planar and formed by a layer of compacted, finely-crushed quartz ranging in thickness from ~200nm-1μm. The variation in thickness of the layer results from the significant topography along the boundary with the intact quartz substrate. The resolvable size of gouge particles within this layer ranges between 10nm - 200nm, with particle size

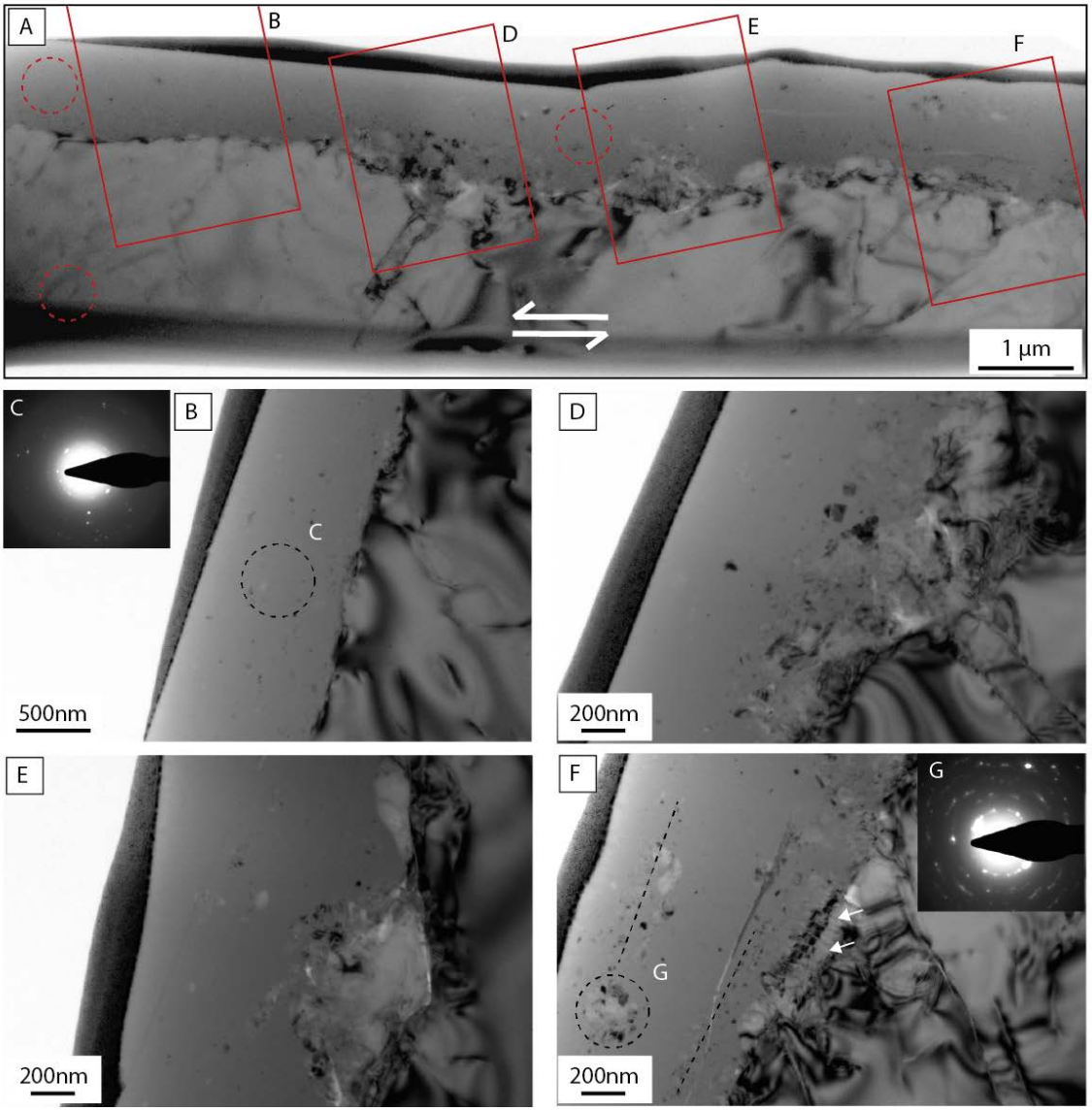

Figure 16: FIB Section 6, BIS041 - Low velocity stick-slip experiment cut perpendicular to the slip surface and parallel to slip direction.
All TEM micrographs are bright-field images with the exception of the SAED patterns. (A) Low magnification image of the FIB section. Location of the higher magnification images is indicated by the red rectangles. Arrows indicate the sense of fault motion. FIB section was milled into fractured patch on the slip surface of BIS041. An amorphous film is clearly visible as the largely homogeneous region of uniform intensity between the platinum layer and crystalline substrate and is very similar in appearance to the melt layers observed following high velocity slip events. (B) Micrograph showing the numerous small randomly oriented crystalline particles within the amorphous layer. Note the essentially gouge free nature of the amorphous-substrate boundary. (C) Inset shows the diffraction pattern taken at the indicated location and shows a broad diffuse amorphous ring with numerous randomly oriented crystals. (D) Amorphous-crystalline boundary showing numerous gouge particles. Pores within the gouge particles are recognisable by their higher intensity. Note embayed margins on many of the clasts. (E) Amorphous-substrate boundary showing melt penetration of a gouge-rich zone. Note the formation of a low angle fracture from the surface of the melt (lower left hand corner). (F) Crystalline clasts within the amorphous layer appear to form diffuse elongate trails approximately parallel with melt-substrate boundary, as indicated by dashed lines. Clast at interface shows the development of a dense array of amorphous-filled microfractures as indicated by arrows. (G) SAED pattern of gouge particles and amorphous matrix at the location indicated. The ring-like configuration of the diffraction spots indicates numerous irregularly oriented particles.

increasing away from the principal slip zone. A few much larger, fractured, but unrotated grains occur close to the undamaged substrate and have a diameter of approximately 0.5μm.

During high resolution SEM imaging, the morphology of the lineated patches pointed to the formation of a non-crystalline matrix, recognisable by its film-like properties. However, TEM analysis of the fine-grained quartz within the gouge zone proved difficult due to the relative thickness of the sample (~100nm) compared with the size of gouge particles and potential for overlap of fragments and pores. For this reason identification of potentially amorphous material was extremely difficult using bright-field imaging and consequently dark-field imaging was employed [cf. *Yund et al.*, 1990]. In dark field mode, potential amorphous material is found to have an intermediate contrast between the bright crystalline gouge fragments, whose reflections fall within the objective aperture, and the low intensity of the crystalline material whose reflections fall outside the aperture. Comparative bright-field and dark field images are shown in Figure 17(B-E).

A comparison of the dark-field images suggests that amorphous material occurs within the gouge layer over a depth of 50-500nm, partially bonding the quartz particles. It is uncertain whether this ‘amorphous’ material represents particles with grain sizes less than the resolvable 10nm that is simply too small to image, or whether it is a true amorphous material resulting from the loss of long range crystalline order. However, this ‘amorphous’ material appears to be mainly in the 100nm immediately adjacent to the principal slip zone, with an increase in the crystalline fraction beyond this depth. The possibility that the uppermost layer of the gouge zone had been damaged during sample preparation was considered, but it is argued that the ‘amorphous’ material extends beyond the possible 30nm of damage that could occur prior to, and during the deposition of the platinum coat. Further, crystalline clasts are observed to occur across the full depth of the gouge layer (see red arrows, Fig. 17E), in places forming lenses of crystalline material between the zones rich in ‘amorphous’ material (see red arrow, Fig. 17C). These features suggest that the ‘amorphous’ material is not an artefact of the sample preparation process.

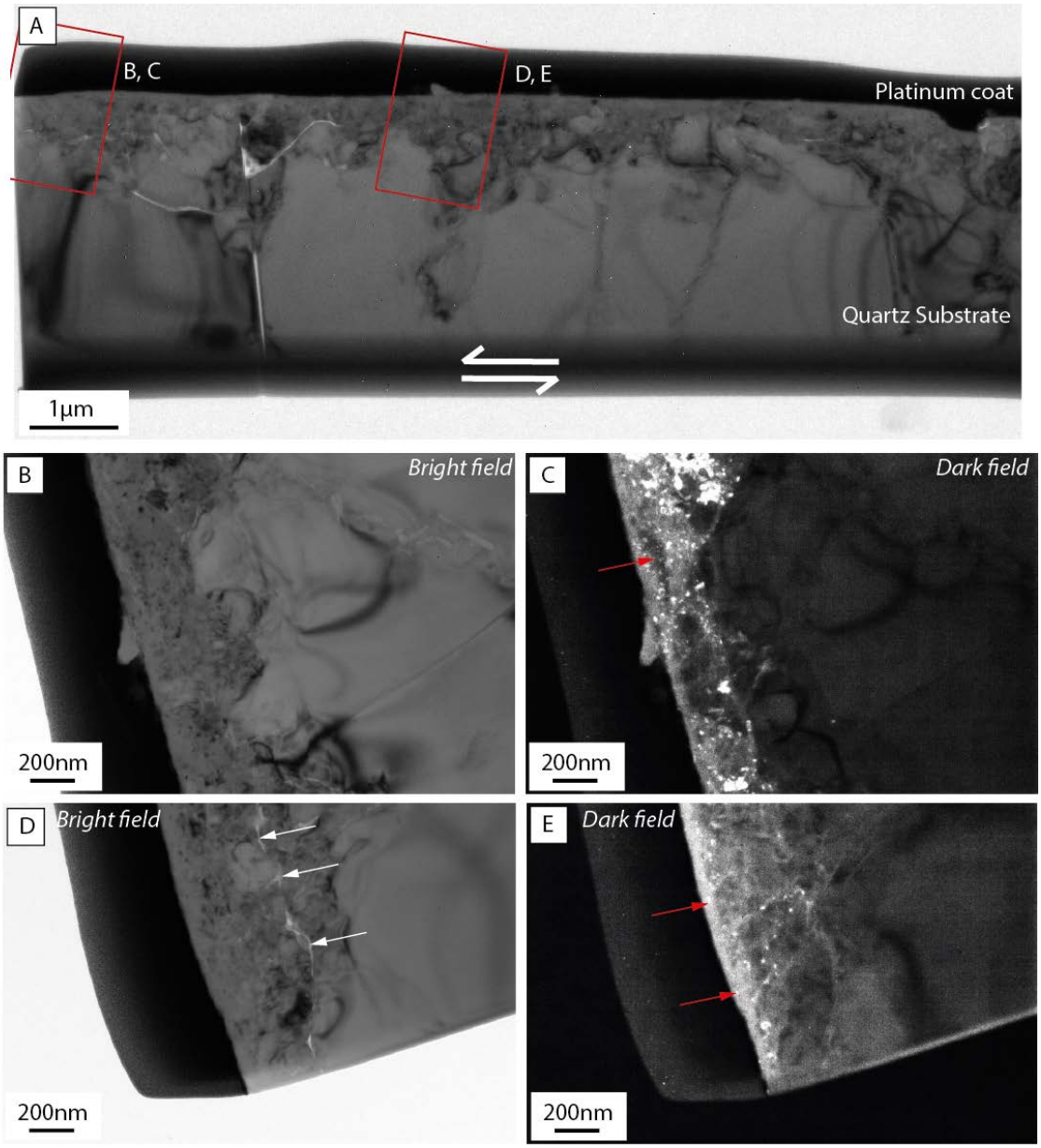

Figure 17: FIB Section 7, BIS037– Aseismic creep experiment cut perpendicular to the slip surface and parallel to slip direction.
(A) Low magnification image of the FIB section with arrows indicating the sense of fault motion. Location of the higher magnification images is indicated by the red rectangles. This FIB section was milled within a lineated region of densely compacted particles at the slip surface of BIS041. This region can be seen as the finely crushed material adjacent to the slip zone beneath the platinum coat. Note the several highly porous zones recognisable by the low contrast in bright-field imaging. These areas are assumed to be fractures or poorly compacted regions within the layer (see also white arrows in image D). It is unknown whether they formed during slip or are an artefact of unloading. (B-C) Comparative bright-field (B) and dark-field (C) images showing the agglomerated gouge zone adjacent to the slip surface. Bright and dark regions within the fine grained layer represent variably diffracting quartz clasts. Dark-field image reveals the possible presence of 'amorphous' material that is identifiable by the mid-range contrast. Note the occurrence of lenses of essentially crystalline material (see red arrow) within the predominantly 'amorphous' zone. (D-E) Comparative bright-field (D) and dark-field (E) images of showing the fault interface at another point on the sample. 'Amorphous' material can again be seen within the gouge zone with the highest concentration occurring close to the fault surface. In the dark-field image crystalline clasts whose reflections fall within the objective aperture are shown by having very low contrast and occur throughout the full depth of the zone. Red arrows indicate crystalline clasts adjacent to the slip surface.

3.3.2 Hydrothermally-treated fault surfaces

A TEM foil was milled on the surface of BIS028, an experiment involving hydrothermal treatment for 1hr at 500ºC following melt-inducing slip. The area that was chosen was one of the regions interpreted as a melt generation surface on the basis of SEM analysis, which indicated the presence of linear fractures perpendicular to the slip direction, as well as lobate domains interspersed with fine particles (e.g., Fig. 10C-D). Unfortunately this foil represents far from ideal sample preparation with the platinum coat and small particles separating from the substrate.

TEM imaging indicates the sample surface has a microstructure very different from the slip surfaces that had not been hydrothermally treated. Fractures and other fault surface damage appear to have largely healed during the 1 hour of hydrothermal treatment. The partially healed fractures are decorated by trails of elongate fluid inclusions which range in size from <5nm-70nm (Fig. 18). The activation of dissolution-precipitation processes is reflected by the development of euhedral grain shapes in gouge particles (Fig. 18E) and a rounding of the surface topography (Fig. 18D-E).

An amorphous film, with a maximum thickness of ~30-40nm, is observed to coat many of the fault surfaces adjacent to the slip zone; this includes both surface particles and the cohesive slip surface. It is uncertain whether these zones of material represent remnant melt, with the exposed surfaces forming dissolution zones; sites of silica precipitation upon quenching or hydrous crystalline epitaxial overgrowths that have been ion beam damaged prior to the deposition of the platinum. Previous research suggests that experimentally generated crystalline overgrowths can be sensitive to electron beam damage [e.g., *Rutter and White*, 1979] and the fact that the layer is not evenly deposited on all exposed surfaces suggests that the layer is not the product of quenching.

3.4 XRD analysis

The potential for silica polymorphs to have formed on the fault surfaces during slip was tested *in situ* using multiple-pass scans on a X-ray powder diffractometer. The slip surfaces of samples BIS036, BIS037 and BIS039 were mounted using a custom built holder. No evidence was found for any experiment related phases other than quartz and copper; the presence of the latter arises from injection of the copper sleeve onto the outer edges of the fault surfaces during the high temperature deformation (see Appendix 5).

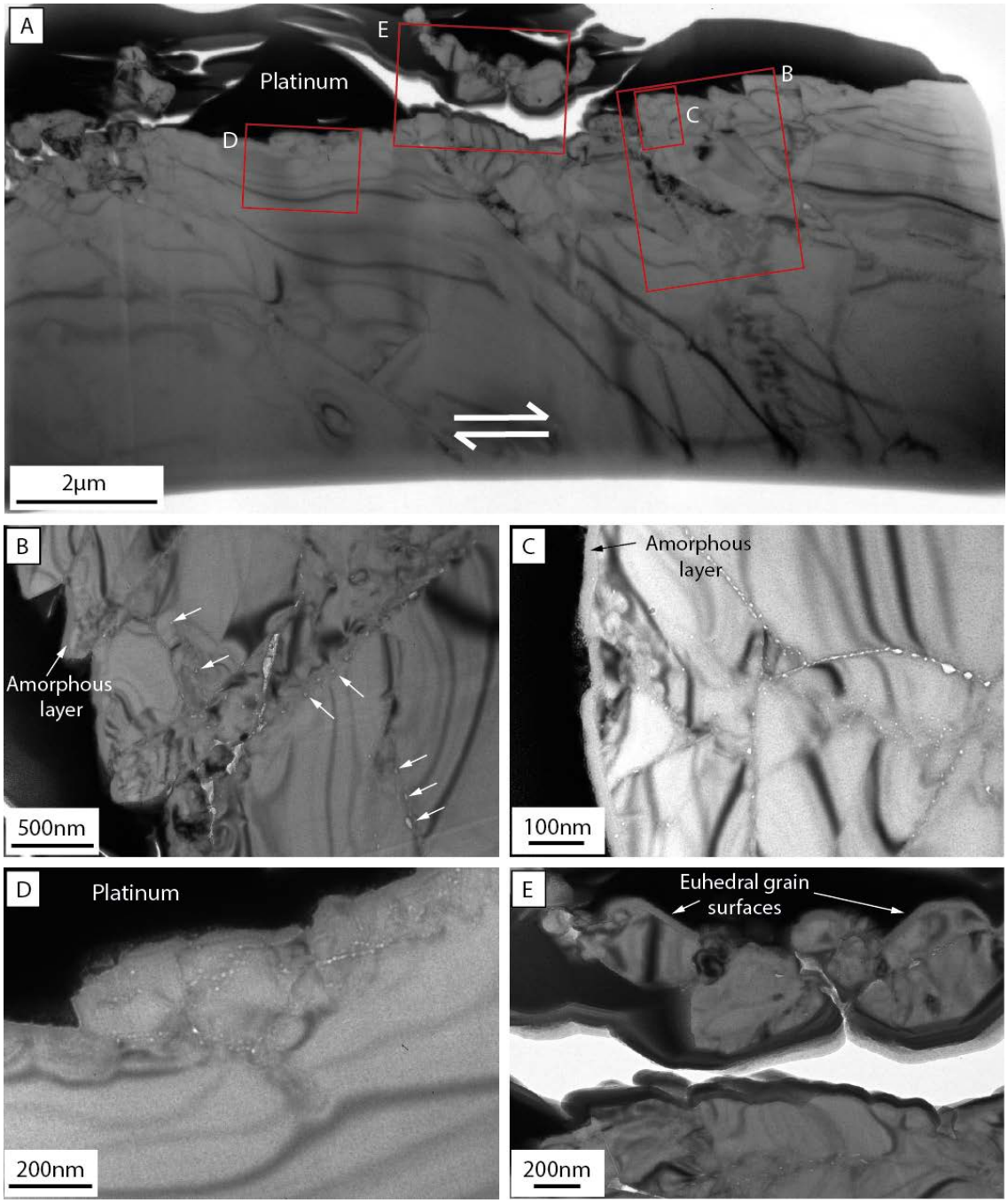

Figure 18: FIB Section 8, BIS028 – Hydrothermally treated sample cut perpendicular to slip surface and parallel to slip direction.
All TEM micrographs are bright-field images. (A) Low magnification image of the FIB section with arrows indicating the sense of fault slip. Location of the higher magnification images is indicated by the red rectangles. This FIB section was milled in a region that was thought to have been a melt generation surface. (B) Healed fractures can be seen by decorated by trails of inclusions (see white arrows). Some porosity still exists, as shown by the bright, high intensity regions. A 30-40nm layer of amorphous material coats the surfaces adjacent to the platinum coat. (C) Higher magnification image of a region of microcracking shown in (B). Trails of inclusions are clearly visible. (D) Region showing hydrothermal healing of a slip-damaged surface. A network of fluid inclusions indicates the location of healed microfractures and the uneven topography of the fault interface is rounded through dissolution-precipitation processes. (E) The development of euhedral grain surfaces is visible in the outlines of a number of the small clasts on the fault surface. The dark material on the underside of the clasts in the void between the platinum layer and the sample is thought to be a product of the re-deposition of material during the milling process.

4. Discussion

4.1 Amorphisation on fault surfaces

In the preceding section, it has been shown that the development of amorphous material is a significant feature in the microstructural development of the experimentally slipped faults in quartz sandstone under nominally dry conditions. The process of quartz amorphisation within fault zones and its potential impact on the behaviour and stability of faults remains poorly understood, especially at high ambient temperatures and high normal stresses. In the following section the mechanisms that cause amorphisation are briefly described and discussed in terms of how they may relate to conditions and processes active in the fault zone. An overview is then provided of experimental work that has been undertaken over the past several decades with respect to the role that amorphisation plays in influencing mechanical behaviour during slip in fault zones. Finally a series of simple thermal calculations are presented to gain insights into the conditions required for frictionally induced thermal melting; feasibility of the results are assessed in terms of the observed microstructures, mechanical behaviour and fault strength.

4.1.1 Mechanisms for amorphisation

Amorphous material or glass can be defined as a solid phase that has lost long-range crystalline order (lattice periodicity) and assumed a liquid-like structure where a short-range order, similar to that found in the original crystalline lattice, can still be present. Although thermal induced melting, followed by quenching, is the most common way for a crystal to lose long-range structure, numerous other mechanisms exist that result in the same structural changes. These include: mechanical amorphisation that results in defect accumulation and structural disorder (includes processes such as comminution and frictional shear amorphisation) [*Tkacova et al.*, 1993; *Nakamura et al.*, 2012], high isostatic pressure [*Hemley et al.*, 1988; *Kingma et al.*, 1993] and particle irradiation. These methods all represent a large departure from thermodynamic equilibrium conditions [*Delogu*, 2004].

The large differences in stress states between processes such as comminution and amorphisation during isostatic compression, suggests that amorphisation occurs in quartz over a wide range of stress states [*Kingma et al.*, 1993; *Dmitriev et al.*, 2003].

Many of these stress states lie within what is traditionally considered to be the thermodynamic stability field of crystalline quartz, thus potentially making mechanical amorphisation during faulting feasible. It has been shown experimentally that increasing differential stress lowers the transition pressure between crystalline and amorphous phases of silica [*Cordier et al.*, 1993], possibly through the formation of dynamic instability [*Watson and Parker*, 1995].

It has been observed [*Winters et al.*, 1992], that the structure and properties of amorphous SiO_2 subtly change depending on the method of synthesis, with pressure amorphisation resulting in an increased number of densified atomic defects (5 and 6 fold coordination defects). Conceivably variations in the structure and short-range order of the amorphous material may provide diagnostic methods of identifying the mode of amorphisation. However, given the very small quantity of amorphous material present on the experimentally slipped faults produced in this study, this is likely to prove difficult (and beyond the scope of the current research).

4.1.2 Influence of amorphisation on mechanical behaviour

While numerous experiments performed on frictional welding apparatus [*Spray*, 1987, 1995, 2010] and rotary shear apparatus [e.g., *Shimamoto and Tsutsumi*, 1994; *Di Toro et al.*, 2006a; *Proctor et al.*, 2014] have produced unequivocal evidence of frictional heating and melting on many rock types, melt has been less prevalent during the experimental deformation of in pure-quartz rocks such as quartzites [*Goldsby and Tullis*, 2002], cherts [*Hayashi and Tsutsumi*, 2010] and novaculites [*Di Toro et al.*, 2004]. In quartz-rich rocks such as granites, quartz is generally observed to be the one of the last minerals to melt, commonly forming residual clasts in a silica-depleted melt matrix, thus suggesting non-equilibrium melting [e.g. *Lin and Shimamoto*, 1998]. This could be a result of the very high melting temperature of quartz relative to the other minerals, the sluggish kinetics of quartz melting or a consequence of the low normal stresses used during the rotary shear experiments.

The effect of frictionally-induced melt on the behaviour of fault interfaces has been a source of debate for many decades, with suggestions that the melt layer could act as either a lubricant [*Di Toro et al.*, 2006a], dramatically reducing dynamic friction coefficients, or alternatively, acts to restrain or even terminate seismic slip, depending

on viscosity and thickness of the melt layer [*Koizumi et al.*, 2004]. High velocity rotary shear experiments on gabbro and other ultra-mafic rocks [*Tsutsumi and Shimamoto*, 1997; *Hirose and Shimamoto*, 2005b; *Proctor et al.*, 2014] point towards at least two phases of fault weakening that are separated by significant strengthening just prior to the development of a continuous melt layer on the slip interface. The first stage of fault weakening is attributed to flash heating [*Hirose and Shimamoto*, 2005b], where asperities under high normal stress are frictionally heated and lead to the formation of incipient melt patches on the asperity interfaces. Possible mechanisms for fault weakening during flash heating include: lubrication of the asperity tips [*Hirose and Shimamoto*, 2005b], or generation of melt pressure through localised volume expansion, resulting in a reduction of normal stress across the interface [*Brown and Fialko*, 2012]. The second period of fault weakening is associated with continuous melt formation and is regarded as the stage at which many natural pseudotachylytes are formed [*Hirose and Shimamoto*, 2005b]. The strengthening regime just prior to the onset of continuous melting is inferred be the result of the growth and coalescence of the initial melt patches into a thin continuous layer. Potential edge effects of the thin, semicontinuous melt film, produce high effective viscosities within the melt layer and result in a strengthening of the interface with increasing melt surface area [*Hirose and Shimamoto*, 2005b]. Alternatively, low fault surface temperatures at the onset of melting result in high melt viscosities that leads to fault strengthening [*Di Toro et al.*, 2006b]. High velocity experiments conducted on tonalite and novaculite produce similar results with peak strength being reached prior to the onset of continuous melting. However, in these experiments the frictional weakening associated with the onset of continuous melting is not as pronounced as is observed for the ultra-mafic samples [*Di Toro et al.*, 2006a].

During high velocity rotary shear experiments undertaken at low normal stresses, the displacement incurred between the onset of flash heating and continuous melting can amount to more than 20 metres. Such large displacements result in overprinting and destruction of the early microstructures and the potential development, during experiments, of phenomena atypical of natural fault zones within the continental seismogenic zone. In comparison, while experiments performed on a triaxial apparatus are limited in terms of overall slip displacement, they do provide an opportunity to explore the behaviour and microstructures of small seismic events without imposing a velocity and slip distance. Unfortunately, there are few recorded observations of melt

being formed on triaxially deformed samples. *Friedman et al.,* [1974] reported glass on polished surfaces of an impure quartz sandstone during sliding experiments undertaken at P_c*=14-500MPa* and *T< 410ºC,* although analysis was limited to the identification of melt textures using low resolution optical microscopy. Similar phenomena was observed by *Rutter and Mainprice* [1978] on the same Tennessee sandstone starting material as used by Friedman et al., [1974]. *Koizumi et al.,* [2004] observed melt textures in granite experiments following large stress drop stick-slip events, with a slip displacement in the order of 300μm. The novel use of sensors and a high speed data acquisition system during the experiments allowed the determination of an exact time of the onset of melting relative to the start of a stick-slip event and the observation of a remarkable recovery in frictional strength of the fault just prior to the cessation of slip. Importantly, the onset of melting occurs during the stick-slip event, with significant relative weakening and displacement having occurred prior to this point. This suggests that the formation of melt is a product of the rapid sliding during the slip event rather than the instigating cause of the instability.

The origin of fault instabilities remains one of the most significant unanswered questions in the study of earthquake fault mechanics. Significant fault weakening has been observed to arise with the formation of amorphous material on fault interfaces [*Yund et al.,* 1990; *Di Toro et al.,* 2004], although whether this is a causal process or consequence of rapid slip remains open for debate. Rotary shear experiments on quartz-rich rocks [*Yund et al.,* 1990; *Di Toro et al.,* 2004] generated a porous, possibly gel-like amorphous material in the damage/gouge layer of the fault surface; slip was accompanied by significant fault weakening. TEM analysis by *Yund et al.,* [1990] showed the gouge was comprised of approximately 40-50% amorphous material, but it was unclear whether the lack of crystalline diffraction was the result of the genuine amorphisation arising from the loss of long range crystalline order, or was a consequence increased structural damage associated with a very small particle size (i.e., many particles < 10 nm in diameter). However, it has been argued [*Di Toro et al.,* 2004], that the presence of amorphous material alone is not sufficient to produce the extraordinary weakening that is observed in some of their experiments (dynamic friction coefficient <0.3). It was speculated that the observed significant fault weakening is the result of thixotropic behaviour of a tribolayer of silica gel [*Di Toro et al.,* 2004] that

forms as a result of the interaction between the highly chemically reactive amorphous material [*Yund et al.,* 1990] and moisture from the atmosphere.

The apparent absence of amorphous material on many bare interface frictional sliding experiments undertaken on triaxial apparatus [e.g., *Stesky,* 1974], at high confining pressures and moderate-high temperatures has given rise to the argument that the formation of amorphous material requires larger displacements (>3-4mm) than can be obtained using a triaxial apparatus [*Goldsby and Tullis,* 2002]. However, other experiments suggest that this is not the case, with quenched melt textures (glass) being produced during stick-slip events on granite interfaces undertaken at room temperature using a triaxial apparatus and P_c*=150MPa* [*Koizumi et al.,* 2004]. Amorphous, clast laden material has also been reported in the low displacement triaxial deformation of simulated granite gouge at conditions below those considered necessary to produce frictional melt [*Pec et al.,* 2012]. Frictional pin-on-disk experiments on quartz single crystals at room temperature [*Navrotsky,* 1994] have been shown to generate amorphous material at low to intermediate slip rates (3.2mm/s – 75mm/s). Raman spectroscopy of the frictional wear tracks from these experiments reveal peaks consistent with the formation of partially densified silica glass, moganite and coesite, indicative of pressure- and strain-induced amorphisation, and similar to observations reported for high pressure experiments using diamond anvil cells [*Hemley et al.,* 1988; *Kingma et al.,* 1993].

While the experiments discussed above clearly demonstrate the propensity of frictional interfaces to produce amorphous material, the mechanisms of formation and, to a large extent, their influence on sliding behaviour, remain poorly constrained. However, from the observation reported in previous studies, it can be concluded that amorphisation occurs at areas of real contact on the fault surfaces, either through pressure- and/or mechanically-induced amorphisation or through frictionally-induced thermal melting.

4.1.4 Thermal modelling of fault surfaces

The transformation of frictional energy to heat is thought to be one of the primary mechanisms responsible for the increase in temperature of fault surfaces during slip. While the exact location of this energy transformation is not known [*Kennedy,* 2001], frictional heat is concentrated within the areas of real contact between the sliding interfaces (for discussion about areas of real contact see Appendix 5). To undertake a

quantitative analysis and explore the potential thermal evolution of the asperity contacts on fault interfaces in quartz sandstone, two different thermal models have been employed. The first assumes uniform heating across a fault of variable width, in an infinite material. The goal is to provide a first order estimate of the change in temperature of the fault surface. The second model places bounds on asperity size, and after Jaeger [1942], assumes a uniform circular heat source on a moving body to calculate the change in temperature at asperity contacts. Calculations are undertaken using the experimental data to determine maximum attainable 'flash' temperatures, although these calculations are only valid up to the onset of melting, after which the rate and mechanisms of heating are assumed to be no longer frictionally controlled. These calculations have a number of limitations, including the oversimplification of asperity geometry and the significant reliance on fixed parameters that, in reality, are likely to evolve spatially, temporally and with changing stress states during the frictional sliding. It is also assumed that all energy produced during frictional sliding is converted instantaneously into heat with no energy being expended through the production (by fracturing and wear) of new surfaces and gouge, or through other modifications of the microstructure (such as dislocation processes).

4.1.4.1 Calculating the frictional heating on the fault surfaces

The highest temperatures on the fault surface occur at the asperity contacts during the process of flash heating. The cumulative effect of flash heating over the duration of slip is to raise the average temperature of the fault surface. Accordingly, the maximum temperature (T_{max}) at any given point on the fault surface can be estimated by three contributing factors:

$$T_{max} = T_{amb} + \Delta T_{fs} + \Delta T_{asp} \quad (1)$$

where T_{amb} is the ambient starting temperature, ΔT_{fs} is the temperature change on the sliding surface as a result of cumulative heating from the dissipation of heat from asperity contacts, and ΔT_{asp} is the change in temperature of the asperity contacts [*Kennedy*, 2001]. Assuming that the rate of heat production per unit area (q) is given by:

$$q = \sigma_n \cdot \mu_k \cdot v \quad (2)$$

where, σ_n is the normal stress acting on the fault, $\mu_k$is the coefficient of kinetic friction and v is the sliding velocity [*Jaeger*, 1942; *Sibson*, 1975], the one dimensional heat transport at constant velocity can be expressed as:

$$\frac{\partial T}{\partial t} = \frac{Q(x,t)}{\rho c_p} + \kappa \frac{\partial^2 T}{\partial x^2} \tag{3}$$

where T is temperature, t is time, Q is the rate of heat generation per unit volume ($Q = q/w$, with w being the width of the fault zone), x is the distance perpendicular to the fault plane, measured from the centre of the fault zone, ρ is the density of quartz (2650 kg m^{-3}), c_p is the specific heat (1186 J kg^{-1} K^{-1} for quartz) and κ is the thermal diffusivity of quartz (2.23x10^{-6} m^2 s^{-1}). Assuming that prior to fault slip $Q = 0$ the solution to (4) is given by *Morse and Feshbach* (1953) as:

$$T_{fs}(x,t) = T_{amb} + \frac{1}{2\rho c_p \sqrt{\pi\kappa}} \int_0^t \int_{-\infty}^{\infty} exp\left[\frac{-(x-x_0)^2}{4\kappa(t-t_0)}\right] \frac{Q(x_0,t_0)}{(t-t_0)^{1/2}} dx_0 dt_0 \tag{4}$$

Further assuming that the frictional heating is uniform across the width of the fault and is independent of time during slip, heat generation per unit volume can be expressed as [*Cardwell et al.*, 1978]:

$$Q(x,t) = \frac{\tau d}{wt}\left[H(x+\frac{w}{2}) - H(x-\frac{w}{2})\right] \tag{5}$$

where H() is the Heaviside step function, and τ is the macroscopic shear stress acting on the fault. *Cardwell et al.*, (1978) showed that the temperature at any point at distance x, from the fault at time *t* could be calculated by substituting equation (5) into (4) giving:

$$T_{fs}(x,t) = T_{amb} + \frac{\tau d}{2\rho c_p w t_{slip}} \int_0^t \left[\text{erf}\left(\frac{x+(\frac{w}{2})}{\sqrt{4\kappa(t-t_0)}}\right) - \text{erf}\left(\frac{x-(\frac{w}{2})}{\sqrt{4\kappa(t-t_0)}}\right)\right] dt_0 \tag{6}$$

$$\text{for } 0 < t < t_{slip}$$

$$T_{fs}(x,t) = T_{amb} + \frac{\tau d}{2\rho c_p w t_{slip}} \int_0^{t_{slip}} \left[\text{erf}\left(\frac{x+(\frac{w}{2})}{\sqrt{4\kappa(t-t_0)}}\right) - \text{erf}\left(\frac{x-(\frac{w}{2})}{\sqrt{4\kappa(t-t_0)}}\right)\right] dt_0 \tag{7}$$

for $t > t_{slip}$

This equation has been calculated numerically, using published thermal and physical properties of quartz (see Appendix 5) and exploring parameters such as fault width, duration of slip, and displacement. Calculations suggest that for a fault width less than 5μm, the width has essentially no impact on the calculated maximum fault temperatures (Fig. 19A). Therefore, the maximum temperature of the fault surface, assuming $w = 0$, can be estimated by [*Cardwell et al.*, 1978]:

$$\Delta T_{fs} = T_{amb} + \frac{\tau d}{\rho c_p \sqrt{\kappa t_{slip}}} \tag{8}$$

Using the experimental data (see Appendix 5) the increase in fault temperature is calculated to be between 2.5º - 55ºC, assuming that the contact stresses on the fault surface are equivalent to the bulk experimental observations (Fig. 19B). These calculations use shear stress values between 71-207MPa and slip velocities of between 2-20mm/s.

4.1.4.2 Calculating the frictional heating on asperity contacts

For the calculation of the frictional heating occurring on asperity contacts, it can be reasoned that at slow slip rates, competition exists between the generation of heat at contacts and the diffusion of that heat away over the lifetime of the asperity, resulting in a small temperature rise and negligible effect on contact strength. However, at higher slip rates, there is insufficient time for heat generated at contacts to diffuse resulting in increased contact temperature [*Kennedy*, 2001] (Fig. 19C and see Appendix 5). This effect is described by the dimensionless Péclet number (*L*), which is defined as:

$$L \equiv vr/2\kappa \tag{9}$$

where, v is the slip velocity and r is the radius of the asperity contact.

The change in asperity temperatures is calculated based on the assumption that the heat is generated at the area of true contact. For the experimental data, this is the estimated true contact area for the fault, which is assumed to form a single circular asperity contact. It is also assumed that the asperity can only support a load up to the critical compressive failure strength of quartz. Assuming a broad range of potential Péclet

numbers and using the mathematical models of *Archard [1958/1959]* and *Greenwood [1991]*, the maximum estimated steady-state temperature change at asperity contacts is approximated as:

$$\Delta T_{asp} \approx \frac{2\sigma_n \mu_k vr}{k\sqrt{\pi(1.273 + L)}} \tag{10}$$

where k is the thermal conductivity of quartz (estimated to be $7\mathrm{W/mK}$) and L is defined in equation 9. It is assumed that the heat generated is divided equally between the two asperities on either side of the slip interface. The effects of uncertainty, resulting from parameters including asperity contact radius, real contact area, asperity strength and slip velocity, on estimated maximum asperity temperature is explored in Figure 19D-F (see also Appendix 5).

The maximum asperity temperatures, allowing for both ambient temperature and experimentally-induced heating, have been explored as a function asperity contact radius, using the mechanical data derived from the current experiments and assuming a 10% real contact area [*Logan and Teufel*, 1986] (Fig. 19D). The maximum asperity temperature is expected to occur where the asperity diameter is equal to the total displacement of the rapid slip event (i.e., heat generation on the asperity occurs for the entire slip duration). These points are indicated by the stars in Figure 19D. Calculated maximum asperity temperatures using the experimental data are insufficient to cause frictional melting. However, microstructural observations indicate that in some locations melting is initiated within the first 50μm of slip, suggesting that the calculated temperatures fall short of the minimum melting temperatures by more than 500°C.

If the change in asperity temperature is considered as a function of asperity strength and real contact area, assuming that the relationship between real contact area and applied normal stress is linear [e.g., *Logan and Teufel*, 1986; *Stesky and Hannan*, 1987], it can be seen in Figure 19E that for very high asperity strengths (>4GPa) and low < 5% real contact areas, enough heat can be produced to achieve frictional melting. Although these results seemingly provide a reasonable fit with the observation of melt textures on

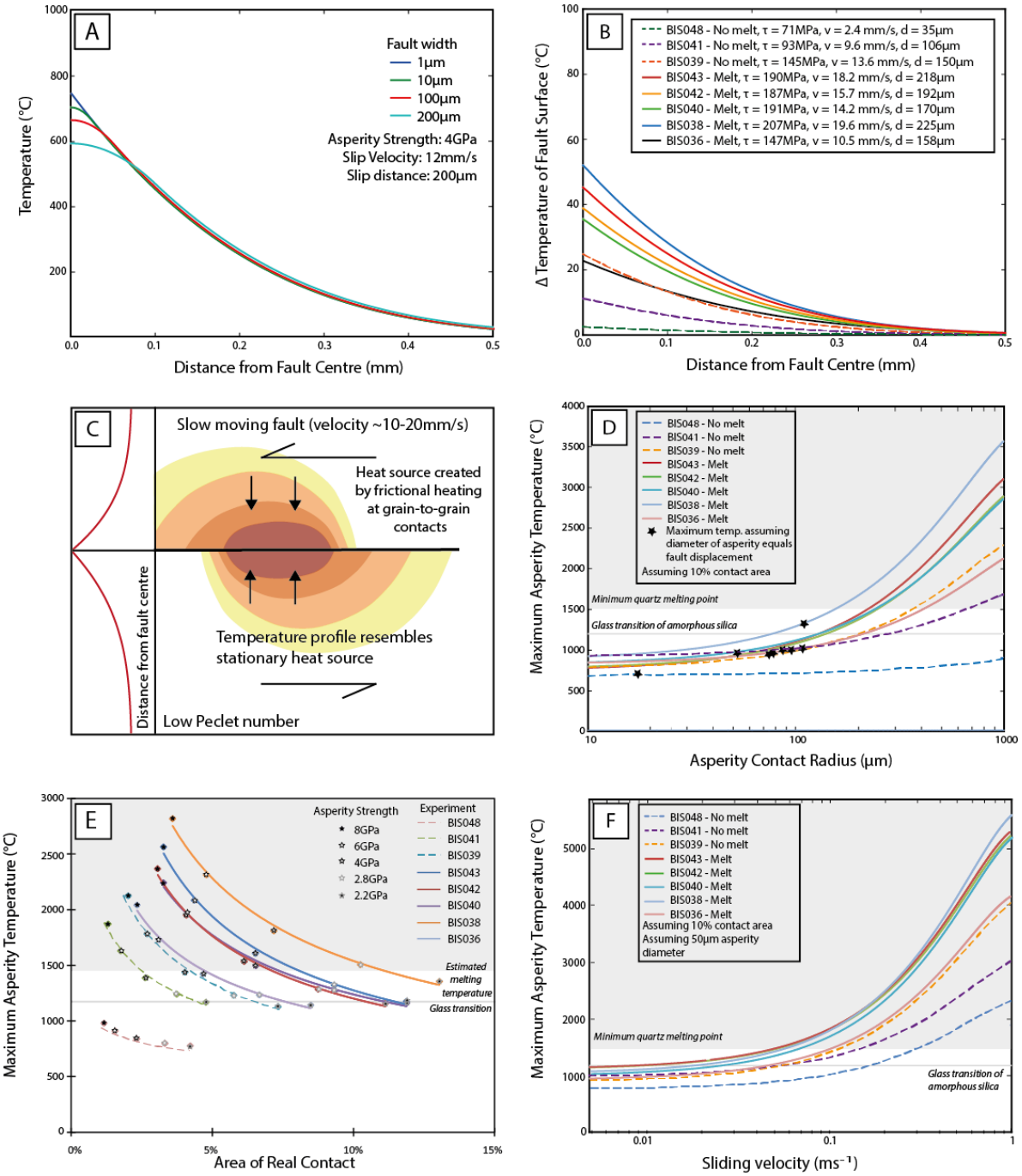

Figure 19: Thermal calculations for the production of heat on the fault surfaces
(A) Sensitivity of the model 1 (used to calculate frictional heating of the fault surfaces) to changes in fault width. When fault widths <5µm, there is essentially no impact on calculated fault temperatures. Faults in the current suite of experiments have a fault width of approximately 1-2µm. (B) Estimated increase in fault surface temperature using data acquired from experiments. Estimated slip velocities is derived from seismic data. The change in estimated temperature with increasing distance from the interface suggests a low Péclet number. (C) Schematic illustration of the effect of a slow moving heat source (low Péclet number) [after *Stachowiak and Batchelor*, 1993]. (D) Maximum asperity temperatures shown as a function of asperity radius using experimental data (see Appendix 5) and assuming a real fault contact area of 10% [*Logan and Teufel*, 1986]. Estimated normal stress acting on asperities (real contact area) ranges from 0.9-2.9GPa. (E) Maximum asperity temperature as a function of real contact area. Real contact area is assumed to be controlled by a linear relationship between the macroscopic normal stress acting on the fault and the shear strength of quartz. (F) Maximum asperity temperature as a function of sliding velocity, assuming a 10% contact area and 50µm asperity diameter.

the slip surface, there are a number of inconsistencies. For example, if the full slip displacement is required to generate sufficient heating to melt an asperity contact, a maximum melt area of between 4-8% could be expected. This compares with areas of between 10-60% on the actual fault surfaces. Microstructural observations also suggest that melting occurs between gouge particles <1μm in diameter, indicating that heat calculations significantly under-represent the true extent of the frictional heating.

Finally, maximum asperity temperature is considered as a function of sliding velocity, using the mechanical data derived from the experiments and assuming both a 10% contact area and 50μm asperity diameter (Fig. 19F). Results indicate that sliding velocities greater than $0.1ms^{-1}$ are required to induce melting on the experimental slip surfaces. The seismometer data acquired during experiments suggests velocities of $0.002\text{-}0.02ms^{-1}$, which would be insufficient to generate frictional melting on the fault surfaces. However, potential undersampling of the slip event by the seismic instruments may result in an overestimation of the slip duration (Section 2.1) and consequently lower calculated temperatures. Further, it has been previously recognised that natural fault ruptures propagate in a 'pulse-like' way [*Heaton*, 1990]. If the laboratory induced slips behave in a similar way on a microscopic scale, it could result in significant additional complexity with variations in velocity with both time and space. The uncertainty surrounding slip velocity highlights the need for better constraint on slip velocity during rapid slip events. Progress that has been made towards the development of an interferometry system that will improve sample time resolution by up to four orders of magnitude (improving the sampling rate from between 100-1000 samples per second to potentially in excess of a million samples per second) is discussed in Chapter 4.

The significant understatement of estimated maximum asperity temperatures using experimentally-derived mechanical data is a significant result within itself. It suggests that the micromechanical processes occurring at the fault surface are more complex than the bulk measurements indicate, with significant variations in real contact area, asperity strength, normal stress and velocity. However, temperatures sufficient to induce frictional melting over the experimental slip displacements can be achieved if it is assumed that normal stress is highly concentrated at asperity contacts and that slip occurs at sub-seismic to seismic slip velocities ($0.1\text{-}1ms^{-1}$). Another important result from the thermal calculations is the correlation between estimated maximum asperity

temperatures and microstructural observations of melt textures. Experiments that form ribbon-like textures and slip-dispersed melt consistently produce higher expected temperatures than experiments that result in the formation of undispersed fractured glass patches.

4.2 Coupling mechanical behaviour and microstructural evolution

After theoretically exploring the parameters necessary to cause flash heating and frictional melting of asperity contacts, this section will focus on coupling the mechanical behaviour recorded during the experiments with some of the key microstructures observed on the slip interfaces. Experiments have shown the development of complex sliding behaviours over a range of temperatures and confining pressures with multiple transitions between stable sliding and stick-slip behaviour. Up to approximately 600ºC fault behaviour is characterised by stable sliding, that is similar to previous experimental observations made under moderate to high normal stresses [e.g. *Friedman et al.*, 1974; *Stesky*, 1974; *Paterson and Wong*, 2005]. However, above 600ºC the fault interfaces develop instabilities resulting in sudden stress drop and the formation of melt on the slip surfaces (Fig. 20). The following discussion is structured to broadly follow these phases of microstructural development. Discussion commences with the processes of brittle fracturing, mechanical amorphisation and gouge formation associated with early slip and stable sliding, before moving on to the nucleation of seismic rupture, flash heating and the development melt related microstructures.

The onset of aseismic creep at the commencement of deformation is characterised by fracture development and the formation of gouge on the interface surfaces. This is to some extent driven by stress concentrations arising from the Hertzian loading of asperity contacts within a macroscopically porous material. However, crack development is also influenced by the crystallographic orientation of the grains relative to the prevailing stress orientations. Although quartz does not have a well-defined cleavage plane, the numerous examples of dense arrays of approximately parallel fractures, and the formation of dislocations aligned parallel to the basal plane, suggests that crystallographic planes of weakness play a significant role in the development of fractures and wear products.

A notable feature with respect to the brittle evolution of the sliding surface is the extensive fracturing of the substrate in experiments that have experienced seismic

rupture. In some of these experiments, rupture has occurred prior to the onset of any significant aseismic slip along the fault surface; it is therefore suggested that a combination of both dynamic mechanical and thermal stresses may influence fracture development and the formation of the characteristic fractures oriented perpendicular to the sliding direction (Fig. 20). Similar microstructures are observed on slip surfaces in other triaxial experiments where melt is generated [*Koizumi et al.,* 2004]. The difference in morphology compared with material produced during stable sliding suggests some influence by the highly localised and extreme contact temperatures that develop during seismic slip. These microstructures bear a striking similarity to thermo-induced cracking and wear observed during sliding of ceramic surfaces [*Lee et al.,* 1993; *Hsu and Shen*, 1996] and 'chatter marks' observed in some natural fault zones.

One of the most interesting microstructural observations was the discovery of 'amorphous' material within the gouge layer adjacent to the slip surface of an experiment (BIS037) that was deformed at nominal aseismic slip rates (0.72 μm/s) over a sample axial displacement of <0.5mm. The mechanical behaviour of BIS037 was characterised by a high yield stress, followed by approximately 0.15mm of significant strain hardening at which point peak stress was reached and a phase of relatively rapid slip weakening commenced. Microstructural analysis revealed potentially amorphous material interspersed between crystalline clasts, forming a film-like matrix that is similar in appearance to the gels produced during some high velocity sliding experiments [*Goldsby and Tullis*, 2002; *Di Toro et al.,* 2004]. The relative abundance of the 'amorphous' material within the gouge layer increases towards the principal slip zone, suggesting a positive correlation with increasing shear strain and slip localisation.

The mechanism of amorphisation is thought to result from intense comminution of the gouge particles resulting in a loss of crystalline structure, in a similar manner to the gouges observed by *Yund et al.,* [1990]. However, gouges from the current experiments were formed over a slip distance that is on the order 0.2% of the displacement achieved in the experiments of *Yund et al.,* [1990], although at a significantly higher normal stress (260MPa as opposed to 50MPa). The mechanical behaviour of the slow-slip experiments shows remarkable similarities to the behaviour observed by *Pec et al.,* [2012] during their gouge experiments using granitoid cataclasites. Interestingly

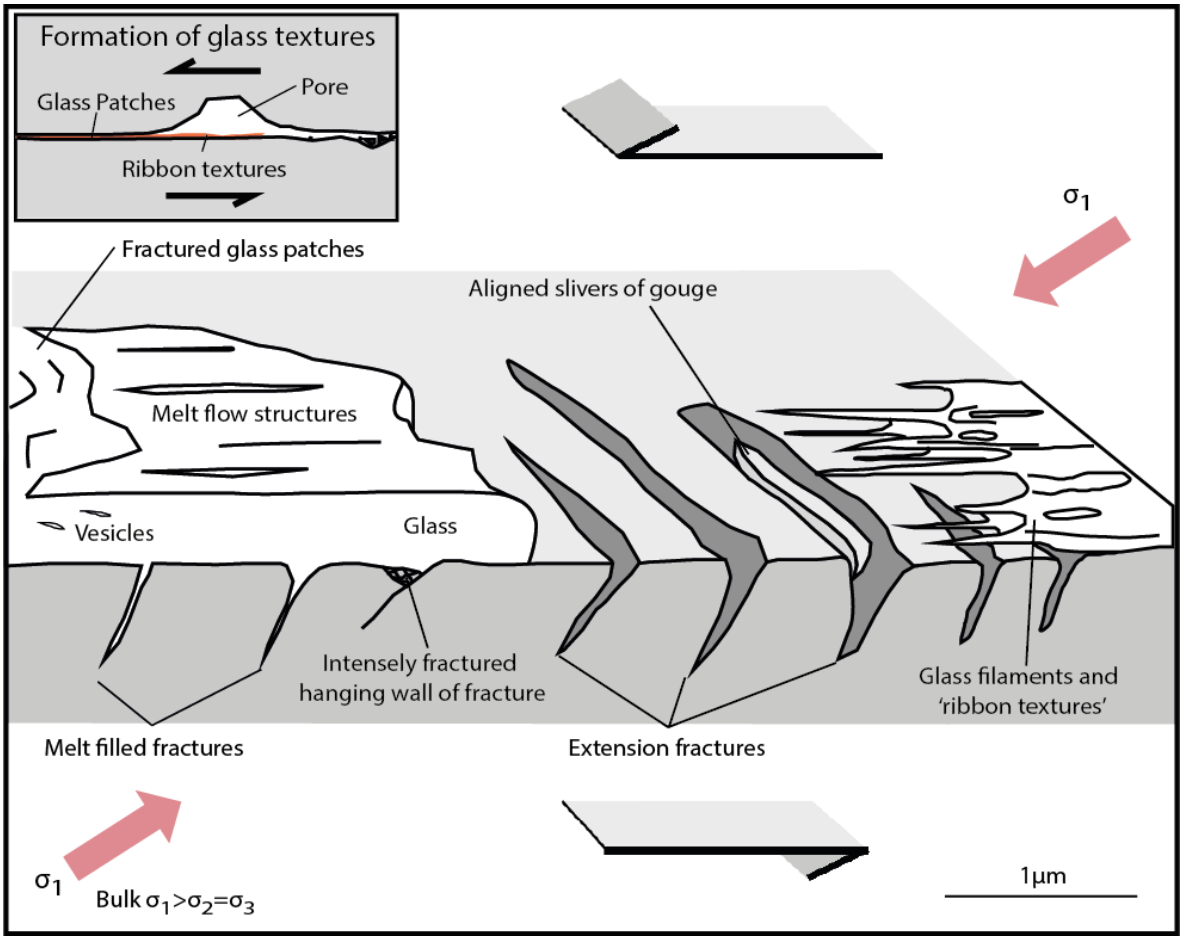

Figure 20: Characteristic microstructures of the slip interface.
Schematic interpretation of microstructures formed during seismic slip on the fault interfaces. Relationship of the microstructures to fault kinematics is also shown to provide detail on the use of some microstructures as shear sense indicators. Brittle deformation includes the formation of extension fractures typically forming perpendicular to the sliding direction and dipping away from the direction of motion of the fault (at a high angle to σ_3). One mechanism for the production of gouge is through the interaction of these fractures which result in the development of slivers of quartz that are subsequently crushed. Melt structures include the formation of striated areas of melt that are lineated by flow textures, glass filaments and drawn out ribbon-like textures and elongated vesicles. These textures occur when the melt is slipped adjacent to a pore (see inset). Melt that was formed at the end of slip, essentially welding the asperities together, is recognised by the formation of fractured glass patches.

however, the chemical composition of the amorphous material formed during the experiments of *Pec et al.*, [2012] is less silicic than the bulk rock composition, with quartz exhibiting the least deformation of any phase.

The small displacement over which amorphisation has occurred under realistic normal stress and high ambient temperatures in the current experiments and those of *Pec et al.*, [2012], has significant implications for fault behaviour and stability under crustal conditions. Many of the other frictional experiments that have formed amorphous

material [e.g. *Yund et al.*, 1990; *Di Toro et al.*, 2004; *Nakamura et al.*, 2012] have done so at room temperature and low normal stress. Consequently the frictional properties and behaviours of amorphous material on a fault surface at high temperature and pressures remain largely unexplored. Whether amorphisation could provide a mechanism for the dynamic weakening associated with fault rupture in an anhydrous environment is, at this point, unknown.

Evidence of amorphisation occurring away from the slip interface is observed in BIS043, where an amorphous-crystalline mixture occurs within an accumulation of gouge located beneath a melt film. It is not certain whether it represents a mechanically induced amorphisation as described above, or is the result of partial melting of the gouge prior to deposition in its current location. Due to the uncertainty surrounding the origin of this amorphous material, it is difficult to comment on its potential influence on fault behaviour. However, in the same experiment amorphous material is observed along fractures and dislocations over 1μm from the melt-substrate boundary. This raises the possibility that this amorphous material is a result of heterogeneous melting or the product of solid-state or shock amorphisation.

The formation of dislocations within the crystalline quartz substrate provides an indication of the very large stress concentrations [e.g. *Blacic and Christie*, 1984] existing at the slip interface, arising from both Hertzian loading and transiently associated with fault rupture. However, there is no evidence for the development of planar deformation lamellae often associated with the onset of solid-state amorphisation at pressures above 5GPa [*Cordier et al.*, 1993; *Kingma et al.*, 1993]. The formation of amorphous material along fractures and possibly at the site of dislocations suggests that the melt front is able to propagate distances greater than 1μm into the crystalline substrate. This hypothesis is supported by the recognised heterogeneity of the melting process [*Wagstaff*, 1969; *Wolf et al.*, 1990], with melting observed to nucleate at external surfaces such as grain boundaries or on internal defects, such as fractures and dislocations.

Despite evidence of the formation of amorphous material on the experimental slip surfaces, the origin of the dynamic weakening that culminates in the development of temperature-dependent stick-slip remains unclear. Slip instability on nominally dry fault interfaces has often been attributed to high velocity weakening mechanisms such as the

formation of melts [*Di Toro et al.*, 2006a], gels [*Di Toro et al.*, 2004; *Nakamura et al.*, 2012] and nano-particles [*Han et al.*, 2011], but it would seem that these highly rate-dependent mechanisms are a consequence of the high slip velocities rather than the underlying cause of the initial instability. The evolution of the melt microstructures observed in the current suite of experiments, coupled with the thermal calculations (Section 4.1.4) support the argument that an increase in temperature and the ensuing weakening are the result of high velocities and increasing slip distance.

Fault rupture and accompanying coseismic slip, result in rapid and significant temperature increases at asperity contacts, causing frictional-induced melting. The velocity of the slip has a significant effect on the morphology of the resulting melt, with high velocity slip producing glass that is recognisable by the formation of stretched glass filaments, 'ribbon-like' textures and flow structures (Fig. 21). In contrast, low-velocity slip forms localised, fractured glass patches devoid of melt-flow textures, and in doing so, provides a mechanism by which the various rapid slip events can be differentiated. By classifying experiments according to the microstructural morphology of the glass, it can be seen that stick-slip events that produce dispersed melt are characterised by both a higher peak vertical acceleration and slip displacement than the events producing localised fractured glass patches (Fig. 21C). Further, the formation of distributed melt on the slip surfaces results in much larger stress drops in comparison with the localised melt (Fig. 21B) and shows a strong positive correlation with both an increased peak shear stress and peak normal stress compared with the slip events that produce glass patches (Fig. 21D). This simple microstructural classification also provides insights into the bracketing of behaviour for the given experimental conditions, with the high temperature, high pressure region of Figure 21E being associated with the formation of dispersed melt textures, whereas the low-velocity slip events of the high temperature, low pressure sector generating localised glass patches.

Although as much as 60% of the slip interface is covered by melt textures, none of the experiments produced a continuous glass film that completely wets the entire fault surface. This implies a partial contact regime where melt generation is restricted to areas in real contact and correlates with the concept of 'flash heating' and melting at asperity tips [*Rice*, 2006]. Many previous high velocity experiments

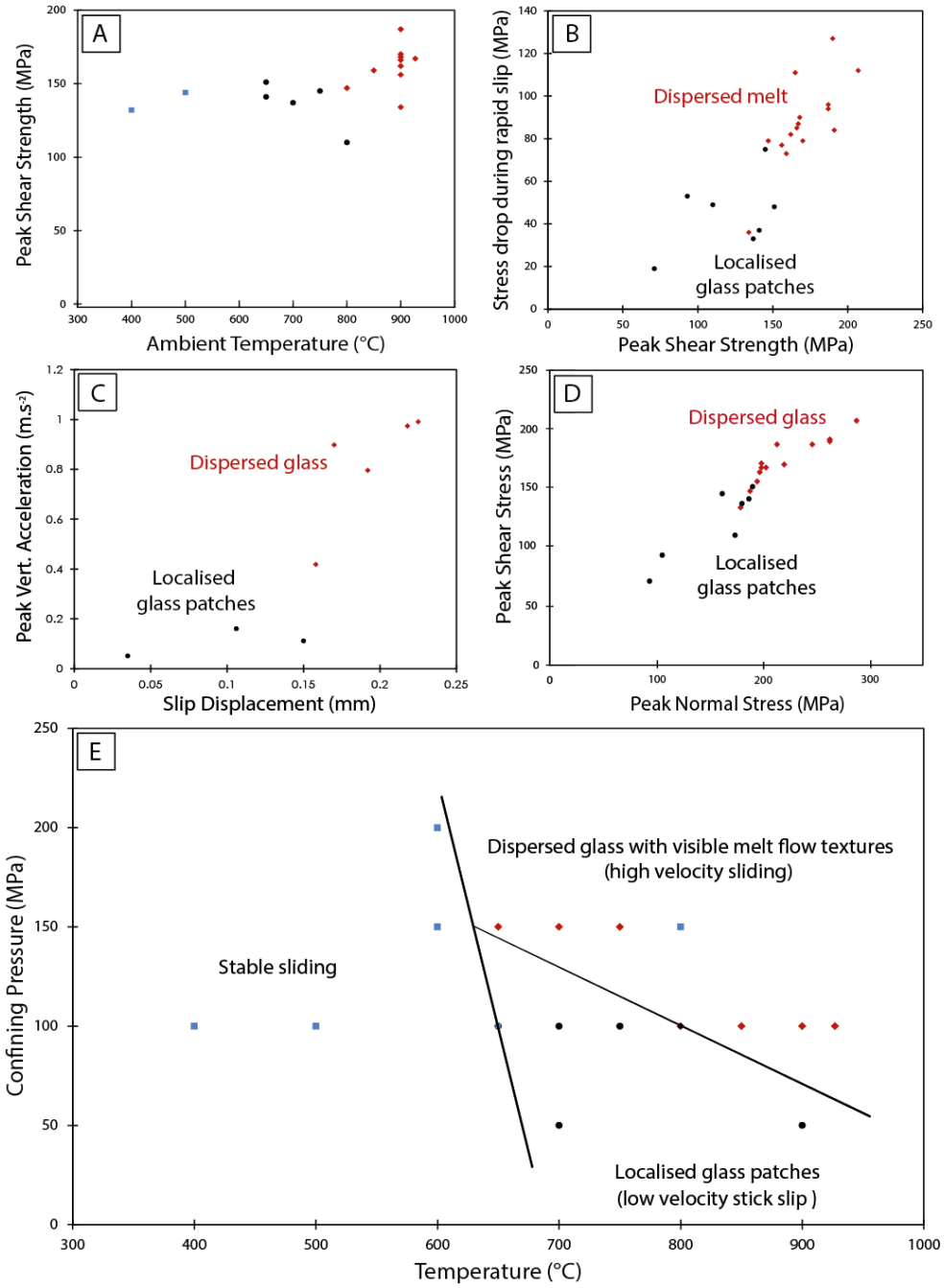

Figure 21: Relationship between experimental conditions, mechanical behaviour and the formation of melt.
For all graphs blue squares indicate experiments where the behaviour was characterised by stable sliding, black circles represent stick-slip with the formation of localised glass patches, and red diamonds indicate experiments where rapid slip events formed dispersed glass with melt textures. (A) Comparison of experiments at P_c=100MPa showing the relationship between increasing temperature and peak shear strength. (B) The stress drop that occurs during a stick-slip event is plotted as a function of peak shear strength, showing that larger slip displacements are associated with higher peak strength and these events correlate with the formation of dispersed glass on the slip surface. In contrast low acceleration/displacement experiments produce localised glass patches. (C) Relative peak vertical acceleration during the first stick-slip event is plotted as a function of displacement showing that events resulting in the production of dispersed melt have both a higher peak acceleration and larger displacement during slip than slip that produced localised melt. (D) Correlation between the formation of melt and both peak normal stress and peak shear stress. (E) Identification of regions of different sliding behaviours as a function of confining pressure and temperature.

[e.g. *Tsutsumi and Shimamoto*, 1997; *Koizumi et al.*, 2004; *Hirose and Shimamoto*, 2005b; *Proctor et al.*, 2014] have shown that the onset of flash melting is accompanied by significant weakening, but is followed by rapid strength recovery during melt coalescence. A second stage of weakening is associated with the development of a continuous melt layer. The strengthening observed prior to continuous melting could contribute to strengthening that ultimately terminates slip on current experiments.

Two of the characteristic microstructures associated with both natural and experimental pseudotachylites is the formation of a clast laden melt [*Hirose and Shimamoto*, 2005b; *Lin*, 2008b] and the development of injection veins, usually at a high angle to the melt generation surface [*Sibson*, 1975]. In the current suite of experiments, the abundance of relict clasts within melt layer varies inversely with slip velocity. As the majority of clasts occur at the melt-substrate interface, their occurrence may be attributable to either brittle processes or as the result of thermal fragmentation and passive assimilation during melt generation and slip. The variation in clast shape, from angular to highly rounded, may result from variations in clast size, the method and stage of formation, or the heterogeneity of the melting process. The development of textures such as embayed margins and melt-filled intragranular fractures indicate that some clasts were partially melted.

The formation of injection veins is often cited as evidence of the high pressure and mobility of the frictionally generated melt [e.g., *Sibson*, 1975]. In faults with a low melt viscosity, injection veins are understood to form by the extrusion of the melt away from the slip-surface into dynamically formed extension fractures. However, microstructures developed on fault surfaces associated with distributed melt (such as lobate melt textures, drawn out ribbon-like filaments and the absence of melt intrusion into pores), suggests that the melt formed during these experiments is extremely viscous. It is therefore thought unlikely that most of the observed melt-filled fractures are injection veins. Instead it is proposed that the majority of these structures form by the heterogeneous propagation of melt along crystal defects such as fractures and dislocations. The larger aperture grain boundary fractures (e.g., see white arrow, Fig. 14A), are thought to be more akin to true injection veins, forming by the high pressure injection of melt. In these fractures air pockets are trapped at the junction between the main fracture and subsidiary fractures, indicating incomplete wetting of the fracture surfaces during melt injection.

The frictional melt textures observed on the fault surfaces show evidence of a complex history, even within a single slip event. The debris-free patches and areas of fracturing are observed to overprint regions of striated melt, which in turn overlies an extensively fractured substrate. The overprinting relationships indicate multiple cycles of flash heating, melt formation, quenching and brittle deformation. Similar melt-freeze cycles have been inferred from the simultaneous development of both gouge and melt on the slip surfaces of high displacement frictional melting experiments [*Spray*, 1987, 1992]. However, the common occurrence of well-preserved melt patches with limited evidence of brittle fracturing, suggests that in areas the glass remained ductile until after the cessation of slip. Such observations are consistent with results from other experimental and natural faults [*Spray*, 1992; *Swanson*, 1992].

The formation of glass patches on the fault surface suggests that melt may weld the fault interfaces at the end of slip increasing the cohesive strength of the fault. Fault strengthening is reflected in the stress-displacement curves that show an increase in shear stress required to nucleate subsequent ruptures. Re-fracturing that occurs during the secondary slip events can either take place within the glass layer, at the interface between melt and quartz substrate, or within the quartz substrate depending on the relative strengths of the pseudotachylyte and the wall rock.

4.3 A model for the formation of quartz melt

This section aims to bring together mechanical data, microstructural behaviour and thermal modelling to provide insights into the processes occurring on the slip interface, culminating in the formation of dispersed melt patches. While an approximate continuum of behaviours is proposed (Figs. 22-23), each behaviour type can occur separately, and is dependent on experimental conditions.

The onset of aseismic creep at the yield point is characterised by fracture development and the formation of gouge on the slip surface. With continued sliding, fracturing, intense comminution and mechanical amorphisation result in the formation of compacted areas of granular material, some of which form asperity contacts (Fig. 22A-C). Due to the very slow slip rates during this stage of the deformation, the rate of heat production is limited by heat diffusion and a steady state temperature is reached that is only marginally elevated from the ambient experimental temperatures (Fig. 23E).

With the formation of fault instability and the initiation of rapid sliding, the temperature of the fault surface increases, resulting in frictional melting of asperity contacts on fault surface (Fig. 22D-G and 23A-D). The process of melt generation is a complex interaction between heat generation, melt formation and the transition from brittle-frictional to a viscous-shear-dominated behaviour. In the following section, the mechanical and microstructural insights that have been afforded by the current suite of small-displacement experiments will be compiled to provide a possible model of how melt forms, propagates and potentially lubricates the fault surface.

It is thought that the densely compacted patches of fine-grained wear products formed during early aseismic slip could behave in a solid-like manner, allowing efficient frictional heating to occur during the subsequent high velocity slip. In quartz, where the viscosity of the melt is extremely high (~10^8 Pa s) [*Mysen and Richel*, 2005], and the kinetics of the crystal-melt transition are slow, appreciable superheating of the particles [*Ainslie et al.*, 1961] is likely to occur. The 'melt-front' then propagates heterogeneously outwards from the principal slip zone along grain boundaries and crystal defects such as fractures and dislocations [*Wagstaff*, 1969; *Wolf et al.*, 1990]. The lag-time between heating and melting, coupled with low thermal conductivity of quartz, facilitates superheating of the asperity contacts on time scales of the seismic ruptures. Such a process would allow the asperity temperatures to rise well above the estimated temperature of fusion for quartz.

Any free water within the fault zone, whether from interfacial fluids or trapped in fluid inclusions, could serve to depress melting temperatures and lower melt viscosity by effectively depolymerising the silicate chains [*Spray*, 1992]. However, given the trace quantities of water present in the samples, it is thought unlikely to be a controlling factor in either melt formation or the associated fault weakening. Nonetheless, water contaminants may serve as a localised flux within the fault zone.

When the melt-front migrates through the asperity contact, the rheology changes from being friction-dominated to viscous flow, at which point the generation of heat is buffered by the inverse correlation between heating, viscosity and surface shear strength [*Fialko and Khazan*, 2005]. This constrains the extent of possible melt generation within one flash heating episode. However, if the rate of heat production prior to this brittle-viscous transition is high enough to produce an 'over-shoot' of the temperature

of fusion (Fig. 23A), resulting in superheating the crystalline asperities and melt, the viscosity of the melt would be reduced, causing it to lubricate the asperity contacts and resulting in significant dynamic weakening [*Koizumi et al.*, 2004; *Hirose and Shimamoto*, 2005b; *Proctor et al.*, 2014]. This is interpreted to result in the generation of the observed high-velocity slip events (Fig. 22E). In the case of the 'low' velocity stick-slip events, it is suggested that sliding ceases before temperatures become high enough to achieve a significant reduction in viscosity, even though the temperature of fusion may have been exceeded (Fig. 22D and 23C).

If low viscosity melt is the mechanism for fault weakening associated with high velocity slip, then heating to the point where the viscosity of the melt is reduced suggests higher temperatures and a greater 'over-shoot' of the temperature of fusion (Fig. 23). Higher temperatures would enhance the kinetics of melting and lead to complete fusion of most clasts, thereby producing the low density of clasts observed in the melt layer of the high-velocity slip events. In contrast, melts produced during low velocity slip events are characterised by a significantly higher abundance of clasts. This indicates a lesser degree of thermal overshoot relative to the melting temperature, and therefore a significantly higher viscosity, resulting in the failure to facilitate fault weakening. However, melt layers typically have a thickness in the range 0.3μm to 1.7μm, regardless of whether they formed under a high- or low velocity slip regime. Accordingly, the thickness of the melt layer is probably dictated by the maximum temperature overshoot prior to the transition into the viscous-shear regime [*Cardwell et al.*, 1978; *Fialko and Khazan*, 2005]. Continued deformation and potential coalescence of the melt patches into a continuous melt layer may result in the widening of the melt layer as has been observed in high displacement rotary shear experiments [*Tsutsumi and Shimamoto*, 1997; *Hirose and Shimamoto*, 2005b]. However, slip distance in the current experiments is insufficient to achieve melt coalescence.

The ability of a mineral to superheat is largely determined by the relationship between the rate of heat generation and the rate of fusion. Cristobalite, quartz and albite are the only silicate minerals conclusively shown to significantly superheat under laboratory conditions [*Ainslie et al.*, 1961; *Dietz et al.*, 1970]. The ability of these minerals to superheat has been attributed to their anomalously high viscosity and their strongly bonded framework [*Mysen and Richel*, 2005]. For many of the common low-viscosity pseudotachylyte-forming minerals, the rate of fusion is much higher than for quartz,

with the concurrent heat adsorption being so rapid as to prevent the interior of the crystal from becoming appreciably superheated [*Ainslie et al.*, 1961]. Further, the formation of highly fluid melts rapidly produces a low viscosity film or boundary layer around the clasts, inhibiting further frictional heat generation, but concurrently achieving a state of effective lubrication [*Fialko and Khazan*, 2005]. This would result in the formation of clast-laden pseudotachylytes observed both in nature [e.g. *Lin*, 1994; *Wenk et al.*, 2000; *O'Hara*, 2001; *Pittarello et al.*, 2008] and experiment [e.g. *Lin and Shimamoto*, 1998; *Hirose and Shimamoto*, 2005b]. However, field observations of cooling structures and clast abundance within natural pseudotachylites, combined with numerical modelling of fault vein temperatures [*Di Toro and Pennacchioni*, 2004; *Magloughlin*, 2005], suggests the possibility that melt superheating could occur in other mineral assemblages than the quartz system explored in this study.

The termination of slip could be influenced by the changing dynamic properties of the melt layer, which is assumed to behave largely as a Newtonian fluid [*Hirose and Shimamoto*, 2005b]. A number of previous studies suggest a non-Arrhenian model for the temperature dependence of viscosity of highly siliceous melt [*Dingwell*, 2007; *Lavallee et al.*, 2007] resulting in a faster than exponential increase in viscosity with cooling, with the potential to rapidly terminate slip [*Koizumi et al.*, 2004; *Hirose and Shimamoto*, 2005b]. Further, the shear resistance of the molten layer is inversely proportional to the layer thickness, with any reduction in the width of the melt layer resulting in a significant increase in the shear stress required to maintain slip [*Hirose and Shimamoto*, 2005b]. Upon cooling, viscosity will increase most rapidly at the fault zone boundaries, potentially localising strain within the fault core and effectively reducing melt layer thickness.

Re-examining the decades old question, ‘is comminution a necessary precursor to pseudotachylyte generation?’ [e.g. *Wenk*, 1978; *Spray*, 1995] the mechanical and microstructural evidence from the current experiments would suggest that the answer is both yes and no. There is clear evidence of brittle fracturing, gouge formation and mechanical amorphisation on the fault surface prior to, and during the early stages of rapid slip. However, numerous experiments show melt textures forming on interfaces that apparently have experienced limited damage prior to sudden stress drop (indicated

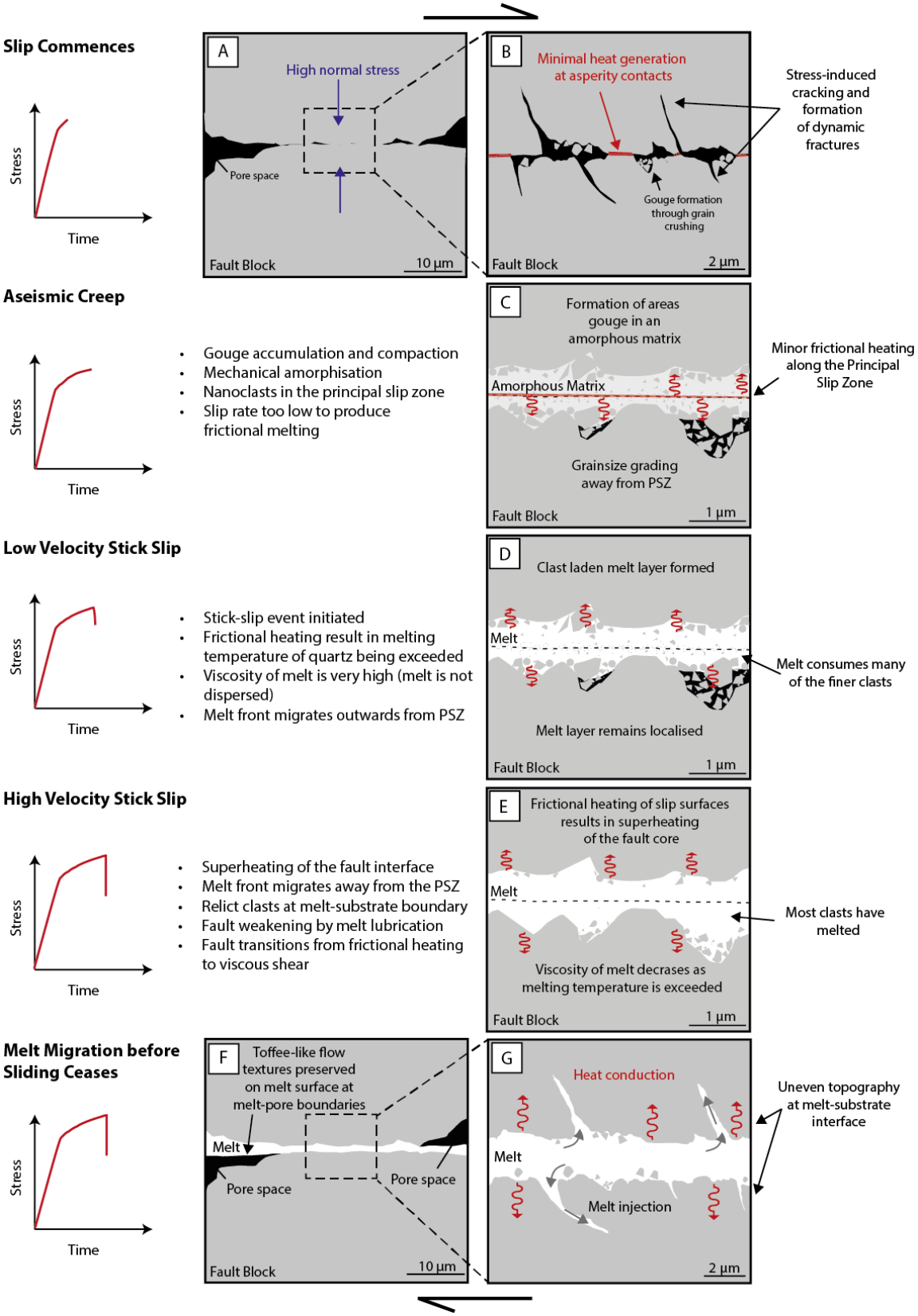

Figure 22: Continuum of behaviours associated with the formation of frictional melt
Grey indicates the original quartz sandstone, black indicates pore space, pale grey in the fault core indicates possible amorphous material and white indicates melt. See text for discussion.

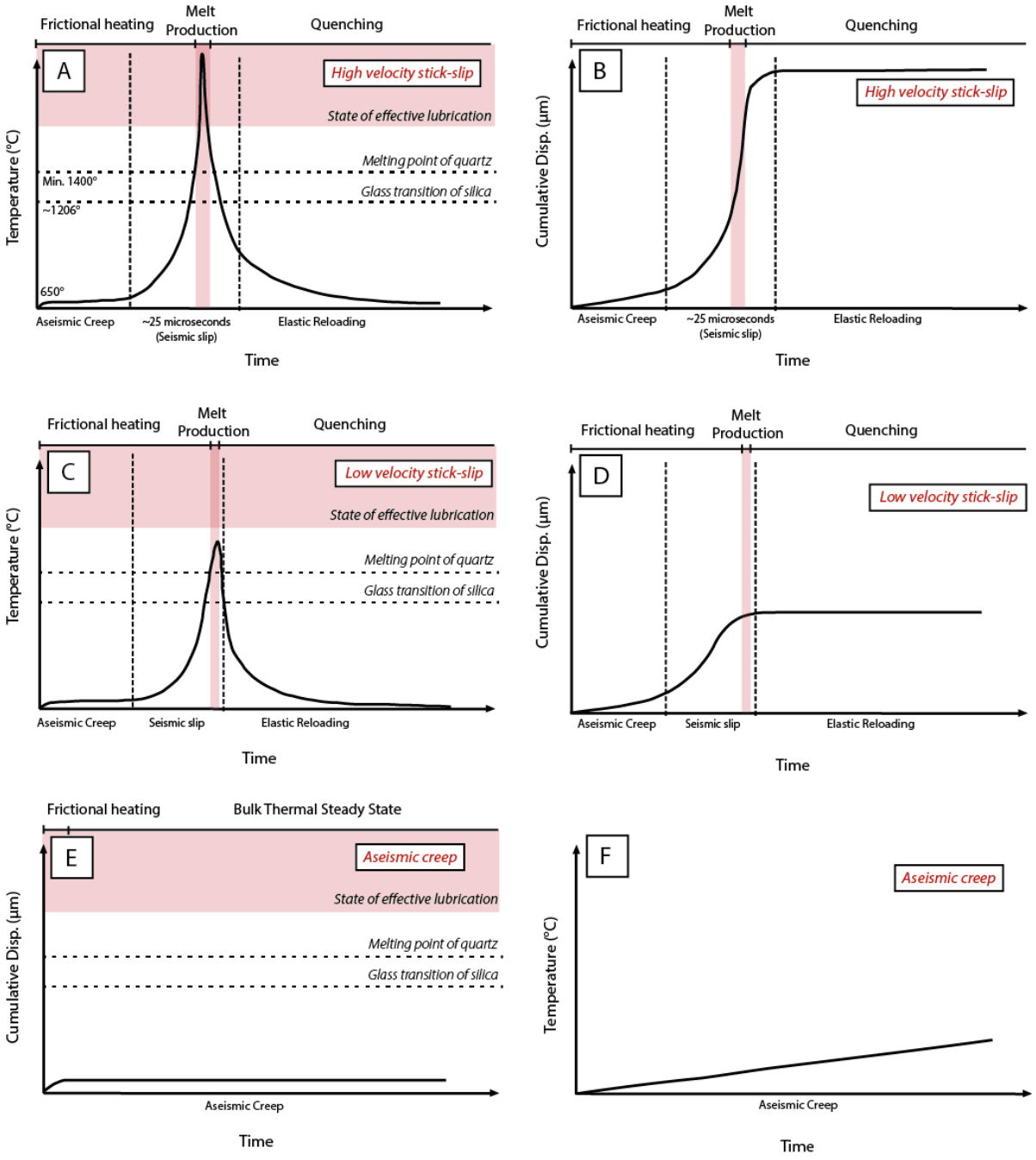

Figure 23: Melt development as a function time and displacement.
(A-B) Shows estimated temperature and displacement evolution during a high velocity slip event. Frictional heating occurs during the early part of slip. As the fault temperature exceeds the temperature of effective lubrication, velocity increases and a large displacement ensues. Further heating is limited by the negative relationship between temperature and velocity, and the shear strength of the viscous layer increases with cooling and thinning, resulting in the cessation of slip. (C-D) Predicted temperature and displacement profile during rupture for a low velocity slip event. Frictional heating results in an overshoot of the melting temperature but the state of effective lubrication is not attained, resulting in a shorter slip displacement. (E-F) Temperature and displacement evolution during aseismic creep. The temperature increases slightly with sliding but rapidly attains a bulk thermal steady state where temperature generation is equally matched by thermal diffusion. Displacement accumulates linearly during slip. Possible mechanical amorphisation on slip surfaces.

by a rapid transition from elastic loading to rapid stress drop on the stress-displacement curves). However, the observation of both clean and clast-laden melt-substrate boundaries, suggest that both gouge and larger grain-to-grain contacts may provide sources of heat generation and melt production.

The model of melt formation in quartz presented here suggests a continuum of behaviours based on the mechanical and microstructural phenomena observed during the current suite of experiments. While broadly consistent with previous models [e.g. *Spray*, 1992, 1995; *Fialko and Khazan*, 2005], the current observations suggest a number of behavioural nuances that have not previously been observed. The current experiments reveal that at high temperatures and confining pressures potentially mechanically amorphized material forms over small displacements (< 200μm) and low slip rates (< 1μm/s), consistent with the observations of *Pec et al.,* [2012]. The formation of this 'amorphous' material during aseismic creep could provide a precursory mechanism for fault instability and the dynamic weakening associated with seismic rupture. While the behaviour and stability of the mechanically 'amorphized' material remains poorly constrained it may be possible that this material could have tribological weakening effects in much the same way as dynamically activated gouge [*Han et al.,* 2010; *Reches and Lockner*, 2010] or silica gels [*Goldsby and Tullis,* 2002].

It is anticipated that once fault rupture nucleates, superheating of crystalline structures at asperity contacts could play a significant role in the formation of melt in a quartz system due to the slow melting kinetics of quartz and high melt viscosity. This places constraints on the slip velocities and stress concentration needed to generate quartz melt and perhaps provides a tangible reason why experimental generation of pure quartz pseudotachylites has been so difficult to recognise. These observations have significant geological implications, in terms of rupture setting, and possible occurrence that will be discussed in the final chapter of the thesis.

5. Conclusions

A series of triaxial deformation experiments has been conducted on Fontainebleau sandstone over a range temperatures between 400-927°C and confining pressures between 50-200MPa. The aim of these experiments has been to explore the behaviour and stability of faults in nominally dry conditions at increasing depth in the continental

crust. The mechanical results are coupled with microstructural analysis using multiple techniques (including optical microscopy, high resolution FESEM, and FIB-TEM) that provide insights into mechanisms controlling fault behaviour at the macro-, micro- and nano-scale. Key and novel findings of these experiments have been the identification of (1) possible mechanically amorphized silica and (2) the early stages of frictional melting, on pure quartz interfaces during small slip events (<200µm). The identification of these phases has allowed, for the first time, an exploration of the possible role of different mechanisms of amorphisation in modifying the mechanical behaviour and stability during the early stages of slip on quartz faults interfaces.

Complex transitions in the sliding behaviour occur with changing temperature and pressure conditions. This behaviour has been bracketed into three regimes: low temperature (<600ºC) stable sliding; high temperature (>650º), low pressure, stick-slip behaviour that results in relatively low velocity sliding; and high temperature, high pressure stick-slip that results in relatively high velocity sliding. Accompanying the different mechanical behaviours is the formation of three distinguishable styles of amorphous material. Stable sliding is associated with the formation of a partially amorphous layer of nano-gouge. Low velocity slip results in the formation of localised melt patches, and high velocity sliding produces dispersed melt textures. It has been proposed that these different sliding regimes represent a continuum of possible behaviours that can occur on the fault interface, providing insights into conditions leading to gouge formation and amorphisation, fault instability and the generation of melt. The high viscosity nature of the silica melt has meant that over the experimental conditions explored in this chapter, different stages of melt generation, ranging from flash heating through to localised melting, have been captured and preserved, providing valuable insights into early processes associated with melt formation.

The mechanically amorphized silica that forms at aseismic slip velocities and high ambient temperatures is distinguished by the striated nature of amorphized patches on slip surfaces. The amorphous material is interspersed between crystalline quartz clasts, forming a film like matrix that is similar to ‘gels’ produced previously during high velocity sliding experiments. This amorphous material is interpreted as forming by intense comminution of the gouge particles resulting in a loss of crystalline structure in a similar manner to previously observed grinding or mechanically induced amorphisation. The frictional properties and behaviour of the mechanically amorphized

material at high temperature and confining pressures remains largely unexplored, but it is speculated that this material could be a contributing factor in the development of sliding instability.

The development of a sliding instability results in fast slip that culminates in the rapid frictional heating of asperity contacts. Flash heating and frictional melting can occur within 50μm of the onset of slip, resulting in the formation of continuous flow structures that are > 150μm in length, and provide a microstructural record of the slip event. Critical textures that demonstrate localised melting include the formation of drawn-out glass filaments, elongate vesicles and striated melt textures that are preserved when the melt is translated during slip from a quartz-quartz interface to a quartz-pore interface. At grain-to-grain interfaces diagnostic textures of melt formation are fractured, debris-free welded patches on the slip interface. The amorphous structure has been confirmed using FIB-TEM and shows that the melt textures identified on the fault surface using high resolution FE-SEM are 'pure' silica glass layers up to 2μm thick.

Simple two-dimensional thermal modelling indicates that sufficient frictional heating can occur during rupture to cause frictional melting over these displacements, provided that normal stress is highly concentrated at asperity contacts and that slip occurs at approximately seismic velocities. Using these assumptions, the calculated maximum asperity temperatures are consistent with the mechanical and microstructural observations. Experiments generating high velocity slip are characterised by higher maximum asperity temperatures than experiments with low velocity slip.

The rise time for heat generation and melt production is estimated to be ~10ms (but could be up to an order of magnitude faster), which is significantly shorter than previously recognised in experiments and is attributed to the high normal stresses (>200MPa) and elevated ambient temperatures in the present experiments. The generation of dispersed melt is shown to modify the sliding behaviour, leading to relatively high velocity stick-slip events, characterised by larger displacements, greater stress drops and higher peak accelerations than low velocity stick-slip events that generate more localised melt patches. It is therefore suggested that, at least initially, the formation of high velocity, high temperature melt results in the lubrication of the asperity contacts, thus facilitating slip.

Finally, it is suggested that a time lag exists between heat generation and the propagation of the 'melt-front' into the substrate and away from initial asperity contacts, resulting in significant superheating of both the crystalline clasts and the melt. During the high velocity slip events, sufficient 'overshoot' of the temperature of fusion lowers melt viscosity, causing melt lubrication at asperity contacts. In comparison, low velocity slip events never achieve the temperatures necessary to lower the viscosity of the melt, resulting in the formation of more localised melt patches.

Chapter 3

Experimental insights into the mechanics and microstructures associated with the reactivation of misoriented faults

1. Introduction

In the actively deforming continental lithosphere, earthquake rupture nucleation dominantly occurs in the upper half of the crust, representing the zone of brittle failure and unstable frictional sliding that is, to a first order, governed by the empirical Coulomb failure criterion. Theoretical, experimental and field evidence indicates that most rocks fail at orientations between 25-30º to the maximum principal stress [*Anderson*, 1905; *Jaeger et al.*, 2007], assuming typical frictional properties of intact rock [*Byerlee*, 1978]. However, analysis of the resolved shear and normal stress acting upon a given fault plane suggests that under most crustal conditions and assuming a cohesionless fault, it is preferential to reactivate an existing fault rather than to form a new failure. Accordingly, it is inferred that many fault ruptures occur along pre-existing faults [*Scholz*, 2002]. Repeated reactivation is confirmed by field and microstructural evidence that records rupture history, revealing that some faults may be reactivated hundreds to thousands times [*Cowie and Scholz*, 1992; *Cowie and Roberts*, 2001]. There is also compelling geological evidence that many faults, in various tectonic regimes, remain active despite having become unfavourably oriented for reactivation relative to the prevailing regional stress field [e.g. *Sibson*, 1989; *Sibson*, 1990b; *McClay and Buchanan*, 1992; *Fournier*, 1996; *Sibson*, 2007; *Collettini et al.*, 2009b]. This suggests that even under non-ideal conditions for reactivation, fault zones can remains as comparatively weak structures within the host rock. In simple mechanical terms, reactivation is achieved when there are large disparities between the cohesive strength and frictional properties of the fault zone when compared with surrounding rock mass.

Time dependent strength evolution and recovery also has important implications for fault reactivation and earthquake recurrence interval, with both natural and experimental studies [*Karner et al.*, 1997; *Tenthorey et al.*, 2003; *Tenthorey and Cox*, 2006] indicating that during the interseismic period faults recover a portion of their frictional and cohesive strength. In terms of fault mechanics, as cohesive fault strength increases, the stress and fluid states necessary to reactivate a fault become increasingly similar to that required to generate intact rock failure [*Streit and Cox*, 2001; *Cox*, 2010]. Where faults are unfavourably oriented for reactivation, even relatively small increases in cohesive strength (<50% of intact rock strength), significantly reduces the range of conditions under which a fault can reactivate leading, in many situations, to the failure of a new fault.

Sibson [1985, 1990b] introduced terminology to describe faults depending on their frictional properties and orientation relative to the prevailing stress field. The terms 'optimally- oriented', 'misoriented' and 'severely-misoriented' were coined to define faults in terms of the ratio of the effective principal stresses required to induce sliding. This definition requires knowledge of stress conditions and/or frictional properties of the fault, so for more general discussion where such parameters may not be known, faults are described in terms of being 'favourably' or 'unfavourably' oriented. Favourably oriented faults are close (say, +/- 10°) of an ideal failure angle assuming normal frictional properties, while unfavourably-oriented faults represent more significant deviations in orientation relative to the maximum principal stress. Examples include low-angle normal faults [*Wernicke*, 1995], steep reverse faults [*Sibson et al.*, 1988] or segments of the strike-slip San Andreas Fault [*Mount and Suppe*, 1987].

Critical failure conditions of unfavourably-oriented faults are notionally achieved through the evolution of stress states and pore fluid pressures during fault loading [*Sibson*, 1985, 1990b; *Sleep and Blanpied*, 1992; *Axen*, 1999; *Streit and Cox*, 2001; *Scholz*, 2002; *Cox*, 2010] including possible rotation of far-field stress orientations locally within the fault zone [*Rice*, 1992; *Faulkner et al.*, 2006; *Healy*, 2008]. The existence of high fluid pressures is thought to be integrally coupled with the reactivation of unfavourably-oriented faults [*Sibson et al.*, 1988; *Sibson*, 1992, 1994; *Cox*, 1995; *Nguyen et al.*, 1998], with the porosity, permeability and fluid flux in fault zones influencing the development of regions of fluid overpressure. While fault rupture in tight, low porosity crystalline rocks enhances permeability [*Sibson*, 1981; *Smith et al.*,

1990; *Evans et al.*, 1997], faults in porous rocks such as in sedimentary basins, may serve to create low permeability barriers [*Antonellini and Aydin*, 1994; *Caine et al.*, 1996], impeding or re-directing fluid flow and potentially creating a fluid seal, trapping pressurized fluids.

The reactivation of unfavourably-oriented faults has also been ascribed to chemically or physically induced changes in frictional properties leading to an inherent fault weakness. This has been attributed to mechanisms such as the development of frictionally-weak mineral phase [*Wintsch*, 1995; *Imber et al.*, 1997; *Collettini et al.*, 2009b], dissolution-mediated frictional sliding [*Cox*, 1998], or fault zone weakening related to the development of anisotropic fabrics within the fault core [*Collettini et al.*, 2009a]. Even in low temperature, essentially pure quartz systems, water-rock interactions are thought to extend beyond the hydraulic reduction in effective normal stress to other physical and chemical effects resulting from changes in specific surface energy and friction coefficient of the fault interface [e.g., *Rutter and Mainprice*, 1978; *Hadizadeh and Law*, 1991; *Zang et al.*, 1996; *Baud et al.*, 2000; *Frye and Marone*, 2002; *Reviron et al.*, 2009], thus reducing fault strength and potentially facilitating reactivation of apparently unfavourably-oriented faults.

Despite the ample geological, geodetic, and seismic evidence [*Sibson*, 1990b; *Bernard et al.*, 1997; *Axen*, 1999; *Sibson*, 2007] of frictional slip occurring on faults oriented at a high angle to the regional maximum compressive stress, the majority of experimental rock deformation studies undertaken to date have focused on understanding the mechanical, behavioural and microstructural evolution of faults slipped under stress conditions favourable to their reactivation [e.g. *Scholz et al.*, 1972; *Menendez et al.*, 1996; *Paterson and Wong*, 2005]. A small number of experimental studies have investigated the mechanical properties of faults reactivated under unfavourable stress conditions [e.g., *Jaeger*, 1959; *Handin*, 1969; *Mitchell et al.*, 2011], although the microstructural development of these faults remains poorly explored.

This chapter presents the results of an investigation that has encompassed both a sequence of novel triaxial deformation experiments, as well as revisitation of a number of classic rock friction experiments to more comprehensively explore the mechanics and microstructures associated with the reactivation of unfavourably-oriented faults. Experiments have been performed at room temperature on a series of pre-ground, bare-

interface fault surfaces, that are oriented at various angles ranging from optimally-oriented through to severely misoriented, to gain insights into fault behaviour and microstructural processes under increasingly unfavourable stress conditions. The use of both nominally dry and water-saturated conditions has allowed a comparison to be made of fault behaviour and microstructural evolution resulting from slip that is activated by either changes in stress states or pore-fluid pressures.

In the preceding chapter the concept of mechanical and thermal alteration to the crystalline structure of the slip interface was discussed as a possible mechanism for modifying fault strength and stability. While a quasi-static weakening mechanism is required to initiate slip on unfavourably-oriented faults, the high normal stress associated with misoriented fault reactivation provides an ideal environment in which to further explore possible amorphisation processes at room temperature. Additionally, the physical and/or chemical modification to the fault interface during dynamic slip processes has been investigated in terms of its ability to either enhance or suppress further fault reactivation. A combination of multiple microstructural techniques including high resolution FE-SEM, cathodoluminescence and microcomputed X-ray tomography are used to provide insights into mechanisms controlling fault behaviour over a range of scales and in both two- and three-dimensions.

2. Experimental and analytical methods

2.1 Experimental methodology

Experiments were undertaken at room temperature in a Paterson gas-medium deformation apparatus that allows independent control and measurement of confining and pore fluid pressure, axial displacement rate and axial load (Fig. 1A). Deformation was undertaken at confining pressures between 50-100MPa, pore fluid pressures up to 85MPa and at the nominal axial shortening rate of 3.63 μms^{-1}. The Paterson rig is a 'soft' apparatus; significant elastic strain accumulated during loading is imparted into a specimen during failure, resulting in higher displacements and stress drops than would be produced using a more rigid apparatus.

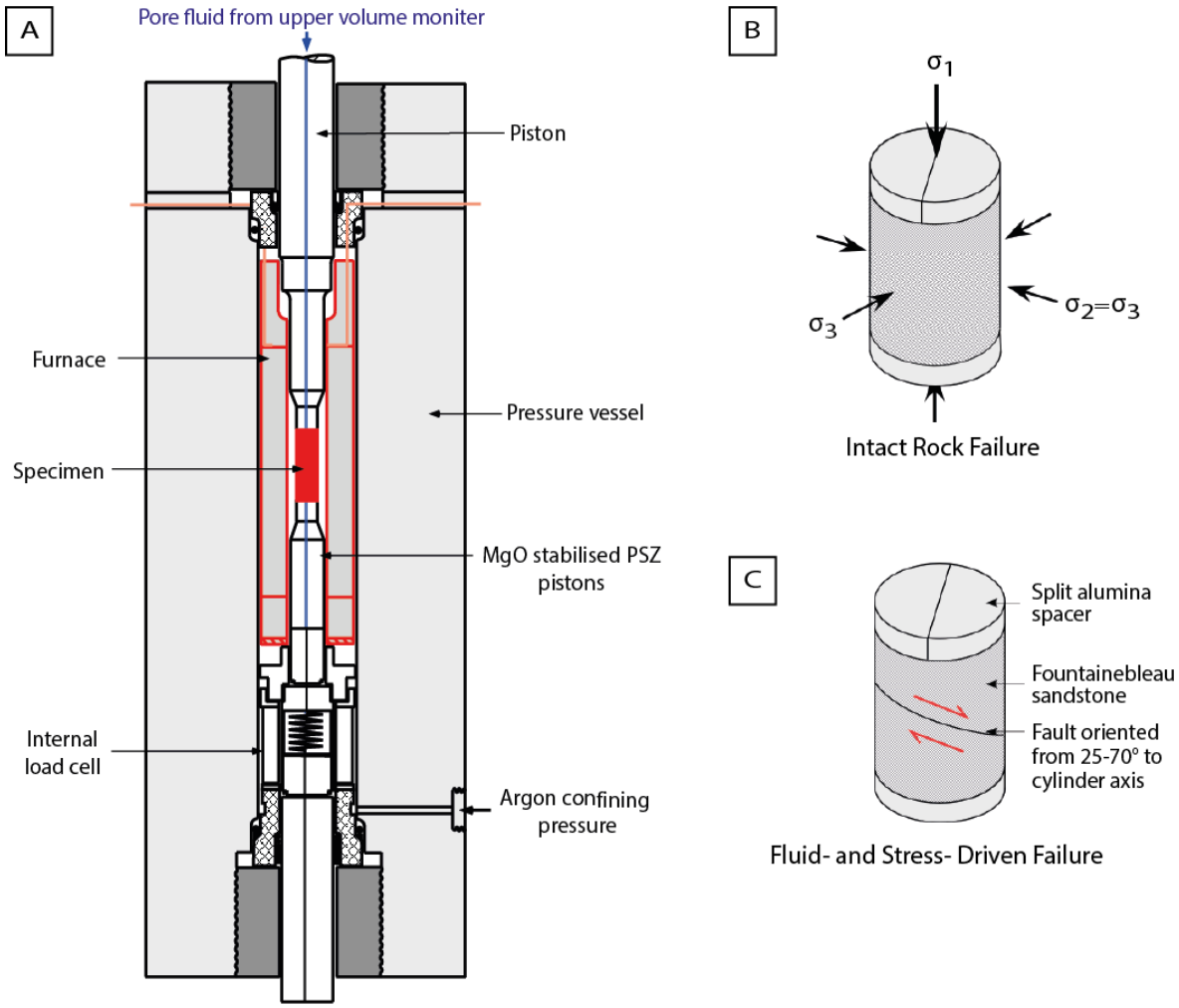

Figure 1: Apparatus and sample configuration.
(A) Schematic illustration of the pressure vessel showing the major components and sample location. (B) Sample configuration for intact rock failure experiments. A split alumina spacer is used to facilitate access of the pore fluids to the sample during fluid-driven failure experiments. (C) Sample configuration for the fault reactivation experiments. The fault orientation changes with 5° increments over a range of 25° - 70° to the maximum principal stress.

Experiments were conducted on Fontainebleau sandstone; a well-sorted, equigranular, essentially pure quartz sandstone with an average grainsize of approximately 200-250µm and a porosity between 6-8%. In experiments with elevated pore fluid pressures, deionised water was used as the pore fluid. Fluid access to the sample is provided through the conduit formed by the hollow centre of the loading pistons. The high connectivity of the pore structure within the Fontainebleau sandstone allows even distribution of the fluids through the sample and along the fault interface. Pore fluid pressure was limited to a maximum of 85% of the confining pressure to preserve the integrity of the assembly seals during the experiments.

Two different experimental configurations were used during the deformation experiments performed in this study. To understand the strength and mechanical properties of the Fontainebleau sandstone, the first group of experiments involved the brittle failure of an intact sandstone cylinder (Figs. 1B, 2B). These experiments were undertaken either (1) dry, over a range of confining pressures between 15-70MPa, with the samples either being loaded until failure at a constant axial displacement rate (stress-driven failure, Fig. 2A), or (2) under water-saturated conditions, where the axial load was held constant while the pore fluid pressure was increased using a volume monitor until failure occurred (fluid-driven failure, Fig. 2A). The second group of experiments aimed to investigate the reactivation of an existing fault and involved either the stress- or fluid-driven reactivation of an existing pre-ground fault surface (Figs. 1C, 2D). As for intact rock failure experiments, stress-driven fault reactivation was achieved by increasing differential stress at a nominally constant axial displacement rate until slip occurred on the existing fault or a new fault was formed (see path A, Fig. 2C). These experiments were undertaken either without pore water, or with pore water held at a constant pressure, with the latter being referred to as 'wet stress-driven' fault reactivation (see path A', Fig. 2C). Fluid-driven fault reactivation was achieved by maintaining a constant axial load while increasing the pore-fluid pressure until failure occurred (see path B, Fig. 2C). By controlling pore fluid pressures using a volume monitor, insights were obtained about the inelastic volume changes within the sample. These volume changes reflect the microstructural evolution of the sample during deformation, resulting in either dilatancy or compaction, and is manifest by the changing volume monitor travel distance required to achieve a given pore fluid pressure.

The sample arrangement for both stress- and fluid-driven fault reactivation experiments consisted of two cylindrical specimens (diameter of 10mm), ground at a specific angle relative to the axial shortening direction, forming a fault plane. This fault surface was inclined at an angle (θ_r), of between 25º and 70º to the bulk maximum principal stress (σ_1), thereby simulating faults that vary from optimally oriented to severely misoriented for failure, assuming a static coefficient of friction of 0.75 [*Byerlee*, 1978] (Fig. 1C, 2D). The leading edge of the fault surface was blunted by the grinding of a slight chamfer on the outer edge of the sample to prevent jacket puncture during slip events. All samples were ground to a length of 21mm and oven dried prior to use.

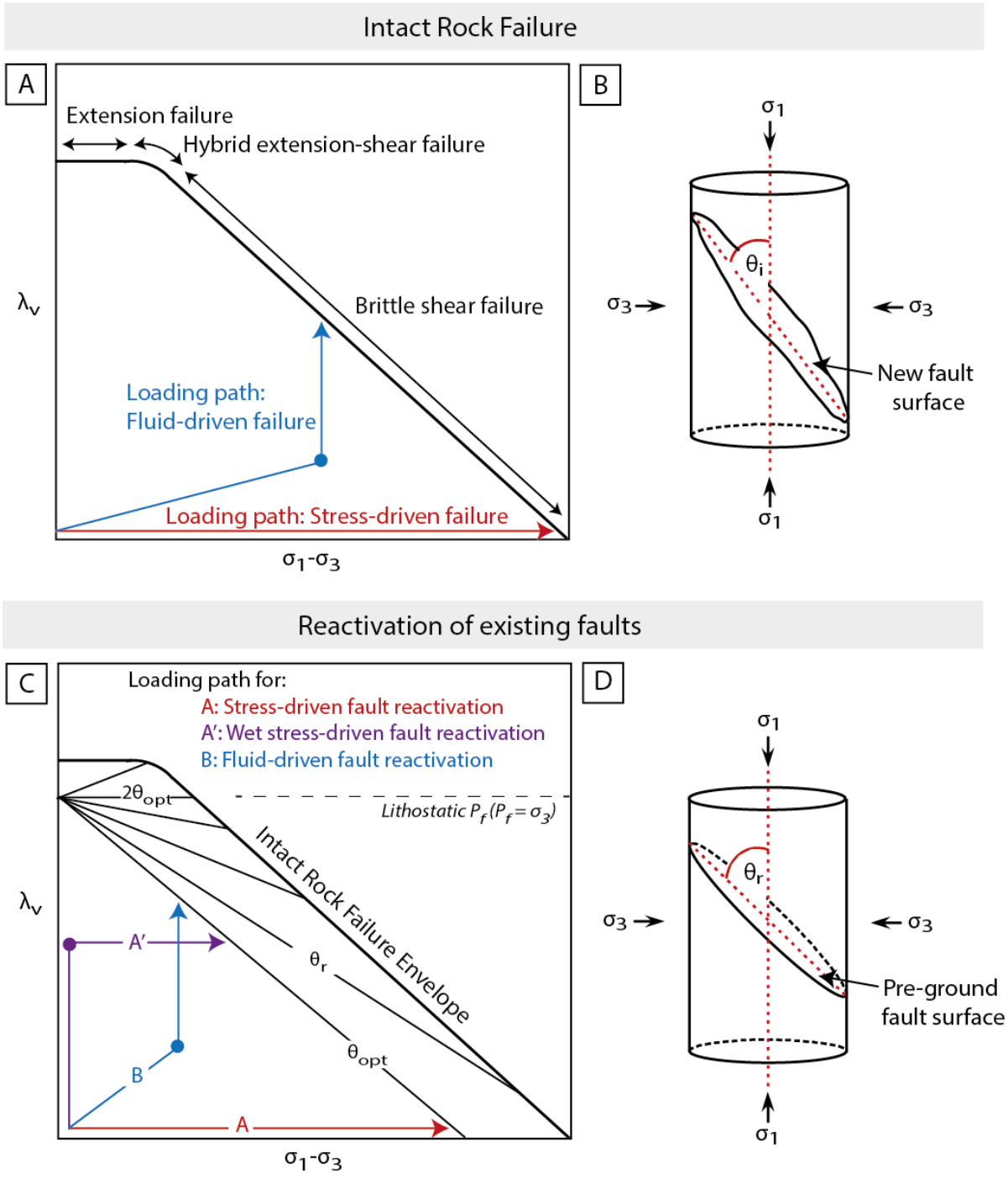

Figure 2: Loading pathways leading to the different modes of failure.
(A) Schematic failure mode diagram showing pore fluid factor as a function of differential stress for a given confining pressure. A generic failure envelope for extension, hybrid extensional-shear, and shear mode failure are shown for intact rock in in a compressional regime. The loading paths used in the intact rock failure experiments are shown and illustrate the combination of differential stress and pore fluid pressure that can be used to drive failure. (B) Diagram illustrating the initiation angle (θ_i) for intact rock failures. (C) Generic failure mode diagram showing the effect of the reactivation angle (θ_r) on the differential stress and pore fluid conditions required to re-shear on a cohesion-less fault of a given frictional value. The loading paths for fault reactivation in the current study are shown. The definition of angle θ_r is shown in (D) and corresponds to the angle between the ground fault surface and the maximum principal stress.

The specimens and loading pistons were contained within an impervious, thin-walled, annealed inner copper sleeve and outer jacket to ensure the separation of pore fluid and confining medium. To accurately determine the sample strength a correction for the strength contribution of the jacket and sleeve has been applied using data derived from jacket calibration experiments (see Appendix 2). During slip on the fault interfaces, displacement results in a reduction in the contact area of the fault interface. A reduced contact area results in an increase in stress on the remaining interface; this effect is most significant on faults inclined at a high angle relative to the sample axis. A correction has been applied to the data by calculating the change in fault surface area as a function of shear displacement, assuming that displacement on the fault occurs only during the periods of non-elastic strain (see Appendix 2).

To examine the stability of deformation-induced microstructures under conditions simulating interseismic healing in a fluid-active environment, an investigation was undertaken on a fault oriented at $\theta_r = 60^o$ where a single slip event had occurred as a result of stress-driven fault reactivation. This experiment used an outer iron jacket to allow the high temperature experiments to be undertaken without the need to re-jacket the assembly. The significant additional strength of the iron jacket at room temperature in comparison to a copper jacket, was not considered an issue as the experiment was performed purely to observe the microstructural evolution and healing of the fault zone during hydrothermal treatment. Following slip on the unfavourably oriented fault, the differential stress was reduced to zero and deionised water was introduced to the sample via the hollow upper pistons. Confining pressure, pore fluid pressure and temperature were then elevated until P_c = 250MPa, P_f = 150MPa and T = 900ºC; these conditions were maintained for 6 hours. Although not reflective of ambient temperatures in the seismogenic upper crust, the use of high temperatures during this experiment increased reaction kinetics, thereby allowing processes normally occurring over timescales of earthquake recurrence (decade to centuries) to be activated on laboratory timescales.

2.2 Microstructural analysis techniques

Following removal of the sample from the pressure vessel, the outer copper jacket was peeled off leaving the sample contained within the inner copper sleeve. As the samples were extensively fractured and contained non-cohesive material, impregnation under vacuum in a heat-curing epoxy (Petropoxy 154) was necessary to ensure the specimen structure was preserved during sample preparation. Once cured the sample was cut

along the long axis of the cylinder perpendicular to the fault slip plane. Half of the sample was mounted in an epoxy block and polished using a progressively finer sequence of silicon carbide powder and diamond paste. To achieve the finial polish suitable for high resolution back-scattered electron imaging, the epoxy block was polished for up to 4 days using a slurry of water and 0.05μm alumina on a vibrating polishing machine and finally polished using 0.05μm colloidal silica on a soft polishing cloth.

The polished blocks were carbon coated and analysed using an Angle selective Backscattered electron (AsB) detector on a high resolution Zeiss UltraPlus Field Emission Scanning Electron Microscope (FE-SEM). The AsB detector, located at the objective lens, detects larger angle backscattered elections, thereby providing information about both crystallographic orientation and composition (from the mean atomic number - Z contrast). A working distance of 8.5mm, 10.0kV accelerating voltage and the use of a 60μm aperture allowed high-contrast and high-resolution imaging of the damage zones and fracture networks. Analysis of the entire longitudinal section was achieved through automated stage control and image stitching, which allowed the creation of high-resolution mosaics of the sample surface. SEM imaging was undertaken at the Centre for Advance Microscopy located at the Australian National University.

Cathodoluminescence (CL) investigations were undertaken at room temperature using a FEI Verios high resolution FE-SEM fitted with a Gatan MonoCL4 Elite cathodoluminescence system with a working distance of ~6.3mm, 0.8nA beam current and 5.0kV accelerating voltage. The same sample preparation techniques were used for the CL investigations as were used for BSE-SEM imaging. The CL is excited using a stationary electron beam at normal incidence to the sample and is measured using a parabolic mirror collector inserted into the electron path between the sample and the objective lens. Imaging was undertaken using the panchromatic mode, which produces an 8 bit panchromatic grey scale CL image. ‘Colour’ images are obtained using bandpass filter monochromators, which produce a grey-scale representation of the light emitted at a particular wavelength (red 595-800nm, green 520-570nm, blue 380-500nm). Spectral analysis was undertaken in monochromatic mode over a wavelength range from 300-800nm and was corrected for total instrument response. Spectral data, which are collected as a function of wavelength, have been converted to energy *E* (eV),

where it has a dominantly Gaussian shape. Spectra have been fitted using a multi-parameter Gaussian function that provides an estimate of peak position. Using a minimum number of peaks, the position, width and integrated area under the curves were iteratively refined until residuals were minimised. All CL work was undertaken at the Australian National Fabrication Facility, located at the Australian National University in Canberra.

Insights into the development microstructures in three-dimensions have been obtained using microcomputed X-ray tomography [*Sakellariou et al.*, 2004] acquired using the micro-CT apparatus developed and built at the Department of Applied Mathematics, Australian National University. Samples have been imaged using X-rays over a 360º rotation at 0.125º intervals, with differences in X-ray attenuation providing information on different phases (quartz, epoxy and air filled voids, epoxy impregnated gouge) within the sample. A limiting resolution of between 1.5-7µm is achieved depending on sample size, and operating voltage.

Radiographic data collected from a micro-focus X-ray source and corrected for optical and camera distortion have been acquired for 3 separate specimens; for MIS031 the entire sample (ϕ = 10mm, $l \approx$ 18mm) was scanned, while the other two samples (MIS012, MIS018) had a cylinder cored (ϕ = 3.5mm and a $l \approx$ 5mm) with the long axis parallel to the fault and perpendicular to the slip direction. The collected data was reconstructed using a modified Feldcamp algorithm [*Sakellariou et al.*, 2004] to generate a 2048^3 voxel tomogram, where resolution is dictated by the voxel edge length. The full sample tomogram has a resolution of 5µm, whereas the two smaller samples have a resolution of 1.5µm. Voxel density information is provided by the X-ray signal intensity, with partially filled voxels indicating a lower density than the surrounding material. Accordingly, density contrast information in this essentially two-phase system has allowed the identification of fracture networks and the spatial distribution of fault wear-products (such as gouge and melt). Using Drishti 2.5 software, a program written for the visualisation of volumetric data, this information has been used generate 3D models of the fault zone that can be rotated, scrutinized and explored from any angle.

3. Results

3.1 Mechanical behaviour

3.1.1 Mechanical properties of intact Fontainebleau sandstone

To develop an understanding of the frictional properties and strength of the Fontainebleau sandstone, a series of experiments was undertaken over a range of confining pressures using intact cylindrical samples that were loaded until failure (Appendix 4). A typical loading curve for these experiments, showing differential stress as a function of time, is shown in Figure 3A. Loading is characterised by an initial period of essentially pure elastic loading, followed by a slight decrease in slope approaching the peak stress and the onset of macroscopic failure (for stress-strain curves see Appendix 5). The region that deviates from pure elastic loading is assumed to mark the onset of irreversible deformation, most likely in the form intra- and inter-granular micro-cracking. At peak stress, a violent macroscopic brittle shear failure occurred that was clearly audible from outside the high-pressure isolation area.

Significant displacement and stress drop occurred at shear failure with axial shortening of up to 0.97mm and a co-seismic stress drop of up to 588MPa, occurring during a single slip event. When the specimens were retrieved from the apparatus the failure zone and resulting sample offset was clearly visible through the outer copper jacket. The significant displacement and stress drop that occurred at failure is attributed to the release of accumulated stored elastic strain from the apparatus into the sample [*Paterson and Wong*, 2005].

The angle of fault initiation (θ_i), which is defined as the acute angle formed between the fault surface and orientation of the maximum principal stress (Fig. 2B), is found to vary with confining pressure. At confining pressures $\geq$ 50MPa the failure zone is typically oriented between θ_i = 23-25º whereas at lower confining pressures (P_c = 15-30MPa), θ_i = 16-17º, indicating a possible transition towards axial splitting. Following shear failure, a number of experiments were halted immediately and retrieved for microstructural analysis, while for others, deformation was continued until steady-state sliding was achieved.

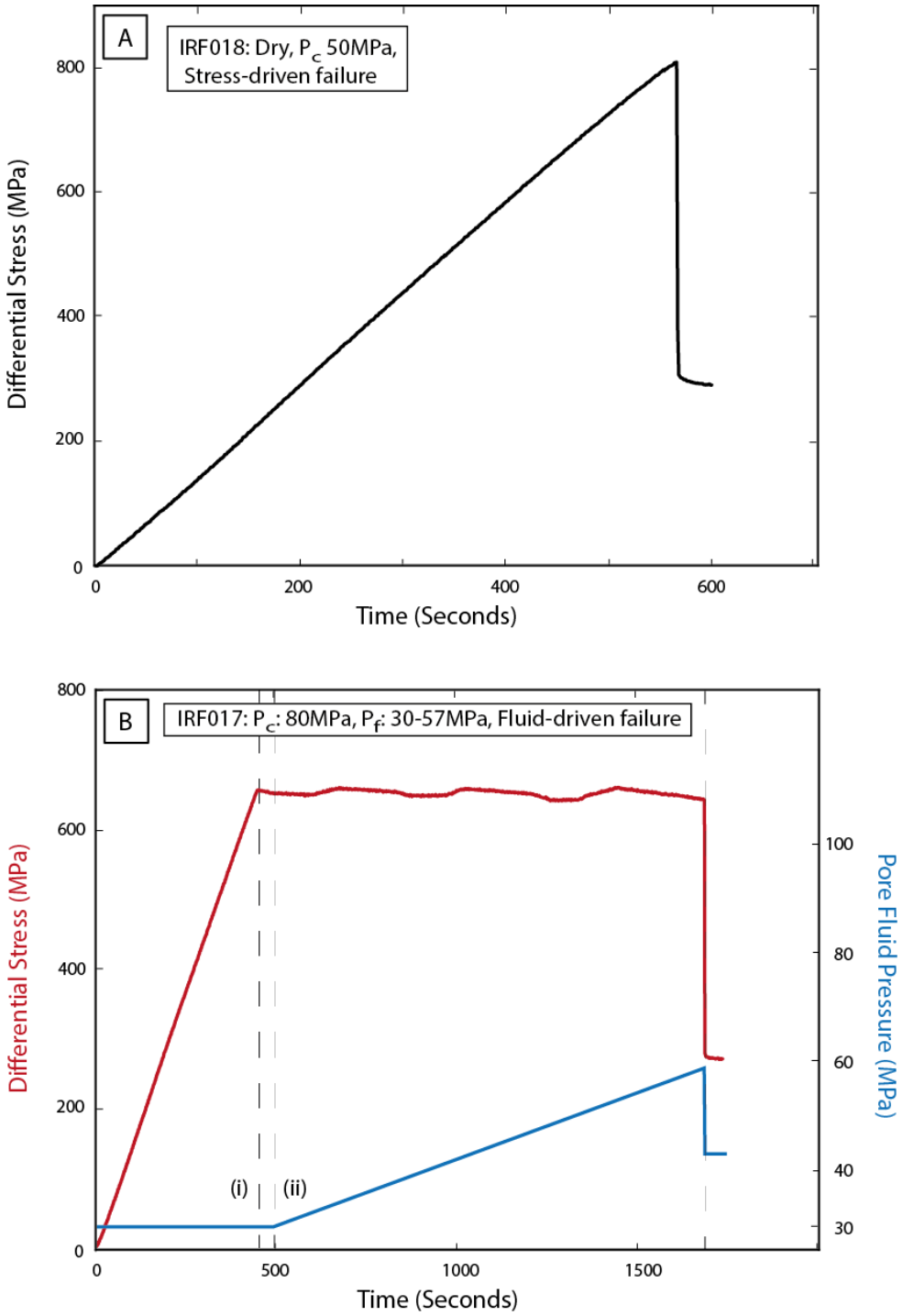

Figure 3: Representative loading curves for intact rock failure experiments.
(A) Illustrates the temporal evolution of differential stress during the stress-driven failure of an intact rock sample. The large, almost instantaneous stress drop represents the onset of strain localisation and macroscopic failure of the specimen. (B) Shows differential stress and pore fluid pressure as a function of time for fluid-driven failure of intact rock. The differential stress is initially increased to approximately 80% of the yield value of the Fontainebleau sandstone and held approximately constant while the pore fluid pressure is increased until macroscopic shear failure of the sample occurs.

Where failure was induced through an increase in pore fluid pressure, samples were loaded to a differential stress of approximately 80% of the failure strength of the Fontainebleau sandstone and held constant while the pore fluid pressure was gradually increased. A comparison of the resulting loading curves with those of samples deformed by stress-driven failure, reveals a very similar mechanical behaviour. The resulting macroscopic failure coincides with significant co-seismic stress drop (between 54-60% of peak differential stress) and rapid displacement along the newly-formed fault (Fig. 3B). A sudden drop in pore fluid pressure at the time of rupture indicates that failure is associated with co-seismic dilatancy within the sample.

3.1.2 Stress-driven fault reactivation and failure

Twenty-nine bare interface fault experiments were undertaken in nominally dry conditions (Appendix 4) with existing fault angles ranging from θ_r = 25°-70°. The experiments were conducted at two confining pressures, P_c = 50MPa / 100MPa, thus allowing the effect of varying confining pressure on the behaviour and microstructural development of the fault zone to be explored. The experimental data displays good reproducibility and the faults show largely comparable mechanical behaviour between the two confining pressures (for comparison loading curves see Appendix 5). As the existing fault orientation increases from θ_r = 25° to θ_r = 55°, mechanical behaviour is characterised by increasing fault strength at the yield point. Following yield, the fault experiences slip hardening (Fig. 4A), and the rate of slip hardening also positively correlates with the increasing angle of misorientation.

As the slip distance increases, the sliding behaviour transitions into a stick-slip regime, where fault behaviour alternates between elastic loading and rapid sliding accompanied by co-seismic stress relief. The load that the fault supports before initiating rapid slip also rises with the increasing θ_r, resulting in an increase in stored elastic strain within the apparatus and the development of large stress drops and slip displacements during stick-slip events.

Samples where θ_r = 60° show little evidence of slip on the pre-existing fault prior to the onset of stick-slip behaviour. These samples do not display an apparent yield point, although there is a slight inflexion on the stress-strain curve prior to the first slip event, possibly indicating the onset of microfracturing, minor frictional slip or pore collapse. After the occurrence of the first major stick-slip event on θ_r = 55°-60° faults, the

samples experience nearly pure elastic re-loading until a second stress peak, which is followed by the macroscopic shear failure of a new, approximately optimally-oriented fault. During the second loading period, some samples, especially those where $\theta_r = 60^o$, show a distinct yield point and roll-over of the loading curing, immediately prior to the onset of failure of the new fault. Experiments MIS017 & MIS018 (with $\theta_r = 60^o$) were undertaken to observe the microstructural development of the new favourably oriented fault. MIS017 was halted immediately after the first slip event and MIS018 was stopped just after the second yield point, prior to the onset of the failure of the new fault.

The mechanical behaviour of samples MIS028 and MIS029, in which $\theta_r = 65^o$ and 70^o respectively, are characterised by loading curves very similar to that observed during intact rock failure, with elastic loading followed by the macroscopic failure along a new fault. A rapid stress drop and axial shortening of between 600-800µm accompany failure. However, in contrast to the loading curve of the intact rock failure experiments, these samples have a markedly better defined yield point which occurs approximately 10 seconds prior to rupture and possibly indicating the onset of fracture development. The retrieved samples show that where a new fault has formed and $\theta_r, \leq 60^o$, the new fault has a 'strike' similar to that of the existing fault, but dips at a more favourable angle relative to the sample shortening direction. In the samples where $\theta_r \geq 65^o$, the fault trace of the new fracture is not consistent with the location and orientation of the pre-ground surface, supporting the idea of complete frictional-lock up of the original fault.

Two stress-driven slip experiments were undertaken on the Fontainebleau sandstone at controlled pore fluid pressures (see Appendix 5 for loading curves). These experiments involved activating slip on the pre-existing fault by increasing differential stress at a nominally constant axial shortening rate, while maintaining a constant pore fluid pressure. The first experiment (MIS022) was undertaken at an effective confining pressure of 50MPa (P_c = 80MPa, P_f = 30MPa) on a sample with a fault oriented at θ_r = 60°. The results show behaviour very similar to that of the nominally dry experiment undertaken at equivalent conditions (MIS012). A second experiment (MIS023) was undertaken where θ_r = 55°, and at an effective confining pressure of 25MPa (P_c = 80MPa, P_f = 55MPa). During this experiment, the wet stress-driven reactivation experiment resulted in a much lower yield strength (211MPa as opposed to 391MPa), consistent with the effective confining pressure being approximately half that

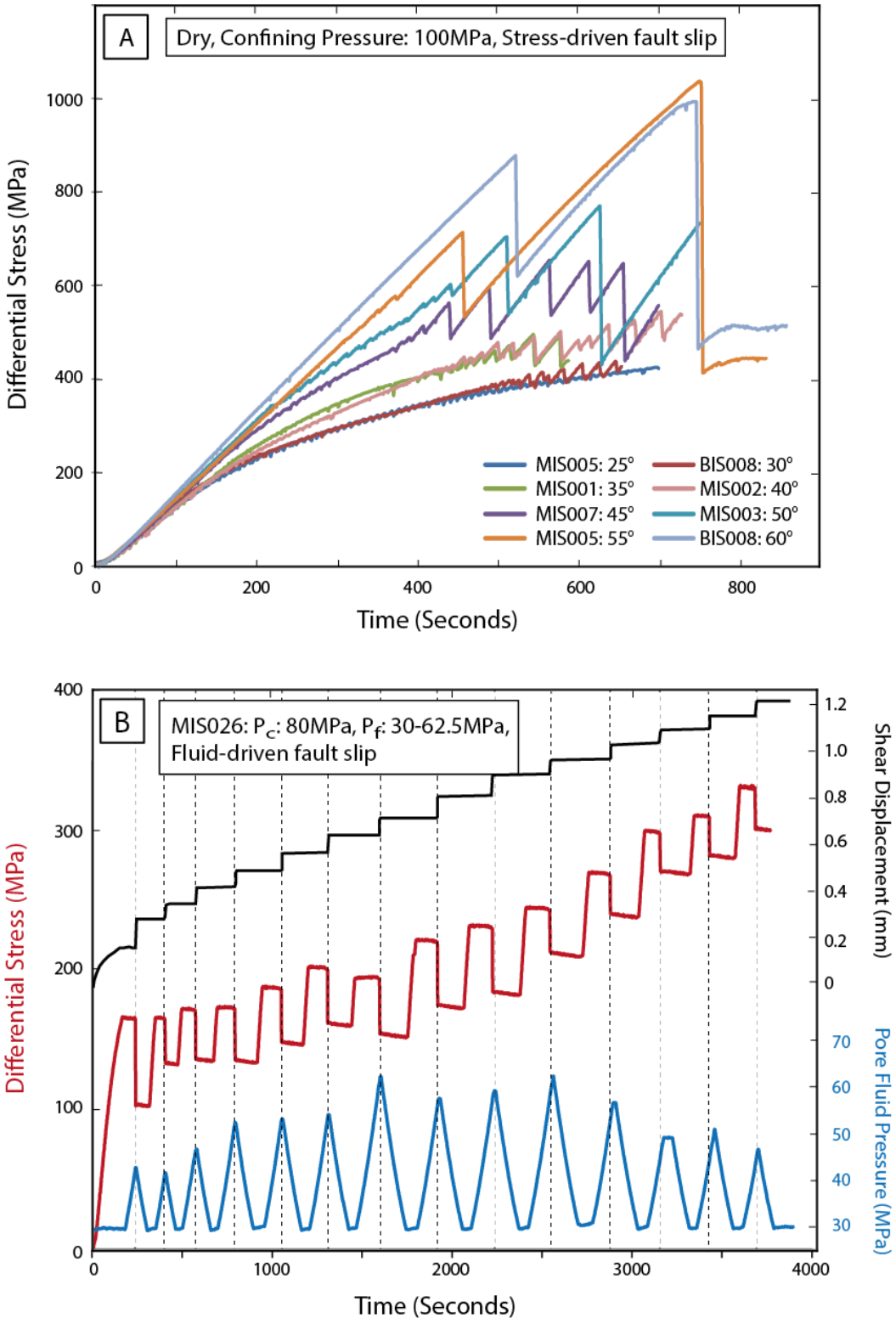

Figure 4: Representative loading curves for the misoriented fault experiments.
(A) Composite plot of the loading curves for a suite of misoriented fault experiments undertaken at 100MPa confining pressure. The different experiments show the effect of changing the angle of the fault relative to the maximum shortening direction from 25º to 60º. (B) Shows the temporal evolution of differential stress, pore fluid pressure and fault displacement for a fluid-driven fault reactivation experiment. Each stress drop represents an incremental slip event on the θ_r=50º fault. Note how small the stress drops and displacements are in comparison with the stress-driven failures on a similarly oriented fault, reflecting the lower σ_n.

of the dry experiment. The behaviour of the fault after the yield point in both experiments is characterised by slip hardening followed by the ultimate failure along a new optimally-oriented fault.

3.1.3 Fluid-driven fault reactivation and failure

The fluid-driven reactivation of unfavourably-oriented faults was investigated during a number of experiments in which θ_r = 40°, 50°, 55º and 60°. As for the procedure used during the fluid-driven failure of intact rock, the sample was loaded to approximately 80% of its dry yield strength under comparable effective confining pressures, then load was held constant while the pore fluid pressure was gradually increased until slip occurred (Path B, Fig. 2D). Following slip, the pore fluid pressure was reduced to the starting levels of 30MPa (Fig. 4B).

Results show that fluid-driven reactivation could be induced on all of the unfavourably-oriented faults. However, for samples where θ_r = 60°, the first slip occurred on the existing unfavourably oriented fault, but during the second loading, shear failure occurred along a new, favourably-oriented fault resulting in a more significant coseismic stress drop and audible click. For samples in which θ_r = 40º - 55º, the fluid-driven fault reactivations resulted in relatively small displacements (maximum slip distance of ~60μm for θ_r = 40º and ~120μm for θ_r = 50º) and accompanying stress drop of approximately 30 and 60MPa respectively. The small incremental displacements resulted in up to 28 failures being instigated on the fault to achieve approximately 1.3mm of fault displacement (Fig. 4B). The θ_r =55º fault experienced a number of small displacement (~35-100μm) initial slip events that were accompanied by stress drops in the order of 20-40MPa. After approximately 325μm of episodic fault slip, larger slip events developed (110-270μm) that were associated with increasing co-seismic stress drops (up to 157MPa). During the final slip event, a new more favourably oriented fault developed and accompanied by an audible click. The timing relationships suggested here are supported by fault offsets and overprinting microstructures described in Section 3.3.3.

Following the first slip event in samples oriented at a high angle to the shortening direction (θ_r > 55º), continued axial loading and the pore fluid pressure cycling

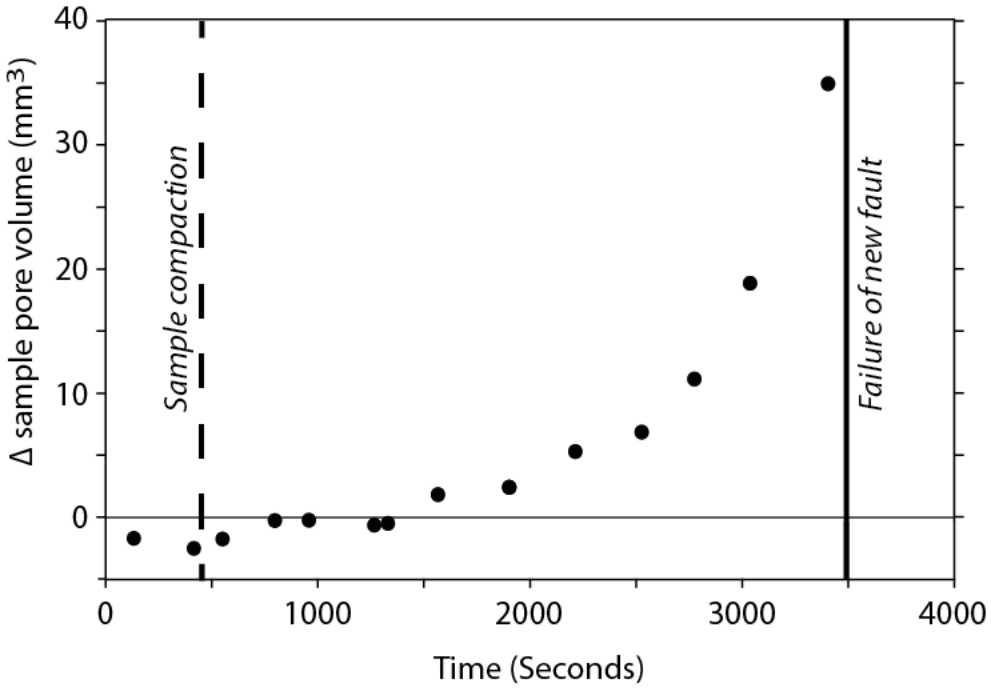

Figure 5: Change in pore volume as a function of time.
Data points represent the volumetric change in the pore volume of the sample relative an initial baseline. During experiment MIS041 (θ_r >55º), the pore fluid pressure is increased, slip activated and then the pore fluid pressure is returned to the baseline of 30MPa. The pore volume initially decreases slightly, possibly representing crack closure, before increasing gradually. After approximately 2000 seconds, the pore volume is observed to increase exponentially prior to the failure of the new more favourably oriented fault.

associated with fluid-driven fault reactivation is accompanied by progressively increasing sample dilatancy (Fig. 5). Dilatancy is accompanied by a relaxation of the axial load and is thought to correlate with an increase in fracturing and strain accommodation within the sample. Where a new, favourably oriented failure occurs (θ_r >55º), a co-seismic fluid pressure drop is observed upon the failure of the new fault. While similar behaviour is observed during the fluid-driven failure of intact rock, the size of the fluid pressure drop is approximately an order of magnitude less than is observed during the intact rock failure experiments. This is consistent with the possibility that much of the sample fracturing occurs prior to macroscopic failure of the new optimally oriented fault on samples containing a pre-existing fault, as opposed to approximately co-seismically during intact rock failure.

3.2 2D Microstructural analysis using BSE-SEM imaging

Two-dimensional microstructural analysis was undertaken on polished blocks of the experimental samples using high contrast BSE-SEM imaging. In the following section the observed microstructures are described for each experiment type (intact rock failure

or fault reactivation) and failure method (stress- or fluid-driven). Within each section, microstructural observations are made starting at the larger scale with description of fault geometry and the microstructural features of the damage zone. This is followed by a description of the microstructures and morphology of the fault core, including areas of slip localization and, where present, the formation of frictional melt.

3.2.1 Intact rock failure

Fault geometry and the damage zone

The microstructure of the fault zone produced during the failure of the intact rock samples is characterised by widespread damage, both within the fault core and adjacent wall rock, culminating in the formation of a slightly undulatory cataclastic slip zone (Figs. 6 & 7). Not all failures produced a single fault core; some samples develop multiple slip surfaces and conjugate faults, possibly reflecting the bulk experimental stress state in which $\sigma_2 = \sigma_3$. Even where single fault zones have developed, there is evidence of growth, interaction and coalescence of multiple, closely spaced slip surfaces, with isolated lenses of damaged wall-rock between the fault surfaces. However, there are few observable differences between the microstructures formed during the fluid- and stress-driven failure modes in the intact rock samples. Accordingly, the general microstructures are discussed collectively in this section.

The fault damage zones show the development of subsidiary fault strands (Figs. 6A & B, see red arrows, Fig. 7B) and the formation of intra- and inter-granular fractures, with many of the latter oriented sub-parallel to the maximum principal stress. The undulating nature of the main slip zone appears to influence the formation of the damage zone by the formation of compressive and dilatant regions along the fault plane during continued slip (Fig. 6B and see white arrow, Fig. 7A for an example of a dilatant bend). Many secondary fault strands are observed to be in various stages of development, nucleating in response to the increase in stress concentrations associated with the compressive zones on the main fault structure (Figs. 6A & B, see red arrows Fig. 7B). The progressive accommodation of strain along the developing fault strand involved the formation of sub-parallel arrays of intergranular dilatant cracks that form at a high angle to the developing slip surface. These fractures have a similar geometry

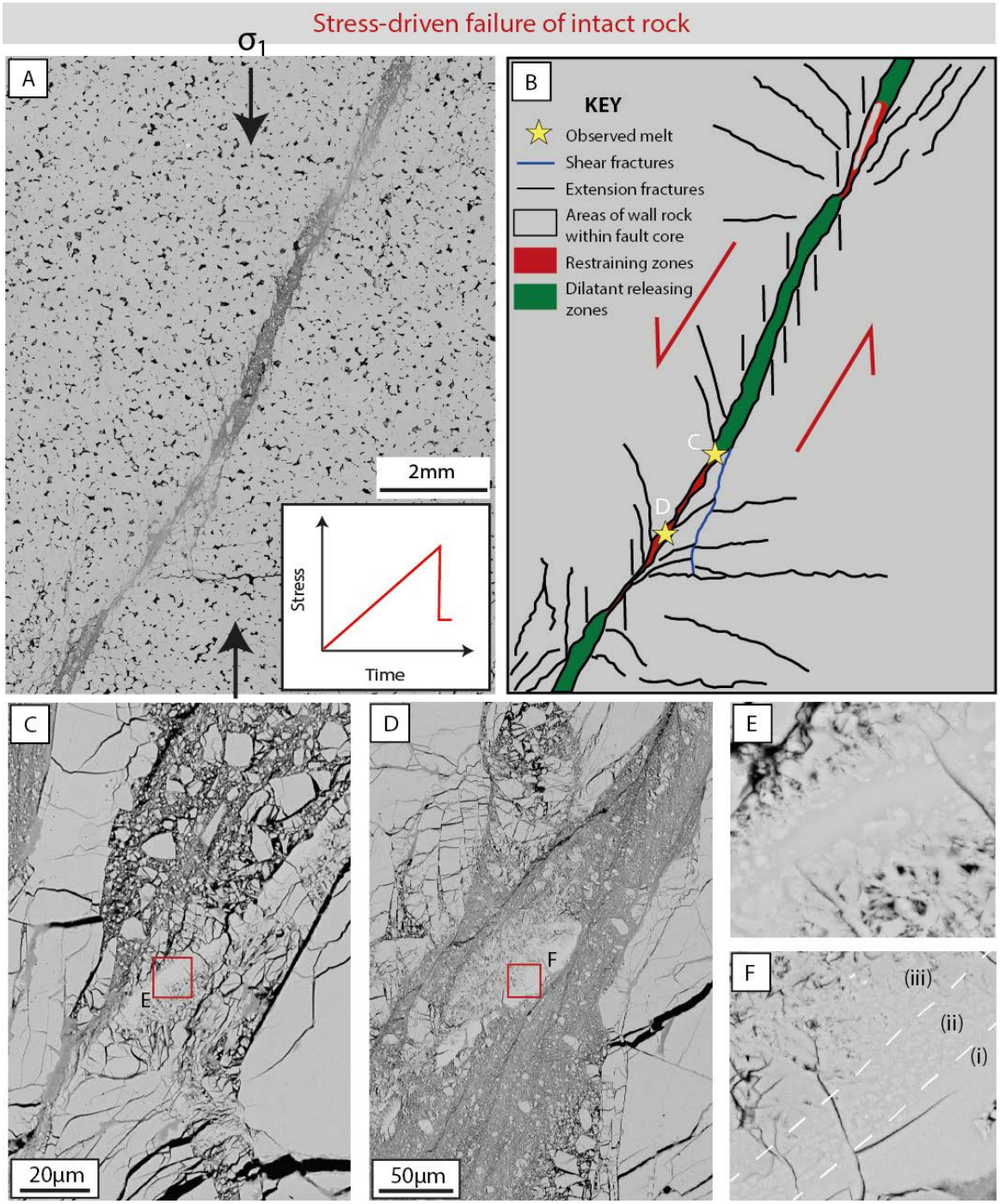

Figure 6: Microstructures produced during stress-driven failure of intact rock.
(A) Overview of the sample following deformation. The axial loading direction is indicated by the black arrows and the small inset shows a schematic loading curve for the experiment. A 200-300µm wide failure zone is evident and an interpretative diagram is provided in (B). It can be seen that the slightly undulatory nature of the failure zone leads to the formation of releasing and constraining zones during the subsequent slip. Secondary fault traces are developed around some of the compressive zones. Melt is also observed to form within the restraining zones at locations C and D, indicated by the yellow stars. (C)-(D) Images showing the morphology of the melt produced within the fault core as indicated in (B). (E) Higher magnification image of the inset shown in C, depicting melt forming vein-like structure. Towards the centre of the melt the even texture suggests a low porosity melt with few relict clasts. However, towards the edges of the melt zone there is a transition to an essentially melt indurated gouge. (F) High magnification image of inset shown in (D). The melt in this image can be divided into three zones (i) shows a clast-free melt, (ii) has rounded clasts within a melt matrix and (iii) shows melt indurated gouge textures, similar to those in (E).

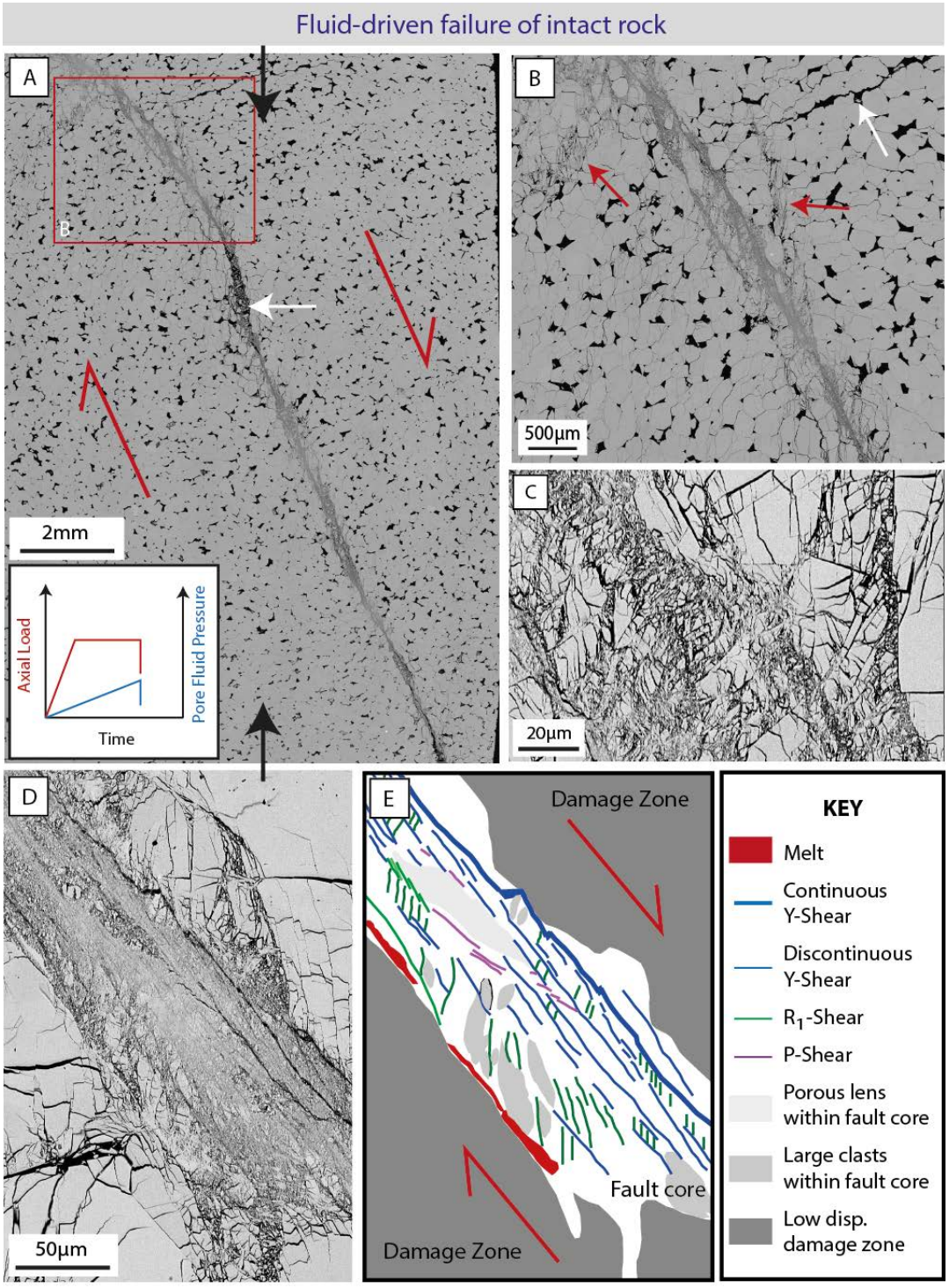

Figure 7: Microstructures produced during fluid-driven failure of intact rock.
(A) Overview of IRF015 following shear failure. The black arrows indicate orientation of sample axial compression. A schematic illustration of the temporal evolution of axial load and pore fluid pressure is provided in the inset. Note the formation of a dilatant zone or jog (indicated by the white arrow) formed by the separation of an uneven fault surface. (B) Detail of part of the fault zone (location indicated on A). Fault zone appears to be formed by the linkage of a number of fault segments resulting in the development of isolated lenses of wall rock within the fault core. Note also the development of secondary fault traces indicated by the red arrows. The white arrow points to a dilatant facture with the similar geometry to a wing fracture at a fault tip. (C) Intensely fractured/pulverised rock that shows only minimal shear displacement. (D-E) Image and interpretative drawing of a region of the fault core. Note the abundance of very fine-grained (submicron) gouge material within the core and the formation of numerous Riedel shears.

to wing cracks and could have formed as a result of the development of localised tensile stresses resulting from successive and heterogeneous slip episodes along the newly forming slip zone.

The geometry and microstructures of the fault core

The inner fault core is approximately 200-300μm wide and is characterized by cataclastic deformation microstructures resulting in extensively fractured grains and the formation of fault gouge. This highly angular and often poorly sorted gouge is comprised of particles ranging in size from submicron material to residual fractured grains up to approximately 100μm in diameter. A fining of gouge material is often observed towards the principal slip zones. In many places the fault core shows evidence of slip localisation with the development of slip zones obliquely oriented to the fault boundary. These shear bands are referred to as Riedel shears [*Logan et al.*, 1992; *Passchier and Trouw*, 2005] and form a hierarchy of overprinting shears with increasing slip localisation within the fault core. Early shears, often the R_1 shears that form at a low angle to the fault zone boundary, are overprinted by boundary-parallel Y shears, which are interpreted to be slip surface where the majority of slip occurred. Zones of less damaged material are also present, commonly forming lenticular to irregular domains within the fault core. Sigmoidal lenses of poorly compacted gouge are also present and include larger clasts and are more porous than the surrounding fault core (Fig. 7D-E). The lenticular shaped clasts are often oriented parallel to the R_1 shears, whereas the sigmoidal lenses provide a shear sense indicator analogous to S-C fabric within ductile shear zones. Slip is often localised around these lenses forming shear bands such as P-shears.

A notable feature within the core of faults formed by fluid-driven failure is the abundance of sub-micron gouge. Regions of fine-grained gouge are not always accompanied by evidence of slip localisation through the formation of Riedel shears or significant grainsize variation / fining across the fault core. In places the fine-grained gouge has been injected into fractures on either side of the fault core.

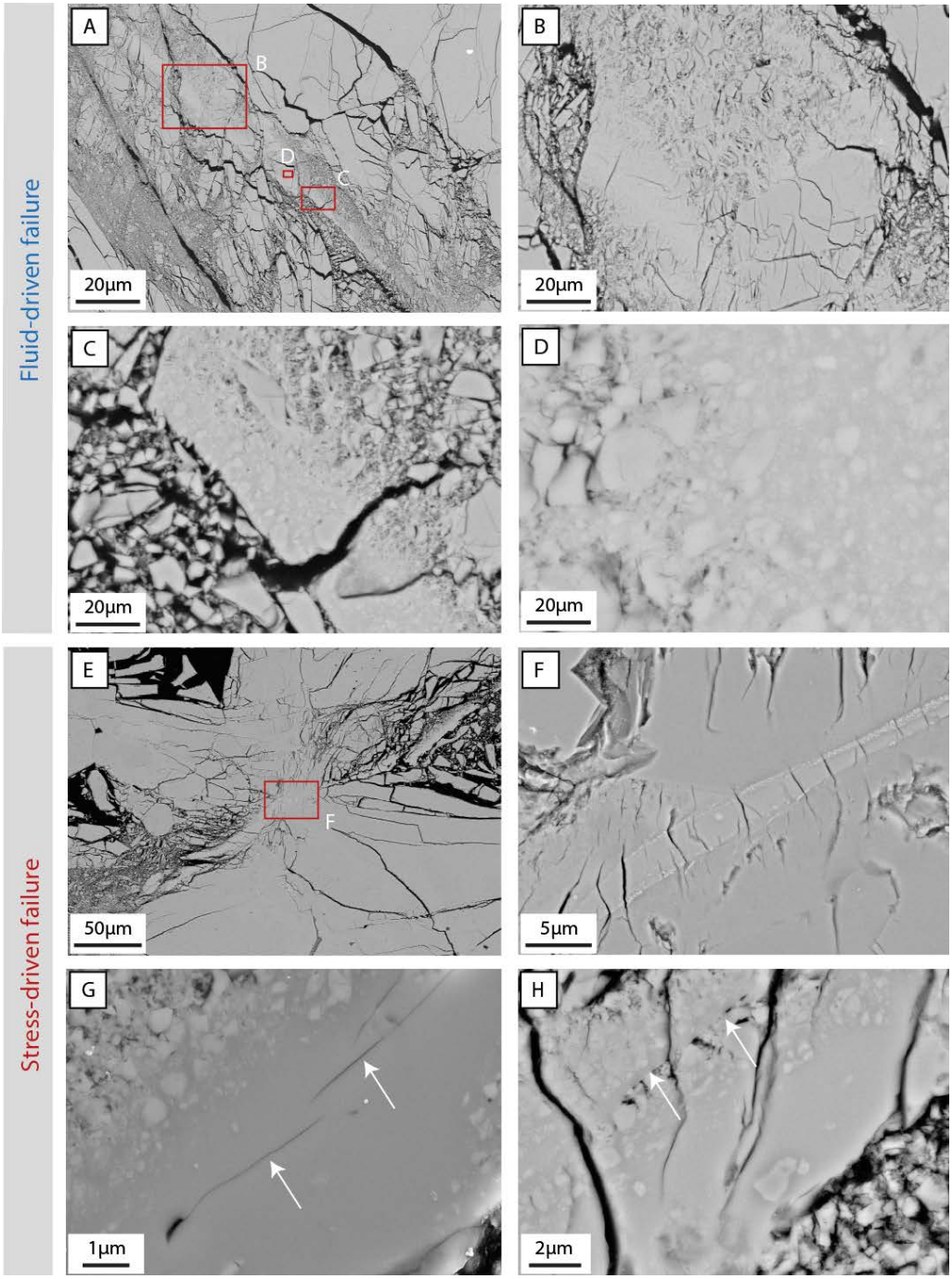

Figure 8: Comparison of melt microstructures produced during fluid- and stress-driven failure of intact rock.
(A-D) IRF016 fluid-driven failure of intact rock sample. (A) Area of significant volume of melt within a sample generated by fluid-driven failure. (B) The light fractured regions in the lower centre of the image represent clast free melt, while the porous material in the upper centre of the image illustrates the texture of melt indurated gouge. (C) Clast laden melt layer showing a planar edge on one side and grading into melt-indurated gouge on the other. (D) High magnification image showing rounded clasts within a melt matrix. (E)-(H) IRF018 nominally dry stress-driven failure of intact rock. (E) Highly stressed contact between two asperities on a fault surface formed during stress-driven failure. Hertzian fractures can be seen radiating from the impinging contact and a layer of melt has formed at the interface. (F) Higher magnification image of the melt layer formed at the contact between asperities shown in (E). Note the formation of 'ladder' cracks in melt layer that are possibly associated with anisotropy in the compressibility of the adjacent quartz. (G) Arrows highlight fractures formed in the core of the melt layer, parallel to the sliding surface. (H) Banding within the melt supports the possibility of multiple episodes of melt formation during the single slip event. Arrows point to a possible second melt generation surface.

Development of frictional melt

Frictional melt forms within the fault core of both stress- and fluid-driven failures in intact rock (Fig. 8). While the melt has rapidly quenched to form a silica glass, in this chapter the term 'melt' is used to describe any quenched melt textures or material that has been frictionally heated and melted. This is done to highlight the processes involved in its formation.

Frictional melt is most commonly located within the compressive regions of the fault core where slip on an undulating fault plane can lead to significant stress concentration (i.e. restraining bends). Recognition of quenched melt requires high-resolution BSE imaging and the combined use of slow scan and line integration noise reduction techniques to resolve the melt textures. However, the glass is most easily identified when clasts are suspended within the solid melt-matrix. At low magnifications quenched melt is recognised by the formation of elongate zones of bright material within the fault core, typically having either a very linear edge, parallel to the fault zone boundary, or smeared within a gouge layer adjacent to an asperity contact. The core of the melted zones has a lower porosity than the surrounding fault gouge and consequently at low magnification appears brighter in BSE-SEM imaging than the epoxy impregnated gouge. At higher magnifications, the glass is recognised in both SE- and BSE-SEM imaging by having slightly lower electron intensity than the surrounding quartz. In the case of SE imaging, this is interpreted to be the result of the glass forming a topographic low within the sample due to preferential removal of the slightly softer glass during polishing. The slightly lower intensity of quenched melt during BSE imaging possibly arises from either a lower orientation contrast from a non-uniform reflection of low-loss BSEs in the non-crystalline structure, or a reduced Z contrast (representing mean atomic number) due to the lower density of the glass compared with its crystalline equivalent. The observation that the amorphous material has lower intensity during BSE imaging is consistent with observations of glass filled veins and amorphous deformation lamellae formed during meteoritic impacts [*Bruijn*, 2014]. Many of the features observed in BSE-SEM imaging are identical to microstructures observed on the high temperature fault interfaces (see Chapter 2); these include the presence of fractures forming parallel to the fault surface in the centre of a welded vein (see arrows Fig. 8G), the formation of elongate vesicles and even the formation of rare, ribbon-like filaments of glass.

From observations of the slip zone produced by intact rock failure experiments, two styles of melt zones are recognised in cross section: the first is characterised by a sharp planar boundary on one side, that grades progressively into a melt-indurated gouge (Figs. 8A-D). These zones typically are associated with extensive pulverisation of adjacent crystalline material forming platy, shard-like textures (e.g. Fig. 8B). The second melt morphology is characterised by the formation of a short melt 'vein' between two impinging asperities (Figs. 8E-G). The radiating Hertzian-style fractures at these sites are interpreted to be the indicative of high stress concentrations (Fig. 8E). The volume of melt produced during slip varies greatly between the intact rock failure experiments. The dense clast-free melt zone is generally between 1-2μm wide and up to approximately 200μm in length while in contrast, the indurated gouge may extend over a similar length (100-200μm) but affects a much wider zone (up to 60μm). Although both stress- and fluid-driven failure results in the formation of frictional melt, areas of melt produced during fluid-driven failure have a higher clast density than similar areas produced during stress-driven failure, possibly indicating a lower melt temperature. However, melt is not abundant within the samples forming 2-3 localised areas of melt within any given sample. Consequently any conclusions drawn from the observations must be tempered by the potential bias associated with limited examples.

Planar textural banding is present within the melt layer of some samples. The banding is characterised by alternating layers of clast-free melt, clast-rich layers within a melt matrix and porous bands (Fig. 8H). These structures are interpreted to represent areas where multiple episodes of melt generation have occurred during a single slip event, corresponding with a single co-seismic stress drop. The ability to follow the clast-free bands within the melt layer until they terminate within a discrete slip localisation zone in the adjacent gouge supports the hypothesis that these textures formed as a result of multiple melt-generation events within a single episode of rapid slip, rather than as flow banding within the melt layer.

Melt formed adjacent to the fault core boundary in Figures 7E-F appears to have been generated early in the slip event with the late stage Y-type or boundary shears forming on the opposite side of the fault zone. This suggests that melt generation was short-lived and once heat production stopped, the strengthening of quenching melt resulted in the transfer slip to elsewhere in the fault core where subsequent shear bands have formed. However, in other examples (Fig. 8A) the lack of significant deformation and cataclasis

of the melt layer when compared with the surrounding fault core indicates possible melting late in the slip event through slip localisation within a well-developed gouge layer.

3.2.2 Slip on existing fault surfaces

3.2.2.1 Dry stress-driven fault reactivation and failure

Fault geometry and evolution of the damage zone of existing faults

With an increasing reactivation angle and continued displacement beyond yield and initial slip, there are significant variations in the microstructural development of reactivated faults. Faults oriented at between 25-30° to the cylinder axis are characterised by the limited development of a fault damage zone, with the majority of damage occurring immediately adjacent to the slip surface and within the fault core. However, even at largely favourable reactivation orientations (θ_r = 25-35°), the generation of damage is observed to positively correlate with increasing slip distance and confining pressure. Mature, large displacement faults show evidence of well-developed Riedel shears and sigmoidal-shaped lenses of fine-grained gouge occurring within a 100-200μm wide fault core. This is accompanied by an increasingly developed low displacement damage zone in the ~200μm on either side of the fault core.

With an increasing reactivation angle, the extent of slip-related damage is observed to increase both within the fault core and surrounding damage zone. Splay-like fractures develop in the dilatant ends of the faults oriented at θ_r =35-50° (Fig. 9A). With continued deformation, these evolve into a series of more favourably oriented slip surfaces. Fault damage and gouge production reaches a peak on faults with a reactivation angle, θ_r = 45-55° and coincides with a high level of microfracturing immediately adjacent to the slip surfaces with a width typically < 200μm. Much of the damage surrounding the fault zone is preferentially located on the dilatant sides of the fault ends, forming wedge-shaped, asymmetrical damage zones (e.g. Fig. 9A, 10B). The compressive domains near the fault tips remain virtually damage free except for dilatant intergranular horizontal fractures; these nucleate from the sample edge and are thought to form as a result of rotation of the fault tip as the dilatant ends of the fault become increasingly damaged and incohesive with continued slip (Fig. 9A).

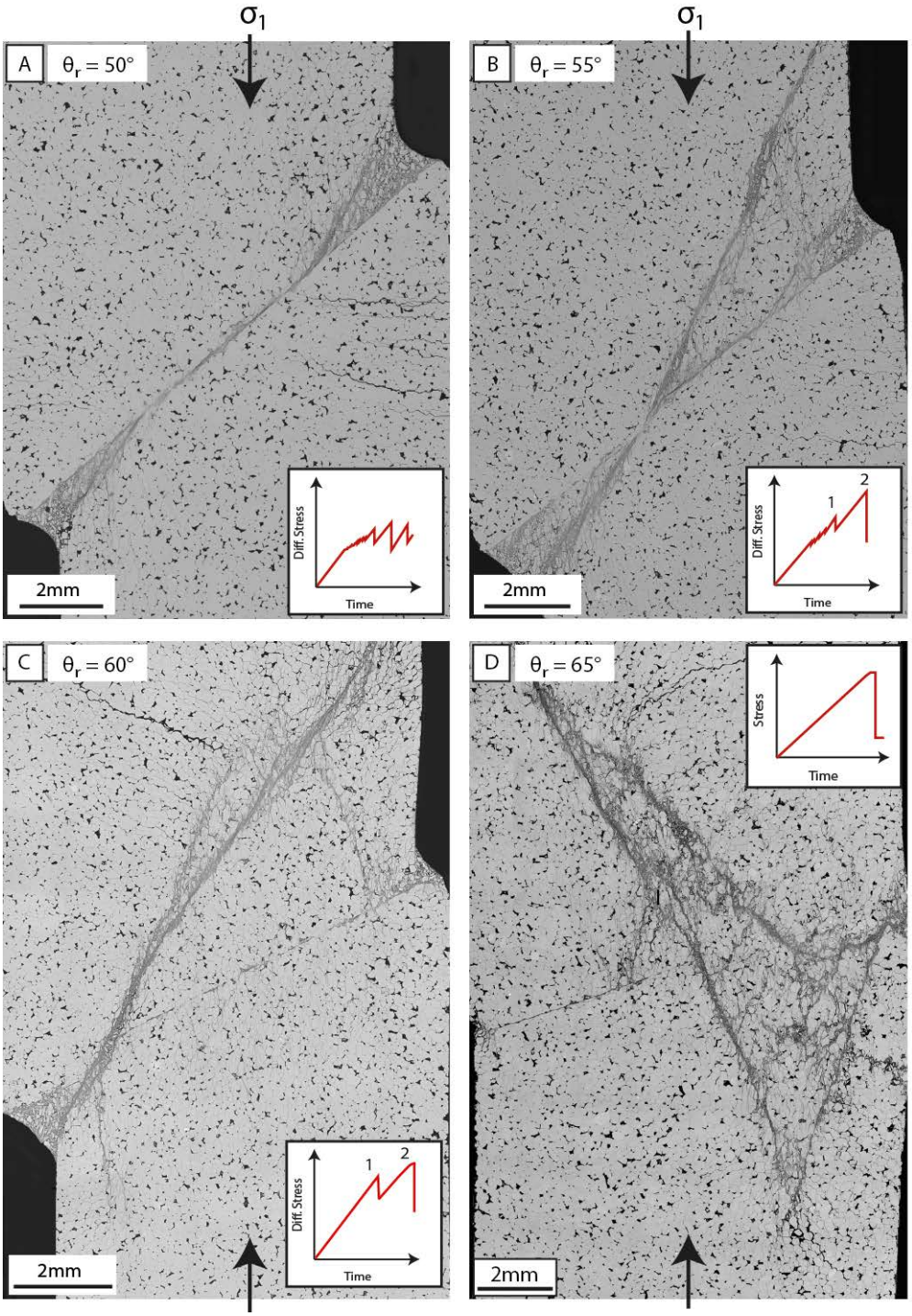

Figure 9: Sample scale microstructures produced during dry stress-driven fault reactivation. BSE-SEM images showing an overview of microstructures formed during fault reactivation and failure over a range of reactivation angles (θ_r). Insets show a schematic loading curve for each experiment. All experiments undertaken at P_c = 50MPa (A) MIS010, θ_r = 50º, fault reactivates initially by slip hardening then transitions into stick-slip behaviour. Fault shows development of splay-like fault traces at the fault ends. (B) MIS011, θ_r = 55º, fault slip hardens then evolves into a stick-slip regime. On the second major slip event (indicated in the inset) the sample fails along a new, more favourably oriented fault. The footwall fracture resembles a splay-like fault, similar to those seen in A, but the hanging wall is bisected by a new fault trace. (C) MIS012, θ_r = 60º, fault elastically loads and slips once on the misoriented fault, before reloading and failing on a new fault. Similar microstructures to (B), but note the formation of a secondary fault trace and accompanying wing cracks in the hanging wall. (D) MIS028, θ_r = 65º, fault is frictionally locked and sample failures through a complicated network of newly formed faults after a period of nearly pure elastic loading.

Experiments where θ_r = 55°-60° show clear evidence of slip having occurred on the existing unfavourably oriented fault, before becoming frictionally locked and subsequent failure occurring on a new favourably oriented fault (Fig. 9B-C). The generation of the new, optimally-oriented slip zone is associated with the second slip event in the loading curve (see insets Fig. 9B-C). Initiation of slip on this zone typically is associated with a larger stress drop than the prior slip event on the misoriented fault surface. At the specimen scale, the offset of the copper jacket indicates fault movement on both the existing and newly formed faults. Similarly, the microstructures of the fault core of the unfavourably oriented fault reveal damage indicating slip. The geometry of the new fault is very much controlled by the position of the existing fault, forming in the same orientation but more steeply inclined than the misoriented fault. In the samples deformed at confining pressures, $P_c \leq$ 50MPa, the new fault mainly transects the hanging wall of the existing fault but with increasing confining pressure the newly formed fault becomes increasingly symmetrical within the sample, cutting both the hanging and footwall of the unfavourably oriented fault.

In experiments where the existing fault is oriented with $\theta_r > 65º$, this surface remains frictionally locked, with no mechanical evidence of slip. Rather the sample has failed by formation of a complex network of more favourably-oriented faults (Fig. 9D). The formation of multiple faults, including well-developed conjugates, in orientations different to that of the pre-ground misoriented fault suggests that the geometry of the newly ruptured fault is less influenced by stress changes arising from movement on the existing fault.

The evolution and structure of new favorably oriented faults

The appearance and morphology of faults formed during the rupture of new optimally oriented faults is similar to that observed during intact rock failure experiments (Section 3.2.1), although the fault is less steeply inclined relative to the direction of shortening. The new fault is undulatory in places, formed by the linkage of en echelon fault segments (Fig. 10), and the development of secondary fault traces (Figs. 9C). The development of wing-crack type fractures at the tip of some of the secondary fault traces demonstrates heterogeneous accommodation of strain within the sample (Fig. 9C). A number of the samples that have failed along a new favourably oriented fault also have formed conjugate fault traces, with many of these fractures forming between the newly

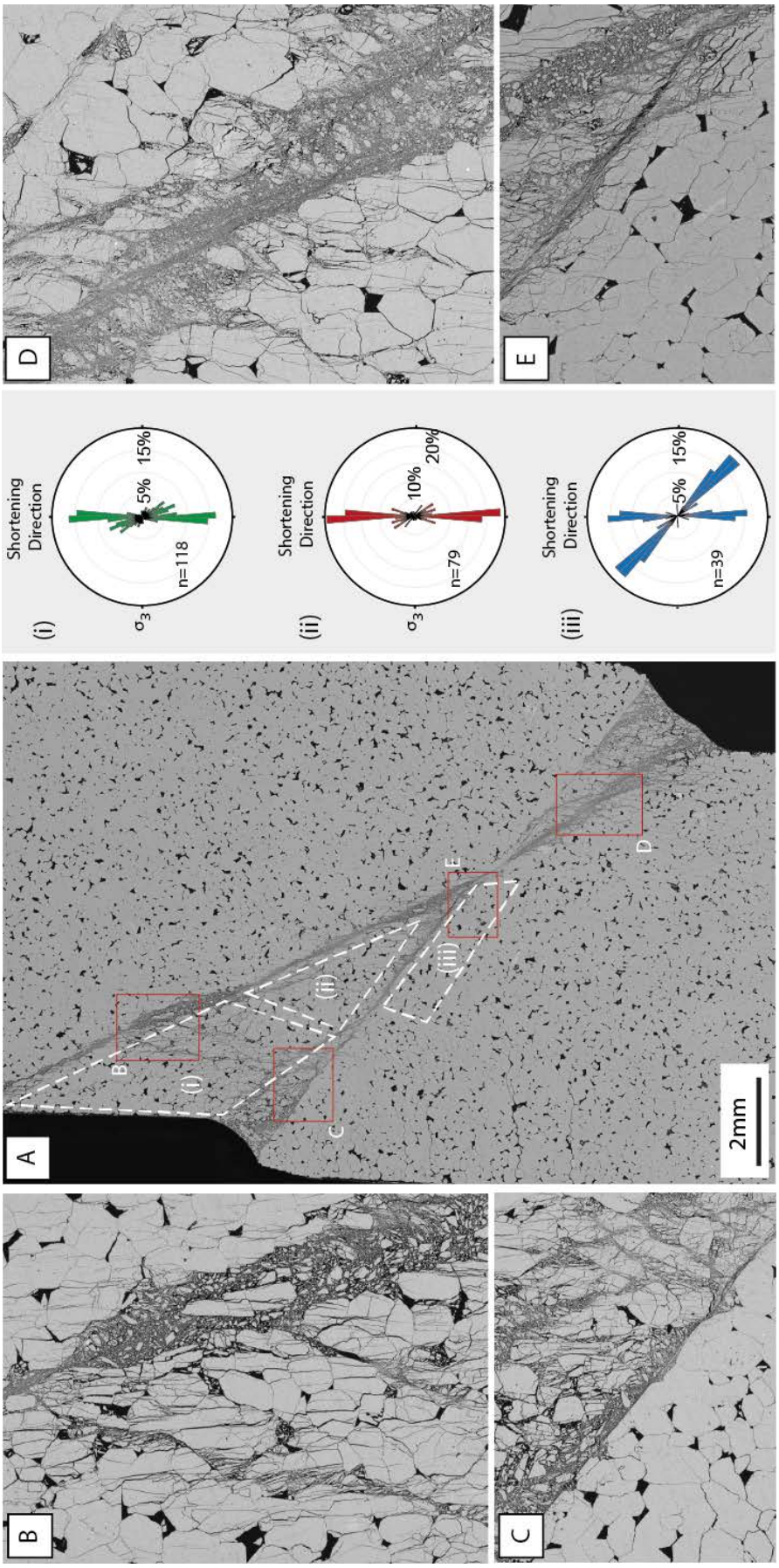

Figure 10: Damage zone microstructures formed during stress-driven reactivation of a θ_r=55° fault.
Sample MIS011. (A) Overview of the deformed sample showing the damage zone formed during reactivation of the misoriented fault and subsequent failure of a new more optimally oriented fault. Variations in orientation of microfractures found in the areas indicated by the white dashed areas labelled (i)-(iii) are shown on the adjacent rose diagrams. The rose diagrams are plotted with a 5°-sector width and show the fracture orientation relative to the bulk shortening direction. (B) Shows the development of linkage or conjugate fractures between the new main shear fracture and the existing misoriented fault. (C) Asymmetry in the development of fault damage on the existing fault. (D) In places the new fault appears to have formed by the linkage of a series of en echelon fractures. (E) Example of fracture rotation in the footwall of the unfavourably oriented fault. Dominant orientation of fractures in the footwall is approximately parallel to the pre-ground fault surface (also see rose diagram (iii)).

formed fault and the original ground slip surface. Little offset is observed on the conjugate structures. However, the truncation and separation of the conjugate faults by the main rupture surface suggests the contemporaneous formation of these faults.

The process of development of the new optimally oriented faults was explored over a series of experiments that were halted and retrieved at different stages within the rupture sequence. MIS017 was halted immediately after the first slip event on the misoriented fault (Fig. 11A-C) and MIS018 was halted at the second peak in stress, just prior to the rapid slip event that would have resulted in the macroscopic failure along the new fault. (Fig. 11D-F) At the sample scale, the first experiment (MIS017) is characterised by the formation of very little damage with microfracturing and associated damage being limited to approximately a single grain width (250μm) on either side of the slip surface (Fig. 11C). A small amount of damage is evident at the fault tips forming a wedge shaped damage zone at the fault ends (Fig. 11B).

Reloading of the sample following slip on the existing fault is associated with a significant increase in fracture density and an overall increase in width of the damage zone. However, the distribution of microfractures is not pervasive throughout the sample, but rather, occurs extensively around the original fault surface and in a zone of inferred high stress that approximately coincides with the area where the new fault forms, leaving large areas of the sample essentially damage free. The formation of extension fractures appears to be a precursor to the development of the new fault with the fractures linking and coalescing to form the new fault zone (Fig. 11F). Significant strain is accommodated without stress drop by the new fault prior to its full formation and macroscopic failure. The original $\theta_r = 60°$ fault is offset by approximately 200μm at the point where the new optimally-oriented fault intersects the original unfavourably oriented fault (Fig. 11E). The heterogeneous accommodation of strain within the sample is observed to form dilatant grain-boundary fractures oblique to maximum principal stress at the newly-forming fault tip (see dashed lines, Fig. 11F), and is thought to largely result from the imposed constraints of the assembly configuration which prevent slip occurring into the samples' ends. Such movement is thought to place controls on the geometry of the newly forming fault and promote its continued development by altering stress states at the fault tip.

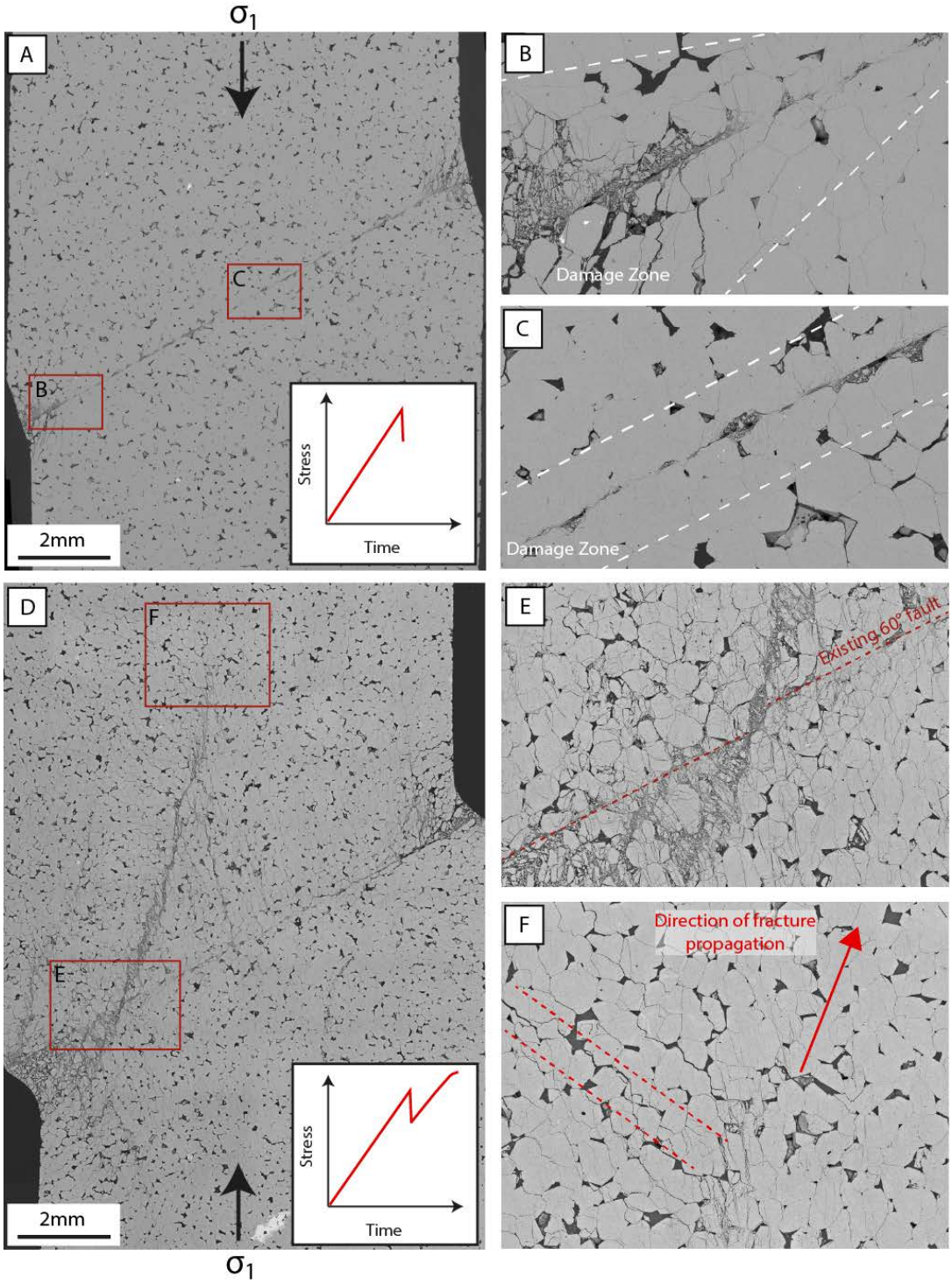

Figure 11: Formation of a new optimally oriented fault following frictional lock-up on a θ_r = 60° fault.

(A-C) Images from experiment MIS017 that was halted immediately following the first slip event (see loading curve in inset). (A) Overview of sample. (B-C) The damage zone is not well developed with the formation of minor intergranular fractures and grain crushing at the fault tips and dominantly intragranular fracturing along the rest of the fault. (D-F) MIS018 – experiment was halted at the onset of macroscopic shear failure along a newly-formed fault. The new fault is in the process of forming and, when compared with MIS017, significant damage is present. Although the fault zone is not fully developed, shear strain has been accommodated along the developing fault through the formation of en echelon fracture arrays at the fault tip – see the offset of the existing fault (E) and the formation of dilatant fractures, parallel to the dashed lines in (F).

If extension fractures are assumed to form approximately perpendicular to the minimum principal stress (σ_3), variations in the orientation of these fractures within the damage zone may provide insights into deviations in local stress orientations from the assumed bulk principal stresses. The fracture orientations of three sub-regions within the damage zone of MIS011 ($\theta_r = 55^o$) (Fig. 10A) are displayed in the rose diagrams (Fig. 10A). The orientation of the microfractures have been measured relative to the sample shortening direction, with a maximum of three cracks being considered for any given grain. The results show that while vertical crack formation is a significant component of the results for all three regions (being approximately parallel with the shortening direction), the area in the footwall immediately adjacent to the pre-ground unfavourably oriented fault, is dominated by fractures which are sub-parallel to the misoriented fault (Figs. 10A, E, (iii)). The region between the two faults has a significant number of fractures aligned with the orientation of the newly-formed, favourably-oriented fault (Figs. 10A(i)-(ii)). Many of the microfractures outside these orientations are interpreted to result from Hertzian or impingement microcracking where the stress orientations are significantly perturbed at the grain scale [e.g., *Gallagher et al.*, 1974]. Many of the intragranular cracks also have associated wing-cracks at the fault tips suggesting a component of shear along many of the microfractures.

Evolution of the fault core in pre-ground fault surfaces

The fault core, or zone of high strain resulting from the localisation of fault slip, forms a microstructurally distinctive layer that ranges in width between <2-300 μm, with fault-core width on the pre-ground faults being strongly related to total displacement (Fig. 12-13). Mature fault cores (those that have experienced multiple rapid slip events, or stable sliding >1mm) are dominated by the formation of wear products such as fractured grains and fault gouge, with evidence of some grainsize sorting, and rudimentary development of slip localisation structures such as Riedel shears. A number of the favourably oriented, high displacement faults that have slipped by macroscopic stable sliding, show evidence of the formation of sigmoidal shaped lenses of fine gouge and multiple generations of Riedel shears, many of which truncate and overprint earlier shears. As the reactivation angle increases the process of gouge formation transitions from high displacement damage, produced by wear and the attrition of asperities, to being largely *in situ* damage, resulting from intense grain crushing and fracturing. Much

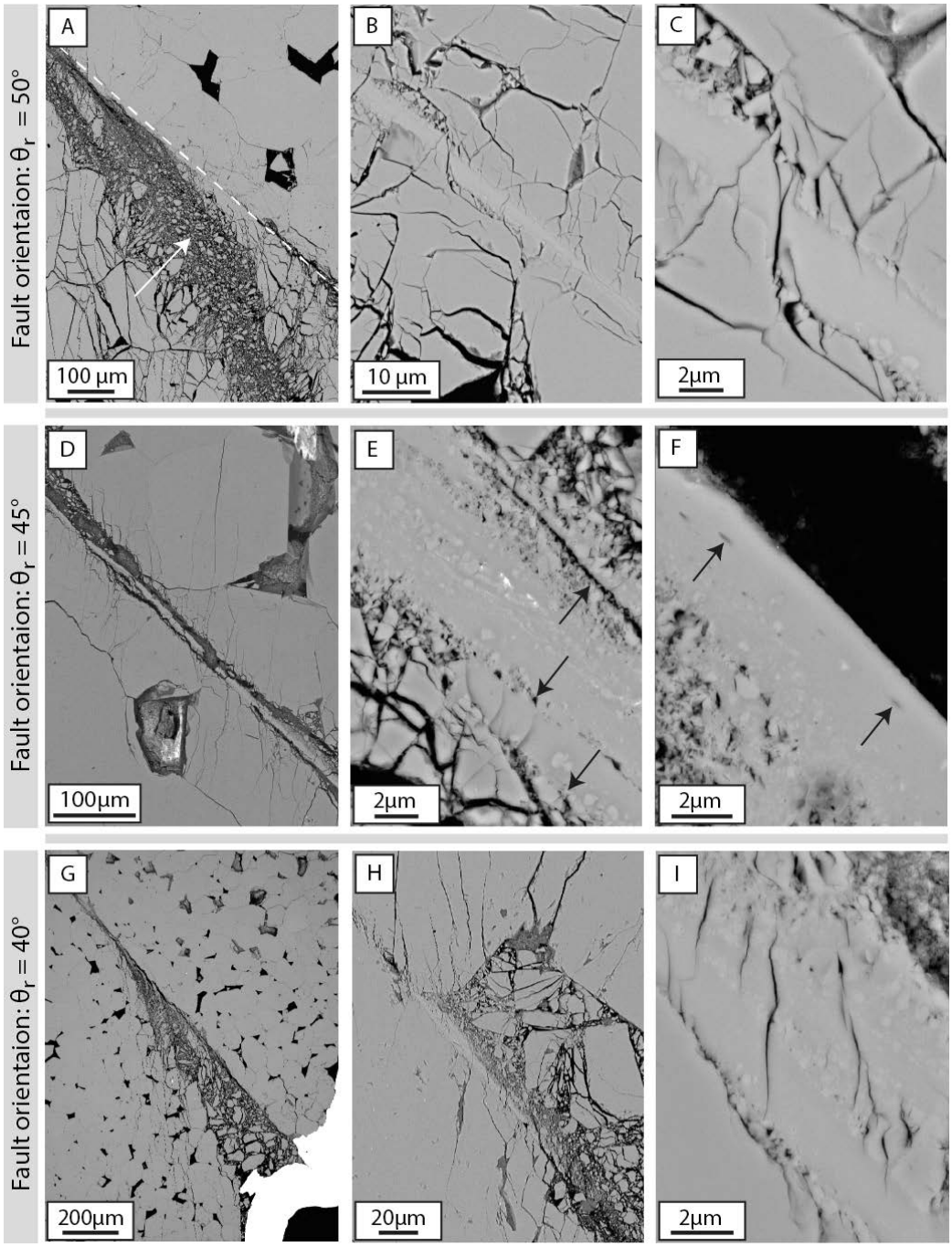

Figure 12: Comparison of microstructures with varying fault angle (θ_r).
The direction of axial shortening is parallel with long axis of all micrographs. Three images of different magnifications are shown for each fault orientation, with the orientation indicated at the beginning of the row. (A) Formation of secondary fault traces (indicated by the white arrow) at the misoriented fault ends. Note that the misoriented fault immediately adjacent to the new fault (on the right hand side) has been welded together with frictional melt. (B-C) Zones of continuous melt that weld the existing fault surfaces together. Note the offset in the boundary of the fault zone. (D) $\theta_r = 45°$, melt can be seen in many places separated from the fault walls forming a low-porosity band within the fault core. (E) Banding of the melt layers between layers of clasts and high porosity (see black arrows) indicating the possibility of multiple melt generation events. (F) Quenched melt layer adjacent to a pore space. Note the elongated vesicles within the melt layer. (G-I) Images of microstructures and melt formed within a sample where the fault is oriented at $\theta_r = 40°$. On $P_c = 50$MPa melt formation has become more sporadic, with melt mainly forming at asperity contacts (H). However, there is evidence of banding within individual melt zones (I), possibly suggesting multiple melting events.

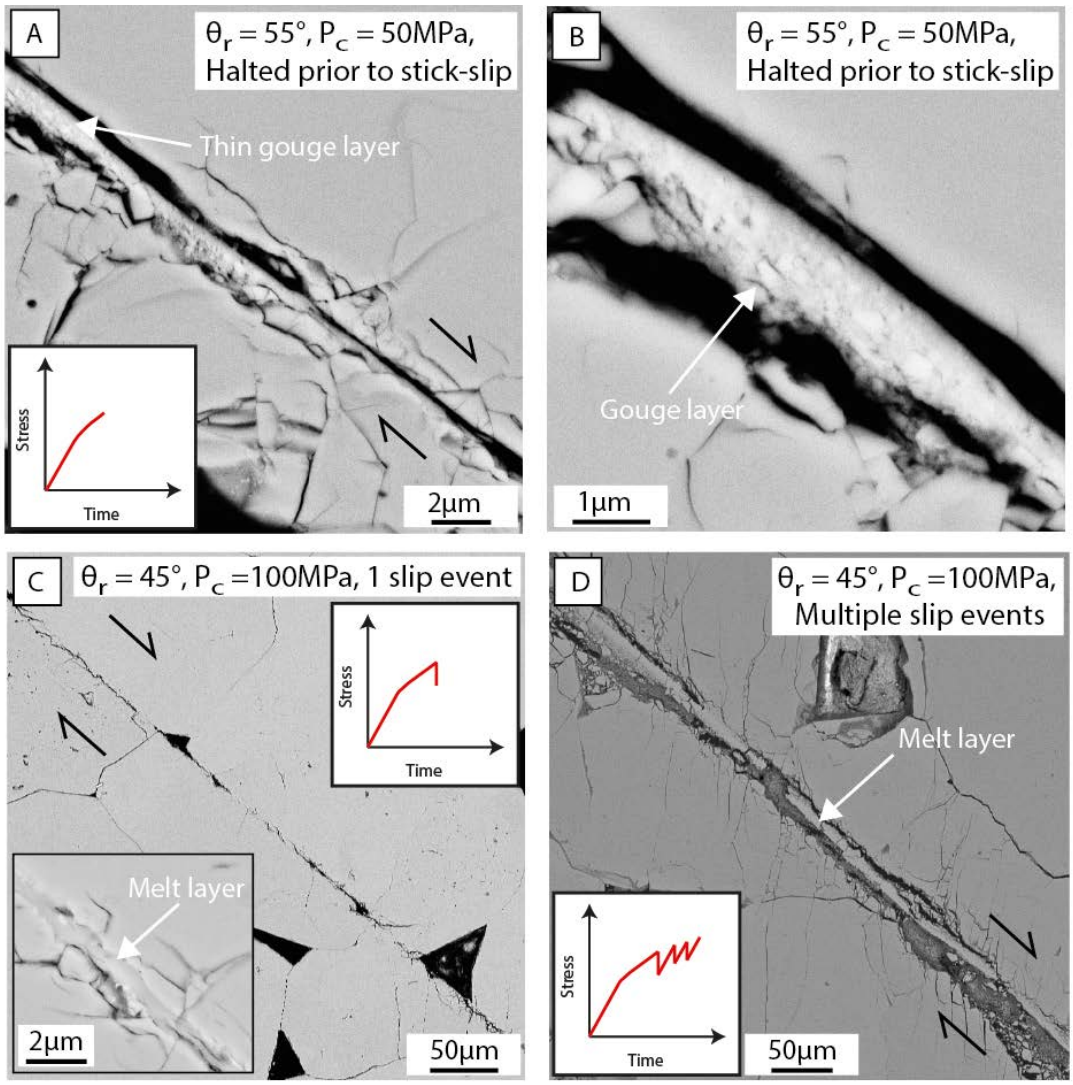

Figure 13: Evolution of the fault surface with increasing slip displacement.
Images show a comparison between fault surfaces produced during different experiments that were halted after varying amounts of slip. Schematic loading curves illustrate the how much slip occurred prior to halting the experiment. (A-B) MIS035: experiment was halted after the yield point but prior to the first stick-slip event. The slip surface does not show any evidence of melt generation, however very fine (sub-micron sized) gouge material has been produced and is supported within an ultra-fine grained matrix. The matrix particles cannot be resolved in the BSE-SEM imaging. However, the morphology of these zones is very similar to the structure of melt zones produced after stick-slip. (C) MIS037: experiment halted after a single stick-slip event. Melt welding is observed along parts of the fault core (see higher magnification inset). Note the absence of damage beyond approximatley 50μm on either side of the fault core. (D) MIS007: experiment halted after 6 stick-slip events (total shear displacement = 2.63mm). The fault core is notably wider, and the damage zone is more extensive than the fault core formed during a single slip event (shown in C). The melt layer is now largely isolated from the wall rock and sits within ultracataclasite in the fault core.

of the damage present on the unfavourably-oriented faults ($\theta_r \geq 55º$) is low displacement damage. However, most samples also have a layer of unconsolidated fine clasts (ranging in size from <100nm-10μm) within the principal slip zone that have been translated and rotated from their original position forming an irregularly oriented gouge.

Frictional melt on pre-ground fault surfaces

In samples with pre-existing faults that have reactivated at fast slip rates, a significant microstructural feature of fault cores is the formation of frictional melt (Fig. 12). As is the case for the frictional melt observed in the intact rock failure experiments, the melt is distinguishable in BSE-SEM imaging mode by having a slightly lower intensity than the surrounding quartz. Where the melt forms an uninterrupted layer between the two fault surfaces, the quartz wall rock immediately adjacent to the melt (in a zone <500nm wide) often has a higher intensity, forming subtly brighter bands on either side of the melt. Microstructures within the melt layer are readily correlatable with textures observed in the confirmed glass layers formed at high temperatures using SEM and TEM techniques (see Chapter 2). These textures include the formation of strained vesicles (see arrows, Fig. 12F), and the melt invasion of adjacent fractures forming an uneven melt substrate-boundary with the appearance of submicron melt injection veins (Fig. 12C). Samples from experiments halted prior to the activation of a rapid slip event show evidence of the formation of thin bands of sub-micron (~100-500nm) sized gouge within an unresolvable matrix. This material forms a discontinuous layer along the slip surface (Fig. 13A-B), and is similar in appearance to that observed following aseismic sliding in the high temperature experiments (Chapter 2).

Experiments halted immediately after the first rapid slip event have microstructures characterised by a weakly developed damage zone with rare intragranular fractures, a narrow fault core (between 1-5μm wide), and the formation of frictional melt (Fig. 13C). Interestingly, even after this single slip event, samples exhibit semi-continuous bands of melt that extend between the two fault interfaces. Upon quenching, the melt welds the opposite surface of the fault together (see inset, Fig. 13C). Intragranular and grain boundary fractures have formed alongside the melt-welded sections of the fault. This indicates that either the fractures formed while the frictional melt was still in a low viscosity state, or that the quenched melt had a considerable cohesive strength and resulted in the preferential failure of the damaged adjacent wall rock. Fracturing of the

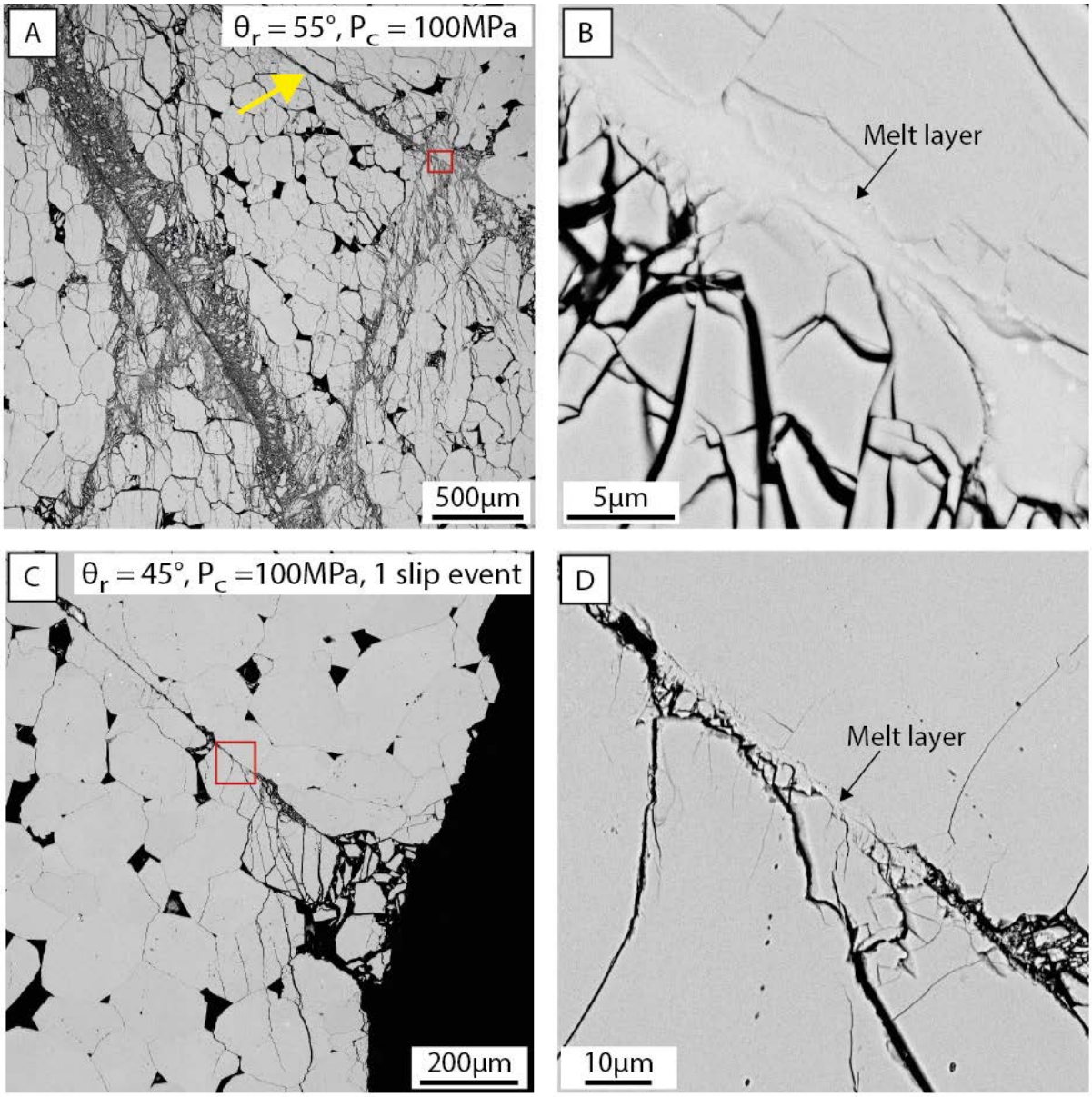

Figure 14: Melt-welding and its influence on the microstructural evolution of the fault surfaces. Many of the zones where splays and secondary fault traces are observed to develop appear to initiate from sites on the reactivated fault that are melt-welded, suggesting that the frictional melt influences the microstructural evolution of the fault surface. (A)-(B) are images taken of the fault zone in MIS006, showing a melt welded location that has subsequently been the site of the formation of a conjugate fault linking the existing fault and the new more favourably oriented fault. The pre-ground unfavourably oriented fault is indicated the yellow arrow. (B) Higher magnification image of the zone indicated by the red rectangle in (A). (C)-(D) Show the microstructures after a single slip event on MIS037. Fractures can be seen developing around the melt-welded section, beginning to form the splay-like damage zones at the fault tips. (D) Higher magnification view of the area indicated by the red box in (C). Note in both high magnification images that damage often occurs in the crystal adjacent to the melt zone, rather than within the quenched melt.

melt layer and entrainment of fractured glass particles within the principal slip zone indicates brittle deformation of the solidified melt and signifies quenching on timescales less than the duration of the slip event. Continued deformation results in the evolution of the fault core with sustained fracturing, melting and gouge formation. In areas were melt-welding is prevalent during early slip, damage is observed to form along the melt-wall rock boundary, widening the core and detaching the melt so that it occurs isolated within the gouge layer (Fig. 13D). The formation of melt has a remarkable impact on the subsequent development of microstructures within the fault zone, with the formation of secondary faults and splays nucleating from, or be spatially associated with a site of melt welding (Fig. 14).

An increase in confining pressure and/or reactivation angle results in the more prevalent formation of frictional melt, with fault surfaces transitioning from a localised melting at $\theta_r \leq 40^o$ (Fig. 12G-I), to the development of semi-continuous melting between $\theta_r = 45^o$-50° (Fig. 12A-F). Localised melt development occurs at asperity contacts, with discontinuous melt forming either between or adjacent to the asperity (Fig. 12H). Despite localised melting occurring in experiments where the fault is essentially favourably oriented (assuming normal range of frictional values), multiple slip events can result in the formation of numerous layers of melt at a single location; this is recognisable by the development of a banded texture where essentially clast-free layers of melt are laminated between gouge zones and also areas of increased porosity (Fig. 12I). Importantly, these banded textures are also identifiable within the melt of samples that have experienced only a single rapid slip event, suggesting that on the millisecond timescales of a single slip event, there can be multiple episodes of melting and quenching at an individual location on the fault surface.

Microstructures of fault cores and formation of melt in new favourably-oriented faults

The structure and appearance of the fault core in the new, favourably-oriented faults that form during deformation of samples where $\theta_r \geq 55^o$, is similar to that observed in the intact rock failure experiments. The cores of individual fault traces are up to several hundred microns wide including both the intensely fractured transition with the damage zone and the principal slip zone. However, in contrast to the intact rock failure experiments, where formation of melt is fairly rare and largely constrained to compressional zones within the fault core, the new faults formed during the misoriented

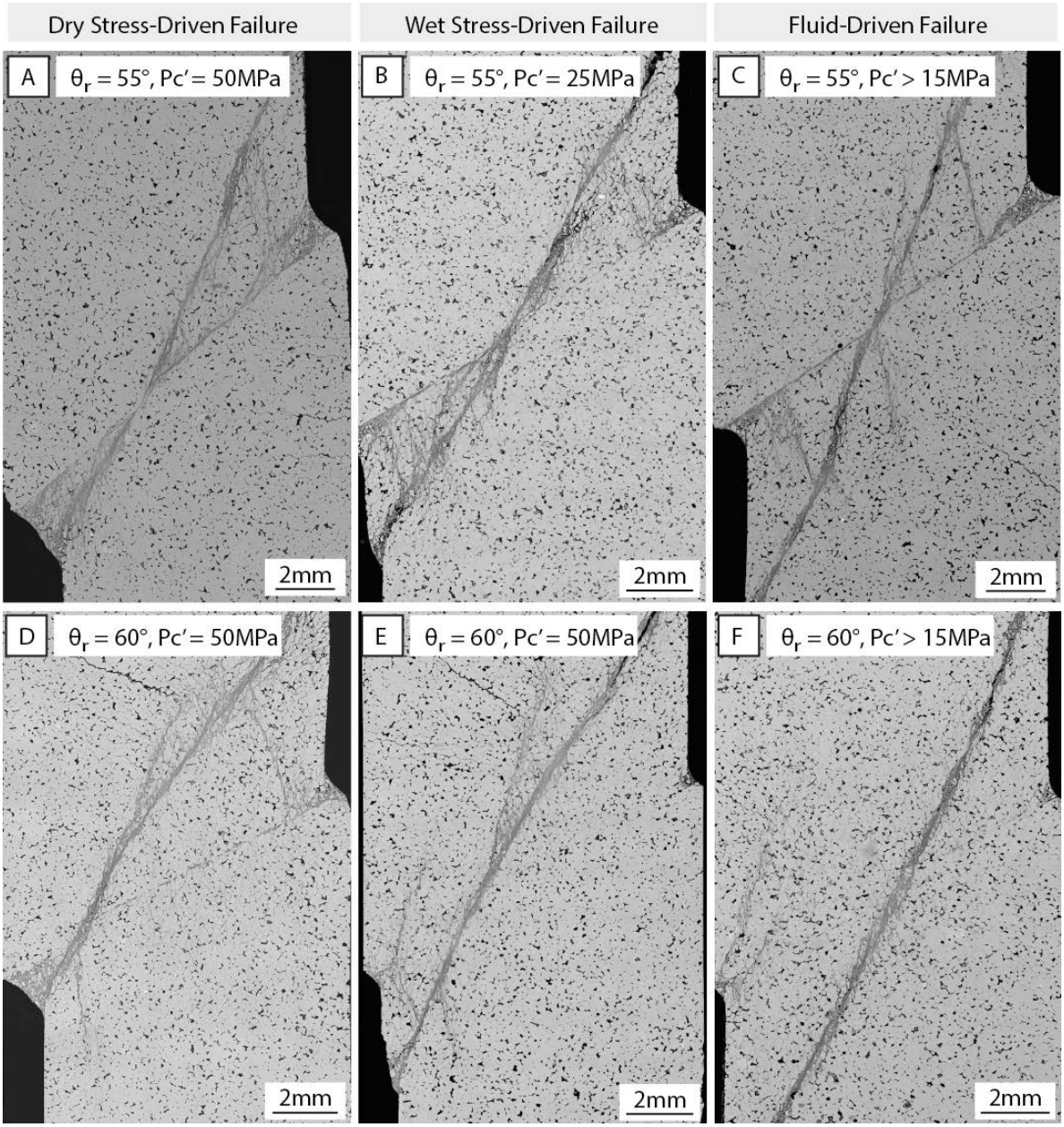

Figure 15: Comparison of sample scale microstructures of experiments reactivated and failed by different loading methods.

The use of image stitching software has enabled the creation of sample scale montages depicting the two-dimensional microstructures formed parallel to the slip direction. Each of the above images comprises of between 80-100 BSE-SEM micrographs and provides a comparison between faults with a reactivation angle, θ_r = 55º and 60º, following different modes of failure. (A & D) Faults reactivated and failed under dry stress-driven loading conditions. (B & E) Microstructures produced during water-saturated stress-driven failure and (C & F) provide an example of the faults formed during fluid-driven failure. Note the reactivation of the unfavourably oriented fault, recognisable by the offset of the sample edges. The new optimally oriented fault can be identified by the wide damage zone and formation of the steeply inclined fault.

fault reactivation experiments show the formation of extensive bands of frictional melt, up to 1.2mm long and 20µm wide. These melt zones are generally characterised by one approximately planar surface, which is interpreted as the melt generation plane, and a melt zone that grades into a more porous region of melt-indurated gouge. In many cases the relict wall rock adjacent to the melt layer is extensively fractured, often to point of pulverisation, where grain shattering is so intense that particles are often submicron in size, but show very little evidence of shear, thus preserving their original grain structure. However, apart from a few fractures, the quenched melt layer is largely intact and forms a distinctive band of cohesive material within the fault core.

Fault gouge is readily distinguishable from the low displacement damage zone in the fractured and pulverised wall rock. The gouge particles tend to be angular to sub-rounded, and largely equant suggesting comminution and rounding during grain movement. In contrast, fractured grains are generally angular, and form shards and blocks that have not rotated significantly from their original position. Both gouge and fractured material have particle sizes ranging from sub-micron to in the order of tens of microns in diameter.

3.2.2.2 Saturated stress-driven fault reactivation and failure

Two stress-driven deformation experiments have been undertaken at controlled pore water pressures and with θ_r = 55º-60° (MIS023 and MIS022, respectively). To a first order, the microstructures formed during these experiments (Figs. 15B-E) are very similar those developed during dry stress-driven fault reactivation and failure experiments (Figs. 15A-D) with the initial activation of the misoriented fault surface followed by the formation of a new non-planar fault surface. The new faults are characterised by the development of one dominant high-displacement fault surface and numerous secondary fault traces that accommodate much less slip. However, on closer examination there are subtle differences between the experiments undertaken dry and those deformed in the presence of fluids. There is less damage along the existing fault, especially around the fault tips, and the new, more favourably-oriented faults are more steeply inclined, truncating and offsetting the original unfavourably oriented fault closer to the centre of the sample. The development of secondary fractures from the leading fault tip of the unfavourably oriented θ_r =60º are more similar to microstructures observed in the hanging-wall of fluid-driven failure experiments (see Section 3.2.2.3)

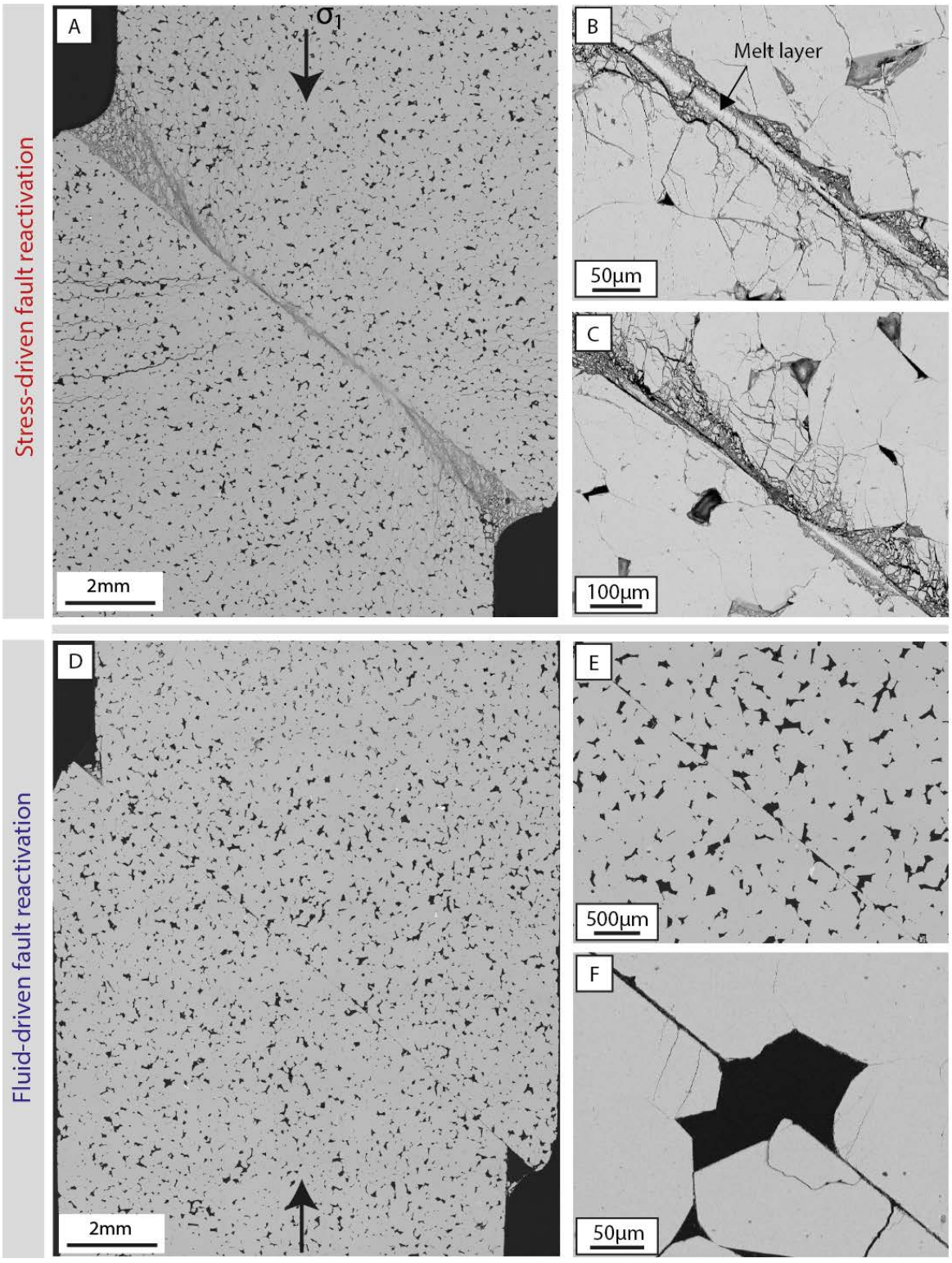

Figure 16: Comparison of microstructures between stress- and fluid-driven fault reactivation (θ_r = 50°).

Orientation of maximum principal stress is indicated by the black arrows. (A-C) MIS010: stress-driven fault reactivation. (A) Overview montage of sample showing the more extensive damage caused during stress-driven failure and the formation of splay-like structures at the fault ends. (B-C) Higher magnification images of the fault core showing the asymmetry of damage adjacent to the fault core. A line of largely continuous melt can be seen within the fault core – see arrow in image B. (D-F) MIS026: fluid-driven fault reactivation. (D) Overview montage of sample showing essentially no damage on the fault surface. This is confirmed in the higher magnification images (E-F).

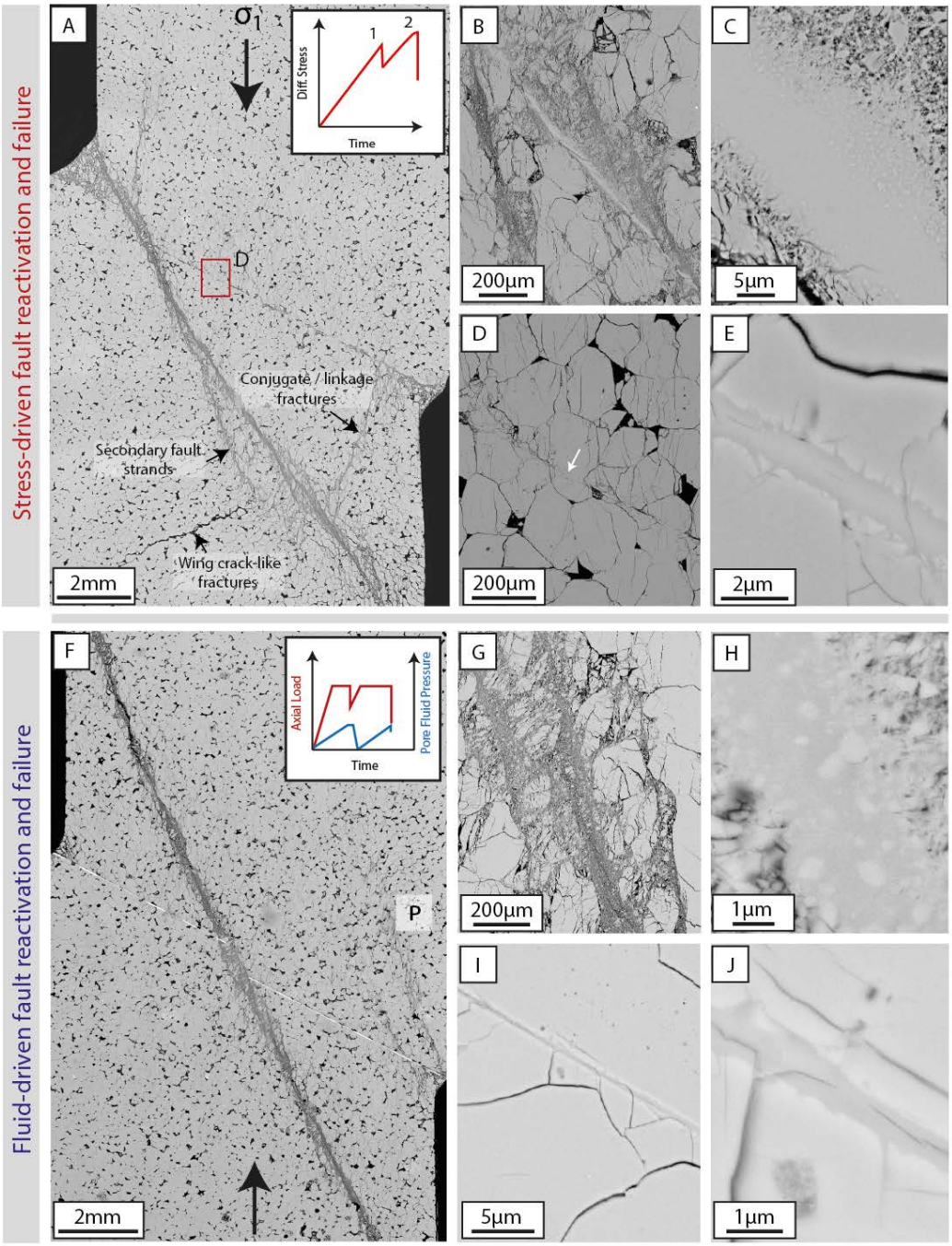

Figure 17: Comparison of melt produced during stress- and fluid-driven fault reactivation and failure.
Samples shown have an existing fault (θ_r = 60º) that has reactivated forming significant melt before reloading and failing on a new optimally oriented fault – see loading curves shown in insets. Black arrows indicate direction of axial shortening. (A) Overview image montage of sample MIS012 showing the development of a new fault, conjugate/linkage structures and secondary fault strands by stress-driven failure. (B-C) Different magnification images showing the formation of frictional melt in the core of the newly-formed fault zone. (D-E) Pseudotachylyte forming a continuous melt layer between the misoriented fault surfaces. Note the injection/melt filled veins at the melt-wall rock boundary. (F) MIS027, fluid-driven fault reactivation and development of a new, more favourably oriented fault zone. Overview of sample – note the formation of a through going fault, which is not significantly influenced by the damage geometry of the existing fault. Small secondary faults can also be seen developing from the fault tip of the 60º misoriented fault at P. The location of the original unfavourably oriented fault is highlighted with a white dashed line. (G-H) Low and high magnification images of quenched melt in the newly formed fault. (I-J) Pseudotachylyte welding of the misoriented fault surfaces.

suggesting that there are subtle changes to local scale stress fields within the sample arising from the presence of pore fluids. It must be noted however, that these observations are based on a limited number of samples and the formation of microstructures could be affected by heterogeneities within individual samples.

The first order similarities between microstructures developed during dry and saturated stress-driven failure extend to the deformation structures formed in the fault core. Under saturated conditions melt textures are present on both the original misoriented fault and on the new, more favourably oriented fault, despite MIS023 having a significantly lower effective confining pressure than the comparison nominally dry experiment. The abundance of the melt on slip surfaces appears not to be significantly influenced by the presence of pore fluids, although, under lower effective confining pressures (MIS023) the melt volume is somewhat reduced. In the fluid-saturated samples, melt also welds the fault surfaces and many secondary fractures nucleate from melt-welded sites, indicating that the formation of glass localises much of the subsequent fault damage.

As with the dry stress-driven slip zones, the fault core of the new favourably-oriented fault in fluid-saturated experiments, is dominated by the formation of gouge that contains numerous sub-micron particles. The undulatory nature of the new fault generates dilatant releasing bends and compressive restraining zones during slip. The latter regions localise the distribution of much of the frictional melt. The melt formed in the core of the new fault has a higher clast density than observed in the dry stress driven failure experiments.

3.2.2.3 Fluid-driven fault reactivation and failure

The architecture of faults reactivated under conditions where the axial load is held constant and the pore fluid pressure increased, is noticeably different from that produced during stress-driven failure under both dry and fluid saturated conditions. Where the fault zone is oriented at $\theta_r = 40^o$ - 50^o and the sample is reactivated by fluid-driven processes, there is a remarkable lack of damage along the slip interface, despite having slipped between 14 and 28 times (Fig. 16D-F). A few rare intragranular microcracks are observed in the grains adjacent to the slip surface, but it is not certain whether these formed during experimental deformation or were the result of the initial grinding of the fault interfaces.

With increasing reactivation angles, the microstructures produced during deformation do develop first-order similarities with stress-driven failure experiments, however noticeable differences remain. As in the stress-driven experiments, pre-existing faults where $\theta_r > 55^o$ reactivate once before locking and the generation of a more favourably oriented fault (Figs. 15C & F, 17F–J). However, during fluid-driven failure, the new fault is less affected by the geometry of the existing fault, forming a single through-going fault that is largely symmetrical within the sample. Numerous distributed extension fractures also have formed throughout the sample, although the concentration of damage is still observed to be asymmetrically concentrated around the pre-existing unfavourably oriented fault. Damage within the core of the pre-existing fault is also significantly less than is the case for stress-driven failure events and appears to be largely a result of repeated re-shearing and damage following the generation of frictional melt.

3.2.3 Hydrothermally-treated, reactivated fault

One experiment (MIS038) has been undertaken to examine effects of hydrothermal conditions (6hrs at 900ºC, P_c = 250MPa, P_f = 150MPa) on the stability of frictional melt, as well as fracture and fault zone healing. Following the reactivation of an unfavourably oriented fault ($\theta_r = 60^o$) at room temperature, under conditions that had previously been demonstrated to reliably produce frictional melt, hydrothermal conditions were achieved by introducing pore fluids and increasing both confining pressure and temperature. Microstructural analysis of the slip interface following hydrothermal treatment indicates that the fault has undergone substantial healing (Figs. 18A-D). Gouge particles have become compacted with the destruction of porosity; all evidence of sub-micron-sized gouge particles is gone, and many of the extension fractures associated with deformation have healed. Other fractures, possibly those with wider apertures, are partly healed and can be identified by trails of fluid inclusions or by the presence of relict open fracture segments (see white arrow, Fig. 18B). The population of completely unhealed fractures (Fig. 18B) are thought to arise from either volume changes associated with the alpha-beta phase transition of quartz and/or depressurisation at the end of the experiment, or as a result damage caused during subsequent sample preparation.

In places the fault is completely healed with the pre-ground slip interface being essentially indistinguishable from the undamaged rock when imaged in BSE-SEM mode. There is no evidence of the characteristic variation in back-scattered electron intensity associated with the presence of melt in untreated experiments. Fault geometry indicates that these entirely healed zones are within the fault core and are thought to exist where melt welding has previously occurred. In regions where the fault damage consisted mainly of gouge formation, porosity is significantly reduced with compaction of the high porosity gouge. Most gouge particles no longer have the angular and shard-like shapes associated with formation by cataclastic processes, but instead are rounded to polygonal and have faceted, euhedral grain surfaces adjacent to remnant pores.

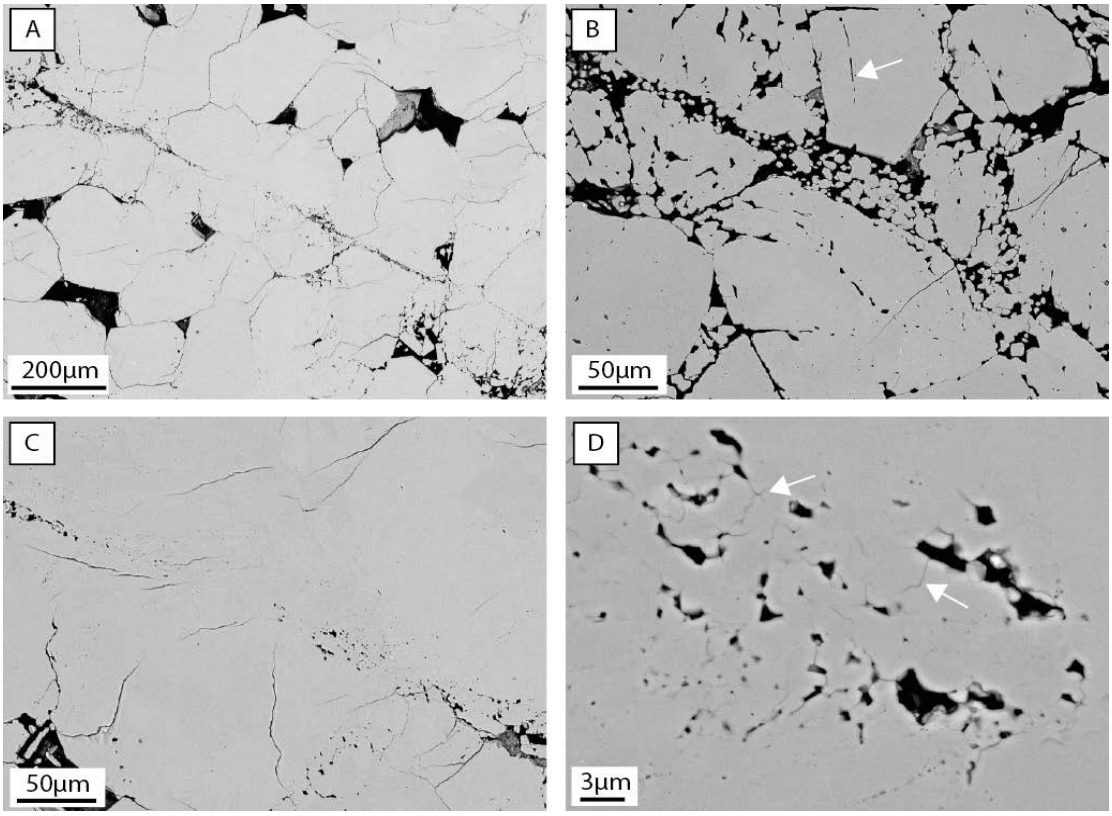

Figure 18: Microstructures produced during hydrothermal treatment of a reactivated fault.
MIS038, θ_r = 60º: sample was loaded until the there was one reactivation on the existing fault. The sample was then hydrothermally treated for 6 hours at 900ºC. After hydrothermal treatment, BSE-SEM images taken of the cross-section of the fault indicate extensive healing at the fault interface. (A) Low magnification image showing the extent of healing in the damage zone during hydrothermal treatment. In places the pre-ground fault is almost completely healed (i.e. no porosity). (B) Example of partially healed microstructure. White arrow indicates a microfracture that is segmented by the uneven precipitation of quartz along its length. Note the heterogeneous porosity distribution associated with partial cementation/compaction of gouge and the rounding of particles. (C) Image of an area of the original fault trace that is almost completely healed. (D) High magnification image of gouge zone that is partially healed. White arrows point to fractures along possible grain boundaries. The reduction in porosity and significant rounding of grains is evident.

Where grain boundaries are evident within the partially compacted gouge (see white arrows, Fig. 14D) a number appear to show evidence of grain interpenetration, although it is unclear whether the grain interpenetration is the result of grain-to-grain dissolution, or caused by the overgrowth of hydrothermally quartz. However, BSE-SEM imaging is an unreliable technique for monitoring the evolution of grain shapes and grain boundaries under hydrothermal pressing as any precipitated overgrowths of quartz are indistinguishable from the original grains. Consequently, it is uncertain whether dissolution-precipitation creep is active over the timescales of the hydrothermal treatment. There is evidence of complete dissolution and removal of sub-micron gouge clasts within the fault core and silica precipitation in fractures and as overgrowths on clast surfaces, but, there is insufficient evidence to determine whether dissolution occurs preferentially at stressed grain contacts. Further, BSE-SEM imaging cannot resolve whether the melt dissolves or simply devitrifies and crystallizes *in situ*. High-resolution cathodoluminescence imaging and spectroscopy were explored as a possible technique to distinguish between the original quartz grains, melt and the hydrothermally precipitated quartz to provide insights into melt generation, dissolution, precipitation and overprinting. The results of this investigation are discussed in the following section.

3.3 2D Microstructural analysis using high resolution SEM-CL

Microstructural studies using high resolution SEM-CL have been undertaken on the fault cores of a number of samples to investigate how the high stress concentrations and transiently high temperatures associated with slip, have influenced the cathodoluminescence of material in the fault core. Representative samples of (1) melt-welded, unfavourably-oriented faults, (2) high-displacement favourably-oriented faults, (3) melt-welded faults produced at saturated conditions, and (4) the hydrothermally-treated fault, were investigated using both panchromatic imaging and monochromatic spectral analysis. The use of a low accelerating voltage (5kV) reduces the electron interaction volume and allows high resolution (sub-micron) CL imaging to be achieved. Corresponding BSE images were collected concurrently using a mirror detector (MD) located inside the objective aperture of the SEM. This detector is not located in a position to allow the collection of low angle backscattered electrons, so provides little information on crystallographic orientation and consequently the melt zones are more difficult to recognise than in the images described in Section 3.2. All samples were

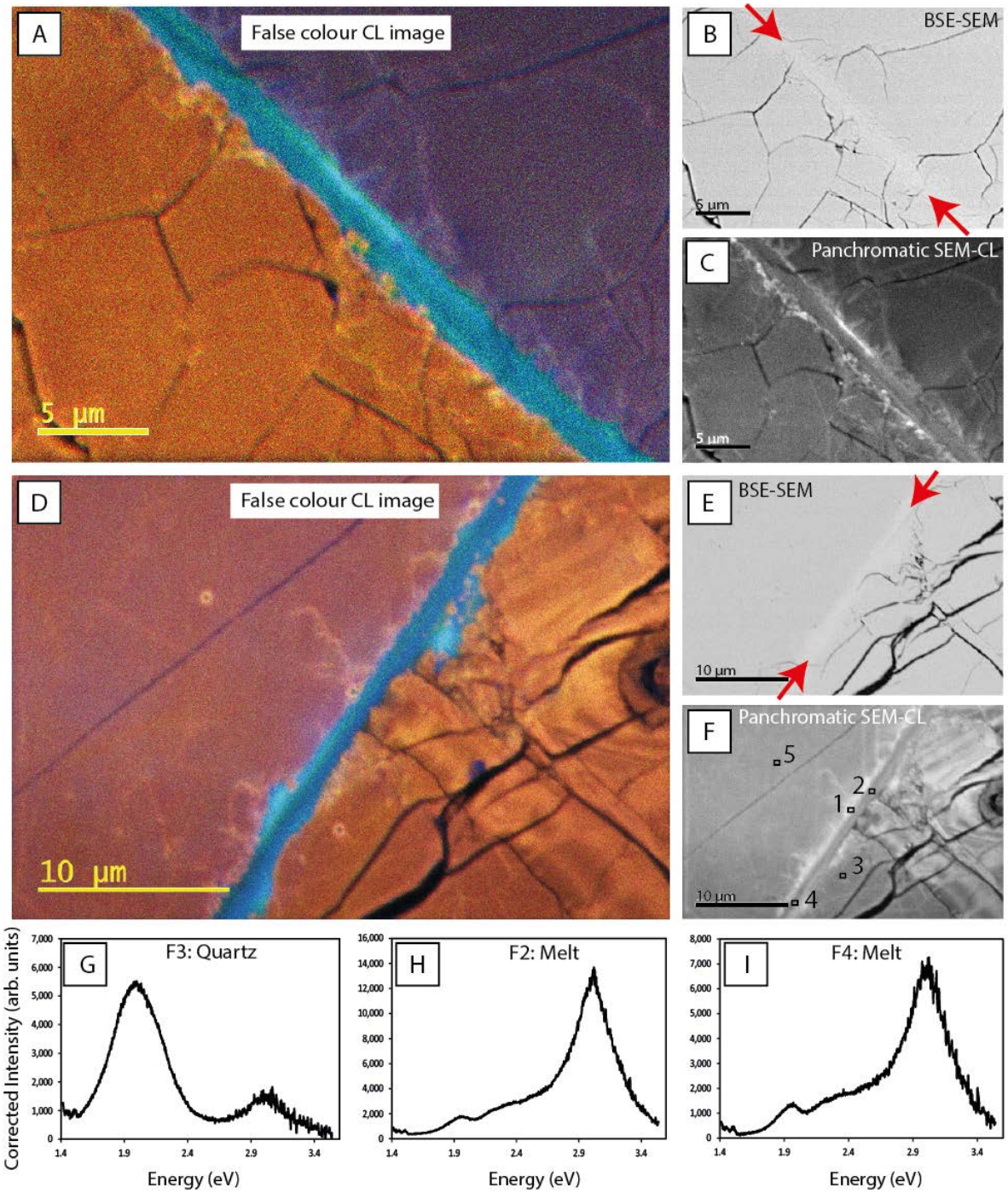

Figure 19: Cathodoluminescence analysis of a melt-welded interface created by the stress-driven reactivation of a θ_r=60° fault under nominally dry conditions.
Images and spectra acquired from MIS017, reactivated at P_c = 50MPa. (A) False colour CL image of a melt-welded section of the fault. Quartz appears as either orange-brown or purple and the central melt layer appears as blue to blue-green. (B)-(C) BSE-SEM and panchromatic CL images (respectively) of the location shown in (A). Red arrows in (B) identify the location of the melt welded fault. Note the higher emissions along the edge of the fault in the CL image. (D) False colour image of another section of melt welded fault. Note the clasts within the melt layer that have the same CL emissions as the adjacent wall rock. (E)-(F) BSE-SEM and panchromatic CL images of the area shown in (D). Red arrows in (E) identify the location of the fault. The locations of spectral analysis are shown on the panchromatic image. Representative spectra for quartz and melt are shown in figures (G)-(I) and all spectra collected are shown in Appendix 5. The formation of melt results in an increase in the broad peak centred at ~3.0eV and a decrease in the 2.0eV peak. The intensity of the emissions produced by the melt varies considerably, although most spectra acquired suggests emissions of <10,000 counts.

found to be sensitive to modification from the electron beam, with an observable decrease in the intensity over all wavelengths occurring during prolonged analysis. To minimise time-dependent change to CL responses, the analysis times were kept short (5 seconds) and the beam was blanked while analysis was not in progress.

The undeformed quartz in all samples has emissions in the red or red-blue wavelengths, forming broad spectral peaks between 1.9-2.0eV (λ = 620-640nm) with red-blue samples forming a secondary dominant peak at ~3eV (λ = 410nm) (Figs. 19-22). Narrow emission lines or peaks are rare. Using the panchromatic colour filters the original quartz is revealed in red-brown to purple hues. It has been suggested that the discrepancies in CL colours of the detrital grains arise from differences in provenance and metamorphic history of the sediments [*Ramseyer et al.*, 1988; *Gotze and Zimmerle*, 2000]. Authigenic overgrowths are clearly visible in CL-imaging, being recognisable by their commonly-different intensity and wavelength luminescence compared with the detrital grains. These overgrowths form the euhedral grain surfaces that are visible around pores when using in other forms of SEM imaging. Within individual grains, a history of brittle deformation is evident from the presence of numerous, commonly cross-cutting, healed microfractures with different luminescent properties.

3.3.1 Stress-driven failure of unfavourably-oriented faults

MIS017 (P_c = 50MPa) was examined as an example of an unfavourably oriented fault (θ_r = 60º) which has undergone a sudden slip event. Cathodoluminescence imaging reveals important characteristics that are not readily visible using other imaging techniques. The most apparent feature is the change in luminescence associated with the formation of the melt layer. The melt is clearly distinguishable from the adjacent grains, both in terms of emission intensity and wavelength and can be used to identify numerous sub-micron scale features such as melt-filled fractures in the adjacent crystal. Spectrally the melt layer shows a shift in the broad maximum luminescence, present in the primary detrital quartz, towards lower energy (higher wavelengths) and the development of a distinctive peak shape that is consistent between locations and samples. Similarly to the quartz spectra, the peaks associated with the melt are broad suggesting an intrinsic structural source (see Section 4.2). The dominant peak of spectra collected within the melt layer is located within the blue spectrum at ~3.0eV

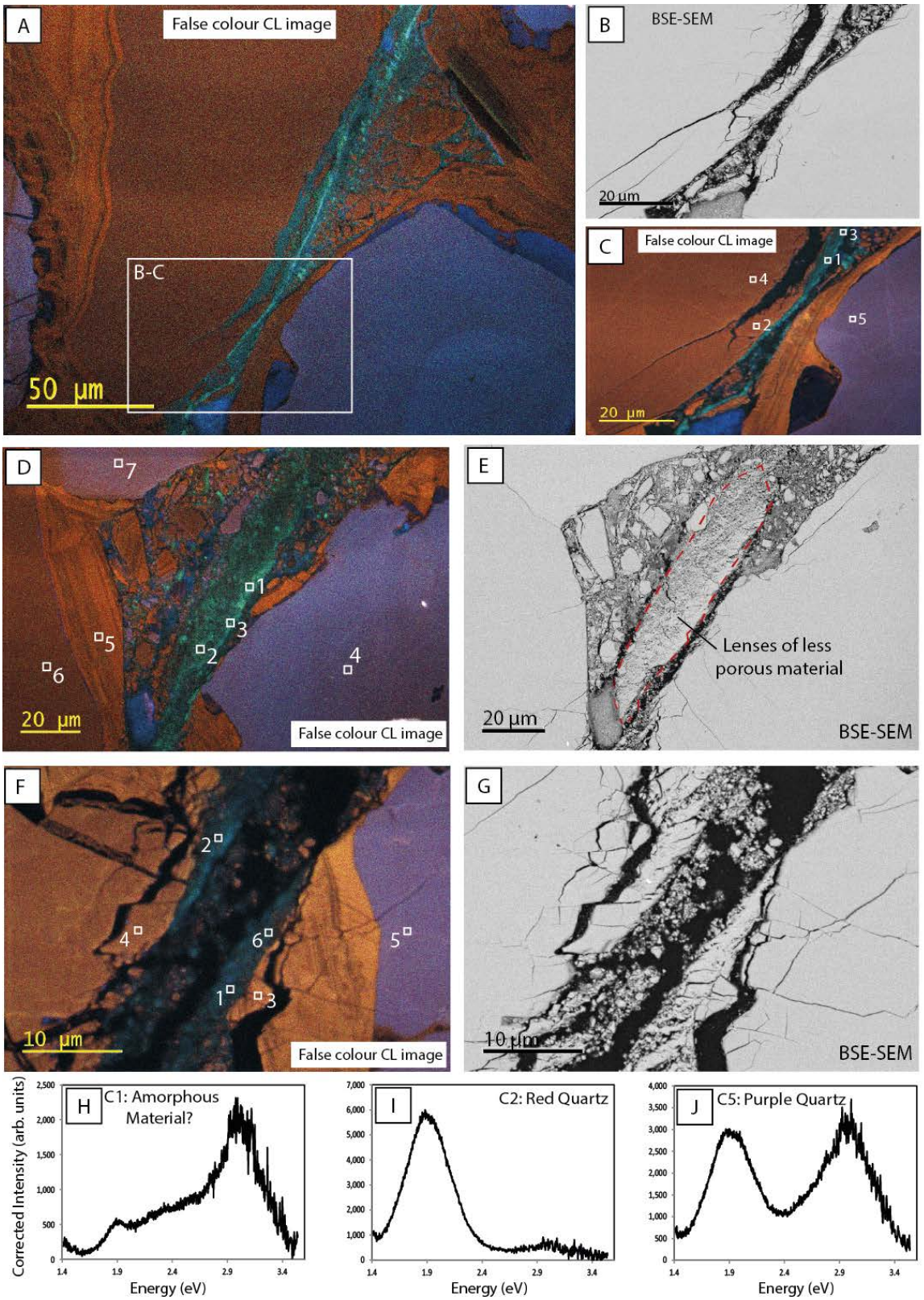

Figure 20: Cathodoluminescence of a mature, favourably oriented fault that has slipped aseismically.

Images and spectra acquired from BIS001 (F)-(G) and BIS004 (all other images), both reactivated at P_c = 100MPa. False colour panchromatic CL and comparative BSE-SEM images are shown. The locations of spectral acquisition points are indicated on CL images. Representative spectra are shown in images (H)-(J) – for all other spectra for numbered locations see Appendix 5. See text for further discussion of the images.

(λ = 410nm), with secondary peaks forming at between 2.4-2.6eV (λ = 477-517nm) and ~2.0eV (λ = 620nm). The intensity of the luminescence of the melt layer varies between samples and even within single field of view, revealing luminescent texture within the melt layer (Fig. 18A, C-D). In false colour panchromatic images this makes the melt zone vary between blue and blue-green, forming a unique colour that is distinct from the surrounding primary and authigenic quartz.

Importantly for understanding the process of melt-generation, the CL images reveal the presence of clasts of unmelted material with the same luminescence as the adjacent host rock. This may indicate that cataclastic processes have occurred prior to formation of melt and that melting results in a structural change in the silica that is reflected in cathodoluminescence. Interestingly, the wall rock immediately adjacent to the melt forms thin (<1μm) luminescing rims at the fault – melt interface (most clearly seen in the grey-scale panchromatic images; e.g. Fig. 18C & F). The spectrum taken at location 1 (Fig. 18F), shows a significant increase in the intensity of the peak centred at ~3.0eV (λ = 410nm), indicating a possible transition between the defects forming the emissions in the quartz and the melt. However, it must be noted that the interaction volume of the electron beam potentially limits the resolution of such features. Using a Monte Carlo simulation of the present operating conditions, the interaction width of the electron beam is in the order of 200nm.

3.3.2 Stress-driven failure of favourably-oriented faults (aseismic slip)

During BSE-SEM imaging of mature optimally-oriented (θ_r = 30°) faults (with displacement > 4mm), a number of textures were identified that were noticeably different from normal gouge and cataclastic damage (Fig. 20). Less porous and more cohesive lenses of material form in the gouge of the fault core either adjacent to an asperity contact (Fig. 20E), or adjoining the slip interface (Fig. 20B & G). Cathodoluminescence analysis was undertaken on two optimally-oriented samples, BIS001 and BIS004, both of which had slipped for approximately 4.5mm at P_c = 100MPa and at a nominal axial displacement rate of ~3.63μm.s^{-1}. BIS001 showed no evidence of macroscopic stick-slip during deformation, while BIS004 transitioned from the yield point directly into a regime with small amplitude stick-slip ($\Delta[\sigma_1-\sigma_3]$ = 10MPa).

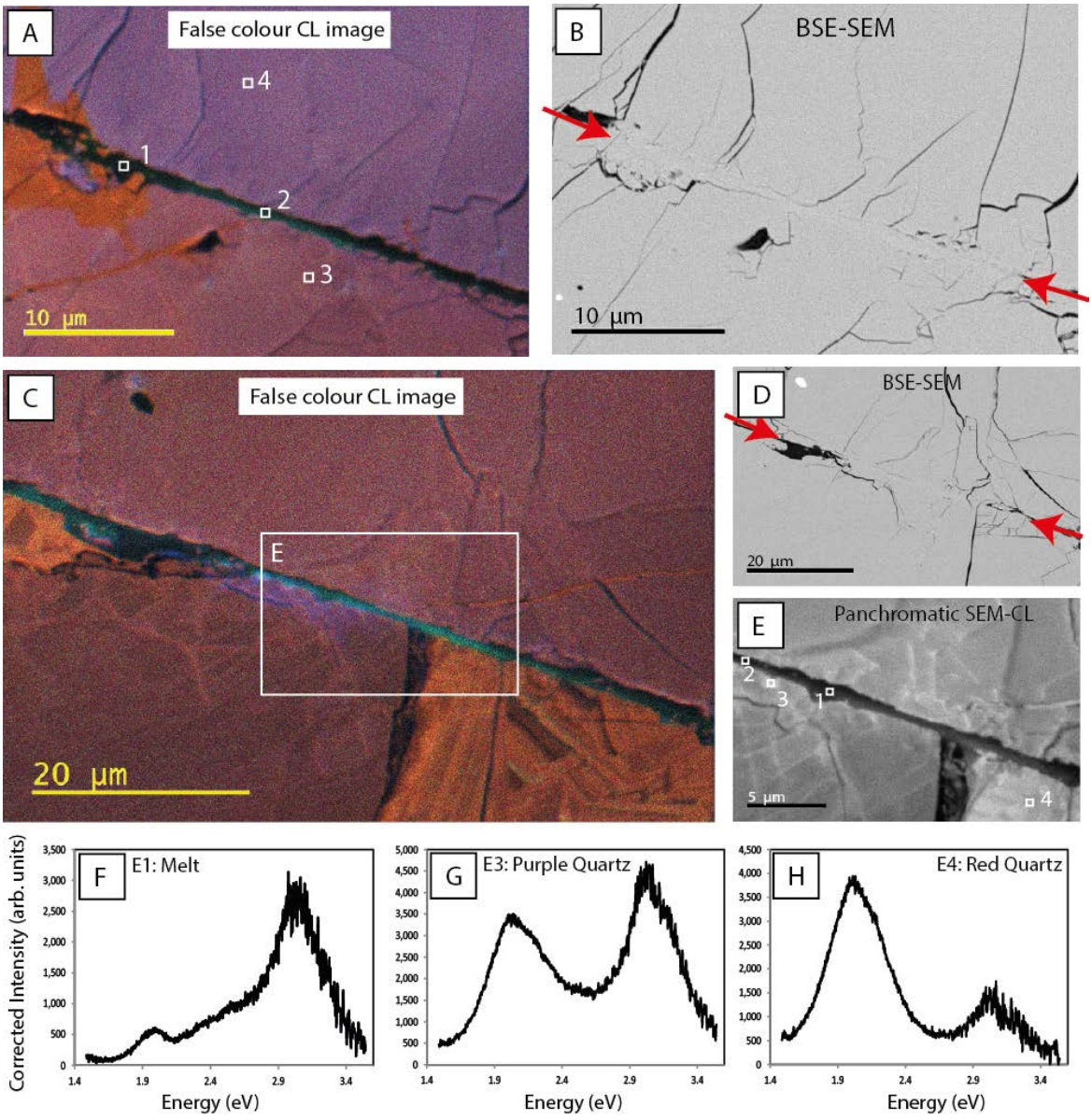

Figure 21: Cathodoluminescence of unfavourably oriented (θ_r=60º) interface reactivated by fluid-driven failure (stick-slip behaviour).
Images and spectra acquired from MIS027, reactivated at P_c = 80MPa, P_f = 50MPa. (A) False colour panchromatic CL image of a melt welded section of the fault. The melt layer cuts across the centre of the image at an inclined angle from the upper left to lower right side and appears as black to blue-green. Note the epoxy in these images appears as black (non-luminescing). (B) BSE-SEM image of the same area shown in (A). Red arrows indicate the location of the fault zone. (C) False colour panchromatic CL image of another section of melt welded fault. Note the variation in intensity of emissions within the melt layer. (D) BSE-SEM images of the area shown in (C). Red arrows indicate location of the fault zone. (E) Panchromatic CL image showing the region indicated in E and indicating the locations of recorded spectral analyses. Representative spectra for the melt and quartz shown in images (F)-(H), with all recorded spectra shown in Appendix 5. As for melt formed in dry conditions, the melt formed under water-saturated conditions has a broad peak centred at ~3.0eV and secondary peaks at approximately 2.0eV and 2.4eV. The intensity of the emissions produced by the melt formed in saturated conditions is lower than those recorded in nominally dry conditions, with emissions <5,000 counts.

The original quartz grains show CL spectral peaks consistent with those described previously, with the broad main quartz peaks occurring at ~1.9-2.0eV (λ = 620-650nm) and ~3.0eV (λ = 410nm). However, the textually altered zones described above show a luminescent signature that is very different from the quartz, with sharp boundaries delineating the original quartz and damaged material (Figs. 20C & F). The intensity of the luminescence in these zones is generally lower than the quartz, although zones of locally higher CL intensity are present (Figs. 20A & D). The CL spectra produced by the damaged material has characteristics and overall shape similar to those measured for the melt layer in the unfavourably oriented fault. The main peak occurs at ~3.0eV (λ = 410nm), with secondary peaks forming at 2.55eV (λ = 485nm) and ~1.9eV (λ = 650nm). However, the relative peak strength of the blue, 3.0eV peak is less intense than in the melt layer, causing the sample have a distinct green to green-blue hue, in the false-colour panchromatic image stacks (Fig. 20A, C, D, F). It is clear from the images and analysis that cataclastic processes and the formation of gouge, do not, in themselves, cause the observed changes in the CL signature of the damaged material. Gouge clasts with the same luminescence as the adjoining host quartz are abundant in the pores adjacent to the fault, and are even interspersed within the damaged material. Likewise the damaged material is fragmented and intermingled in the gouge, suggesting cataclastic re-working of previous slip surfaces and damaged material.

3.3.3 Fluid-driven failure of unfavourably-oriented faults

The melt-welded interface of MIS027, a sample with a fault oriented at $\theta_r = 60°$ and reactivated by fluid-driven failure, was examined using SEM-CL to provide a comparison between the CL signatures of melt formed under nominally dry and fluid-saturated conditions. BSE-SEM imaging had revealed that melt generated during both fluid- and stress-driven failure was largely indistinguishable. However, the greater sensitivity of CL to subtle variations in composition or structure related to changes in defect density (for example OH defects), intimated that this method could be useful for identifying potential differences between the melts. The acquired spectra revealed a strong similarity between both the location and shape of the main peaks and those peaks identified during analysis of the melt formed under dry conditions, with the main peak occurring at ~3.0eV (λ = 410nm), and secondary peaks forming at 2.4eV (λ = 517nm) and ~2.0eV (λ = 620nm) (Fig. 20). The overall emission intensity is lower for the melt

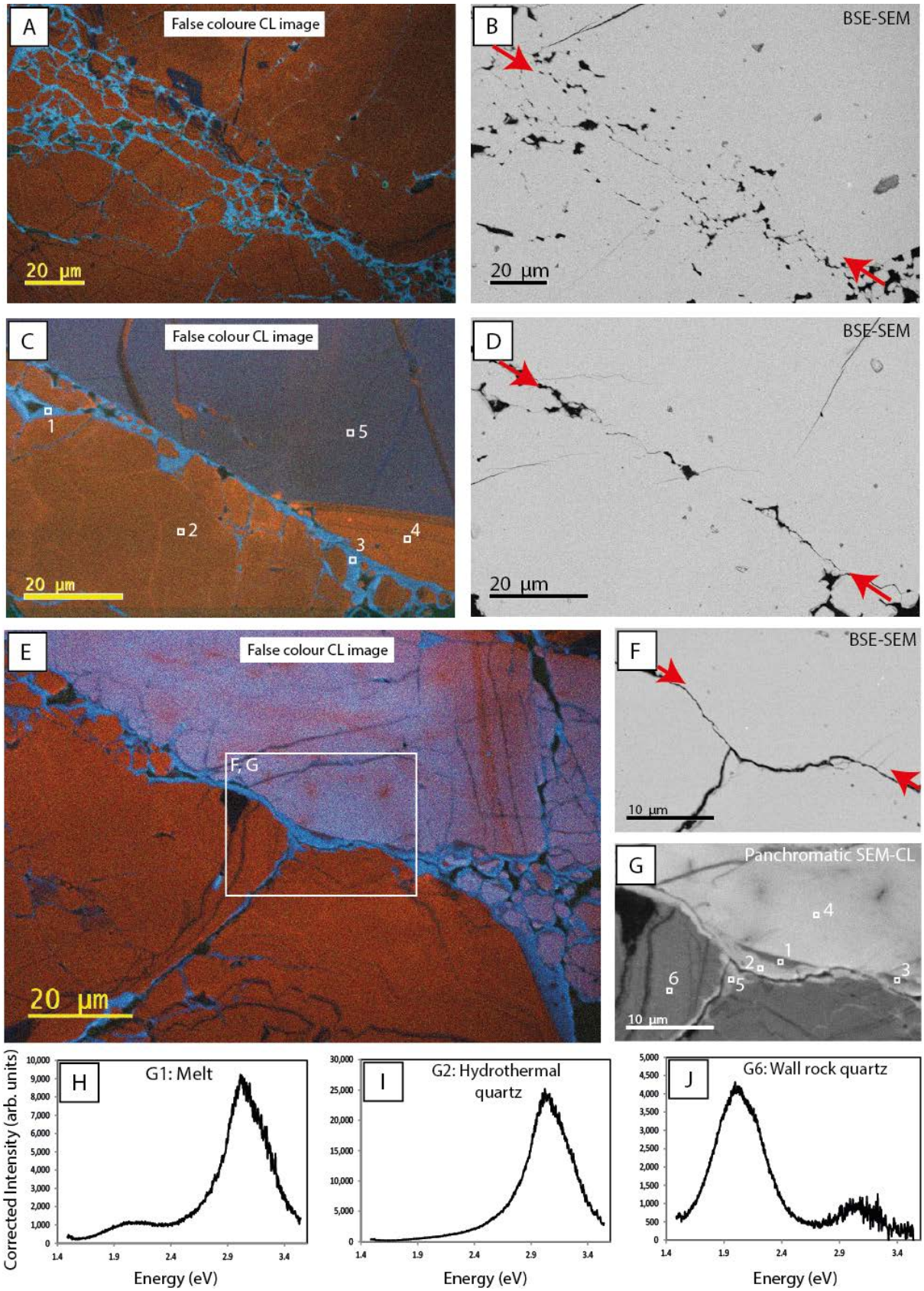

Figure 22: Cathodoluminescence of hydrothermally treated, melt-welded interface.
Images and spectra acquired from MIS038, reactivated at P_c = 50MPa, then hydrothermally pressed for 6 hours at T = 900ºC, P_c = 250MPa and P_f = 150MPa. For description please see following page.

formed under fluid-saturated conditions and in many places is not sufficient to produce a distinctive colour during the panchromatic imaging. However, where the luminescence is sufficiently intense, the false colour images indicate that the melt layer has a similar hue to the damaged material produced under aseismic conditions, with a distinctive green-blue shade (Figs. 21A & C).

As with the melt formed during dry stress-driven failure, the melt generated under water saturated conditions shows internal variation in the intensity of the luminescence within the melt layer (Figs. 21A & C). The melt exhibits rudimentary banding and localised zones of higher luminescent intensity. Quartz clasts with the same luminescence as adjacent quartz grains are incorporated within the melt layer and typically show relatively sharp melt-clast boundaries.

3.3.4 Hydrothermal treatment of a melt-bearing slip surface

As described in Section 3.2.1, BSE-SEM imaging has limitations for monitoring the evolution of grain shapes and boundaries where the overgrowths are essentially of the same composition and have the same mean atomic number (Z-contrast) as the original material. Variations in trace impurities and defects between the original quartz and overgrowths mean that CL can provide useful information about processes occurring during hydrothermal hot-pressing. CL imaging and analysis of MIS038 (θ_r = 60°), slipped at room temperature and then hydrothermally treated for 6 hours at 900ºC, reveals that quartz overgrowths formed during hot-pressing have a high intensity blue luminescence, with the main peak centred at ~3.0eV (λ = 410nm). Although these quartz overgrowths have the same main peak location as the melt, the overall shape of the spectra acquired in analysis of the hydrothermal overgrowths is distinctive, with the

Figure 22 continued.
In false colour CL images hydrothermal overgrowths occur as the bright blue cement between the clasts. Epoxy appears as dark green to black regions that correlate with the black areas in the BSE-SEM images. Red arrows in the BSE-SEM images indicate the estimated locations of the faults prior to hydrothermal treatment. (A) – (B) False colour panchromatic CL and corresponding BSE-SEM image of extensively fractured region that has subsequently undergone significant healing. Note the absence of very fine-grained clasts. (C)-(D) False colour panchromatic CL and corresponding BSE-SEM image of an area of the fault that, in places in the BSE-SEM images, appears completely healed. Hydrothermal quartz forms deposits up to ~5μm thick around some grains. (E)-(F) False colour CL and BSE-SEM image of a melt welded region of the fault core that reveals both the formation of hydrothermal overgrowths and also the preservation of small patches of melt. (G) Panchromatic CL image showing the enlarged region indicated in E with the location of recorded spectral analyses detailed. (H)-(J) Representative spectra for the residual melt, hydrothermally precipitated quartz and undeformed quartz respectively. Areas of analysis are indicated in image G. Other recorded spectra are shown in Appendix 5.

notable absence of secondary peaks. The hydrothermal overgrowths are particularly sensitive to modification from the electron beam with a progressive decrease in emission intensity of the ~3.0eV peak from 50,000 counts to approximately 10,000 counts in the space of 1.5 minutes of continuous exposure.

The panchromatic images (Figs. 22A, C and E) reveal the absence of sub-micron sized gouge particles and the substantial cementation of the remaining gouge and fractured grains. Quartz cementation, and possibly compaction, has resulted in a reduction of fault-core porosity and the production of the extensively healed fault zone observed during BSE-SEM imaging. There is no evidence of interpenetration between particles forming the original gouge; rather clasts are observed to be mantled with quartz overgrowths that are uneven in thicknesses up to 5μm. In the false colour images overgrowths luminesce with a distinctive pale blue hue. The partially healed to fully healed microfractures are similarly illuminated during the CL imaging. TEM investigation undertaken by Giger *[2007]* suggests that the overgrowths are epitaxially accreted crystalline quartz with little apparent variation in the crystal structure between areas of original quartz and the overgrowths.

In a number of locations relict melt formed prior to hydrothermal treatment is preserved. The lenses of melt abut the quartz wall rock on one side and are separated from the fault zone on the other side by an approximately 2μm thick reaction zone of hydrothermal quartz. It is interpreted that the melt is preserved where fluid-melt interaction is hindered by a lack of fluid access; such as in Figures 22E-G. Interestingly, the melt layer in contact with pore fluids is primarily not dissolved and transported away from the site, but rather appears to potentially devitrify and crystallise *in situ* leading to the crescent shaped rim of hydrothermal quartz surrounding the residual melt. The CL spectra collected in the melt layer and quartz wall rock are typical of the emission spectra associated with each of these materials and described previously (Figs. 22H,J). The spectra from the reaction zone is dominated by the strong emissions centred at approximately 3.0eV (λ = 410nm), and lacks significant secondary peaks giving the same peak profile as the hydrothermal quartz (Fig. 22I).

3.4 3D Microstructural analysis using microcomputed X-ray tomography

Microcomputed X-ray tomography is a technique that allows the non-destructive

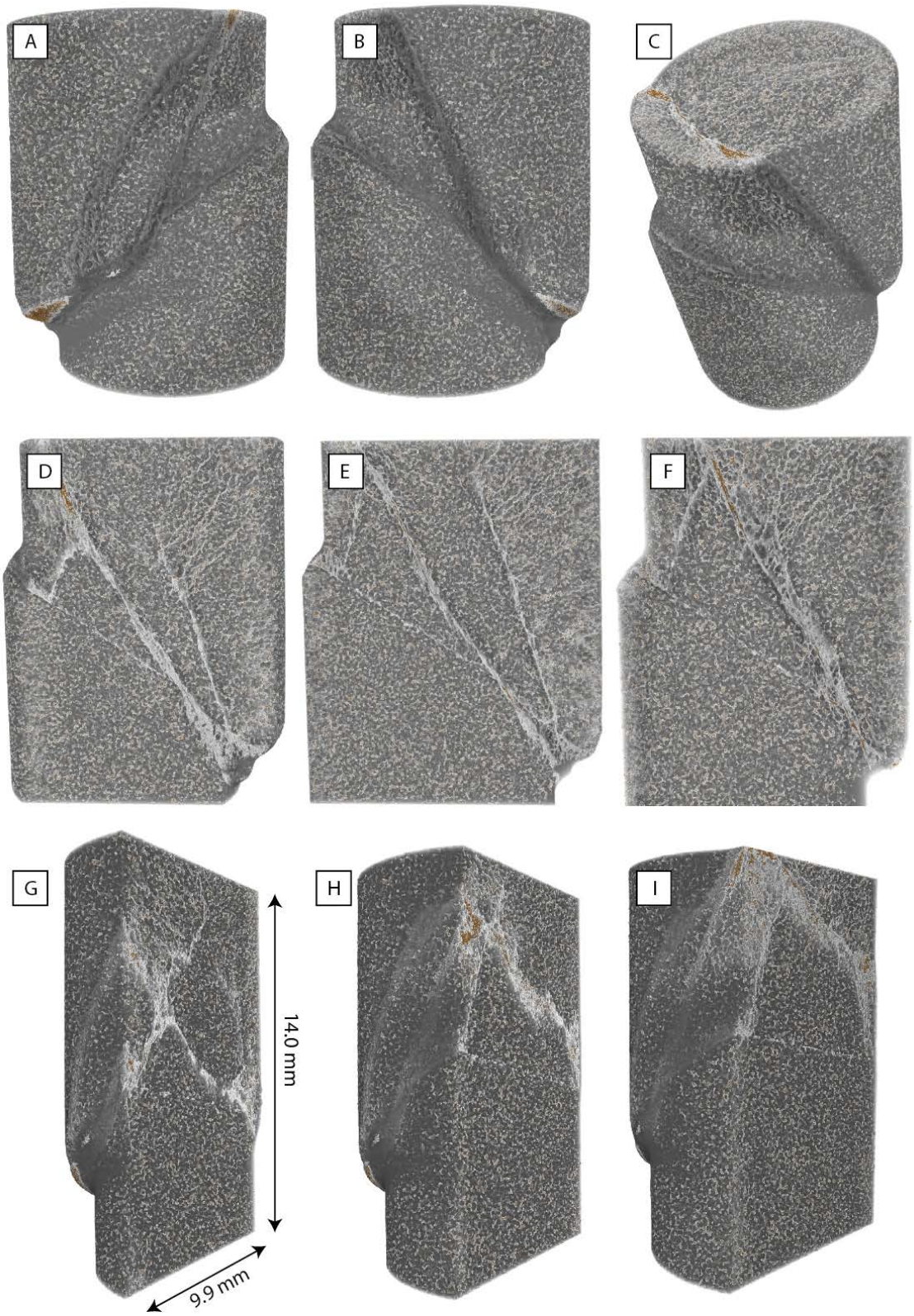

Figure 23: X-ray micro-tomography images and slices showing the 3-D structure of a full sample. Deformed specimen of experiment MIS031 was imaged using micro X-ray CT. Image has a resolution (voxel size) of approximately 5µm. (A)-(C) Show the exterior structure of the sample following deformation. (D)-(F) Slices made through the sample parallel to the slip direction. (G)-(I) Slices made perpendicular to the slip direction. Note that the change in intensity near the outer edges of the sample, giving the impression of radial fractures, are an artefact of beam hardening due to the sample being imaged inside its copper jacket.

imaging and investigation of internal features of an object in 3D. The simple, essentially single-phase mineral composition of Fontainebleau sandstone used during these experiments creates a bimodal X-ray attenuation distribution based on average density of any given volume or voxel, enabling the tomographic data to be separated into pore and mineral phases. In addition, the density contrast between the quartz grains and epoxy/air filled voids allows the identification of many fractures, enabling three-dimensional visualisation of damage associated with fault rupture. As part of the microstructural investigation of this suite of experiments, three samples were imaged using the microcomputed X-ray tomography method. MIS031 was imaged with a voxel size of ~5μm to provide a macroscopic view of the entire sample (due to beam hardening and end effects, the data presented in Figure 23 shows the full sample diameter for the length of the fault zone rather than the full sample), allowing spatial relationships between the pre-ground existing faults and newly developed fractures to be visualised (Fig. 23). 2D slices through the sample can also be taken at any orientation. Serial sectioning of the 3D dataset, via 2D slices reveal interconnectivity between the new fractures and the pre-existing fault plane that is not immediately apparent using two dimensional analytical methods such as BSE-SEM.

For the other two samples (MIS012 and MIS018), a smaller volume has been imaged at a higher resolution. A subset of the high-resolution data obtained from MIS018 with a voxel size of 1.5μm is shown in Figures 24 & 25. Individual voxel density information has been used to segment the dataset, allowing colours to be assigned to the different phases. By visualising only the pores and large aperture fractures, the damage zone on either side of the fault can be explored, revealing significant damage-zone asymmetry. The characteristic pore shape and geometry of the Fontainebleau sandstone is essentially undamaged on one side of the fault, whereas extensive fracturing increases porosity and modifies the pore structure on the other side (Fig. 24B &G).

A further subset of the tomography data for MIS018 was created to specifically investigate the fault zone and immediately adjacent grains (Fig. 25). Imaging only the damage network in this subset of data allows an inferred spatial distribution of the melt-welded areas on the fault surface to be quantified. This methodology assumes that, as the melt has the same atomic composition and similar density to quartz, the melt layer

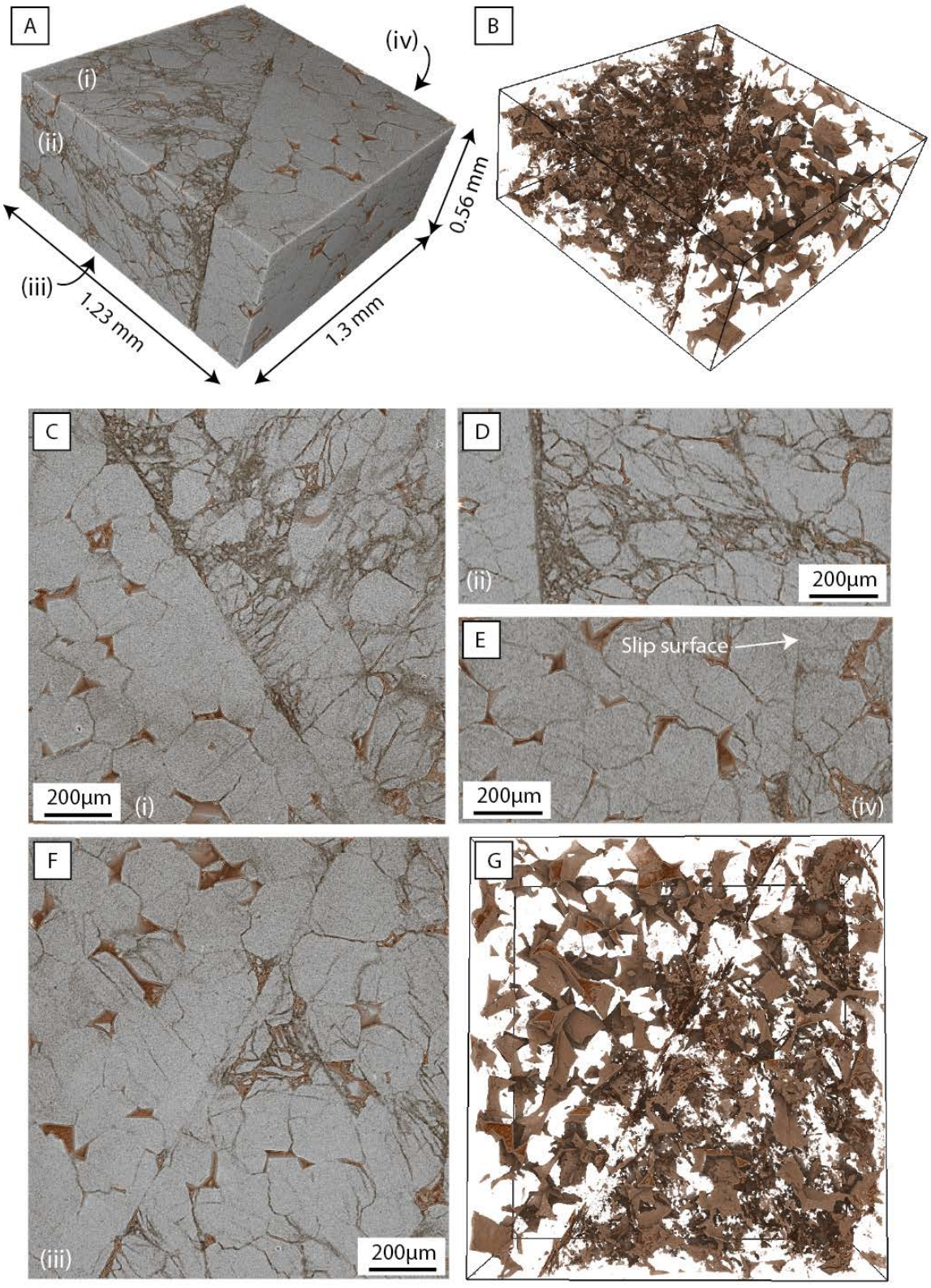

Figure 24: High-resolution X-ray tomography images showing the 3-D structure of a small volume. This sample is a subset of the high-resolution data obtained from MIS018 and has voxel size of 1.5µm. The tomography data has been assigned colours with quartz being shown by pale grey, fractures by dark grey and pores are in shades of brown. (A) A 3D image of a sub-set of data from MIS018 showing the unfavourably oriented fault. The different faces are indicated by Roman numerals and shown in 2D slices in images (C)-(F). Images (B) and (D) show the pore and large aperture fracture network produced during the deformation of the sample. Note the asymmetry in the damage formed on the different sides of the fault.

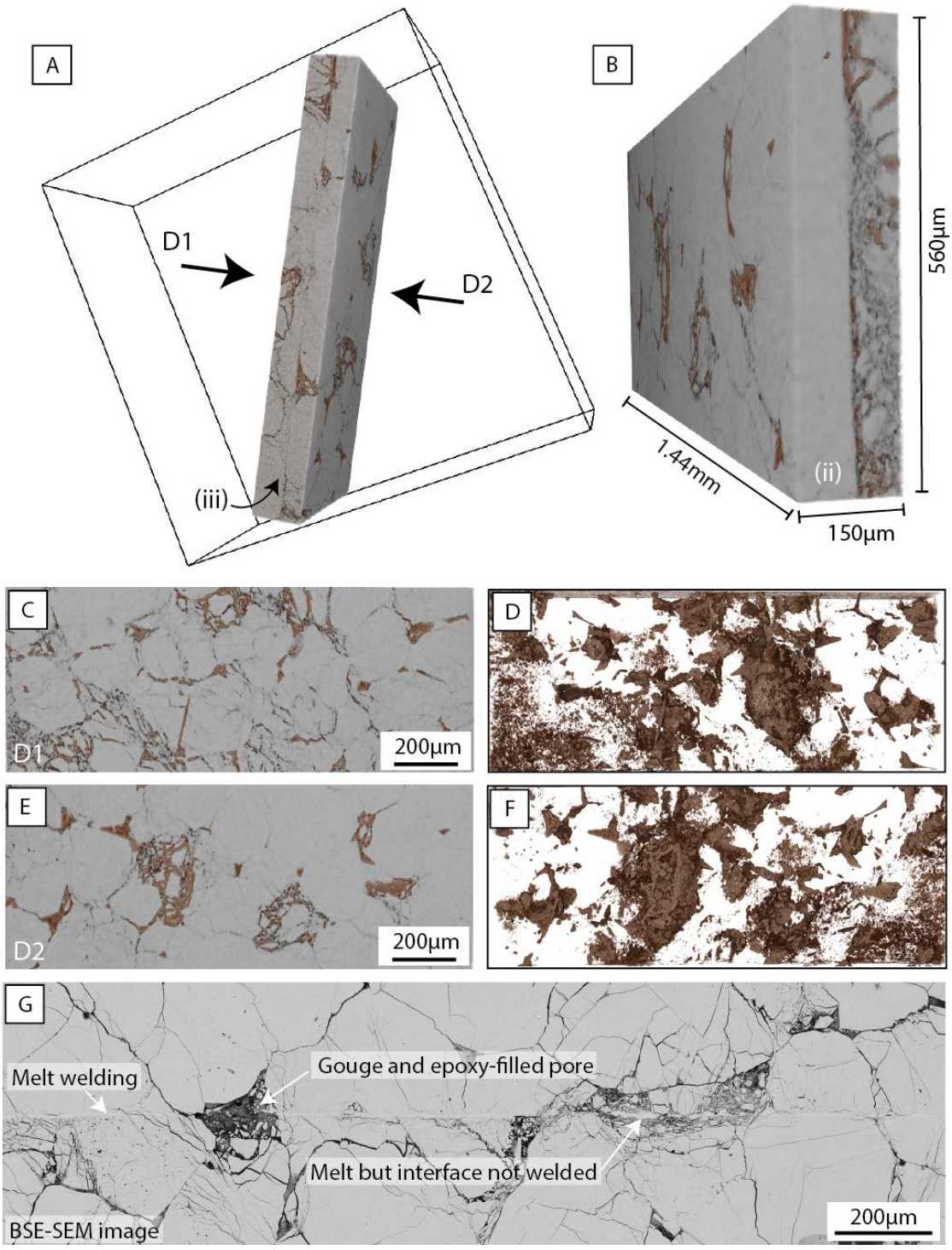

Figure 25: High-resolution X-ray tomography images of the fault zone.
Images are from a subset of the high-resolution data shown in Fig. 24 obtained from MIS018. (A-F) Shows the location of the sub-sample relative to the data set shown in Fig. 24. The tomography data focuses specifically on the fault zone and adjacent ~75µm of rock. The faces indicated by Roman numerals correlate with the faces defined in Figure 24. D1 and D2 refer to directions of viewing the fault that are orthogonal to the fault surface. Images looking in direction D1 are shown in C-D, while images looking in direction D2 are shown in images E-F. Figure (D) and (F) show the pore network and damage zones associated with images (C) and (E) respectively. As the quartz is transparent in images (D) and (F), the white zones represent areas where grain interfaces that are frictionally welded, producing continuous SiO_2 through the full depth of the imaged section. (G) A 2D BSE-SEM image mapped in the same sample (MIS018) showing the different morphology of the fault zone where there is a thin melt layer between grain contacts as opposed to grains adjacent to pores or damage zones.

will not significantly alter the attenuation of X-rays during scanning; this makes the melt-welded regions appear as continuous quartz. It follows that if the segmented data associated with the quartz is removed or made transparent during visualisation (Figs. 25D & F), any transparent region across the fault zone represents areas where the grain interfaces are frictionally welded, forming a continuous quartz - silica glass transect through the imaged section. The validity of this assumption is confirmed using BSE-SEM imaging of a region from the same sample (Fig. 25G) which shows melt-welding at every grain-to-grain interface. This method does, however, understate the volume of melt that is produced, especially were melt has formed and been displaced to a position adjacent to a pore space (e.g. highlighted region in Fig. 25G which shows melt adjacent to a damage zone).

Although there is likely to be significant variation in the extent of melt welding within the sample due to factors such as the formation of damage zones at the fault tip, the microcomputed tomography data allows quantification of the 3-D spatial extent of the melt. Analysis using the software package, Image J, indicates that approximately 48% of the fault shown in Figure 25 is melt-welded. This could have significant influence on the cohesive strength of the fault.

4. Discussion

The experiments described in this chapter have, for the first time, demonstrated the formation of semi-continuous frictional melt on essentially pure quartz fault interfaces that have slipped at room temperature and in both dry and water-saturated environments. The generation and subsequent quenching of sub-micron thick layers of melt has a significant influence on the ensuing mechanical behaviour and microstructural development of both the fault and its associated damage zone. These ideas will be considered and elaborated in the following section; discussion commences with a brief analysis of the recorded mechanical data and how it relates to Mohr-Coulomb failure theory.

4.1 Misoriented fault reactivation: A comparison with theoretical principles

While a detailed deliberation of the mechanics of fault reactivation is beyond the scope of this thesis, having been examined in depth elsewhere [*Jaeger*, 1959; *Sibson*, 1985,

1990b; *Hill and Thatcher*, 1992; *Jaeger et al.*, 2007], the following overview provides context for the discussion.

In the brittle regime, potential for fault reactivation, as opposed to fault initiation, can be assessed, to a first order, by comparing the parameters of cohesion and coefficient of friction between the fault zone and surrounding rock mass. Within the intact rock samples, conditions of failure can be defined by:

$$\tau_f = C + \mu\sigma_n' = C + \mu(\sigma_n - P_f) \qquad 1$$

where τ_f is the critical shear strength, C is the cohesive strength of the rock, μ is the coefficient of internal friction and σ_n' is effective normal stress given by $(\sigma_n - P_f)$, where is σ_n is normal stress and P_f is the pore fluid pressure, where present [*Hubbert and Rubey*, 1959]. In the case of re-shear along an existing cohesionless fault, failure strength is broadly defined by Amontons' law:

$$\tau = \mu_s\sigma_n' = \mu_s(\sigma_n - P_f) \qquad 2$$

where μ_s is the coefficient of static friction. These equations have been used to define a failure envelope for both the intact Fontainebleau sandstone and the pre-ground sliding surfaces (Fig. 25). A coefficient of internal friction of 1.17 is estimated for the intact rock failure of Fontainebleau sandstone; this value falls outside the typical range for most intact rocks ($0.5 < \mu < 1$) [*Hoek*, 1965; *Jaeger et al.*, 2007]. The cohesive strength of the intact rock is estimated to be ~81MPa based on the intersection point of the shear failure envelope with the y-axis. However, it is likely that, as confining pressure is reduced, the failure criterion deviates from the linear Coulomb relationship (see Appendix 5). Under laboratory conditions, maximum cohesive strength values for sandstones and granites have been estimated to between 20-30MPa [*Handin et al.*, 1963; *Jaeger et al.*, 2007] and possibly represent a more realistic strength approximation. A decrease in the cohesive strength of ~9MPa is observed for new faults forming after frictional lock-up. For the pre-ground sliding surfaces, the estimated coefficient of static friction is 0.54, assuming that these faults are cohesionless at the time slip. This value is lower than the experimentally-determined friction coefficients of *Byerlee* [1978] that indicate friction coefficients of sliding surfaces usually lie within the range $0.6 < \mu_s < 0.85$. However, the coefficient of static friction is consistent with findings of Cox [1998] for bare interface sliding experiments on the same material.

If it is assumed, for the current suite of experiments, that the existing fault plane contains the σ_2 axis, stress conditions for the reactivation of faults oriented at varying angles to the maximum principal stress, can be defined in terms of the ratio of the effective principal stresses as [*Sibson*, 1985]:

$$R = \frac{\sigma_1{}'}{\sigma_3{}'} = \frac{(1 + \mu_s cot\theta_r)}{(1 - \mu_s tan\theta_r)} \qquad 3$$

where R is the effective stress ratio, θ_r is reactivation angle defined as the angle of the fault relative to the orientation of the maximum principal stress. A fault can be defined as being optimally-oriented for reactivation (θ_{opt}) when R has a minimum positive value and is calculated by:

$$\theta_{opt} = 0.5tan^{-1}(1/\mu_s) \qquad 4$$

[*Sibson*, 1974]. As θ_r increases or decreases away from θ_{opt} the effective stress ratio increases (Fig. 26), ultimately approaching infinity and causing lock-up at $2\theta_{opt}$. In order to achieve fault reactivation under such conditions, either $\sigma_1' \rightarrow \infty$ or $\sigma_3' \rightarrow 0$, as $P_f \rightarrow \sigma_3$. Where $\theta_{opt} < \theta_r < 2\theta_{opt}$, faults are referred to as 'misoriented', whereas faults with orientations greater than $2\theta_{opt}$ is regarded as 'severely-misoriented'. For $\theta_r > 2\theta_{opt}$ reactivation can only be achieved if the effective minimum principal stress is tensile ($P_f > \sigma_3$) [*Sibson*, 1985, 1990a]. This analysis indicates that the optimal angle for fault reactivation for the current suite of experiments is ~31°, and that frictional lock-up should occur at ~62°. These estimates are consistent with the experimental observations that fault reactivation occurs for θ_r up to 60°, and that failure on a new optimally-oriented fault occurs for θ_r = 65°.

The current suite of experiments highlights the point that there can be major differences in the shear strength during intact rock failure and reactivation of an existing optimally-oriented fault. Although part of this difference is related to the high cohesive strength (~81MPa) of intact rock, an important result is that the coefficient of internal friction (~1.17) is substantially higher than the coefficient of static friction (~0.54) associated with fault reactivation. The resulting differences in shear strengths have a significant impact on the relative ease of reaction of misoriented faults versus nucleation of new intact rock failure.

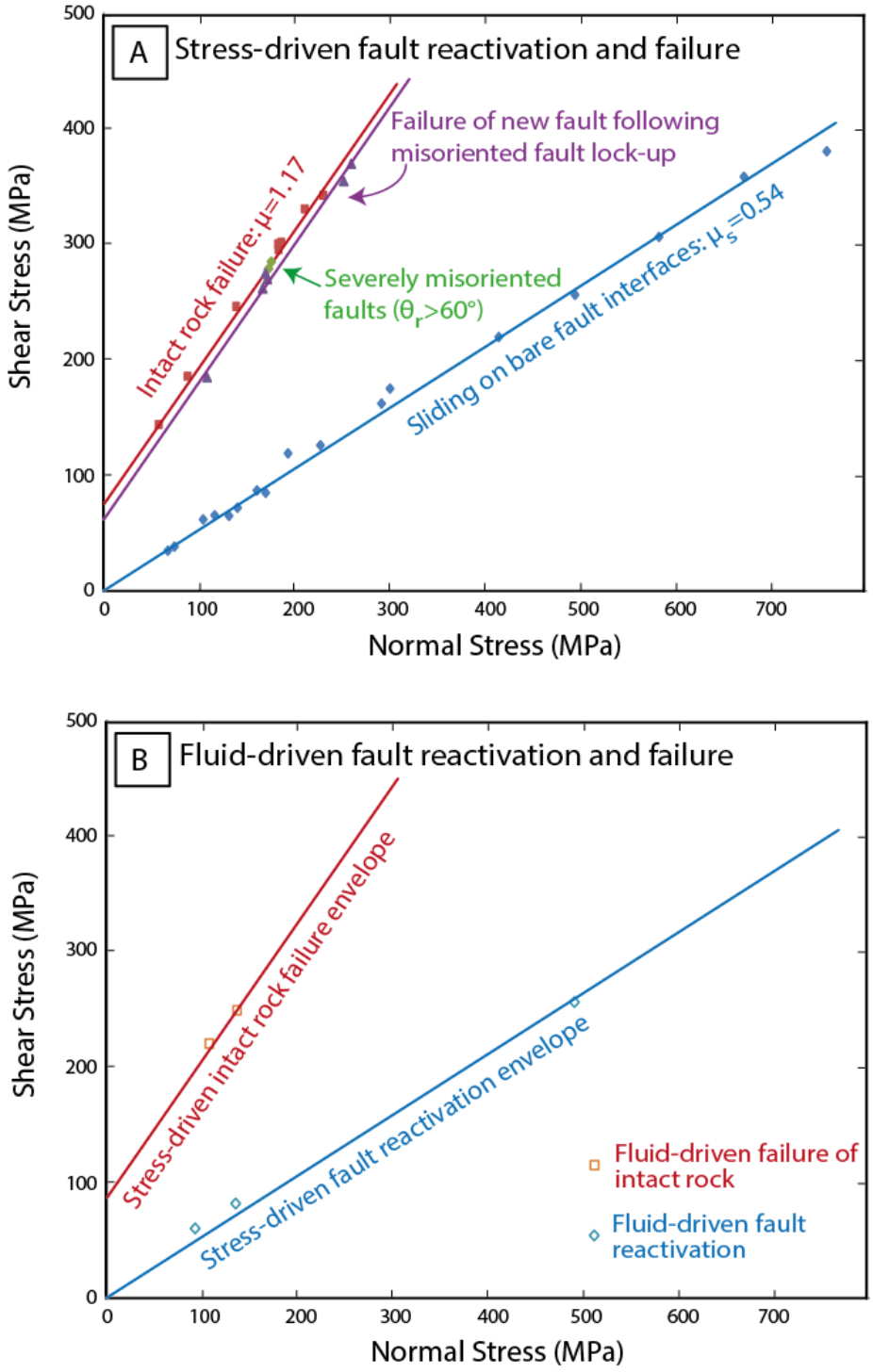

Figure 25: Failure envelopes and theoretical analysis of the mechanical results.
(A) Failure and reactivation envelopes for stress-driven deformation events. Data points represent shear and normal stress values at failure or fault reactivation. The slope of the associated failure/reactivation envelope (assuming a Mohr-Coulomb relationship) represents either the coefficient of internal friction for rock failure (1.17) or the coefficient of static friction for fault reactivation (0.54). The intercept of the envelope with the y-axis provides an indication of the cohesive strength of the sample. A second failure envelope is also shown for the data generated upon failure of the new optimally-oriented fault after lock up of the existing fault (indicated by the purple line). Normal stress and shear stress values of two severely misoriented (frictionally locked) faults are plotted in green. These points lie very close to the estimated failure envelope for intact rock. (B) Shear stress and normal stress data from the fluid-driven failure and fault reactivation experiments are plotted alongside the failure envelopes defined by the stress-driven failure/reactivation data. Note the good fit with the existing envelopes.

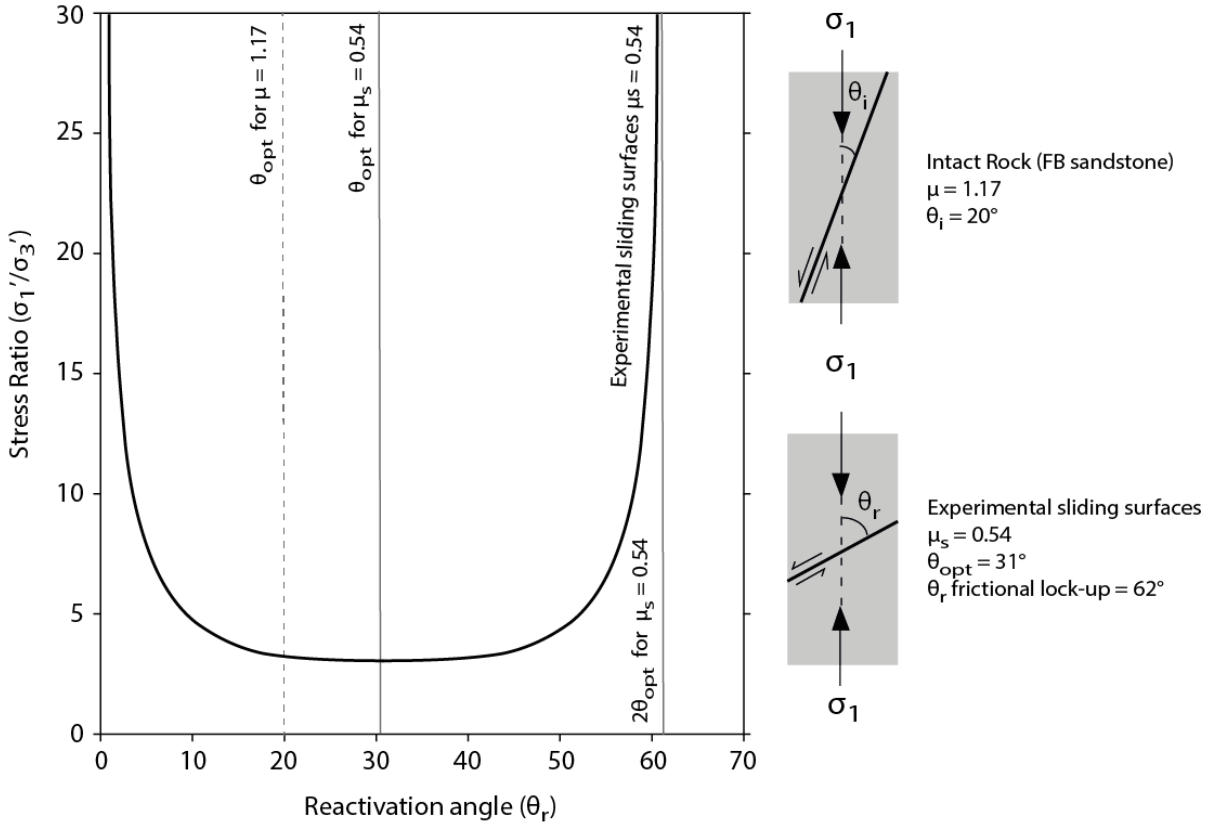

Figure 26: Conditions for the reactivation of existing faults.
The effective stress ratio for the reactivation of cohesionless faults plotted as function of the reactivation angle [after *Sibson*, 1985], for experimental sliding surfaces where μ_s = 0.54. The low frictional value of the experimental faults (compared with the typical range for experimental faults [*Byerlee*, 1978] increases the range of fault orientations that can theoretically be reactivated prior to frictional lock-up, encompassing experimental faults inclined from θ_r = 25-60º to the cylinder axis. The orientation of θ_{opt} is shown for both fault reactivation (solid line) and intact rock failure (dashed line). Schematic sample cross-sections show the orientation of the formation of new faults in intact rock where μ = 1.17 and the optimal and lock-up angles of faults where μ_s = 0.54.

4.2 Interpretation of microstructural processes

It has been shown, over a series of experiments with progressively increasing reactivation angles, that the mechanical behaviour of the interfaces evolves from aseismic creep, through increasing amplitude stick-slip, to ultimately frictional lock-up and the generation of a new optimally-oriented fault (Fig. 4). The varying mechanical behaviour is accompanied by changes in the development of microstructures at scales ranging from that of the macroscopic damage zone, down to structures developed on sub-micron scales within the fault core. Importantly, microstructural analysis shows the development of (1) highly damaged, possibly amorphous material within the fault core of aseismically-slipped faults and (2) the generation of frictional melt in faults ruptured during stick-slip events. The generation of pseudotachylyte on the fault surface has

significant effects on the strength and behaviour of the fault through a process termed 'melt-welding'. This process significantly contributes to the increase in damage observed along the slip zone.

In this section the key mechanical data and microstructural observations will be integrated to explore the physical processes controlling the reactivation of both favourably- and unfavourably-oriented faults. Due to the fundamental importance of amorphisation and, in particular the generation of frictional melt, on sample-scale behaviour including the development of damage zones, fault lock-up and the formation of new faults, these areas will be discussed first. Amorphisation and the development of frictional melt on nominally dry fault surfaces will be examined in terms of processes leading to their formation, conditions that influence the volume of melt produced, the timing of melting within the rupture, and the influence of the formation of melt on the development of fault damage. The second section then considers the significant microstructural differences between nominally dry and water-saturated experiments, including the formation of melt and other slip-related fault damage. The next section looks at the processes involved in the formation of new, optimally-oriented faults formed after frictional lock-up of misoriented faults; and the final section discusses the interpretation and implications of the high resolution cathodoluminescence investigations.

4.2.1 Amorphisation and the formation of frictional melt in nominally dry slip zones

Production of amorphous material within the fault core

During slip on both favourably- and unfavourably-oriented faults, increasing displacement is associated with increased fracture development and the formation of a variety of damage-related microstructures within the fault core. In this section, discussion will focus on the types and possible mechanisms resulting in the formation of amorphous material on the fault slip surfaces.

In experiments on favourably-oriented faults, slip behaviour is characterised by slip-hardening, aseismic sliding that results in the formation of lenses of highly damaged, low porosity material between and adjacent to, asperity contacts. This material has a lower porosity than the surrounding more granular gouge. In both BSE-SEM and SEM-CL imaging this material is distinct from both the adjacent wall rock and more typical

gouge. The CL spectra acquired within these regions is different from the quartz wall-rock and gouge, and has the same emission profile as the silica melt (see Section 4.3.4). Similarly, unfavourably-oriented faults (θ_r = 55º) halted prior to the onset of stick-slip contain < 1µm thick layers of low porosity material in which, sub-micron diameter clasts are set within an unresolvable, but lower electron intensity matrix. Based on (1) TEM observations made in Chapter 2 of morphologically similar damaged material, (2) CL observations, (3) close proximity of the damaged material to highly stressed contacts, and (4) heat generation estimations, it is suggested that this material may be partially mechanically amorphized. The aseismic sliding rates (axial displacement rate ~3.6µm.s^{-1}) during slip are insufficient to generate sufficient frictional heating to result in frictional melting. However, further TEM analysis on these samples will be required to test this hypothesis.

Increasing reactivation angle and slip displacement is accompanied by the onset of a stick-slip sliding regime. High slip velocities and large displacements during slip (up to ~500µm), are associated with the stick-slip behaviour. Simple thermal calculations (methodology outlined in Chapter 2) indicate that these slip events can result in the intense frictional heating of grain-to-grain contacts and the formation of frictional melt. If it is assumed that slip occurs at velocities > 0.15m.s^{-1}, and that the maximum asperity size is equivalent to the total slip displacement, the increase in asperity temperature is estimated to exceed the non-equilibrium temperature of fusion for quartz (~1500°C [*Navrotsky*, 1994] – see Appendix 5) within the duration of the slip event.

The glass produced by frictional melting exhibits microstructurally distinct textures such as elongate vesicles and rare ribbon-like filaments that were confirmed as being characteristic of glass in Chapter 2 using TEM diffraction patterns. The frictional melt varies in morphology from small isolated clast-rich zones of melt at asperity contacts to semi-continuous essentially clast-free regions of melt located between opposing grain interfaces across the slip surface. Where melt layers have been translated to a position adjacent a pore or void, the glass is generally observed to have a planar surface that is essentially free of incorporated grains and crystalline fragments. Within many samples the melt layer grades into an increasingly clast-rich zone that forms areas of melt-indurated gouge. The differences in clast abundance across the melt layers possibly provides an indication of melt temperatures [*O'Hara*, 2001], with highest temperatures

being associated with regions of few clasts and likely to be at, or close to, the melt generation surface.

During some experiments the amplitude of co-seismic stress drop increases with successive slip events (e.g., MIS003, where $\theta_r = 50^o$ where co-seismic shear stress drop increases from 82MPa to 164MPa), even though there is minimal change in differential stress at the initiation of each stick-slip event. This could result either from (1) an increase in the splay-like secondary fault traces leading to an increased area of fault slip being accommodated on more favourably-oriented fault segments, or (2) progressive changes in fault zone microstructure leading to more effective slip weakening. Microstructural analysis of the fault surfaces at various displacements indicates that the most efficient melt generation occurs during the first slip event on the essentially undamaged fault surfaces (e.g. see MIS037 in Fig. 13). This raises the possibly that a highly viscous melt may actually hinder fault slip during the first slip event by acting as a viscous brake [*Fialko and Khazan*, 2005]. During subsequent slip events, the activation of other, more efficient weakening mechanisms, or smaller volumes of melt, may increase the slip distance.

Conditions that influence the volume of melt produced and implications for fault weakening

Quenched frictional-melt or glass forms within the slip zone of many of the samples in the current suite of experiments. The volume of melt produced during the experiments can be related to (1) the processes of fault development (i.e., the contrast between melt development in samples that contain a pre-existing fault surface but are frictionally-locked and pristine samples of intact rock), (2) the fault reactivation angle (in samples with pre-existing faults), (3) the confining pressure and (4) the net displacement and displacement rate during the rapid slip events. Essentially, the generation of frictional melt correlates with increasing normal stresses and activation of rapid slip events.

One of the main differences between the fault-core microstructures of newly-formed faults (either resulting from intact rock failure or rupture following existing fault lock-up) are the relative volumes of frictional melt formed during rupture. During intact rock failure, frictional melt is not abundant, with only 2 to 3 examples per sample. It typically forms either relict cohesive zones of melt-indurated gouge within an otherwise fine-grained incohesive layer, or develops at locations where grain impingement has

resulted in inferred high local stress concentrations. In contrast, larger quantities of melt are generated during the failure of new, optimally-oriented faults after lock-up of pre-existing misoriented faults. The melt zones are up to 1mm in length and 20μm wide. The differential stress supported by the different sample types (intact versus frictionally-locked) are approximately equal prior to failure; accordingly, the significant differences in melt volume are attributed to differences in rupture style. During intact rock failure experiments, fault propagation occurs approximately co-seismically, as shown by accompanying sample dilation and coseismic pore fluid pressure drop. However, where a new optimally-oriented fault forms after frictional lock-up of a pre-existing fault, the new fault largely develops more slowly (over a period of >10 seconds) prior to its rupture. Fault generation and possible differences in energy expenditure between the two modes of fault development are discussed in greater detail in Section 4.2.3.

During reactivation experiments, melt forms on every fault interface that has experienced rapid slip with co-seismic stress drops > ~60MPa. At more favourable reactivation angles (i.e. $\theta_r \leq 40^o$) and low confining pressures (P_c = 50MPa), the development of melt is sporadic, with discontinuous regions of melt forming mainly at asperity contacts. With increasing misorientation, the increasing displacement associated with stick-slip events is accompanied by an increasing volume of melt generated during slip. Sliding surfaces begin to develop a continuous layer of melt between the two surfaces resulting in localised fault welding. At reactivation angles $\theta_r \geq 55^o$, every grain-to-grain contact is separated by a layer of glass; this results in melt-welding of potentially in excess of 50% of the total fault surface. These melt-welded grain contacts form continuous glass-filled layers between the two fault surfaces over distances of approximately 1mm.

To understand implications of the changes in melt volume in terms of possible weakening and/or strengthening behaviour, especially in the context of previous high-velocity friction experiments, it would be useful to constrain melt volume observations of the current suite of experiments in terms of the existing terminology of ‘flash heating’ and ‘continuous melting’. ‘Flash heating’ was a concept introduced to the fault mechanics field by *Rice* [1999] to describe highly localised frictional heating of stressed asperity contacts, resulting in thermal-induced changes to the frictional properties of the micro-asperities. However, despite a number of experimental studies claiming to have induced fault weakening through flash heating [*Hirose and Shimamoto*, 2005b; *Han et*

al., 2007; *Goldsby and Tullis*, 2011], the meaning of this term, including factors such as the dimensions of the asperities, remain poorly-defined in a geological context.

Goldsby and Tullis [2011] undertook high-velocity friction experiments on a number of crustal silicate rocks in which significant reductions in friction coefficients were observed. Friction coefficients decreased from ~0.6 to 0.1-0.2 with increasing displacement. The remarkable weakening was attributed to flash heating of microscopic asperity contacts. However, limited microstructural work meant that the physical manifestation of this flash heating remained unexplored, including whether or not flash heating resulted in localised melting of asperity tips. A number of other experimental studies [e.g., *Hirose and Shimamoto*, 2005b; *Di Toro et al.*, 2006a] have shown two stages of fault weakening during the onset of frictional melting. The first stage of weakening is typically ascribed to flash heating of micro-asperity contacts, whereas the second stage is thought to relate to the development of a continuous melt layer. However, a microstructural examination of experiments halted during the initial phase of weakening demonstrated the formation of melt patches approximately 110-160μm in diameter, about 7-10μm thick and occupying up to 10% of the fault area [*Hirose and Shimamoto*, 2005b]. The authors suggest that the formation of well-defined melt patches at this point indicates that melting must have proceeded beyond flash heating.

Consequently, while flash heating has been explored theoretically and numerically [*Rice*, 1999; *Rempel*, 2006; *Beeler et al.*, 2008], and is supported by the mechanical data from high velocity experiments [*Goldsby and Tullis*, 2011], the physical processes remain enigmatic, due largely to the difficulty, until now, of recovering fault surfaces that have experienced low displacement and high velocity slip [*Niemeijer et al.*, 2012]. The current experiments highlight both the relevance of conventional experiments in understanding incipient slip processes and also the need for detailed high spatial resolution analytical and imaging work to be undertaken alongside the mechanical observations.

Timing relationships between the formation of gouge and frictional melt

The relative timing of the formation of frictional melt compared with other slip-related microstructures has implications for understanding dynamic processes during fault rupture, including (1) the mechanisms by which melt forms, (2) the timing of high velocity slip and (3) mechanisms of fault weakening and strengthening. The close

spatial association of gouge and pseudotachylytes in both experimental [*Spray*, 1995] and natural fault zones [e.g. *Di Toro and Pennacchioni*, 2005], has led to the view that cataclasis could be a precursor to frictional melting. However, the microstructures formed during the current suite of experiments indicate that the relationship between frictional melting and the formation of gouge particles may be complex with cycles of frictional melting, quenching and gouge formation occurring multiple times within even a single slip event.

Fault zones formed during intact rock failure, or following frictional lock-up of a pre-existing fault surface, have complex structures. These include the presence of multiple fault strands, overprinting Riedel shears, and the development of glass. Microstructural examination of the fault zones indicates that many zones of frictional melt may have formed early during fault development on an initially uneven rupture surface. Slip on the uneven surface is energetically inefficient and the potential weakening effects of melt generation would be short-lived once heat production stopped. It is suggested that strengthening of quenching melt resulted in the transfer of slip to elsewhere in the fault core, thereby resulting in the subsequent formation of brittle shear bands. The overprinting hierarchy of Riedel shears represents a progressive change in slip localisation during rupture [*Logan et al.*, 1992]. However, in other locations, both the lack of significant deformation of the melt layer, relative to the surrounding fault core, and the formation of glass-indurated gouge zones suggests (1) simultaneous formation melt and gouge, and/or (2) melt development late in the slip event as a result of slip localisation within a well-developed gouge layer.

For fault reactivation experiments, in many locations the wall rock adjacent to melt-weld sites is extensively fractured and in some cases pulverised; this has resulted in the formation of fragmented grains, many of which show little evidence of rotation or displacement and are essentially *in situ*. It has been suggested previously that zones of fine-grained gouge could be the result of implosion brecciation [*Sibson*, 1986] or cyclic loading and unloading of normal stress across the fault during earthquakes [*Brune*, 2001]. The large pore spaces in the Fontainebleau sandstone make cyclic loading and unloading feasible for slip events > 50-100μm, on the initially planar pre-existing slip surface. In terms of understanding a deformation sequence, it does not appear likely to be able generate a dense melt layer adjacent to an incohesive and usually highly porous gouge layer. Accordingly, it is suggested that in some situations frictional melting

occurs prior to the formation of gouge. In experiments halted after a single slip event, microstructures are dominated by the presence of frictional melt, with little evidence of fracturing or gouge formation. Further, the scarcity, and at times, absence of clasts within the melt-welded layer of reactivated unfavourably-oriented faults also supports the possibility that cataclastic processes are not always a precursor to frictional melting.

In other locations there is ample evidence of the occurrence of numerous quartz clasts within the melt layer. These clasts could be incorporated either as a result of (1) the melting of a gouge rich-layer, or (2) the passive assimilation of clasts into the melt layer through fracturing and melt invasion of the wall rock during melt formation. As mentioned previously, the differences in clast abundance across the melt layers may provide an indication of melt temperatures [*O'Hara*, 2001] and the location of the melt generation surface. Numerous examples of banded melt textures indicate that, even during single slip events, multiple generations of melt can occur. It is suggested during slip, melt forms at asperity contacts, quenches as the asperities move past each other, and then melt again as new asperities come into contact. Accordingly, banding of melt may not be a reliable indicator of multiple slip events.

Influence of melt generation on the formation of the fault damage zone

The development of fault damage zones potentially has a significant role in the mechanical evolution of a fault zone by influencing the near-field stress orientations [*Faulkner et al.*, 2006], altering fluid distribution by creating conduits, barriers or directionality in flow paths [*Caine et al.*, 1996], and by altering fault strength through modifying the fault structure [*Biegel and Sammis*, 2004; *Mitchell and Faulkner*, 2009]. Therefore, an important aspect of understanding fault development and reactivation is identifying the processes that contribute to the mechanical and microstructural evolution of fault damage zones. In the current suite of experiments the development of the low-displacement fault damage zone adjacent to the principal slip surface has, for the first time, been integrally linked to the generation of frictional melt on the fault surfaces (Fig. 27).

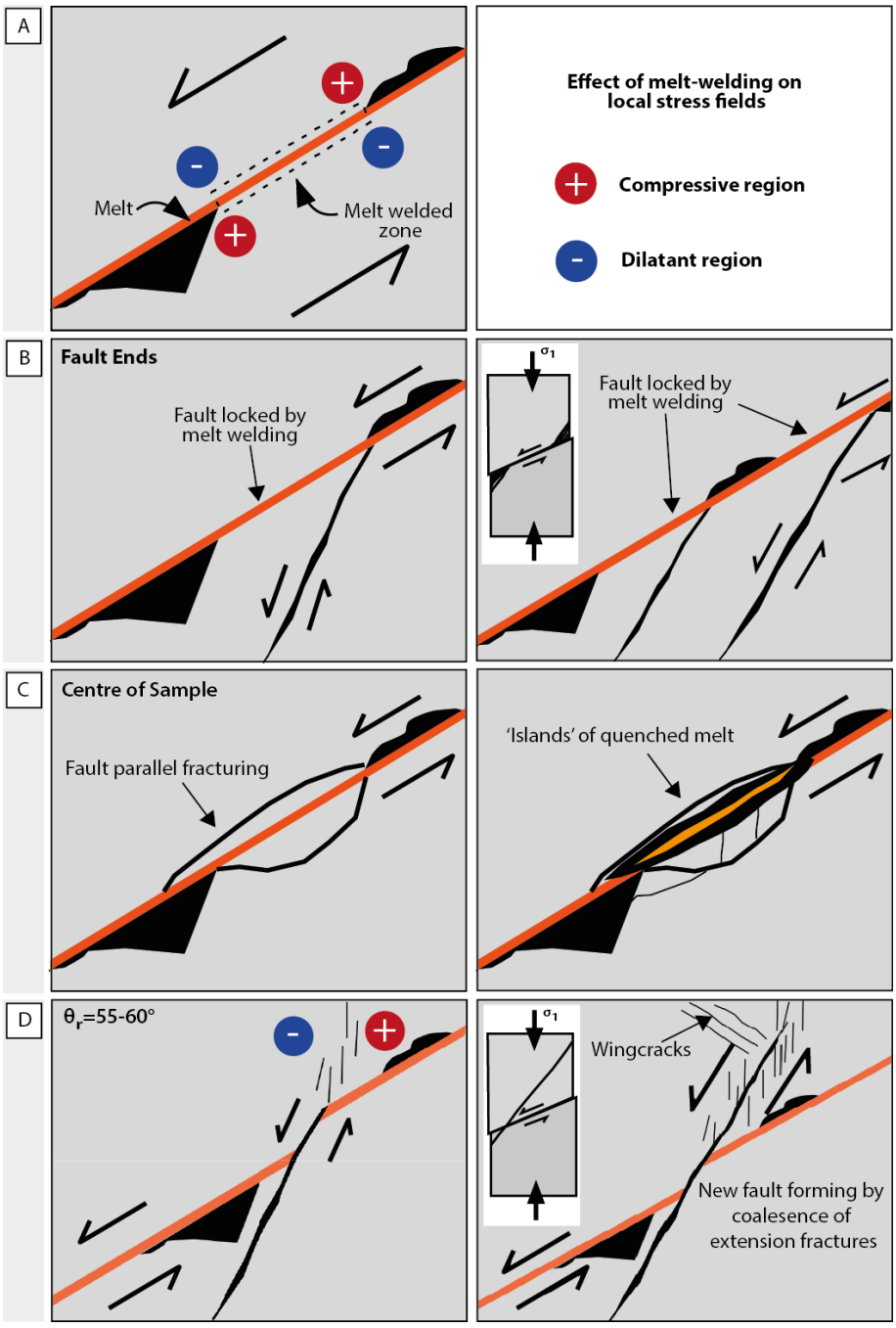

Figure 27: The role of melt-welding in the formation of damage and the development of new faults. (A) A schematic illustration showing a melt welded fault interface. Melt is indicated by the orange layer, pores adjacent to the slip surface are indicated as the black voids and the Fontainebleau sandstone fault blocks are indicated in grey. If the fault zone is subjected to continued loading, the red circles indicate areas of high compressive stress concentration whereas the blue circles indicate regions of dilatant stress. (B) During continued loading, fractures form from dilatant areas. In areas close to the fault tip, these fractures form the splay-like secondary fault traces. Fault movement is accommodated on the new fault traces. Continued reactivation of the existing fault results in additional melt welding and new secondary fault traces forming replacing the first. (C) Towards the centre of the sample, fracturing associated with melt-welding forms parallel with the misoriented fault zone. Ultimately the melt-welded core is isolated from the fault surfaces forming an 'island' of quenched melt. (D) On faults where $\theta_r \geq 55^{\circ}$, a new fault trace develops from a melt-welded zone via the coalescence of extension fractures. Before the fault has propagated through the whole sample, strain is being accommodated on the fault. This in turn, changes the stress concentrations at the fault tip and results in the development of wing fractures at a high angle to the developing fault surface.

At the sample-scale, fault damage associated with the reactivation of misoriented faults, is characterised by the formation of triangular zones of intense fracturing that develop asymmetrically near the fault ends (see inset, Fig. 27B). The location of these damage zones is consistent with areas of dilation associated with fault slip. In this section, the role that melt-welding plays in the development of these damage zones will be discussed in more depth, commencing with insights about the role that increasing displacement has on the microstructural evolution of the damage zone.

Very little fault damage occurs until after the first stick-slip event (e.g., Fig. 11). At this early stage of fault zone development, off-fault damage is limited to a small number of intergranular fractures at the fault tips and minor fracturing within the grains immediately adjacent to the slip zone (e.g., Figs. 11 & 14). However, at the end of the first major slip event, many samples show the development of frictional melt within the fault core, which commonly welds localised segments of the fault. If the fault is subjected to continued loading, these melt-welded areas can modify local stress-fields, resulting in the concentration of compressive and dilatant stresses (Fig. 27A). Fractures begin to form from the dilatant regions [*Chester and Chester*, 2000]. In areas close to the fault tip, these fractures nucleate at a more favourable orientation, forming the splay-like secondary fault traces (Figs. 27B, 15A). Subsequent fault slip is more readily accommodated on the new fractures rather than the melt-welded, pre-existing slip surface. However, with repeated reactivation, additional melt welding occurs at the junction between the existing misoriented fault and the new fault splay, resulting in stress concentrations and the formation of new fractures. The first fracture is deactivated as slip is transferred onto the new fracture, resulting in the development of a series of en echelon slip zones at the fault ends and the progressive decrease in slip on the unfavourably oriented fault segment. Continued deformation at the fault ends leads to the development of largely incohesive zones in the dilatant regions at the fault ends. The process of developing fault-end splays nucleating from melt-welded zones is more prevalent in samples slipped at lower confining pressures (P_c = 50MPa).

Towards the centre of the sample, fracturing associated with melt-welding forms sub-parallel with the misoriented fault zone, by-passing the melt zone and forming a series of fractures at a high angle to the sample shortening direction (Fig. 27C). *Chester and Chester* [2000] showed that locally inhomogeneous stress states along faults can result from variations in fault plane geometry leading to the formation of fractures that locally

range in orientation from parallel to perpendicular to the fault plane. It is suggested that melt-welded zones form 'rheological' asperities that may have a similar effect on local stress states as the geometric asperities formed by varying fault topography.

Many fault-parallel fractures also form asymmetrically around the fault core with extensive damage on one side of the fault and essentially no damage on the other (Figs. 10C, E, 16B, C). Ultimately, after multiple stick-slip events the melt-welded core is isolated from the fault surfaces, forming an undeformed 'island' of quenched melt (Figs. 27C, 13D) and resulting in the progressive widening of the fault core [cf. *Spray*, 1992]. Damage is interpreted to form preferentially on the dilatant side of the fault.

In fault zones where $\theta_r \geq 55^o$, a new, optimally-oriented fault trace nucleates from a melt-welded zone of the misoriented fault through the growth and coalescence of extension fractures [cf. *Anderson*, 1942; *Wilson et al.*, 2003; *Mitchell and Faulkner*, 2009]. These fractures form approximately parallel with the axial shortening direction (Fig. 27D). However, before the fault has propagated through the whole sample, significant strain is accommodated on the fault (e.g., MIS018, Fig. 11E). Constraints imposed on the sample by the assembly geometry result in slip preferentially occurring through translation of the newly forming hangingwall, causing a change in the stress concentrations at the fault tip and the formation of wing fractures at a high angle to the developing fault surface (Fig. 27D).

4.2.2 Formation of damage and frictional melting in a water-saturated environment

One of the key microstructural observations made during this suite of experiments is the difference in the fault-related microstructures between bare interfaces reactivated under dry conditions and those reactivated under water-saturated conditions (either wet stress-driven failure or fluid-driven failure). Although the mechanical data shows comparable shear strength and frictional values immediately prior to failure for both wet and dry stress-driven experiments (MIS022 and MIS012) at the same effective confining pressures, very little wear-related damage occurs on the fault surfaces reactivated in wet conditions. Faults slipped in nominally dry conditions show the formation of high displacement damage such as gouge and splay-like secondary fault traces. In contrast, the saturated faults reactivated under equivalent experimental conditions show no evidence of damage on the slip surface where $\theta_r \leq 50^o$. At a high angle of misorientation ($\theta_r \geq 55^o$), fault damage adjacent to the slip zone mostly consists of low displacement

damage such as extension fractures related to Hertzian loading, and fracturing associated with stress concentrations at the tips of melt-welded zones (see Section 4.2.1).

The relationship between the formation of low displacement damage zones (and related porosity development) and the development of frictional melt in water-saturated is clearly shown in Figure 28. In this graph the temporal evolution of pore volume is shown over the course of an experiment where increases in pore fluid pressure were used to repeatedly induce failure. The pore volume of the sample initially decreased slightly, possibly representing crack closure, before increasing approximately linearly until ~1800 seconds. Up to this point, slip is characterised by regular small displacement stick-slip events. At ~1800 seconds, the size of the slip event increases markedly and is thought to be associated with the first melt-welding slip event. This

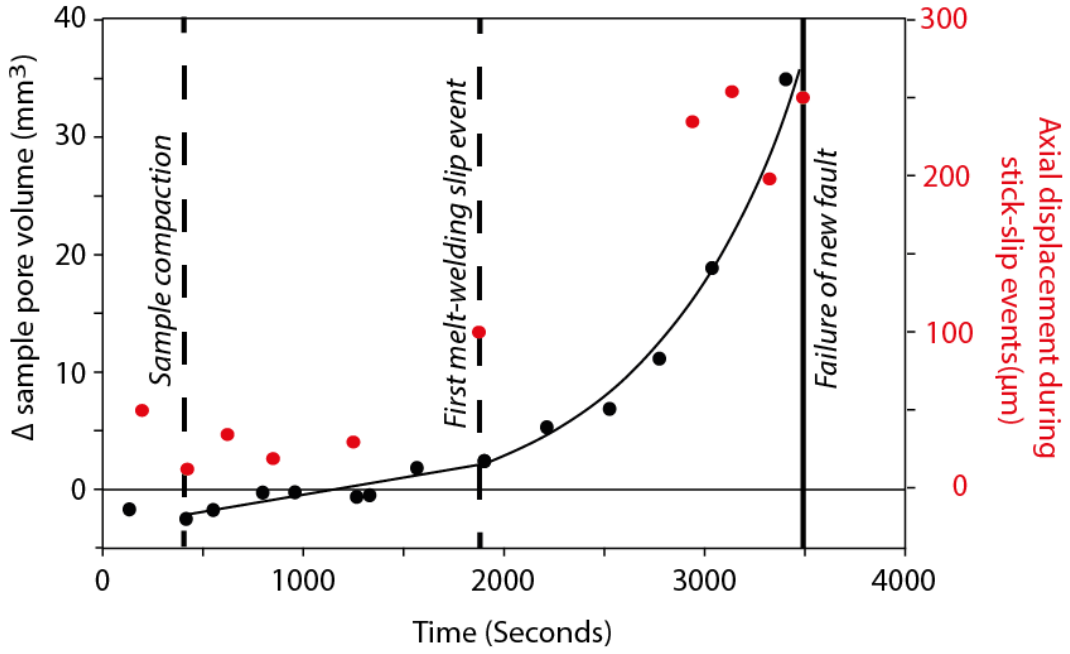

Figure 28: Correlation between change in pore volume, displacement during rapid slip events and damage formation in fluid-driven failure experiment (MIS041).
Black data points represent the change in the pore volume of the sample relative an initial baseline; red data points show the temporal evolution of the axial displacement during rapid slip events, including the estimated onset of melt welding. Pore volume initially decreases slightly, possibly representing crack closure, before increasing approximately linearly until ~1800 seconds and is accompanied by regular small displacement slip events. The first melt-welding slip event has a larger displacement than preceding events. Subsequently the pore volume increases exponentially prior to the failure of the new, more favourably-oriented fault.

supposition is supported by the difficultly that was subsequently encountered in trying to achieve reactivation, indicating the probable influence of melt welding on the cohesive strength of the fault surface. In the period following initial melt welding, fluid-pressure was repeatedly cycled in an attempt to induce failure. During this period, the pore volume was found to increase exponentially prior to the failure of the new, more favourably-oriented fault.

The presence of pore fluids within a fault zone has commonly been cited as a reason for the apparent scarcity of pseudotachylytes in natural fault zones [e.g., *Sibson and Toy*, 2006]. It has been proposed that thermal pressurisation effects could be sufficient to reduce the effective normal stress to a level where frictional melting cannot be achieved [*Spray*, 1992]. Further experimental exploration of these ideas has been hampered by technical limitations of the high-velocity shear apparatus, which to date, has not allow the testing of materials in a high pore fluid pressure regime. However, experiments undertaken during this present study have conclusively demonstrated the formation of frictional melt on unfavourably-oriented, water saturated faults, with effective confining pressures $\geq$ 15MPa. In the following section, a potential mechanism to explain both observations of minimal fault damage and the generation of frictional melt in water saturated environments will be explored. It will be shown that these two seemingly incompatible processes could in fact be integrally linked through a process of fluid lubrication.

The absence of wear-induced damage along the slip surfaces of faults activated in high fluid pressure environments indicates that the pore-fluid has a more complicated effect on the sample interface than merely reducing the effective normal stress. One possible explanation for the differences in observed damage between saturated and dry faults, is that the interstitial fluids between asperity contacts may act as an elastohydrodynamic or boundary lubricant (Fig. 29) [*Hamrock et al.*, 1994; *Brodsky and Kanamori*, 2001]. The concepts of elastohydrodynamic and boundary lubrication arise from engineering studies of friction in bearings and gear assemblies. If a pore fluid is present in a slip interface, as the displacement and velocity of slip increase, the viscous fluid between fault surfaces resists motion forming a localised high pressure gradient [*Brodsky and Kanamori*, 2001]. The increased pressure reduces friction and elastically deforms the fault surface, dilating the two sliding surfaces. If the increase in fault aperture and the thickness of the lubricating film are greater than the surface roughness, there is no

asperity contact and no damage (Fig. 29D) [*Brodsky and Kanamori*, 2001]. Further, as there is no asperity contact there can be no frictional heating or the formation of frictional melt. However, elastohydrodynamic lubrication is sensitive to the viscous properties of the interstitial fluid, ambient pore-fluid pressures and the normal stress acting on asperity contacts [*Johnson et al.*, 1971]. At high normal stresses, the lubricant layer is reduced to a film only a few molecules thick, or even a molecular monolayer with very different properties from the bulk fluid [*Allen and Drauglis*, 1969]. In such situations the lubrication regime shifts from being dominantly elastohydrodynamic through to being ultimately a boundary lubricant where the lubricating properties are controlled by the molecular interactions between the fluid film and fault surface (Fig. 29A, C).

The effectiveness of water as a boundary lubricant is affected by molecular-scale silica-water interactions [*Lasaga and Gibbs*, 1990] that control whether the hydrated fault surface will act as a lubricant. In a boundary lubrication regime there is extensive asperity contact, with the fault load being essentially supported by asperity contacts. Because the two sides of the fault asperities are separated only by the molecular-scale layer, the boundary lubricant is not as effective at reducing either friction or preventing wear as elastohydrodynamic lubricants. It has been suggested that the frictional properties of the fault in a boundary lubrication regime can even be comparable to those of solid-solid interfaces [*Brodsky and Kanamori*, 2001]. With the prevalence of asperities under high normal stress, frictional heating does occur, potentially resulting in frictional melting of asperity contacts.

Although aspects of elastohydrodynamic lubrication share similarities with the principle of thermal pressurisation [*Sibson*, 1973], elastohydrodynamic and boundary lubrication potentially provide a better mechanical solution for the observed microstructural changes. Thermal pressurisation is a process arising from a discrepancy between thermal expansion of the bulk pore fluid and fault rock during frictional heating [*Ghabezloo and Sulem*, 2009]. If the hydraulic diffusivity of a porous or damaged fault zone is sufficiently high that thermally pressurised fluids can escape efficiently from the pressurized slip zone, then fault strength is maintained, and favours the onset of frictional melting [*Rempel and Rice*, 2006]. Although in the current suite of experiments, the Fontainebleau sandstone is a macroscopically porous medium, microscale hydraulic diffusivity at grain-to-grain interfaces is potentially very low.

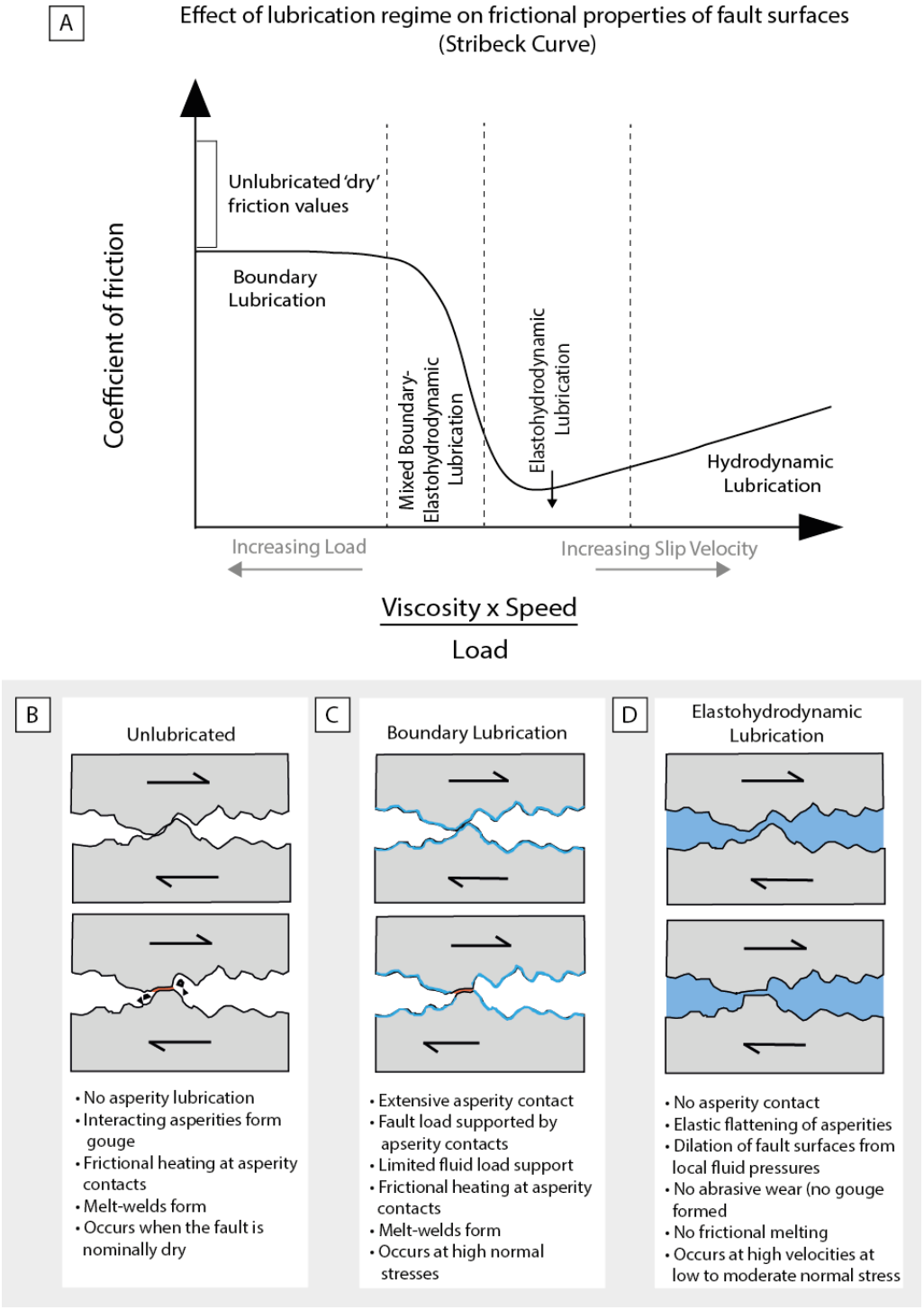

Figure 29: Elastohydrodynamic and boundary lubrication: its effect on the formation of fault gouge and frictional melt.
(A) Schematic illustration of influence of viscosity, speed and load on the lubrication regime and ensuing coefficient of friction. (B) Unlubricated or nominally dry samples are characterised as having a higher coefficient of friction in A and asperity interactions lead to the formation of gouge and/or frictional melting. (C) Boundary lubrication occurs at high normal stresses and low speeds and is indicated as having a high coefficient of friction in A, although not as high as an unlubricated fault. Boundary lubrication is thought to potentially hinder the formation of gouge, but frictional heating at highly stressed asperity contacts could still result in frictional melting. (D) Elastohydrodynamic lubrication occurs at increasing speeds where normal stress is not sufficient cause asperities to penetrate the lubricating film. It results in low frictional values (A) and as asperities are not in direct contact, there is no abrasive wear or gouge formed.

During a fault rupture where slip times are estimated to be < 10ms, the ability of a pressurised interstitial pore fluid to escape along a grain-to-grain interface is questioned. Although aspects of thermal pressurisation almost certainly play a role in the fluid lubrication process, especially in the mixed boundary – elastohydrodynamic lubrication and boundary lubrication regimes where asperity contact occurs (Fig. 29A), this mechanism fails to capture the subtleties of the nano- and molecular scale fluid-rock interactions. Even in a relatively simple quartz-water system, there are complexities in both the physics and chemistry of water-rock interaction that are driven by the extreme dynamic stress and temperature conditions at the fault interface. These include the adsorption of water onto the interface at stressed Si-O bonds, the formation of silica gels on the grain surfaces, and potential interactions between protruding polysilicic acid groups [*Revil*, 2001], all of which could influence the mechanical behaviour of the fault.

In cases where $\theta_r \geq 55^o$, fault surfaces are locally welded by frictional melt. The significant increase in volume of melt between the sample where $\theta_r = 55^o$ and $\theta_r = 60^o$ is consistent with the ~23% increase in peak normal stress with the 5º increase in reactivation angle. It is feasible that asperity contact stresses in a sample where bulk normal stress is between 437-539MPa, could be in excess of 4-5GPa assuming a 10% real contact area [*Logan and Teufel*, 1986]. Such high contact stresses could result in significant frictional heating during fast slip, potentially inducing localised asperity penetration of any lubricating film and/or vaporisation of the interfacial fluid. Any transition from elastohydrodynamic lubrication to boundary lubrication or even an unlubricated state, would result in a drastic change in wear rate and/or rate of heat generation [*Sadeghi*, 2010]. The presence of water at asperity interfaces may also influence melting temperatures and kinetics by serving as a localised flux, potentially resulting in the formation of a hydrated silica melt [*Kennedy et al.*, 1962]. During this process strained Si-O bonds may preferentially re-bond with OH^- anions [*Lasaga and Gibbs*, 1990; *Nakamura et al.*, 2012] assisting in the break-up of the strongly bonded quartz crystal framework. Unfortunately, the small melt sample size has restricted efforts to investigate this possibility using techniques such as FT-IR spectroscopy.

4.2.3 Development of new faults

Cohesive strengthening through melt welding

Fault healing and strength recovery is commonly thought of as a time-dependent process resulting from compaction and cementation of the fault core, over timescales of decades to centuries [*Fredrich and Evans*, 1992; *Tenthorey et al.*, 2003; *Tenthorey and Cox*, 2006]. However, the current suite of experiments demonstrates that cohesive fault strengthening can also occur due to melt welding, almost instantaneously after seismic rupture in a stick-slip regime. The most dramatic examples of the effects of fault strengthening occurs on unfavourably-oriented faults where $\theta_r \geq 55°$. During fault rupture significant areas of the fault interface frictionally heats and melts, forming a

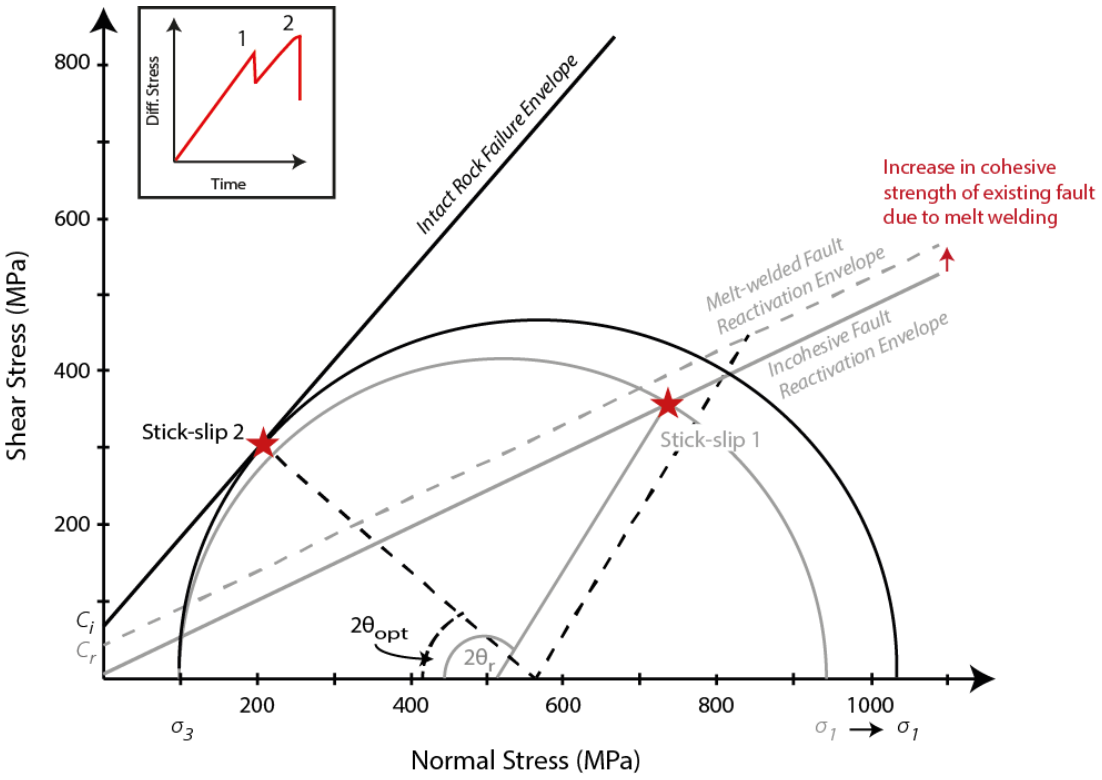

Figure 30: Mohr diagram showing effect of melt welding on the strength of fault surfaces.
Mohr diagram illustrating the experimental data from MIS004, where θ_r=60º. The geometry of the failure/ reactivation envelopes reflect the friction coefficient and cohesive strength defined in section 4.1. C_i refers to the cohesive strength of intact rock and C_r is an indicative estimation of the cohesive strength of the existing fault following melt welding. The first stick-slip event (see inset) occurs on the pre-existing fault surface as shown by the intersection of the first Mohr circle (grey circle) with the incohesive fault reactivation envelope. During this rupture melting occurs over a considerable area of the fault interface, effectively welding the surfaces and increasing the cohesive strength of the fault. Subsequent re-loading results in the second (black) Mohr circle intersecting the intact rock failure envelope prior to conditions being met that would allow the continued reactivation (intersection with melt-welded reactivation envelope).

semi-continuous zone of melt-welding. Subsequent re-loading impedes reactivation of the existing misoriented slip surface, and drives the formation of a new optimally-oriented fault. The evolving stress states in sample MIS004 ($\theta_r = 60^o$) are depicted using a Mohr circle in Figure 30.

During this experiment the first slip event occurs on the pre-existing fault, where $\theta_r = 60^o$ (fault ruptures are indicated on the schematic loading curve shown in Fig. 30 - see inset). Slip occurs when the first Mohr circle (indicated by the grey line) intersects the incohesive fault reactivation envelope, marked with a red star. During this rupture frictional melting occurs on the existing fault interface, welding the surfaces at the end of the slip event. It is assumed that the main change induced by the generation of frictional melt is an increase in the cohesive strength of the existing fault surface and that any change in the coefficient of static friction is negligible. Although, the increase in the cohesive strength of the fault has not been quantified experimentally, a minimum increase can be estimated based on sample behaviour during subsequent re-loading. During the second loading the existing misoriented fault de-activates when a new optimally-oriented fault nucleates. For this to occur, conditions necessary for the failure of intact rock must be achieved prior to the conditions necessary to reactivate the melt-welded existing fault. On the Mohr diagram this is shown by the intersection of the second Mohr circle (black circle indicating the stress states immediately prior to the second failure) with the intact rock failure envelope, as indicated with the second red star.

Differences in fault development processes between intact-rock failure and new faults formed after frictional lock-up of misoriented faults

The mechanical and microstructural data from the current suite of experiments indicate differences in the process of fault development between fault zones formed during intact rock failure and new optimally oriented faults formed following lock-up of unfavourably-oriented faults. Faults formed during intact rock failure are observed to propagate approximately co-seismically, as shown by the significant co-seismic sample dilation and associated large pore fluid pressure drops in experiments where pore fluid pressures were monitored. In contrast, new favourably-oriented faults, generated as a consequence of lock-up of a pre-existing misoriented fault, propagate ‘slowly’ without fast rupture and accompanying stress drop. For ease of discussion, faults that develop by this latter method are referred to developing aseismically (or without sudden,

macroscopic stress drop), although on a grain scale this is unlikely to be true. Previous experiments investigating fault growth have reported acoustic emissions associated with microfracture formation and localisation prior to macroscopic failure [*Lockner et al.*, 1992]. Experiments halted at peak stress and prior to sudden stress drop capture the new fault in the process of development, and indicate nucleation from the pre-existing unfavourably-oriented fault surface in regions of melt welding. Precursory brittle creep on the newly-forming fault is associated with up to ~200μm of displacement.

The volume of frictional melt produced within the new fault zone is also significantly different between the two styles of fault propagation. During intact rock failure, melt is localised, forming mainly at restraining bends created by the uneven fault surface, or at locally impinging grain contacts. In contrast, the new fault developed during reactivation experiments contains much larger volumes of melt, with some melt layers being up to 1.2mm long and 20μm wide. This indicates that there is a significant difference in the way energy is expended during rupture in the two types of experiments.

During rupture propagation and co-seismic slip, elastic energy that is stored in the wall rock, sample assembly and machine is released. The release of this energy produces mechanical work that is commonly referred to as an 'energy budget' that is defined as:

$$W_f = Q + E_s + U_s \qquad 5$$

where W_f is total mechanical work, Q is heat produced during frictional sliding, E_s is energy radiated as seismic waves and U_s is surface energy for gouge and fracture formation [*Scholz*, 2002].

Previous research suggests that the majority of energy is expended in heat production with relatively minor contribution expended as seismic energy [*McGarr*, 1999] and an almost negligible contribution from the formation of the rupture surface [e.g. *Chester et al.*, 2005]. However, the latter of these assumptions is based on Griffith's fracture model where fractures are assumed to propagate under equilibrium conditions [*Scholz*, 2002]. During seismic rupture this contribution may be significantly higher as a result of complex fracture surface development and gouge production [*Reches and Dewers*, 2005]. If a greater dissipation of energy occurs through fracture development, abrasive

wear and dynamic pulverization, the amount of energy that is converted to heat may be reduced, delaying the onset of melting.

In light of this discussion it is suggested that the 'slow' growth of new, favourably-oriented faults results in fault zones that are well-developed prior to the first sudden slip event. The existence of a fault prior to rupture minimises the proportion of energy that is consumed by damage processes and maximises frictional heating and melt production. On the other hand, during sudden intact rock failure, fault growth and slip are more contemporaneous with fault rupture and associated sudden stress drop. Consequently a greater portion of the energy budget is consumed by the formation of damage, which results if lower volumes of melt.

4.3.4 Cathodoluminescence: insights and interpretation

SEM-CL is an optical phenomena based on the generation of visible radiation through the excitation of a sample induced by high-energy electron bombardment [*Pagel et al.*, 2000]. CL arises from imperfections within the crystal lattice, including structural defects and impurities that cause variations in the wavelength and intensity of the luminescent emissions. CL is derived from two main sources, intrinsic luminescence and extrinsic luminescence. Intrinsic luminescence is characteristic of the host material and enhanced by structural defects such as vacancies in the crystal lattice, dislocations and shock damage that distorts the crystal lattice [*Marshall*, 1988; *Gucsik et al.*, 2003]. Extrinsic luminescence is caused by elemental impurities that are incorporated within the crystal lattice as either interstitial ions (occupying a non-structural position) or through the substitution of the silicon cations or oxygen anions by different elements [*Marshall*, 1988]. The broad CL emission bands produced by quartz are often associated with activation by lattice defects (self-trapped exciton, oxygen vacancies, non-bridging oxygen hole centres) and the incorporation of trace elements (e.g. Al, Ti, Ge, Fe, H, Li, Na) [*Stevens Kalceff and Phillips*, 1995; *Gotze et al.*, 2001; *Gotze*, 2012 and references contained therein]. However, assignment of spectral peaks to a particular defect centre or impurity is often difficult due to the complex interaction between the activator and surrounding lattice structure [*Gotze*, 2012].

Interpretation of CL spectra is further complicated by the lack of a unique relationship between the energy of the emitted CL photons and the chemical state of a luminescent impurity, as exists for X-ray emission. Similarly, the intensity of the emission band is

not necessarily proportional to the concentration of the emitter, with the shape and intensity of the CL bands being dependent on a range of factors, including the crystal structure, chemical composition and both the collection conditions and measurement system [*Remond et al.*, 2000; *Gotze*, 2012]. So important are the operating conditions to any measurement, that without corrections for system response and detailed information on the beam and measurement conditions, it may not be possible to directly compare CL spectra acquired with different systems [*Remond et al.*, 2000].

Despite the complexity of understanding the origin of the luminescence, CL provides unique information on the internal structures and growth and deformation history of quartz that are not as readily discernible by any other technique [*Gotze*, 2012]. Although this method can be used to identify subtle changes in crystal structure and composition, it has not been extensively used during the study of experimentally produced pseudotachylytes, possibly due to resolution limitations of many SEM-CL systems. The SEM cathodoluminescence (SEM-CL) results in this study indicate that a unique emission signature is associated with the formation of frictional melt in Fontainebleau sandstone. The CL spectra is dominated by broad peaks and an almost total absence of the sharp emission lines associated with the incorporation of trivalent ions in the form of rare earth elements [*Remond et al.*, 2000].

In one of the few identified studies were CL was undertaken, *Pec et al.*, [2012] used panchromatic SEM-CL to analyse partially amorphous material found within experimentally deformed granite gouges and noted the high levels of luminescence within the slip zones and at sites of high stress. These observations are consistent with the bright luminescence that was observed in the high stress zones immediately adjacent to the melt in fault core of the current suite of experiments and may represent an increase in defect density within the 500nm wide crystalline zone adjacent to the melt (e.g., Fig. 19C, F).

Interestingly, spectral analysis of experimentally shocked natural quartzites shows a distinct difference in the CL spectra between unshocked and shocked samples, with a shift in the centre positions of the broad luminescence bands after experimental treatment at 12GPa and 100-750°C [*Gucsik et al.*, 2003]. The dominant peak forms within the blue light spectrum between 2.9-3.4eV (λ=426-368nm), with exact position depending on the temperature conditions. The peak is attributed to the formation of

intrinsic defects resulting from distortion of the SiO_4^{4-} tetrahedra and possible partial amorphisation. A similar shift in peak shape and location occurs in the spectra collected from melt in the current suite of experiments. A dominant broad band occurs at ~3.0eV (λ = 410nm) and secondary peaks located at ~2.55eV (λ = 485nm) and ~1.9eV (λ = 650nm) (Fig. 20H). The variations in intensity within the melt layers are possibly related to the micro-distribution of activator elements such as aluminium [*Gucsik et al.*, 2003].

The same distinctive spectra are also observed in damaged material in the fault core of optimally-oriented faults that have slipped aseismically for distances > 2mm, and also in melt generated under water-saturated conditions. However, in both cases luminescence is less intense than for melt formed under nominally dry conditions. For the aseismically slipped faults, the slip rates of these experiments are interpreted to be insufficient to induce frictional melting of the fault interfaces (see thermal calculations in Chapter 2). Instead it is thought that these zones may represent mechanically amorphized or partially amorphized material where changes in the lattice structure and development of defects results in the development of a spectral signature similar to that of melt formed under both nominally dry and saturated conditions. *Boggs et al.*, [2001] observed that CL-bright and -dark zones within shocked quartz of the Ries impact structure correspond to the presence of planar deformation features with the non-luminescent regions associated with amorphous material. These observations were attributed to a possible lack of suitable activators or a high density of closely-spaced energy levels that served as traps that prevent the emission of photons. Whether these explanations apply to the present suite of experiments requires further analysis of both the structural and trace element composition of the quartz and damaged materials using such methods as TEM and ion microprobe. However, the identification of a distinct change in CL emissions with the formation of frictional melt and possible amorphous/damaged material, highlights the value of further exploring CL techniques as a means of analysis for experimentally-deformed fault surfaces. This method potentially provides a rapid means of identifying modified or potentially amorphous material that could then be the subject of other analysis.

Within the 6 hour hydrothermal treatment (T = 900°C, P_c = 250MPa, P_f = 150MPa) of a melt-bearing sample, there was almost complete overprinting of melt textures. Imaging using BSE-SEM showed the hydrothermally treated melt zones were indistinguishable

from the surrounding quartz grains. In CL-mode, the distinctive melt-related emissions were almost completely replaced by emissions typically of the hydrothermal quartz with melt being preserved only in a few locations, possibly as a result of isolation from the hydrothermal fluids. These results provide insights into the longevity of melt and the deformation processes activated during hydrothermal isostatic pressing (HTIP).

The hydrothermally precipitated quartz produces a short-lived, high-intensity blue luminescence with an emission band at approximately 3.0eV (λ = 410nm); this is distinguishable from the melt/amorphous material by the lack of secondary bands at 2.55eV and 1.9eV. The high intensity of the CL could result from either an increase in CL activators such as aluminium [*Alonso et al.*, 1983; *Gotze et al.*, 2001], or the presence of defects such as (H_3O_4) centres [*Yang and McKeever*, 1990], both of which are associated with 3.2-3.1eV emissions. Similar CL-bright regions were observed by Giger [2007] in hydrothermal overgrowths produced during the HTIP of fine-grained quartz gouge. Microprobe analysis revealed elevated Al-content in these overgrowth zones.

Previous analysis of microstructures formed during both HTIP and deformation of quartz aggregates [e.g. *Cox and Paterson*, 1991; *Dewers and Hajash*, 1995; *Kanagawa et al.*, 2000; *Giger et al.*, 2007] and fault healing experiments [*Tenthorey and Cox*, 2006] has led to the recognition that dissolution-precipitation creep is activated on laboratory timescales under the same experimental conditions used during the hydrothermal treatment of the melt-welded interface. Evidence for the solution-transfer interpretation includes changes in grain shapes and grainsize distribution, interpenetration of grains and the formation of ridge and plateau structures at grain interfaces. In the current sample, sub-micron sized particles are absent from the HTIP fault surfaces, suggesting coarsening through the process of Ostwald ripening [*Parks*, 1984]. However, the apparent lack of grain interpenetration on remaining gouge particles revealed by the CL imaging suggests that stress-driven solution-transfer processes have not been activated in this sample during the HTIP process.

The rapid overprinting of melt-related textures and accompanying CL spectral signature has implications for thin layers of silica pseudotachylytes in natural fault systems. Within hours of rupture in a fluid-active fault zone, all evidence frictional melting may be removed from the rock record. Given that frictional melt has been shown to form at

normal stresses >300MPa, on room temperature, small displacement (<600μm) slip experiments in a quartz sandstone, it is suggested that frictional melting may play a more significant role in crustal fault processes than previously thought. This idea, and the implications of thin layers of melt forming on natural faults, is discussed in more depth in Chapter 4.

5. Conclusions

A series of room temperature experiments has been undertaken using Fontainebleau sandstone to explore the mechanical and microstructural evolution of fault surfaces inclined between 25º and 70º to the maximum shortening direction, representing faults that vary from optimally-oriented to severely-misoriented for failure. These faults have been reactivated in both dry conditions and at controlled pore water pressures, using two different mechanisms of loading. The first, referred to as 'stress-driven failure' involved increasing the axial load at constant rate until failure, whereas 'fluid-driven failure' was achieved by maintaining a constant axial load and increasing pore fluid pressure until slip occurred.

Although initial reactivation of the faults obeys frictional theory, continued reactivation is strongly influenced by the dynamic evolution of the fault surface, most notably through the development of frictional melt. Rapid slip events in the stick-slip regime are shown to form a locally continuous layer of frictional melt in both the dry and water-saturated samples, with the extent of melt formation being positively correlated with increasing angle of misorientation and associated increase in normal stress. Structural analysis of the fault core over a range of scales, reactivation angles, confining pressures and displacements, has provided unique insights into the evolution of the fault surface. This includes through the development of frictional melt and its subsequent impact on the mechanical strength and microstructural development of the fault. Using BSE-SEM imaging, pseudotachylyte is identifiable in the fault core by the formation glass layers that are a different intensity to the surrounding quartz. Key textures that distinguish this material as being of a melt origin include the presence of entrained clasts within a non-porous matrix, strained vesicles, occasional drawn out filaments and the invasion of adjacent fractures, which produces an uneven melt substrate-boundary. SEM-CL investigations reveal that the melt has a distinctive luminescent signature with the

dominant broad band centred at ~3.0eV (λ = 410nm) and secondary peaks at ~2.55eV (λ = 485nm) and ~1.9eV (λ = 650nm).

Samples in which deformation has been halted prior to the activation of a rapid slip event show evidence of the formation of thin bands of sub-micron-sized gouge that forms a discontinuous, up to 1μm thick layer along the slip surface. The gouge layer is comprised of fragments that range in size between ~100-500nm; they are set within a matrix that is unresolvable using BSE-SEM imaging, and potentially represents a partially amorphous matrix. The formation of this fine gouge layer prior to the first stick-slip event is in broad agreement with the continuum of behaviours proposed in Chapter 2 and is interpreted to form as a precursor to the frictional melt. Aseismic slip on favourably-oriented faults also produces a highly damaged and possibly amorphous material at grain-to-grain contacts. This material is morphologically different from crystalline gouge and in CL produces an emission profile that is essentially the same as the frictional melt.

The generation of pseudotachylyte on slip surfaces has significant effects on the strength of the fault via a process termed 'melt-welding'. In this process melt quenching after melt production welds the grain-to-grain contacts. Microcomputed X-ray tomography of the fault zone has allowed estimation of the three-dimensional spatial extent of frictional melt on slip surfaces. Approximately 50% of the total fault area is fused, thereby significantly increasing the cohesive strength of the fault. Melt-welding is observed to act as a catalyst in the formation of fracture damage along the slip zone, with much of the gouge, microfractures and secondary fault traces observed to initiate at sites where quenched frictional melt is subsequently sheared. On the most unfavourably-oriented faults the increase in cohesive strength due to melt welding is sufficient to drive fault lock-up and results in the generation of a new favourably-oriented fault.

Frictional melt also forms during water-saturated stress- and fluid-driven failure, with no apparent change in peak shear stress between wet and nominally dry samples. Melt formed under hydrous conditions includes a larger number of entrained clasts than melt formed under dry conditions, possibly indicating a lower melt temperature. CL emissions have similar peak location and geometry as melt formed under dry conditions, but luminesces at a lower intensity. Microstructurally the faults reactivated

by fluid-driven processes differ from those reactivated by stress-driven failure, by showing little evidence of fault surface modification by attrition-related wear processes suggesting a mechanical contribution by mechanisms such as elastohydrodynamic and boundary lubrication.

Hydrothermal treatment of the fault zone for a period of 6 hours results in the melt being readily destroyed. CL analysis suggests that quenched melt devitrifies *in situ* and forms epitaxial overgrowths on the adjacent grains. Some local transport and precipitation of the silica has produced mantles of hydrothermally precipitated quartz on clasts in the fault core. However, there is no conclusive evidence for the activation of stress-driven solution transfer processes on the time scale of the hydrothermal treatment.

Finally, the ease with which pseudotachylytes have been generated on these quartz sandstones at room temperature and low effective confining pressures ($P_c' > 15MPa$), indicates that the formation of frictional melt in natural fault zones may be more prevalent than previously thought. However, the preservation potential of thin melt layers on geological timescales is probably low, given the rate at which pure-silica pseudotachylytes devitrify in hydrous environments.

Chapter 4

Frictional melt formation during crustal faulting: implications and future directions

1. Dynamic changes on fault interfaces: implications for crustal faulting processes

The propagation of seismic slip is generally attributed to the activation of fault weakening mechanisms at high slip velocities [*Di Toro et al.*, 2006b]. During seismic rupture, dynamic conditions on the slip interface alter the structure and chemistry of the fault surfaces [*Niemeijer et al.*, 2012]. Extreme thermal and mechanical conditions induce microstructural changes from the micron to molecular scale, resulting in deviations in mechanical behaviour away from that predicted by empirical frictional laws. The increased understanding of dynamic fault processes has led to a growing realisation that in order truly understand the physics of the macro-scale brittle-frictional behaviour, we must first comprehend the microscale processes [*Viti*, 2011]. However, despite the significant advances that have been made towards understanding fault processes at high slip velocities, much remains uncertain. Little is known about the mechanisms that drive fault instability and the microstructural processes that control mechanical weakening have been poorly explored [*Niemeijer et al.*, 2012]. The links between experimental and natural fault surface processes remain largely speculative, due to both apparatus limitations and the meta-stability of many slip-related products. With the exception of frictional melt (pseudotachylyte) formation, none of the experimentally inferred fault weakening mechanisms have been conclusively demonstrated to operate within natural faults. However, the results presented in this thesis contribute new insights into the behaviour and microstructural development of fault surfaces, especially during the early stages of seismic instability.

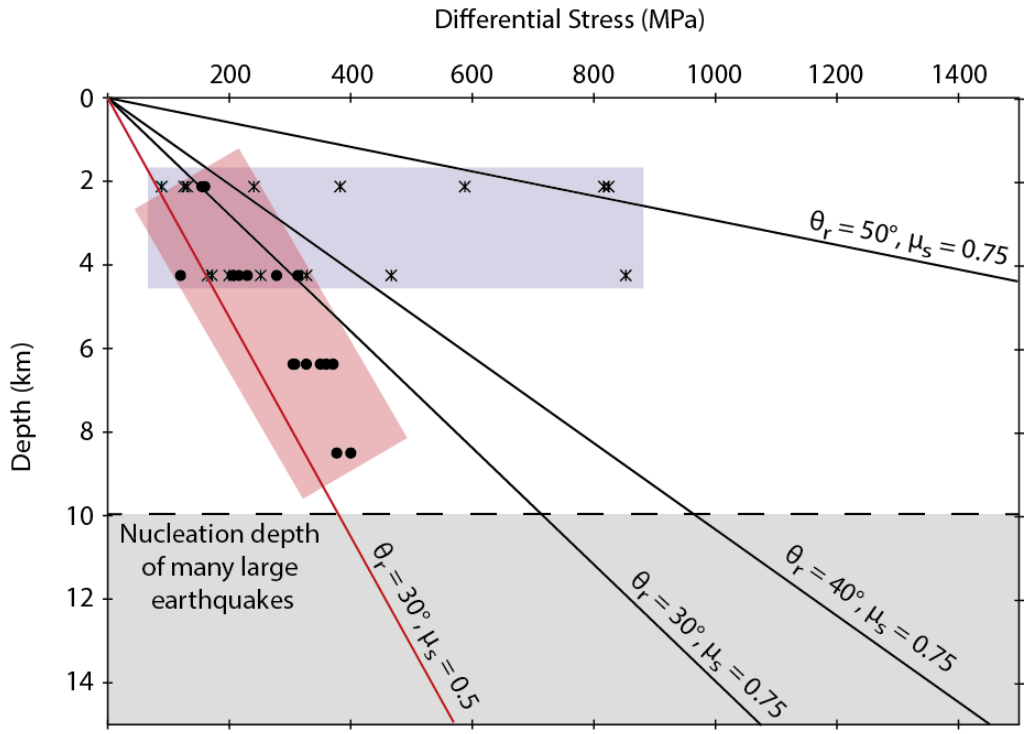

Figure 1: Comparison between experimentally-derived fault strength and the differential stress required to theoretically reactivate cohesionless thrust faults in the dry continental crust
Differential stress profiles for frictional reactivation of a cohesionless thrust fault with varying reactivation angles (θ_r) at increasing depth in the crust. Shaded regions indicate the experimentally-derived strength data. Red area shows the differential stress value at yield point for optimally-oriented fault deformed at elevated temperatures (Chapter 2) and the pale blue rectangle indicates yield point values from the misoriented fault experiments (Chapter 3).

This work is based on the findings of two series of experiments undertaken at realistic crustal stress conditions (Fig. 1) and over small slip displacements using a conventional, internally-heated, triaxial deformation apparatus. Experiments used pre-ground bare interfaces on pure quartz sandstone to simulate the growth and development of localised slip within fault zones. Two types of experiments have been undertaken: the first set of experiments presented in Chapter 2, involved high temperature (400-927ºC) reactivation of approximately optimally-oriented fault surfaces. The second suite (Chapter 3), was undertaken at room temperature on faults oriented at between 25-70º to the shortening direction, representing faults that range from optimally-oriented to severely-misoriented for reactivation. All experiments were slipped at stress conditions comparable to conditions in faults in the upper to lower seismogenic regime in the continental crust. In Figure 1, experimental fault strength data from immediately prior to rupture is compared with the differential stress profiles for frictional reactivation of a cohesionless thrust fault with varying reactivation angles (θ_r) at increasing depth in the crust. The

differential stress at the point of reactivation is assumed to be linearly dependent on depth, assuming that, for a reverse fault, $\sigma_v = \sigma_3$. Differential stress is calculated by:

$$(\sigma_1 - \sigma_3) = \frac{\mu_s(cot\theta_r + tan\theta_r)}{(1 - \mu_s tan\theta_r)}\rho g z \qquad 1$$

Where μ_s is the coefficient of static friction assumed to be 0.75 (within the typical frictional range defined by *Byerlee* [1978]), ρ is crustal rock density (assumed to be 2400kg/m^2, g is gravity and z is depth [*Sibson*, 2004]. The estimated strength of an approximately optimally-oriented thrust fault with the same coefficient of static friction as the Fontainebleau bare slip interfaces (i.e. μ_s = 0.5) is also shown for reference (see red line, Fig. 1).

A novel aspect of this research has been the combination of realistic normal stresses with small displacement, sub-seismic to seismic slip events to examine processes operating during the early stages of fault weakening (Fig. 2). Much of the seminal work

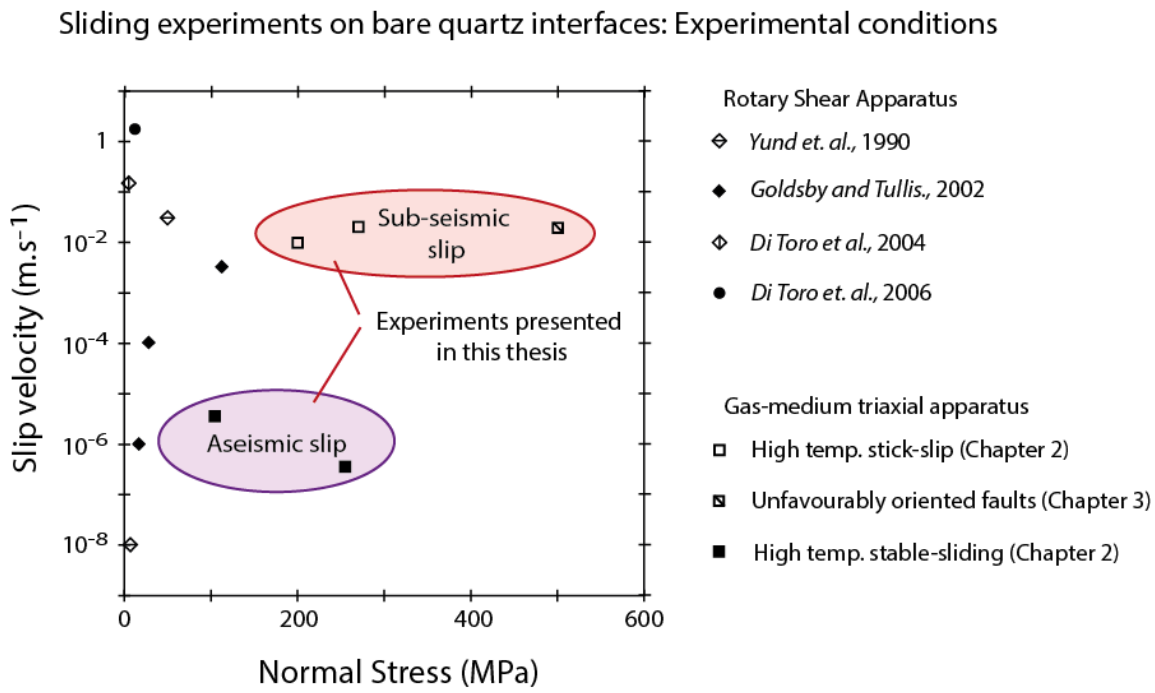

Figure 2: Comparison of experimental conditions for high velocity experiments on quartz interfaces Plot of the range of slip velocities and normal stress conditions for experiments undertaken on pure quartz, bare fault interfaces. The current experiments were undertaken on a gas-medium triaxial apparatus, whereas all other experiments were undertaken on a rotary shear type apparatus. Note that, during the current experiments, significantly higher normal stresses have been used, in contrast to previous high velocity experiments. Note also, that the indicated slip velocities for the current rapid slip experiments are estimated on the basis of the recorded seismic data. However, these slip rates could be considerably faster.

investigating high-velocity slip behaviour, has required the use of unrealistically low normal stresses and large sliding distances [e.g. *Shimamoto and Tsutsumi*, 1994; *Hirose and Shimamoto*, 2005a]. However, these high-velocity experiments have revealed complex, and as yet poorly understood, mechanical behaviour during the initial stages of seismic slip [e.g. *Di Toro et al.*, 2006b; *Proctor et al.*, 2014]. Much of the uncertainty arises from the technical difficulty associated with producing and recovering high velocity, but small displacement slips [*Niemeijer et al.*, 2012]. In contrast, the experiments presented in this thesis show the onset of microstructural changes, such as amorphisation and frictional melting, occurring at slip distances that are up to several orders of magnitude smaller than previously recognised. The use of sophisticated microstructural techniques including, high resolution FE-SEM and CL-SEM, FIB-TEM and microcomputed X-ray tomography, has enabled documentation of these early slip-related microstructures over a range of scales, and in both two- and three-dimensions. These results have significant implications for our understanding of (1) the evolution fault strength and mechanical behaviour, (2) fault behaviour in both hydrous and anhydrous environments, and (3) more broadly, on the conditions and environments in which pseudotachylytes form. These implications are discussed in more detail in the following sections.

1.1 Implications of amorphisation and frictional melting on the strength and mechanical behaviour of faults

The experiments presented in this thesis show, for the first time, an evolution in microstructures on fault surfaces that occur within slip distances of 50-500μm. The microstructural changes are correlated with changes in mechanical behaviour. Initial aseismic sliding is associated with the formation of a gouge layer that is interspersed with potentially amorphous material. After the onset of a sliding instability and rapid slip, the fault surfaces show clear evidence for the formation of pure-silica pseudotachylyte. Previously, the results of high-velocity friction experiments have predicted fault-weakening distances to be in the order of 0.1-1+ metres [e.g. *Di Toro et al.*, 2006a; *Faulkner et al.*, 2010]. However, weakening distances of 4-40μm inferred from models [*Beeler et al.*, 2008], are more consistent with the potential weakening distances in the current small-displacement experiments. The onset of mechanical and microstructural changes during these sub-millimetre displacements has implications for

earthquake source parameters such as fault weakening distances, and potentially for co-seismic fault strength and behaviour.

The potentially amorphous material formed during aseismic slip, at both room temperature and elevated temperatures, is interspersed with crystalline clasts forming a matrix that is similar in appearance to the 'gels' produced during some high velocity sliding experiments [*Goldsby and Tullis*, 2002; *Di Toro et al.*, 2004; *Hayashi and Tsutsumi*, 2010]. This amorphous material is considered to form by intense comminution of the gouge particles resulting in a loss of crystalline structure, in a similar manner to previously observed grinding or mechanical induced amorphisation [*Yund et al.*, 1990; *Watson and Parker*, 1995; *Nakamura et al.*, 2012]. The possible presence of mechanically amorphized material at the slip interface has implications for energy dissipation, dynamic friction properties and fault stability. Once slip has initiated, the early generation of an amorphous layer could significantly reduce the temperatures required to achieve viscous flow (glass transition) [*Navrotsky*, 1994], thereby potentially enhancing formation of frictional melt.

Slip-induced frictional-melting occurs within the first 50µm of rapid fault slip during stick-slip behaviour, forming discontinuous to semicontinuous melt layers up to 2µm thick, over 10-60% of the fault surface. In contrast, slip distances of greater than 3 metres were required for the onset of assumed continuous melting on novaculite surfaces during high velocity friction experiments undertaken at 12.5MPa normal stress [*Di Toro et al.*, 2006b]. In the experiments presented in Chapter 2, changes in the morphology of the frictional melt textures on small displacement slip surfaces are associated with identifiable changes in slip acceleration and velocity. Comparatively high-velocity slip events are associated with the formation of drawn out 'ribbon' textures, glass filaments and striated glass patches, implying a comparatively low melt viscosity. In contrast, low-velocity slip is associated with the formation of localised glass patches that contain a higher abundance of clasts and no evidence of significant melt redistribution resulting from melt flow during slip. These glass patches are inferred to indicate higher melt viscosities.

It was proposed that changes in melt-viscosity could be driven by 'over-shoot' of the melting temperature resulting in the significant superheating of both the crystalline wall rock / clasts and melt. Although potentially applicable to many types of natural fault

surfaces, the relatively high viscosity and polymerised structure of the silica melt means that that superheating may play a more significant role in the formation of melt in a quartz- or other framework-silicate-dominated system, than would perhaps be the case in faults containing other mineral assemblages. Additionally, the relatively fast melting kinetics of more mafic minerals could result in a more rapid transition into a melt-lubricated viscous-shear regime, potentially minimising frictional heating and more sluggish melting of quartz clasts. This work has highlighted the need for a better understanding of the physics of melting processes including (1) how the melt front propagates away from the melt generation surface in different minerals, (2) how the melting process transitions from the generation of localised melt patches into continuous melting, and (3) the relative timing between heating and the onset of melt lubrication. Improved knowledge in these areas would significantly improve understanding of the role of frictional melting in influencing fault mechanics early during slip events.

Experiments show that, upon quenching melt welds the fault slip surface, increasing cohesive strength and contributing significantly to the formation of fault damage during subsequent slip events. In Chapter 3, it was shown that on the most unfavourably-oriented faults, the increase in cohesive strength associated with melt welding drives fault lock-up and generation of new optimally-oriented faults. These results suggest that micron-thick layers of melt may play a 'hidden' role in the development of damage zones in natural faults by modifying local stress-states, resulting in the formation of lateral and terminal damage zones, including the asymmetric damage patterns commonly observed on natural faults [e.g. *Flodin and Aydin*, 2004]. In extreme examples, the generation of pseudotachylyte and melt-welding could result in fault death and the consequent migration of slip to new rupture surfaces within the host rock [e.g., *Di Toro and Pennacchioni*, 2005].

The close spatial association of cataclasites and pseudotachylytes observed in both experimental [*Spray*, 1995] and natural fault zones [e.g., *Di Toro and Pennacchioni*, 2005], has given rise to the view that cataclasis is a precursor to frictional melting. Further, it has been suggested that the transition from cataclasites to pseudotachylytes may, in some situations, record the evolution from aseismic creep to seismic slip [*Di Toro and Pennacchioni*, 2005]. However, the microstructures formed during the current suite of experiments indicate that the relationship between frictional melting and

formation of gouge particles may be more complex. The formation of clast-free layers of pseudotachylyte during the first slip event potentially provides evidence for melt generation without prior gouge formation. With continued loading, fault damage nucleates from areas adjacent to melt-welded regions. Stress cycling induced by the interaction between pores and highly stressed grain-to-grain contacts [*Chester and Chester*, 2000; *Brune*, 2001] may result in the intense fragmentation of areas adjacent to the melt zones. Ultimately continued damage leads to a widening of the fault zone, which may potentially inhibit future slip localisation and melt development.

1.2 Implications of identified fault slip behaviours in hydrous environments

Fault zones play an important role in localising and directing crustal fluid flow [*Caine et al.*, 1996; *Cox et al.*, 2001; *Faulkner et al.*, 2010]. In fluid-active faults, the evolution of shear stress and pore fluid pressures may be coupled in complex ways, resulting in fault rupture being induced by either changes in pore fluid pressure (fluid-driven failure), or changes in stress states (stress-driven failure) [*Cox*, 2010]. The experiments presented in Chapter 3 provide new insights into slip behaviour and the generation of fault damage in a hydrous environment through both stress- and fluid-driven failure. Additionally, the longevity of slip-related microstructures has been explored in both Chapters 2 and 3, through the introduction of hydrothermal fluids following slip. Implications of key results are discussed in greater depth in the following section.

The most notable difference between the microstructures formed in the cores of faults reactivated under dry versus water-saturated conditions, is the absence of gouge and attrition-related wear products in the hydrous faults. These results suggest that pore-fluids have a more complicated effect on the slip interface than simply reducing the effective normal stress. It was proposed that the activation of molecular- to nano-scale lubricating effects of interfacial fluids may inhibit the formation of damage through the process of boundary and elastohydrodynamic lubrication [*Hamrock et al.*, 1994; *Brodsky and Kanamori*, 2001]. Although substantial evidence from the engineering field supports the idea of interfacial fluid lubrication, the concept is experimentally untested in geological materials. Identification and isolation of specific lubricating process would be difficult, especially when coupled with potentially significant changes in co-seismic fault porosity and permeability, and the activation of other mechanisms such as thermal pressurisation. However, the lack of abrasive wear, especially in fluid-

driven reactivation experiments, has implications for the interpretation of fault processes in high pore-fluid factor environments.

There is a long-held belief that pseudotachylytes do not form in saturated environments [*Sibson*, 1973, 1975; *Magloughlin and Spray*, 1992; *Sibson and Toy*, 2006]. At mid- to lower-crustal conditions, the potential for frictional melt generation is reduced by thermal activation of fluid-controlled deformation mechanisms such as hydrolytic weakening and dissolution-precipitation creep [*Griggs*, 1967; *Cox*, 1998 and unpublished data]. In the low temperature environments of the upper crust, fluids are thought to inhibit melt formation by more efficiently transporting heat away from asperity contacts [*Violay et al.*, 2014], or through activation of thermal pressurisation [*Sibson*, 1973] and interfacial lubricating mechanisms [*Brodsky and Kanamori*, 2001]. However, documented examples of natural pseudotachylytes forming in fluid-active settings such as subduction zones [*Austrheim and Andersen*, 2004; *Rowe et al.*, 2005; *Ujiie et al.*, 2007], landslips [*Masch et al.*, 1985; *Lin*, 2008a] and even during drilling processes [*Killick*, 1990] have led a number of authors [*Rempel and Rice*, 2006; *Bjornerud*, 2010] to question these assertions. However, until now technical and apparatus limitations have prevented the exploration of frictional melt formation in hydrous conditions, at controlled fluid pressures.

In Chapter 3, experiments exploring the reactivation of unfavourably-oriented faults conclusively demonstrated that frictional melting does occur on sliding interfaces in quartz rocks under controlled pore-fluid pressures and at high effective normal stresses. Given the fluid-active nature of many crustal faults, these results indicate that the formation of pseudotachylyte in quartz-rich rocks may be more prevalent and play a more significant role in crustal fault mechanics than previously thought. However, the thickness (< 2μm) and metastability of the amorphous material and frictional melt, suggests that similar textures on natural faults might not be preserved over geological timescales, especially in the presence of reactive pore fluids. During the current experiments, it has been shown that under hydrothermal conditions, melt textures are rapidly destroyed over time scales of <1hour at 500ºC. Extrapolating these results to natural fault zones at upper- to mid-crustal conditions, it is suggested that on time scales shorter than interseismic periods, all evidence of frictional melting could be removed from the microstructural rock record. These results provide a tangible reason for the apparent scarcity of silica-rich pseudotachylytes in nature.

1.3 Implication for the conditions and environments in which pseudotachylytes form

The presence of fault-related pseudotachylyte is generally conceded to be the only unequivocal evidence of seismogenic slip within the geological record [*Sibson,* 1975]. As such, understanding conditions of melt formation places important constraints on the interpretation of the history of exhumed faults. Although pseudotachylytes have been documented on faults exhumed from depths from 3-60km, observations of natural pseudotachylytes remain rare [*Sibson and Toy*, 2006]. This has led to the view that certain factors must supress fictional melting on many fault zones [*Bjornerud,* 2010]. Among factors thought to hinder the formation of frictional melt is the thickness of the slip zone, potentially resulting in mechanical work being distributed over a wider area, or the activation of other fault weakening mechanisms. However, the evidence of micron-scale frictional melt that has been presented in this thesis challenges a number of previous conclusions about the environment in which pseudotachylyte forms, including that: (1) frictional melt generation is largely restricted to low porosity crystalline rock [*Sibson and Toy*, 2006]; (2) frictional melting occurs mainly in dry environments with no intergranular pore fluids [*Spray*, 1992; *Sibson and Toy*, 2006]; (3) the host rock is intact or faults have a high cohesive strength [*Sibson and Toy,* 2006]; (4) quartz rocks may not form frictional melt due to the weakening effects of hydrated silica gels [*Goldsby and Tullis,* 2002]; and (5) seismic velocities and slip distances of centimetres to metres are required to frictionally melt rock under crustal conditions [*Di Toro et al.*, 2006b]. These assumptions have been based on observation of both natural pseudotachylytes and high velocity friction experiments.

Importantly, it has been shown in the experiments presented in this thesis, that faults within a macroscopically porous, siliceous sedimentary rock can generate frictional melt under realistic crustal stress conditions, in both dry and water-saturated environments. However, the small melt volumes produced implies that silica-melt potentially could go unrecognised in both field and laboratory settings. This highlights the importance of analysing small displacement faults, using high-resolution microstructural techniques, to explore the evolution of microstructures and micromechanics at the sub-micron scale. Nevertheless, small melt volumes are also susceptible to such processes as devitrification and recrystallization, or mechanical overprinting during continued

deformation, making the microstructural record of the presence of glass potentially transient and readily destroyed.

2. Future research directions

In this thesis it has been demonstrated that frictional melting readily occurs during small displacement (< 500μm) slip events on porous, pure quartz interfaces at normal stresses of ~200-550MPa. These experiments have been completed on both favourably- and unfavourably-oriented faults over a range of experimental conditions including, nominally dry and fluid-saturated environments. Although the results have expanded our understanding of aspects of fault behaviour, they have also generated many questions and highlighted a number of areas that warrant further research. For instance, a closer integration of high velocity, large displacement experiments with low displacement triaxial experiments would increase understanding of the mechanisms that enable the transition from a frictionally locked or aseismically creeping interface to extreme velocity weakening. Better constraints on factors such as real contact area and slip duration would enable improved numerical modelling of the temperature evolution on the slip surface. The microstructural development of unfavourably-oriented faults could be used to guide modelling of stress orientations and thereby improve understanding of the processes involved in the reactivation of inherited faults. Further experiments using different rock types would provide insights into the applicability of the current observations to faults containing other mineral assemblages and levels of porosity. In the following section a number of avenues for potential investigation are discussed including, where relevant, progress that has been made to address them.

2.1 Improved understanding of slip duration and evolution of slip velocities

The novel use of seismic recording equipment has allowed a systematic distinction to be made between low and high velocity slip regimes during stick-slip behaviour on optimally-oriented faults at elevated ambient temperatures (Chapter 2). Differences in sliding velocity were correlated with variations in the development and morphology of the frictional melt, suggesting that melt generation alters the dynamic properties of the slip interface. However, technical limitations of the equipment have resulted in potential under-sampling of velocity during slip events, and consequently there are poor constraints on slip duration and absolute slip velocity. Achieving better precision in the

time resolution of slip duration, velocity and, if possible, characterising the evolution of a single slip event, are crucial to understanding the process of melt generation. Such knowledge is needed to facilitate detailed numerical modelling and allow further exploration of (1) the potential for superheating of both fault interfaces and melt, and (2) the role of pseudotachylyte in initiating and arresting seismic slip.

To address this issue, a system is needed that can sample and record displacement information at the estimated rupture velocity (equating to approximately the shear wave velocity [*Johnson and Scholz*, 1976; *Scholz*, 2002]). In collaboration with the Centre for Gravitational Physics at the Australian National University, work has commenced on developing a laser interferometry system that will have a time resolution of between 10^{-4}-10^{-7}s. The interferometry system involves a single beam of coherent light from a laser source that is split into two identical beams by a beam splitter. Each of the beams travels a different route; one beam path has fixed length and is regarded as a reference, while the other is injected into a fibre that is mounted onto the apparatus on the main vessel. The beam bounces off a corner cube attached to the yoke, and is reflected back into the fibre. This path has a variable length as the upper yoke of the apparatus moves relative to the main pressure vessel during deformation. Its position is comparable to the current location of the existing LVDT that is used to measure sample shortening. The two beams are recombined before arriving at a detector, creating a phase difference or interference pattern that can be used to diagnose and measure changes in displacement along the path. The velocity of the fibre light source relative to the mirror is encoded into a frequency at the detector and displacement is encoded as a number of fringes and relative position between peaks. The data is processed using a custom-written script in MATLAB. The non-calibrated velocity data is scaled against the calibrated displacement data measured by the LVDT thereby allowing precise time and position information to be recovered. Although some aspects of the evolution of slip velocity likely reflect the response of the loading frame during elastic strain release, the recovered data will provide valuable insights about behaviour during slip. These will be used to better constrain thermal simulations. Although the system is still under development, initial tests reveal promising results and development will continue in the latter half of 2015. A representative range of both elevated temperature and misoriented fault experiments will be repeated once the system is operational.

2.2 Quantifying real contact area

The microstructures produced during experimental rupture highlight the point that significant stress concentration occurs at fault asperities, and in the case of porous sandstone, onto individual grain-to-grain contacts. During loading and fault rupture, static and dynamic stresses form large transitory stresses that are sufficient to generate dislocations within the structurally dry quartz. These high stresses have implications for both the formation of amorphous material through mechanical and solid state processes, and for the rapid generation of frictional heat, to the point of superheating the fault core. The temperature of melt can influence the viscosity, the extent of clast melting, fault lubrication and subsequent strength recovery resulting in the termination of slip. Consequently, constraining the area of real contact at slip interfaces under different experimental conditions is an important factor for accurately modelling fault surface processes. While a first order analysis has been undertaken during this study, further quantification could reveal additional insights about the spatial relationships between melt formation, distribution and melt welding, and the role of melt-related processes in influencing the evolution of sudden slip events.

2.3 Constraining structural and chemical variation in the melt

Understanding the structural mechanisms and molecular dynamics associated with frictional melting potentially may help to constrain factors such as melting temperature, melt structure and viscosity that are important parameters for numerical and thermal modelling of interface properties. For instance, temperature of melting could be reduced significantly compared to the equilibrium conditions, if mechanical amorphisation is indeed a precursor to the development of melt, or if fluids present at the fault interface serve as flux, depressing the melting temperature. Additionally, subtle composition changes, such as trace element enrichment or the incorporation of hydroxyl groups within the melt structure, could be activated by the melting process. These may have a significant effect on the rheology and material properties of the melt [*Urbain et al.*, 1982; *Bansal and Doremus*, 1986].

The high resolution cathodoluminescence (CL) investigations undertaken in this study have shown that the melt formed during rapid slip and ‘amorphous’ material formed during aseismic sliding share a distinct emission profile. This could indicate that structural and/or compositional changes induced by the loss of long-range order results in the formation of specific defects that activate or quench the CL. Expanding CL

investigation to include high temperature experiments and coupling CL analysis with other high-spatial resolution analytical techniques, such as FT-IR or Raman spectroscopy, and mass-spectrometry, may help to constrain the origin of the defects. FIB-TEM investigations of the room temperature melt and amorphous material will also provide structural information about these materials, including any evidence of relict crystal structure, defect types and density. Nano Fourier transform infrared spectroscopy (nano-FTIR), with a spatial resolution of approximately 20nm could potentially be used to help constrain the presence of structurally bound water within the melt layer. The use of nano secondary ion mass spectrometry (nanoSIMS) and laser ablation inductively coupled plasma mass spectrometery (LA-ICP-MS) could be investigated to determine if trace element content of the melt layer is significantly different from the wall rock quartz.

2.4 Understanding mechanical amorphisation during aseismic slip

The role that dynamically generated amorphous material plays in modifying fault behaviour and stability remains, to a large extent, poorly understood. Previous experimental work has demonstrated significant dynamic weakening of quartz interfaces at high slip velocities, with this phenomena being attributed to the formation of hydrated amorphous silica gels [*Goldsby and Tullis*, 2002; *Di Toro et al.*, 2004; *Hayashi and Tsutsumi*, 2010]. In the current experiments at both room temperature and elevated temperatures, apparently amorphous material has been generated during aseismic sliding and identified using both CL and TEM methods. These observations have resulted in the hypothesis that mechanical amorphisation may be a precursor to fault instability and thermal melting. However, further experimental work and detailed microstructural analysis using FIB-TEM is needed to explore this possibility. Additionally, work is also needed to explore any potential differences between mechanically amorphized silica and slip-induced 'gels' identified during previous rotary shear experiments.

2.5 Dynamic evolution of fault strength

Further experiments, over a range of conditions, are needed to quantify the magnitude of cohesive strengthening resulting from melt welding. The initial visualisation work undertaken using microcomputed X-ray tomography has shown significant promise in mapping the 3-D extent of the melt-welded surfaces. The use of this technique should be expanded to explore the temporal evolution of the fault surfaces during continued

reactivation, including a quantification of the spatial extent of melt welding over successive slip events. This would provide useful insights into strengthening during the maturation of a fault, including the role of the potentially competing processes of damage formation and fault zone widening. In turn, this could be useful for understanding whether frictional melts are the product of slip on immature faults, as many preserved natural pseudotachylytes suggest [*Wenk et al.*, 2000], or whether frictional melting continues to influence the slip behaviour and strength of mature faults.

During the interseismic period, the presence of amorphous silica produced by rapid slip could potentially increase the rate at which time-dependent fault strengthening occurs under hydrothermal conditions. The high solubility of amorphous silica compared to quartz [*Dove and Rimstidt*, 1994] could serve to increase silica saturation of pore fluids and enhance cementation processes. Expansion of HTIP experiments to include hold-slide-hold experiments would allow investigation of changes in time-dependent healing rates on pseudotachylyte-bearing faults; this knowledge has implications for fault reactivation.

2.6 Expansion of investigations to other rock types

An area that needs further investigation is whether the observations made in this thesis are unique to an essentially pure quartz rock, or whether they have application to a broader range of rock types. A suite of experiments investigating fault reactivation of low-porosity dolomite has been undertaken and is awaiting microstructural analysis; however, a range of other crustal rocks also need to be explored. This would allow a comparison of whether other major crustal rocks types such as felsic, mafic and ultra-mafic igneous rocks, along with various sedimentary and metamorphic rock types, also melt during high normal stress, low displacement stick-slip events. In turn, this could provide an important comparison with the behaviours and microstructures observed during the imposed high velocities, high displacement and low normal stress conditions of rotary shear experiments.

2.7 Improved understanding of fluid-driven fault reactivation

The fluid-driven fault reactivation experiments have shown notable differences in the rupture style and microstructures formed during reactivation, compared with stress-driven experiments. However, as only a small number of experiments have been

undertaken, additional experiments, over a wider range of conditions and materials, are needed to gain a clearer understanding of the mechanisms that cause the observed differences in mechanical behaviour and microstructural response. Exploration of potential elastohydrodynamic and boundary lubrication effects could be accomplished using different pore fluids (e.g. argon or changing pore water chemistry) and undertaking fluid-driven failure experiments over a range of pore fluid pressures. Alternatively, experiments undertaken at controlled pore fluid pressures on a high velocity apparatus would allow direct measurement of frictional values with changing slip velocity.

Precise calibration of the volume monitor during room temperature, controlled pore fluid pressure experiments may allow damage evolution to be quantified by *in situ* measurement of changes in crack porosity in the slip zone. A better understanding of fluid-driven fault reactivation and failure is important for understanding differences between failure modes, which in turn has implications for field interpretation of faults in fluid-active environments, as well as understanding earthquake nucleation, recurrence and the magnitude of co-seismic stress drops.

2.8 Natural faults

The identification of nano- to micro- scale frictional melt on the experimental fault interfaces suggests that there could be significant benefits in applying the nano-scale microstructural approaches used in this thesis to more thoroughly assess the potential distribution of very thin melt layers in natural faults. The current research suggests that pseudotachylyte may be more prevalent than previously thought, but is simply not identified because: (1) the melt layer is very thin, requiring nano-scale microstructural analysis, or (2) due to its thickness and metastability, any frictional melt within the fault zone is rapidly devitrified and/or over-printed, becoming unrecognisable.

3. Outlook

Identifying mechanisms that cause dynamic instability and weakening on faults is important for understanding earthquake dynamics and the seismic cycle. However, the hypocentral depths (10-15km) of many of the large earthquakes make direct observation and study impossible. Consequently developing an understanding of mechanisms and processes that control fault behaviour, strength and stability requires a multi-faceted

research approach that combines experimental, field and microstructural studies with seismic and numerical modelling to build an integrated theoretical framework. Over the past fifteen years significant advances have been made in all these fields, although an identifiable gap exists in experimental research of slip surfaces at confined, realistic stress conditions. Although the development of rotary-shear type apparatus has provided numerous insights into frictional behaviour of faults at high slip velocity, experimental conditions involving imposed velocities on nominally dry samples at low normal stresses and high displacements, imply that the experiments may not be indicative of fault processes at depth. This thesis has demonstrated both the relevance and potential benefits of integrating classic triaxial experiments with other modes of research to provide important insights into potential triggering mechanisms, slip processes and micromechanics at various slip rates early during slip events.

The application of high spatial resolution microstructural analysis in this project has demonstrated that very thin frictional melt layers can be generated during small slip events (< 500μm) and at moderate effective normal stresses (> 200MPa). This discovery opens up potential for greater understanding of the contribution of melting and other amorphisation processes to the mechanics of seismic and aseismic slip. It is hoped that this work stimulates an examination of melting and other amorphisation processes in a wide range of rock types via (1) experimental approaches, and (2) more careful analysis of natural fault damage products employing techniques such as high resolution SEM and SEM-CL, in conjunction with FIB-TEM and high spatial resolution micro analysis tools.

References

Ainslie, N. G., J. D. Mackenzie, and D. Turnbull (1961), Melting Kinetics of Quartz and Cristobalite, *Journal of Phyical Chemistry A*, *65*(10), 1718-1724.

Allen, C. M., and E. Drauglis (1969), Boundary layer lubrication: monolayer or multilayer, *Wear*, *16*, 363-384.

Alonso, P., L. Halliburton, E. Kohnke, and R. Bossoli (1983), X-ray-induced luminescence in crystalline SiO2, *Journal of Applied Physics*, *54*(9), 5369-5375.

Anderson, E. M. (1905), The dynamics of faulting, *Transactions of the Edinburgh Geological Society*, *8*, 387-402.

Anderson, E. M. (1942), *The Dynamics of Faulting and Dyke Formation with Applications to Britain*, Oliver and Boyd, Edinburgh.

Antonellini, M., and A. Aydin (1994), Effect of faulting on fluid flow in porous sandstones: petrophysical properties, *AAPG Bulletin*, *78*(3), 355-377.

Archard, J. F. (1958/1959), The temperature of rubbing surfaces, *Wear*, *2*, 438-455.

Austrheim, H., and T. Andersen (2004), Pseudotachylytes from Corsica: Fossil earthquakes from a subduction complex, *Terra Nova*, *16*(4), 193-197.

Axen, G. J. (1999), Low-angle normal fault earthquakes and triggering, *Geophysical Research Letters*, *26*(24), 3693-3696.

Badro, J., P. Gillet, and J. Barrat (1998), Melting and pressure-induced amorphization of quartz, *Europhysics Letters*, *42*(6), 643-648.

Bansal, N., and R. Doremus (1986), *Handbook of Glass Properties*, Academic Press Inc., London.

Baud, P., W. Zhu, and T. Wong (2000), Failure mode and weakening effect of water on sandstone, *Journal of Geophysical Research*, *105*(16371-16389).

Beeler, N. M., T. E. Tullis, and D. L. Goldsby (2008), Constitutive relationships and physical basis of fault strength due to flash heating, *Journal of Geophysical Research*, *113*(B01401), 1-12.

Bernabé, Y. (1991), Pore geometry and pressure dependence of the transport properties in sandstones, *Geophysics*, *56*(4), 436-446.

Bernard, P., P. Briole, B. Myer, H. Lyon-Caen, J. Gomez, C. Tiberi, . . . G. Stavrakakis (1997), The M_s=6.2, June 15, 1995 Aigion earthquake (Greece): evidence for low angle normal faulting in the Corinth rift, *Journal of Seismology*, *1*, 131-150.

Bestmann, M., G. Pennacchioni, G. Frank, M. Goken, and H. De Wall (2011), Pseudotachylyte in muscovite-bearing quartzite: Coseismic friction-induced melting and plastic deformation of quartz, *Journal of Structural Geology*, *33*, 169-186.

Biegel, R. L., and C. Sammis (2004), Relating Fault Mechanics to Fault Zone Structure, *Advances in Geophysics*, *47*, 65-111.

Bjornerud, M. (2010), Rethinking conditions necessary for pseduotachylyte formation: Observations from the Otago schists, South Island, New Zealand, *Tectonophysics*, *490*(1-2), 69-80.

Blacic, J. D., and J. M. Christie (1984), Plasticity and hydolytic weakening of quartz single crystals, *Journal of Geophysical Research*, *89*(B6), 4223-4239.

Boggs, S., D. Krinsley, G. Goles, A. Seyedolali, and H. Dypvik (2001), Identification of shocked quartz by scanning cathodoluminescence imaging, *Meteoritics and Planetary Science*, *36*, 783-793.

Bourbie, T., and B. Zinszner (1985), Hydraulic and Acousic Properties as a Function of Porosity in Fontainbleau Sandstone, *Journal of Geophysical Research*, *90*(B13), 11,524-511,532.

Bourova, E., and P. Richet (2012), Quartz and cristobalite: high-temperature cell parameters and volumes of fusion, *Geophysical Research Letters*, *25*(13), 2333-2336.

Bowden, F. P., and D. Tabor (1950), *The Friction and Lubrication of Solids: Part I*, Clarendon Press, Oxford.

Bowden, F. P., and D. Tabor (1964), *The Friction and Lubrication of Solids: Part II*, Clarendon Press, Oxford.

Brace, W. F. (1963), Behavior of quartz during indentation, *The Journal of Geology*, *71*(5), 581-595.

Brodsky, E. E., and H. Kanamori (2001), Elastohydrodynamic lubrication of faults, *Journal of Geophysical Research*, *106*(B8), 16357-16374.

Brown, K. M., and Y. Fialko (2012), 'Melt welt' mechanism of extreme weakening of gabbro at seismic slip rates, *Nature*, *488*, 638-641.

Bruijn, R. (2014), A comparison between deformation lamellae and planar deformation features in natural quartz using SEM and SEM with EBSD technology, Utrecht University, Utrecht.

Brune, J. (2001), Fault normal dynamic loading and unloading: an explanation for 'nongouge' rock powder and lack of fault-parallel shear bands along the San Andreas fault, *Eos, Transactions AGU*, *82*(47), S22B-0655.

Brune, J., T. Henyey, and R. Roy (1969), Heat flow, stress and rate of slip along the San Andreas Fault, California, *Journal of Geophysical Research*, *74*(15), 3821-3827.

Byerlee, J. D. (1978), Friction of rocks, *Pure and Applied Geophysics*, *116*, 615-626.

Caine, J. S., J. P. Evans, and C. B. Forster (1996), Fault zone architecture and permeability structure, *Geology*, *24*(11), 1025-1028.

Cardwell, R. K., D. S. Chinn, G. F. Moore, and D. L. Turcotte (1978), Frictional heating on a fault zone with finite thickness, *Geophysical Journal of the Royal Astronomical Society*, *52*, 525-530.

Chester, F. M. (1994), Effects of temperature on friction: Constitutive equations and experiments with quartz gouge, *Journal of Geophysical Research*, *99*(B4), 7247-7261.

Chester, F. M., and J. S. Chester (2000), Stress and deformation along wavy frictional faults, *Journal of Geophysical Research*, *105*(B10), 23421-23430.

Chester, J. S., F. M. Chester, and A. K. Kronenberg (2005), Fracture surface energy of the Punchbowl fault, San Andreas system, *Nature*, *437*, 133-136.

Collettini, C., A. R. Niemeijer, C. Viti, and C. Marone (2009a), Fault zone fabric and fault weakness, *Nature*, *462*, 907-910.

Collettini, C., C. Viti, S. A. F. Smith, and R. E. Holdsworth (2009b), Development of interconnected talc networks and weakening of continental low-angle normal faults, *Geology*, *37*(6), 567-570.

Cordier, P., J. C. Doukhan, and J. Peyronneau (1993), Structural transformation of quartz and berlinite ALPO4 at high pressure and room temperature: a transmission electron microscopy study, *Physics and Chemistry of Minerals*, *20*, 176-189.

Cowie, P. A., and G. P. Roberts (2001), Constraining slip rates and spacings for active normal faults, *Journal of Structural Geology*, *23*(12), 1901-1915.

Cowie, P. A., and C. Scholz (1992), Growth of faults by accumulation of seismic slip, *Journal of Geophysical Research*, *97*(B7), 11085-11095.

Cox, S. F. (1995), Faulting processes at high fluid pressures: an example of fault-valve behavior from the Wattle Gully Fault Zone, Victoria, Australia., *Journal of Geophysical Research*, *100*(12,841-12,859).

Cox, S. F. (Ed.) (1998), *Slickenlines produced experimentally at hydrothermal conditions*, Princeton Unversity Press, Princeton.

Cox, S. F. (2010), The application of failure mode diagrams for exploring the roles of fluid pressure and stress states in controlling styles of fracture-controlled permeability enhancement in faults and shear zones, *Geofluids*, *10*, 217-233.

Cox, S. F., M. A. Knackstedt, and J. Braun (2001), Principles of structural control on permeability and fluid flow in hydrothermal systems, *Reviews in Economic Geology*, *14*, 1-24.

Cox, S. F., and M. S. Paterson (1991), Experimental Dissolution-Precipitation Creep in Quartz Aggregates at High Temperatures, *Geophysical Research Letters*, *18*(8), 1401-1404.

Dell'Angelo, L. N., and J. Tullis (1988), Experimental deformation of partially melted granitic aggregates, *Journal of Metamorphic Geology*, *6*(4), 495-515.

Delogu, F. (2004), Connection between shear instability and amorphisation, *Materials Science and Engineering A*, *367*, 162-165.

Dewers, T., and A. Hajash (1995), Rate laws for water-assisted compaction and stress-induced water-rock interaction in sandstones, *Journal of Geophysical Research*, *100*(7), 13093-13112.

Di Toro, G., D. L. Goldsby, and T. E. Tullis (2004), Friction falls towards zero in quartz rock as slip velocity approaches seismic rates, *Nature*, *427*, 436-439.

Di Toro, G., R. Han, T. Hirose, N. De Paola, S. Nielsen, K. Mizoguchi, . . . T. Shimamoto (2011), Fault lubrication during earthquakes, *Nature*, *471*, 494-498.

Di Toro, G., T. Hirose, S. Nielsen, G. Pennacchioni, and T. Shimamoto (2006a), Natural and experimental evidence of melt lubrication of faults during earthquakes, *Science*, *311*, 647-649.

Di Toro, G., T. Hirose, S. Nielsen, and T. Shimamoto (2006b), Relating high-velocity rock-friction experiments to coseisic slip in the presence of melts, in *Geophysical Monograph Series*, edited, pp. 1-14, American Geophysical Union.

Di Toro, G., S. Nielsen, and G. Pennacchioni (2005), Earthquake rupture dynamics frozen in exhumed ancient faults, *Nature*, *436*, 1009-1012.

Di Toro, G., and G. Pennacchioni (2004), Superheated friction-induced melts in zoned pseudotachylytes within the Adamello tonalites (Italian Southern Alps), *Journal of Structural Geology*, *26*, 1783-1801.

Di Toro, G., and G. Pennacchioni (2005), Fault plane processes and mesoscopic structure of a strong-type seismogenic fault in tonalites (Adamello batholith, Southern Alps), *Tectonophysics*, *402*(1-4), 55-80.

Di Toro, G., G. Pennacchioni, and S. Nielsen (2008), Pseudotachylytes and earthquake source mechanics, *International Geophysics*, *94*, 87-133.

Dieterich, J. H. (1978), Time-dependent friction and the mechanics fo stick slip, *Pure and Applied Geophysics*, *116*, 790-806.

Dieterich, J. H., and B. D. Kilgore (1994), Direct observation of frictional contacts: New insights for state-dependent properties, *Pageoph*, *143*(1/2/3), 283-302.

Dietz, E. D., T. Baak, and H. H. Blau (1970), The superheating of an albite feldspar, *Crystalline Materials*, *132*(1-6), 340-360.

Dingwell, D. B. (2007), Diffusion, viscosity and flow of melts, in *Mineral Physics, Treatise in Geophysics*, edited by G. D. Price, pp. 419-439, Elsevier, Amsterdam.

Dmitriev, V., V. Sinitsyn, R. Dilanian, D. Machon, A. Kuznetsov, E. Ponyatovsky, . . . H. Weber (2003), In situ pressure-induced solid-state amorphization in $Sm_2(MoO_4)_3$ and $Gd_2(MoO_4)_3$ crystals: chemical decomposition scenario, *Journal of Physics and Chemistry of Solids*, *64*, 307-312.

Doblas, M. (1998), Slickenside kinematic indicators, *Tectonophysics*, *295*, 187-197.

Dove, P. M., and J. D. Rimstidt (1994), Silica-water interactions, in *Silica: Physical behaviour, geochemistry and materials applications*, edited by P. J. Heaney, C. T. Prewitt and G. V. Gibbs, pp. 259-308, Mineralogical Society of America, Washington DC.

Dullien, F. (1992), Porous Media - Fluid Transport and Pore Structure, edited, Academic Press, San Diego.

El Bied, A., J. Sulem, and F. Martineau (2002), Microstructure of shear zones in Fontainebleau sandstone, *International Journal of Rock Mechanics and Mining Sciences*, *39*(7), 917-932.

Evans, B. (1984), The effect of temperature and impurity content on the indentaion hardness of quartz, *Journal of Geophysical Research*, *89*(B6), 4213-4222.

Evans, J. P., C. B. Forster, and J. V. Goddard (1997), Permeability of fault-related rocks, and implications for hydraulic structure of fault zones, *Journal of Structural Geology*, *19*(11), 1393-1404.

Faulkner, D. R., C. A. L. Jackson, R. J. Lunn, R. W. Schlische, Z. K. Shipton, C. A. J. Wibberley, and Withjack (2010), A review of recent developments concerning the structure, mechanics and fluid flow properties of fault zones, *Journal of Structural Geology*, *32*, 1557-1575.

Faulkner, D. R., T. M. Mitchell, D. Healy, and M. J. Heap (2006), Slip on 'weak' faults by the rotation of regional stress in the fracture damage zone, *Nature*, *444*, 922-925.

Fialko, Y., and Y. Khazan (2005), Fusion by earthquake fault friction: Stick or slip?, *Journal of Geophysical Research*, *110*(B12407), 1-15.

Fitz Gerald, J., J. Boland, A. McLaren, A. Ord, and B. E. Hobbs (1991), Microstructures in water-weakened single-crystals of quartz, *Journal of Geophysical Research*, *96*(B2), 2139-2155.

Flodin, E., and A. Aydin (2004), Faults with asymmetric damage zones in sandstone, Valley of Fire State Park, southern Nevada, *Journal of Structural Geology*, *26*(5), 983-988.

Fondriest, M., S. A. F. Smith, T. Candela, S. Nielsen, K. Mair, and G. Di Toro (2013), Mirror-like faults and power dissipation during earthquakes, *Geology*, *41*(11), 1175-1178.

Fournier, R. O. (1996), Compressive and tensile failure at high fluid pressure where preexisting fractures have cohesive strength, with application to the San Andraes Fault, *Journal of Geophysical Research*, *101*(B11), 25,499-425,509.

Fredrich, J. T., and B. Evans (1992), Strength recovery along simulated faults by solution transfer processes, paper presented at The 33th US Symposium on Rock Mechanics, American Rock Mechanics Association Santa Fe, New Mexico.

Fredrich, J. T., K. H. Greaves, and J. W. Martin (1993), Pore Geometry and Transport Properties of Fontainebleau Sandstone, *International Journal of Rock Mechanics, Mining Sciences and Geomechanics*, *30*(7), 691-697.

Friedman, M., J. M. Logan, and J. A. Rigert (1974), Glass-indurated quartz gouge in sliding-friction experiments on sandstone, *Geological Society of America Bulletin*, *85*, 937-942.

Frost, H. J., and M. Ashby (1982), *Deformation-mechanism maps: the plasticity and creep of metals and ceramics*, Pergamon Press, Oxford.

Frye, K., and C. Marone (2002), Effect of humidity on granular friction at room temperature, *Journal of Geophysical Research*, *107*(B11), ETG11-11 - ETG11-13.

Fujiwara, T., S. Kodaira, T. No, Y. Kaiho, N. Takahashi, and Y. Kaneda (2011), The 2011 Tohoku-Oki earthquake: displacement reaching the trench axis, *Science*, *334*(6060), 1240.

Gallagher, J., M. Friedman, J. Handin, and G. Sowers (1974), Experimental studies relating to microfracture in sandstone, *Tectonophysics*, *21*, 203-247.

Ghabezloo, S., and J. Sulem (2009), Stess dependent thermal pressurization of a fluid-saturated rock, *Rock Mechanics and Rock Engineering*, *42*, 1-24.

Giannuzzi, L. A., and F. A. Stevie (2005), *Introduction to Focused Ion Beams: Instrumentation, Theory, Techniques and Practice*, 197-204 pp., Springer, New York.

Giger, S. (2007), Permeability and Strength Evolution of Quartz Fault Gouges at Hydrothermal Conditions, 125 pp, Australian National University, Canberra.

Giger, S., S. F. Cox, and E. Tenthorey (2008), Slip localization and fault weakening as a consequnce of fault gouge strengthening - Insights from laboratory experiments, *Earth and Planetary Science Letters*, *276*, 73-84.

Giger, S., E. Tenthorey, S. F. Cox, and J. D. FitzGerald (2007), Permeability evolution in quartz fault gouges under hydrothermal conditions, *Journal of Geophysical Research*, *112*(B07202), 1-17.

Goldsby, D. L., and T. E. Tullis (2002), Low frictional strength of quartz rocks at subseismic slip rates, *Geophysical Research Letters*, *29*(17), 25-21:25-24.

Goldsby, D. L., and T. E. Tullis (2011), Flash heating leads to low frictional strength of crustal rocks at earthquake slip rates, *Science*, *334*, 216-218.

Gomez, C. T., J. Dvorkin, and T. Vanorio (2010), Laboratory measurements of porosity, permeability, resistivity, and velocity on Fontainebleau sandstones, *Geophysics* *75*(6), E191-E204.

Gotze, J. (2012), Application of cathodoluminescence microscopy and spectroscopy in geosciences, *Microscopy and microanalysis*, *18*, 1270-1284.

Gotze, J., M. Plotze, and D. Habermann (2001), Origin, spectral characteristics and practical applications of the cathodoluminescence (CL) of quartz - a review, *Mineralogy and Petrology*, *71*, 225-250.

Gotze, J., and W. Zimmerle (2000), Quartz and silica as guide to provenance in sediments and sedimentary rocks, *Contributions to Sedimentary Geology*, *21*, 1-91.

Greenwood, J. A. (1991), An interpolation formula for flash temperatures, *Wear*, *150*, 153-158.

Greenwood, J. A., and J. B. P. Williamson (1966), Contact of nominally flat surfaces, *Proceedings of the Royal Society London*, *A295*, 300-319.

Griggs, D. (1967), Hydrolytic weakening of quartz and other silicates, *Geophysical Journal International*, *14*(1-4), 19-31.

Gucsik, A., C. Koeberl, F. Brandstatter, E. Libowitzky, and W. Reimold (2003), Scanning electron microscopy, cathodoluminescence and Raman spectroscopy of experimentally shock-metamorphosed quartzite, *Meteoritics and Planetary Science*, *38*(8), 1187-1197.

Haddad, S., R. Worden, D. Prior, and P. C. Smalley (2006), Quartz Cement in the Fontainebleau Sandstone, Paris Basin, France: Crystallography and Implications for Mechanisms of Cement Growth, *Journal of Sedimentary Research*, *76*, 244-256.

Hadizadeh, J., and R. D. Law (1991), Water weakening of sandstone and quartzite deformed at various stress and strain rates, *International Journal of Rock Mechanics, Mining Sciences and Geomechanics*, *28*, 431-439.

Hamrock, B., S. Schmid, and B. O. Jacobson (1994), *Fundamentals of Fluid Film Lubrication*, 2nd ed., McGraw-Hill, New York.

Han, R., T. Hirose, and T. Shimamoto (2010), Strong velocity weakening and powder lubrication of simulated carbonate faults at seismic slip rates, *Journal of Geophysical Research*, *115*(B3), 1978-2012.

Han, R., T. Hirose, T. Shimamoto, Y. Lee, and J. Ando (2011), Granular nanoparticles lubricate faults during seismic slip, *Geology*, *39*(6), 599-602.

Han, R., T. Shimamoto, T. Hirose, J. Ree, and J. Ando (2007), Ultralow fricton of carbonate faults caused by thermal decomposition, *Science*, *316*(5826), 878-881.

Handin, J. (1969), On the Coulomb-Mohr failure criterion, *Journal of Geophysical Research*, *74*(22), 5343-5348.

Handin, J., R. Hager, M. Friedman, and J. Feather (1963), Experimental deformation of sedimentary rocks under confining pressure: Pore pressure tests, *AAPG Bulletin*, *5*, 717-755.

Hayashi, N., and A. Tsutsumi (2010), Deformation textures and mechanical behavior of a hydrated amorphous silica formed along an experimentally produced fault in chert, *Geophysical Research Letters*, *37*(L12305), 1-5.

Healy, D. (2008), Damage patterns, stress rotation and pore fluid pressures in strike-slip fault zones, *Journal of Geophysical Research*, *113*(B12407), 1-16.

Heaney, P. J. (1994), Structure and chemistry of the low-pressure silica polymorphs, in *Silica: Physical behavior, geochemistry and materials applications*, edited by P. J. Heaney, C. T. Prewitt and G. V. Gibbs, pp. 1-40, Mineralogical Society of America, Washington DC.

Heaton, T. (1990), Evidence for and implications of self-healing pulses of slip in earthquake rupture, *Physics of the Earth and Planetary Interiors*, *64*, 1-20.

Hemley, R. J., A. P. Jephcoat, H. Mao, L. C. Ming, and M. M. H (1988), Pressure-induced amorphisation of crystalline silica, *Nature*, *334*, 52-54.

Hill, D. P., and W. Thatcher (1992), An energy constraint for frictional slip on misoriented faults, *Bulletin of the Seismological Society of America*, *82*(2), 883-897.

Hirose, T., K. Mizoguchi, and T. Shimamoto (2012), Wear processes in rocks at slow to high slip rates, *Journal of Structural Geology*, *38*, 102-116.

Hirose, T., and T. Shimamoto (2005a), Slip-weakening distance of faults during frictional melting as inferred from experimental and natural pseudotachylytes, *Bulletin of the Seismological Society of America*, *95*(5), 1666-1673.

Hirose, T., and T. Shimamoto (2005b), Growth of molten zone as a mechanism of slip weakening of simulated faults in gabbro during frictional melting, *Journal of Geophysical Research*, *110*(B05202), 1-18.

Hoek, E. (1965), Rock fracture under static stress conditions, *National Mechanical Engineering Research Institute, Council for Scientific and Industrial Research, CSIR special report: MEG 383*, 1-235.

Holland, T. H. (1900), The charnockite series, a group of Archaean hypersthenic rocks in peninsula India, *Memoirs of the Geological Survey India, 28* (Part 2), 119-249.

Hsu, S. M., and M. C. Shen (1996), Ceramic wear maps, *Wear, 200*, 154-175.

Hubbert, K., and W. Rubey (1959), Role of fluid pressure in mechanics of overthrust faulting: 1. Mechanics of fluid-filled porous solidsand its application to overthrust faulting, *Geological Society of America Bulletin, 70*(3), 115-166.

Hudon, P., I. Jung, and D. R. Baker (2002), Melting of β-quartz up to 2.0GPa and thermodynamic optimization of the silica liquidus up to 6.0 GPa, *Physics of the Earth and Planetary Interiors, 130*, 159-174.

Imber, J., R. E. Holdsworth, C. A. Butler, and G. E. Lloyd (1997), Fault-zone weakening processes along the reactivated Outer Hebrides Fault Zone, Scotland, *Journal of the Geological Society, London, 154*, 105-109.

Jaeger, J. C. (1942), Moving sources of heat and the temperature of sliding contacts, *Proceedings of the Royal Society NSW, 76*, 203-224.

Jaeger, J. C. (1959), The frictional properties of joints in rock, *Geofisica pura e applicata, 43*, 148-158.

Jaeger, J. C., N. G. Cook, and R. W. Zimmerman (2007), *Fundamentals of Rock Mechanics*, 4th ed., Blackwell Publishing, Malden.

Janssen, C., R. Wirth, E. Rybacki, R. Naumann, H. Kemnitz, H. Wenk, and G. Dresen (2010), Amorphous material in SAFOD core samples (San Andreas Fault): Evidence for crush-origin pseudotachylites, *Geophysical Research Letters, 37*(L01303), 1-6.

Johnson, K. L., J. A. Greenwood, and S. Y. Poon (1971), A simple theory of asperity contact in elastohydrodynamic lubrication, *Wear, 19*, 91-108.

Johnson, T. L., and C. Scholz (1976), Dynamic properties of stick-slip friction of rock, *Journal of Geophysical Research, 81*(5), 881-888.

Kanagawa, K., S. F. Cox, and S. Zhang (2000), Effects of dissolution-precipitation processes on the strength and mechanical behaviour of quartz gouge at high-temperature hydrothermal conditions, *Journal of Geophysical Research, 105*(B5), 11,115-111,126.

Kanamori, H., and L. Rivera (2006), Energy partitioning during an earthquake, in *Earthquakes: Radiated energy and the physics of faulting*, edited by R. Abercrombie, A. McGarr, G. Di Toro and H. Kanamori, American Geophyiscal Union.

Karner, S. L., C. Marone, and B. Evans (1997), Laboratory study of fault healing and lithification in simulated fault gouge under hydrothermal conditions, *Tectonophysics, 277*, 41-55.

Kennedy, F. E. (2001), Frictional Heating and Contact Temperatures, in *Modern Tribology Handbook*, edited by B. Bhushan, CRC Press LLC, Boca Raton.

Kennedy, G. C., G. J. Wasserburg, H. C. Heard, and N. R. C (1962), The upper three-phase region in the system SiO_2 - H_2O, *American Journal of Science, 260*(7), 501-521.

Killick, A. (1990), Pseudotachylite generated as a result of a drilling 'burn-in', *Tectonophysics, 171*, 221-227.

Kingma, K. J., C. Meade, R. J. Hemley, H. Mao, and D. R. Veblen (1993), Microstructural observations of α-quartz amorphization, *Science, 259*, 666-669.

Kirkpatrick, J. D., and C. D. Rowe (2013), Disappearing ink: How pseudotachylytes are lost from the rock record, *Journal of Structural Geology*, *52*, 183-188.

Kirkpatrick, J. D., Z. K. Shipton, and C. Persano (2009), Pseudotachylytes: rarely generated, rarely preserved, or rarely reported?, *Bulletin of the Seismological Society of America*, *99*(1), 382-388.

Koizumi, Y., K. Otsuki, A. Takeuchi, and H. Nagahama (2004), Frictional melting can terminate seismic slips: Experimental results of stick-slips, *Geophysical Research Letters*, *31*(L21605), 1-4.

Lachenbruch, A., and J. Sass (1980), Heat flow and energetics of the San Andreas Fault Zone, *Journal of Geophysical Research*, *85*(B11), 6185-6222.

Lasaga, A. C., and G. V. Gibbs (1990), Ab-initio quantum mechanical calculations of water-rock interactions: Adsorption and hydrolysis reactions, *American Journal of Science*, *290*, 263-295.

Lavallee, Y., K. U. Hess, B. Cordonnier, and D. B. Dingwell (2007), A non-Newtonian rheological law for highly-crystalline dome lavas, *Geology*, *35*, 843-846.

Lee, S. W., S. M. Hsu, and M. C. Shen (1993), Ceramic wear maps: Zirconia, *Journal of the American Ceramic Society*, *76*(8), 1937-1947.

Lin, A. (1994), Glassy pseudotachylyte veins from the Fuyun fault zone, northwest China, *Journal of Structural Geology*, *16*(1), 71-83.

Lin, A. (1997), Fluidization and rapid injection of crushed fine-grained material in fault xones during episodes of seismic faulting, *Proceedings of the 30th Internation Congress*, *14*, 27-40.

Lin, A. (2008a), Landslide-related pseudotachylyte, in *Fossil Earthquakes: The Formation and Preservation of Pseudotachylytes*, edited, Springer-Verlag, Berlin Heidelberg.

Lin, A. (2008b), *Fossil earthquakes: The formation and preservation of pseudotachylytes*, Springer Berlin Heidelberg.

Lin, A., and T. Shimamoto (1998), Selective melting processes as inferred from experimentally generated pseudotachylytes, *Journal of Asian Earth Sciences*, *16*(5-6), 533-545.

Lockner, D. A., J. D. Byerlee, V. Kuksenko, A. Ponomarev, and A. Sidorin (1992), Chapter 1 Observations of quasistatic fault growth from accousitc emission, *International Geophysics*, *51*, 3-31.

Lockner, D. A., and B. Evans (1995), Densification of quartz powder and reduction of conductivity at 700°C, *Journal of Geophysical Research*, *100*(7), 13,081-013,092.

Logan, J. M., C. Dengo, N. Higgs, and Z. Wang (1992), Fabrics of experimental fault zones: their development and relationship to mechanical behavior, in *Fault Mechanics and Transport Properties of Rocks*, edited by B. Evans and T. Wong, pp. 33-67, International Geophysics.

Logan, J. M., and L. W. Teufel (1986), The Effect of Normal Stress on the Real Area of Contact During Frictional Sliding in Rocks, *Pageoph*, *124*(3), 471-485.

MacCulloch, J. (1819), *Description of the Western Isles of Scotland, including the Isle of Man*, Constable & Company, Edinburgh.

Maddock, R. H. (1983), Melt origin of fault-generated pseudotachylytes demonstrated by textures, *Geology*, *11*, 105-108.

Magloughlin, J. F. (2005), Immiscible sulfide droplets in pseuodotachylyte: Evidence for high temperature (>1200°C) melts, *Tectonophysics*, *402*(1-4), 81-91.

Magloughlin, J. F., and J. G. Spray (1992), Frictional melting processes and products in geological materials: introduction and discussion, *Tectonophysics*, *204*(3), 197-204.

Malagnini, L., S. Nielsen, K. Mayeda, and E. Boshi (2010), Energy radiation from intermediate- to large- magnitude earthquakes: Implications for dynamic fault weakening, *Journal of Geophysical Research*, *115*(B06319), 1-30.

Marone, C. (1998), Laboratory-derived friction laws and their application to seismic faulting, *Annual Review of Earth and Planetary Sciences*, *26*, 643-696.

Marshall, D. J. (1988), *Cathodoluminescence of Geological Materials*, Unwin Hyman, Boston.

Masch, L., H. Wenk, and E. Preuss (1985), Electron microscopy study of hyalomylonites - evidence for frictional melting in landslides, *Tectonophysics*, *115*, 131-160.

Masuda, T., T. Hiraga, H. Ikei, H. Kanda, Y. Kugimiya, and M. Akizuki (2000), Plastic deformation of quartz at room temperature: a Vickers nano-indentation test, *Geophysical Research Letters*, *27*(17), 2773-2776.

Mavko, G., and A. Nur (1997), The effect of a percolation threshold in the Kozeny-Carman relation, *Geophysics*, *62*(5), 1480-1482.

McClay, K. R., and P. G. Buchanan (1992), Thrust faults in inverted extensional basins, in *Thrust Tectonics*, edited by K. R. McClay, Springer Netherlands.

McGarr, A. (1999), On relating apparent stress to the stress causing earthquake fault slip, *Journal of Geophysical Research*, *104*(B2), 3003-3011.

Menendez, B., W. Zhu, and T. Wong (1996), Micromechanis of brittle faulting and cataclasitc flow in Berea sandstone, *Journal of Structural Geology*, *18*(1), 1-16.

Mitchell, T. M., and D. R. Faulkner (2009), The nature and origin of off-fault damage surrounding strike-slip fault xones with a wide range of displacements: A field study from the Atacama fault zone, northern Chile, *Journal of Structural Geology*, *31*, 802-816.

Mitchell, T. M., J. Renner, and R. Sibson (2011), Experimental fault reactivation of favourably and unfavourably oriented faults, paper presented at AGU Fall Meeting T33J-03.

Mount, V. S., and J. Suppe (1987), State of stress near the San Andreas fault: Implications for wrench tectonics, *Geology*, *15*, 1143-1146.

Mysen, B., and P. Richel (2005), *Silicate Glasses and Melts*, Elsevier B. V., Amsterdam.

Nakamura, Y., J. Muto, H. Nagahama, I. Shimizu, T. Miura, and I. Arakawa (2012), Amorphization of quartz by friction: Implication to silica-gel lubrication of fault surfaces, *Geophysical Research Letters*, *39*(L21303), 1-6.

Navrotsky, A. (1994), Thermochemistry of crystalline and amorphous silica, in *Silica: Physical behaviour, geochemistry and materials application*, edited by P. J. Heaney, C. T. Prewitt and G. V. Gibbs, pp. 309-329, Mineralogical Society of America, Washington DC.

Nguyen, P. T., L. B. Harris, C. McA Powell, and S. F. Cox (1998), Fault-valve behaviour in optimally oriented shear zones: an example at the Revenge gold mine, Kambalda, Western Australia, *Journal of Structural Geology*, *20*(12), 1625-1640.

Nielsen, S., G. Di Toro, and W. A. Griffith (2010), Friction and roughness of a melting rock surface, *Geophysical Journal International*, *182*, 299-310.

Nielsen, S., G. Di Toro, T. Hirose, and T. Shimamoto (2008), Frictional melt and seismic slip, *Journal of Geophysical Research*, *113*(B01308), 1-20.

Niemeijer, A., G. Di Toro, W. A. Griffith, A. Bistacchi, L. Smith, and S. Nielsen (2012), Inferring earthquake physics and chemistry using an integrated field and laboratory approach, *Journal of Structural Geology*, *39*, 2-36.

O'Hara, K. (2001), A pseudotachylyte geothermometer, *Journal of Structural Geology*, *23*(9), 1345-1357.

Otsuki, K., and N. Monzawa (2003), Fluidization and melting of fault gouge during seismic slip: Identification in the Nojima fault zone and implications for focal earthquake mechanisms, *Journal of Geophysical Research*, *108*(B4 2192), ESE 4-1: 4-18.

Ozawa, K., and Takizawa (2007), Amorphous material formed by the mechanochemical effect in natural pseucotachylyte of crushing origin: A case study of the Iida-Matsukawa Fault, Nagano Prefecture, Central Japan, *Journal of Structural Geology*, *29*, 1855-1869.

Pagel, M., V. Barbin, P. Blanc, and D. Ohnenstetter (2000), Cathodoluminescence in Geosciences: An Introduction, in *Cathodoluminescence in Geosciences*, edited by M. Pagel, V. Barbin, P. Blanc and D. Ohnenstetter, Springer, Berlin.

Parks, G. (1984), Surface and interfacial free energies of quartz, *Journal of Geophysical Research*, *89*, 3997-4008.

Passchier, C. W., and R. A. Trouw (2005), *Microtectonics*, 2nd ed., Springer, Berlin.

Paterson, M. S. (1970), A High-Pressure, High-Temperature Apparatus for Rock Deformation, *International Journal of Rock Mechanics, Mining Sciences and Geomechanics*, *7*, 517-526.

Paterson, M. S., and T. F. Wong (2005), *Experimental Rock Deformation - The Brittle Field*, 2nd ed., Springer-Verlag, Berlin.

Pec, M., H. Stunitz, R. Heilbronner, M. Drury, and C. de Capitani (2012), Origin of pseudotachylites in slow creep experiments, *Earth and Planetary Science Letters*, *355-356*, 299-310.

Pittarello, L., G. Di Toro, A. Bizzarri, G. Pennacchioni, J. Hadizadeh, and M. Cocco (2008), Energy partitioning during seismic slip in pseudotachylyte-bearing faults (Gole Larghe Fault, Adamello, Italy), *Earth and Planetary Science Letters*, *269*, 131-139.

Proctor, B. P., T. M. Mitchell, G. Hirth, D. L. Goldsby, F. Zorzi, J. D. Platt, and G. Di Toro (2014), Dynamic weakening of serpentinite gouges and bare surfaces at seismic slip rates, *Journal of Geophysical Research: Solid Earth*, *119*, 1-25.

Ramseyer, K., J. Baumann, A. Matter, and J. Mullis (1988), Cathodoluminescence colours of alpha-quartz., *Mineralogical Magazine*, *52*(368), 669-677.

Reches, Z., and T. A. Dewers (2005), Gouge formation by dynamic pulverization during earthquake rupture, *Earth and Planetary Science Letters*, *235*, 361-374.

Reches, Z., and D. A. Lockner (2010), Fault weakening and earthquake instability by powder lubrication, *Nature*, *467*, 452-455.

Remond, G., M. R. Phillips, and C. Roques-Carmes (2000), Importance of instrumental and experimental factors on the interpretation of cathodoluminescence data from wide band gap materials, in *Cathodoluminescence in Geosciences*, edited by M. Pagel, V. Barbin, P. Blanc and D. Ohnenstetter, pp. 59-126, Springer, Heidelberg.

Rempel, A. W. (2006), The effects of flash-weakening and damage on the evolution of fault strength and temperature, in *Earthquakes: Radiated Energy and the Physics of Faulting*, edited by R. Abercrombie, A. McGarr, G. Di Toro and H. Kanamori, American Geophysical Union.

Rempel, A. W., and J. R. Rice (2006), Thermal pressurization and onset of melting in fault zones, *Journal of Geophysical Research*, *111*(B09314), 1-18.

Revil, A. (2001), Pervasive pressure solution transfer in a quartz sand, *Journal of Geophysical Research*, *106*(B5), 8665-8686.

Reviron, N., T. Reuschle, and J. D. Bernard (2009), The brittle deformation regime of water-saturated siliceous sandstones, *Geophysical Journal International*, *178*, 1766-1778.

Rice, J. R. (1992), Fault stress state, pore pressure distributions, and the weakness of the San Andreas fault, in *Fault Mechanics and Transport Properties in Rocks*, edited by B. Evans and T. Wong, pp. 475-503, Academic Press.

Rice, J. R. (1999), Flash heating at asperity contacts and rate-dependent friction, *Eos, Transactions AGU*, *80* (46, Fall Meet. Suppl.), F681l.

Rice, J. R. (2006), Heating and weakening of faults during earthquake slip, *Journal of Geophysical Research*, *111*(B05311), 1-29.

Rodgers, D., and T. Little (2006), World's largest coseismic strike-slip offset: The 1855 rupture of the Wairarapa Fault, New Zealand, and implications for displacement/length scaling of continental earthquakes, *Journal of Geophysical Research*, *111*(B12408), 1-19.

Rowe, C. D., J. Casey Moore, F. Meneghini, and McKeiran (2005), Large-scale pseudotachylytes and fluidized cataclasites from an ancient subduction thrust fault, *Geology*, *33*(12), 937-940.

Ruina, A. (1983), Slip instablity and state variable friction laws, *Journal of Geophysical Research*, *88*(B12), 10359-10370.

Rutter, E. H., and D. H. Mainprice (1978), The effect of water on stress relaxation of faulted and unfaulted sandstone, *Pageoph*, *116*, 634-654.

Rutter, E. H., and S. White (1979), The microstructures and rheology of fault gouges produced experimentally under wet and dry conditions at temperatures up to 400°C, *Bulletin de Mineralogie*, *102*(101-109).

Sadeghi, F. (2010), Elastohydrodynamic lubrication, in *Tribology and Dynamics of Engine and Powertrain: fundamentals, applications and future trends.*, edited by H. Rahnejet, Woodhead Publishing Limited, Cambridge.

Sakellariou, A., T. Sawkins, T. Senden, and A. Limaye (2004), X-ray tomography for mesoscale physics applications, *Physica A: Statistical Mechanics and its Applications*, *339*(1-2), 152-158.

Savage, R. H. (1948), Graphite Lubrication, *Journal of Applied Physics*, *19*(1), 1-10.

Scholz, C. (1998), Earthquakes and friction laws, *Nature*, *391*, 37-42.

Scholz, C., P. Molnar, and T. L. Johnson (1972), Detailed studies of frictional sliding of grainite and implications for the earthquake mechanism, *Journal of Geophysical Research*, *77*(32), 6392-6406.

Scholz, C. H. (2002), *The Mechanics of Earthquakes and Faulting*, 2nd ed., Cambridge University Press, New York.

Shand, S. J. (1916), The pseudotachylyte of Parijs (Orange Free State), and its relation to "trap-shotten gneiss" and "flinty crush-rock", *Quarterly Journal of the Geological Society London*, *72*, 198-220.

Shimamoto, T., and A. Tsutsumi (1994), A new rotary-shear high-speed frictional testing machine: its basic design and scope of research, *Journal of Tectonic Research, Group of Japan*, *39*, 65-78.

Sibson, R. (1973), Interactions between temperature and pore-fluid pressure during earthquake faulting and a mechanism for partial or total stress relief, *Nature Phyiscal Science*, *243*, 66-68.

Sibson, R. (1974), Frictional constraints on thrust, wrench and normal faults, *Nature*, *249*, 542-544.

Sibson, R. (1975), Generation of pseudotachylyte by ancient seismic faulting, *Geophysical Journal of the Royal Astronomical Society*, *43*, 775-794.

Sibson, R. (1977), Fault rocks and fault mechanisms, *Journal of the Geological Society, London*, *133*, 191-213.

Sibson, R. (1981), Fluid flow accompanying faulting: field evidence and models, in *Earthquake Prediction: an International Review*, edited by D. W. Simpson and P. G. Richards, pp. 593-603, American Geophysical Union, Washington D.C.

Sibson, R. (1983), Continental fault structure and the shallow earthquake source, *Journal of the Geological Society*, *140*, 741-767.

Sibson, R. (1985), A note on fault reactivation, *Journal of Structural Geology*, *7*, 751-754.

Sibson, R. (1986), Brecciation processes in fault zones: inferences from earthquake rupturing, *Pageoph*, *124*(1/2), 159-175.

Sibson, R. (1989), Earthquake faulting as a structural process, *Journal of Structural Geology*, *11*(1/2), 1-14.

Sibson, R. (1990a), Conditions for fault-valve behaviour, in *Deformation Mechanisms, Rheology and Tectonics*, edited by R. J. Knipe and E. H. Rutter, pp. 15-28, Geological society Special Publication, London.

Sibson, R. (1990b), Rupture nucleation on unfavourably oriented faults, *Bulletin of the Seismological Society of America*, *80*(6), 1580-1604.

Sibson, R. (1992), Fault-valve behaviour and hydrostatic-lithostatic fluid pressure interface, *Earth-Science Reviews*, *32*, 141-144.

Sibson, R. (1994), Crustal stress, faulting and fluid flow, in *Geofluids: Origin, Migration and Evolution of Fluids in Sedimentary Basins*, edited by J. Parnell, Geological Society Special Publication, London.

Sibson, R. (2004), Frictional mechanics of seismogenic thrust systems in the upper continental crust - implications for fluid overpressures and redistribution, in *Thrust Tectonics and Hydrocarbon Systems*, edited by K. R. McClay, pp. 1-17, AAPG Memoir.

Sibson, R. (2007), An episode of fault-valve behaviour during compressional inversion? - The 2004 M_j6.8 Mid-Niigata Prefecture, Japan, earthquake sequence, *Earth and Planetary Science Letters*, *257*, 188-199.

Sibson, R., F. Robert, and K. H. Poulsen (1988), High-angle reverse faults, fluid pressure cycling and mesothermal gold-quartz deposits, *Geology*, *16*, 551-555.

Sibson, R., and V. G. Toy (2006), The habitat of fault-generated pseudotachylyte: presence vs absence of friction-melt, in *Radiated Energy and the Physics of Faulting*, edited by A. McGarr, H. Kanamori and G. Di Toro, pp. 153-166, AGU Geophysical Monograph.

Siman-Tov, S., E. Aharonov, A. Sagy, and S. Emmanuel (2013), Nanograins from carbonate fault mirrors, *Geology*, *41*(6), 703-706.

Sleep, N. H., and M. L. Blanpied (1992), Creep, compaction and the weak rheology of major faults, *Nature*, *359*, 687-692.

Smith, L., C. B. Forster, and J. P. Evans (1990), Interaction between fault zones, fluid flow and heat transfer at the basin scale, in *International Asscociation of Hydrologic Sciences Selected Papers in Hydrogeology*, edited by S. P. Newman and I. Neretnieks, pp. 41-67.

Spray, J. G. (1987), Artificial generation of pseudotachylyte using friction welding apparatus: simulation of melting on a fault plane, *Journal of Structural Geology*, *9*(1), 49-60.

Spray, J. G. (1992), A physical basis for the frictional melting of some rock-forming minerals, *Tectonophysics*, *204*, 205-221.

Spray, J. G. (1995), Pseudotachylyte controversy: fact or friction?, *Geology*, *23*, 1119-1122.

Spray, J. G. (2010), Frictional melting processes in planetary materials: from hypervelocity impact to earthquakes, *Annual Review of Earth and Planetary Sciences*, *38*, 221-254.

Stachowiak, G., and A. Batchelor (1993), *Engineering Tribology*, Elsevier, Amsterdam.

Steefel, C. L., and P. Van Cappellen (1990), A new kinetic approach to modeling water-rock interaction: The role of nucleation, precursors and Ostwald ripening, *Geochemica et Cosmochimica Acta*, *54*, 2657-2677.

Stesky, R. M. (1974), Mechanisms of high temperature frictional sliding in Westerly granite, *Canadian Journal of Earth Sciences*, *15*, 361-375.

Stesky, R. M., and S. S. Hannan (1987), Growth of contact area between rough surfaces under normal stress, *Geophysical Research Letters*, *14*(5), 550-553.

Stevens Kalceff, M. A., and M. R. Phillips (1995), Cathodoluminescence microcharacterization of the defect structure of quartz, *Physical Review B*, *52*(5), 3122-3134.

Streit, J. E., and S. F. Cox (2001), Fluid pressures at hypocenters of moderate to large earthquakes, *Journal of Geophysical Research*, *106*(B2), 2,235-232,243.

Swanson, M. (1992), Fault structure, wear mechanisms and rupture processes in pseudotachylyte generation, *Tectonophysics*, *204*, 223-242.

Tenthorey, E., and S. F. Cox (2006), Cohesive strengthening of fault zones during the interseismic period: An experimental study, *Journal of Geophysical Research*, *111*(B09202), 1-14.

Tenthorey, E., S. F. Cox, and H. F. Todd (2003), Evolution of strength recovery and permeability during fluid-rock reaction in experimental fault zones, *Earth and Planetary Science Letters*, *206*(2), 161-172.

Thiry, D., M. Ayrault, and J. Grisoni (1998), Ground water-silicification and leaching in sands: Example of the Fontainebleau Sand (Oligocene) in the Paris Basin, *Geological Society of America Bulletin*, *100*, 1283-1290.

Thompson, J. G. (1934), Effect of cold-rolling on the indentation hardness of copper, *Journal of Research of the National Bureau of Standards*, *13*, 745-756.

Tkacova, K., H. Heegn, and N. Stevulova (1993), Energy transer and conversion during comminution and mechanical activation, *International Journal of Mineral Processing*, *40*, 17-31.

Tsutsumi, A., and T. Shimamoto (1997), High-velocity frictional properties of gabbro, *Geophysical Research Letters*, *24*(6), 699-702.

Ujiie, K., H. Yamaguchi, A. Sakaguchi, and S. Toh (2007), Pseudotachylytes in an ancient accretionary complex and implication for melt lubrication during subduction zone earthquakes, *Journal of Structural Geology*, *29*, 599-613.

Urbain, G., Y. Bottinga, and P. Richet (1982), Viscosity of liquid silica, silicates and alumino-silicates, *Geochimica et Cosmochimica Acta*, *46*, 1061-1072.

Van den Kerkhol, A., and U. F. Hein (2001), Fluid inclusion petrography, *Lithos*, *55*, 27-47.

Venkataraman, A., and H. Kanamori (2004), Observational constrainsts on the fractrue energy of subduction zone earthquakes, *Journal of Geophysical Research*, *109*(B05302), 1-20.

Violay, M. S., S. Nielsen, B. Gilbert, A. Cavallo, P. Azais, S. Vinciguerra, and G. Di Toro (2014), Effect of water on the frictional behaviour of cohesive rocks during earthquakes, *Geology*, *42*(1), 27-30.

Viti, C. (2011), Exploring fault rocks at the nanoscale, *Journal of Structural Geology*, *33*, 1715-1727.

Wagstaff, F. E. (1969), Crystallization and melting kinetics of cristobalite, *Journal of the American Ceramic Society*, *52*(12), 650-654.

Watson, G., and S. Parker (1995), Quartz amorphisation: A dynamical instability, *Philosophical Magazine Letters*, *71*(1), 59-64.

Wenk, H. (1978), Are pseudotachylites products of fracture or fusion?, *Geology*, *6*, 507-511.

Wenk, H., L. R. Johnson, and L. Ratschbacher (2000), Pseudotachylites in the Eastern Peninsular Ranges of California, *Tectonophysics*, *321*, 253-277.

Wernicke, B. (1995), Low-angle normal faults and seismicity: A review, *Journal of Geophysical Research*, *100*(B10), 20159-20174.

Wibberley, C. A. J., and T. Shimamoto (2005), Earthquake slip weakening and asperities explained by thermal pressurization, *Nature*, *436*, 689-692.

Wilson, J. E., J. S. Chester, and F. M. Chester (2003), Microfracture analysis of fault growth and wear processes, Punchbowl Fault, San Andreas System, California, *Journal of Structural Geology*, *25*(11), 1855-1873.

Winters, R. R., A. Garg, and S. Hammack (1992), High-resolution transmission electron microscopy of pressure-amorphized α-quartz, *The American Physical Society*, *69*(26), 3751-3753.

Wintsch, R. P. (1995), Fluid-rock reaction weakening of fault zones, *Journal of Geophysical Research*, *100*(B7), 13021-13032.

Wolf, D., P. R. Okamoto, J. F. Lutsko, and M. Kluge (1990), Thermodyamic parallels between solid-state amorphization and melting, *Journal of Materials Research*, *5*(2), 286-301.

Yang, X., and S. McKeever (1990), The pre-dose effect in crystalline quartz, *Journal of Physics D: Applied Physics*, *23*(2), 237-244.

Yund, R. A., M. L. Blanpied, J. Tullis, and J. D. Weeks (1990), Amorphous material in high strain experimental fault gouges, *Journal of Geophysical Research*, *95*(B10), 15589-15602.

Zang, A., C. F. Wagner, and G. Dresen (1996), Acoustic emission, microstructure and damage model of dry and wet sandstone stressed to failure, *Journal of Geophysical Research*, *101*(B8), 17507-17521.

Appendix 1

Apparatus calibration and corrections

1. Overview

Experiments were undertaken using an internally-heated, gas-medium, rock deformation apparatus [*Paterson*, 1970]. Argon is used as the confining medium and the apparatus allows the independent control and measurement of temperature, pore fluid pressure, axial displacement rate and axial load.

The sample is heated by a two-zone, vertically-orientated furnace located within the pressure vessel. The furnace consists of two independent molybdenum windings that provide uniform temperature in an approximately 20mm long 'hot-zone'. The windings are coiled onto a grooved high-density alumina tube insulated by fibrous alumina-silica (ASH) and then tightly packed within a stainless steel can. To minimise thermal instability resulting from convection within the argon confining medium, the space above the hot zone within the central bore of the furnace is filled with a removable steel-alumina sleeve.

Temperature is monitored using a type-K (chromel [90% nickel, 10% chromium] - alumel [95% nickel, 2% manganese, 2% aluminium and 1% silicon]) thermocouple inserted through the upper hollow PSZ pistons to immediately (<1mm) above the alumina spacer at the upper end of the sample.

Axial load is measured using an internal load cell and is generated through axial shortening produced by a rate-controllable hydraulic axial displacement system. The axial load/force can be converted to axial stress (σ_1) if it is assumed that deformation involves constant volume deformation. The amount of axial shortening is measured outside the pressure vessel using a linear variable differential transducer (LVDT).

Axial load is applied to the sample through partially stabilized zirconia (Nilcra™ TS, MgO stabilised PSZ) ceramic pistons. The pistons have a 2 mm diameter axial hole

which allows the pressurised fluid to access the specimen [*Tenthorey and Cox*, 2006; *Giger et al.*, 2008]. To maintain constant pore fluid pressure during deformation, the pressurised fluid is isolated from the pore fluid intensifier and then pore pressure servo-controlled by a volume monitor.

During the first 15 months of the project, significant refurbishments of the apparatus were undertaken, including:

a) The incorporation of a newly-designed, fully digital data recording system
b) Changes to the upper pore fluid volume monitor with the new system eliminating the need for a gear box assembly
c) The construction of a new furnace.
d) Significant maintenance to the confining pressure pumping system

Due to these changes to the apparatus, particularly in the data acquisition processes, a complete recalibration was undertaken. Although calibration techniques have previously been developed, a summary of the methods involved are outlined in the following section.

1.1 Apparatus calibration and corrections

1.1.1 Confining pressure and pore fluid pressure calibrations

Confining pressure is measured by a Harwood manganin cell and pore fluid pressure is measured by an electric resistance strain gauge pressure transducer. The output voltage from these pressure gauges was calibrated using a Heise pressure gauge and an open system between the pore fluid and confining pressure.

1.1.2 Calibration of LVDTs

The linear variable differential transducers (LVDTs) are used to precisely measure displacement and the apparatus contains three: one LVDT measures the piston displacement on the outside of the pressure vessel and two are located in the pore fluid volume monitors and are used to (1) measure the volume of the pore fluid injected into, or leaving the sample, and (2) control the limit switches for servo-controlled pore fluid system. These LVDTs are calibrated by using a micrometer to measure (with an accuracy of approximately 1μm) the displacement and establish the relationship to the LVDT output voltage.

1.1.3 Temperature calibration of the furnace

The ability to independently control the power to the two separate furnace windings allows the furnace to be calibrated to produce a uniform temperature distribution along a 20mm zone corresponding with the location of the sample. Outside this zone there is a steep fall-off in temperature that is necessary to prevent the thermal destruction of the O-ring seals located at the top and bottom of the jacketed assembly.

The calibration of temperature distribution along the length of the sample assembly is undertaken using an assembly of hollow PSZ pistons and a hollow alumina sample that allows an Inconel sheathed type-K thermocouple to traverse the full length of the assembly. The power settings for the upper and lower windings are then adjusted until the desired temperature profile is achieved. The furnace calibration is repeated incrementally over a range of temperatures from 300°C to 927°C and the range of operating confining pressures from 30MPa to 250MPa. As the furnace ages, calibrations are also periodically repeated to assess changes in the temperature profile arising from the deterioration of furnace properties and efficiency.

1.1.4 Calibration of the internal load cell

The internal load cell used in the apparatus consists of four SR-4 strain gauges arranged in a Wheatstone bridge configuration. A critical factor in accessing precise data from the load cell is the accurate measurement of its elastic distortion [*Paterson and Wong*, 2005]. As the distortion of the load cell is measured as a component of the total displacement this includes contributions from elastic distortions in the apparatus frame, pistons and the sample, as well as the load cell.

To eliminate other contributions to overall distortion, the load cell was calibrated by undertaking parallel tests using a symmetrical steel spring with known spring constant and a steel cylinder of known dimensions and Young's modulus. The recorded cylinder displacement is then subtracted from the spring displacement at a common load cell output voltage so that the load cell calibration factor ($\delta L/\delta V$) can be calculated:

$$\delta L/\delta V = \frac{(\delta D_s/\delta V - \delta D_c/\delta V)}{1/k_s - \lambda/\pi r^2 E} \qquad 1$$

where, $\delta D_s/\delta V$ is the ratio of the spring displacement and output voltage, $\delta D_c/\delta V$ is the relationship between the cylinder displacement and output voltage, k_s is the spring constant determined using an Instron Press (pers. comm. *Jackson*, 1997), λ is the length of the steel cylinder, r is the radius and E is the elastic modulus of the steel cylinder.

Calibrations were undertaken at room temperature and over a range of confining pressures from atmospheric pressure – 200MPa. A slight elastic hysteresis was observed between loading and unloading. As the deformation experiments are concerned with the loading of the sample, only the loading phase of the spring and steel cylinder measurements were used in the calculation of the load cell gain.

1.1.5 Corrections for apparatus elastic distortion

For calculations of strain and strain rate, the axial displacement measured using the LVDT must be corrected for the component contributed by the elastic distortion of the apparatus (including the frame, load cell and pistons). The extent of apparatus distortion is typically proportional to the applied force (although some non-linearity occurs at small forces [*Paterson and Wong*, 2005]). A calibration was undertaken in 2004 (pers. comm. *Tenthorey,* 2004) using a specimen composed of LUCALOX, a high purity aluminium oxide ceramic with the same dimensions and assembly as the usual rock samples. The apparatus distortion is calculated by subtracting the portion of displacement accommodated by the LUCALOX from the total displacement (D_T), thus giving an indication of the displacement arising from the apparatus:

$$Apparatus\ Distortion = \frac{D_T}{L} - \frac{\lambda_s}{\pi r^2 E} \qquad 2$$

Where L is load, λ_s is the length of specimen, r is its radius and E is the Young's modulus of the LUCALOX. Apparatus distortion has been calculated to be approximately 0.0149mm/kN axial load (pers comm. *Tenthorey,* 2004).

1.1.6 Determining slip velocity of stick-slip events

Increased constraints on slip duration and insights into seismic slip velocity and acceleration were explored through the installation of a seismometer and accelerometer at the top of the apparatus as outlined in Chapter 2. However, as noted in the earlier discussion, the estimated rupture time is several orders of magnitude less than the sampling rate of the seismic instrumentation and therefore it is suggested the seismic data recorded during the experiments is not sufficient to provide absolute information about rupture propagation. Additional work has been undertaken to increase time-resolution using a laser interferometry system described in the Section 2.1 of Chapter 4. This method has allowed an indirect quantification of sample slip velocity by measuring the vertical motion of the apparatus yoke relative to the pressure vessel. The line-of-sight measurement made by the interferometer is equivalent in its position to the existing LVDT. The calibrated displacement measurements made by the LVDT have been used to scale the interferometry data. Effects of machine stiffness have been estimated and adjusted using the apparatus distortion tests outlined in Appendix 1.1.5.

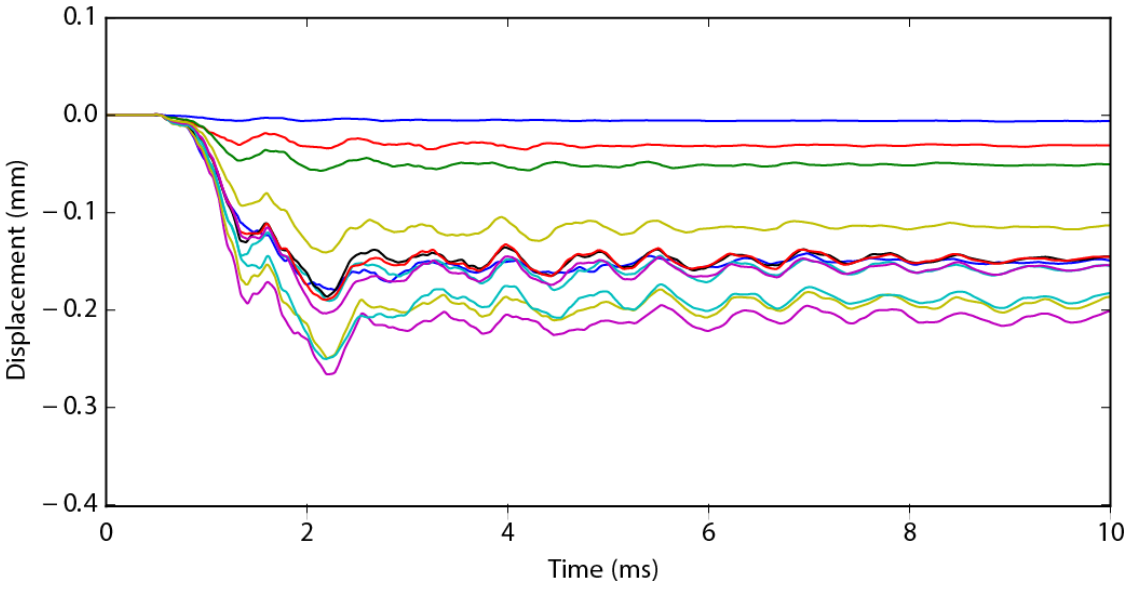

Figure 1: Unprocessed time-displacement curves for a series of experimental tests using the interferometry system.
Each line represents a 10millisecond record of a slip event and the subsequent machine resonance. The largely regular signal oscillations are thought to be the result of reverberation of the stick-slip event through different components of the apparatus. Note the similarity in duration of the different slip events, regardless of displacement.

The interferometry system utilises a trigger system and data acquisition buffer to record 2 seconds of data, prior to, during and after the slip event. Examples of slip events produced during testing of the system are shown in Figure 1. If it is assumed that, to a first order, slip is represented by a logistic function, the duration of the slip event can be estimated (Fig. 2). After the initial slip event, indicated by the significant rapid movement of the yoke at between approximately 0.7-1.7ms, approximately regular oscillations commence that thought to be the result of ringing in the apparatus and loading frame as a consequence of the sample slip. Further investigation is needed to better understand the machine response to slip. However, an estimate of maximum velocity can be calculated by taking the first derivative of the fitted curve and indicates velocities of up to 40cm.s^{-1} for slip on existing fault surfaces (Fig. 2B).

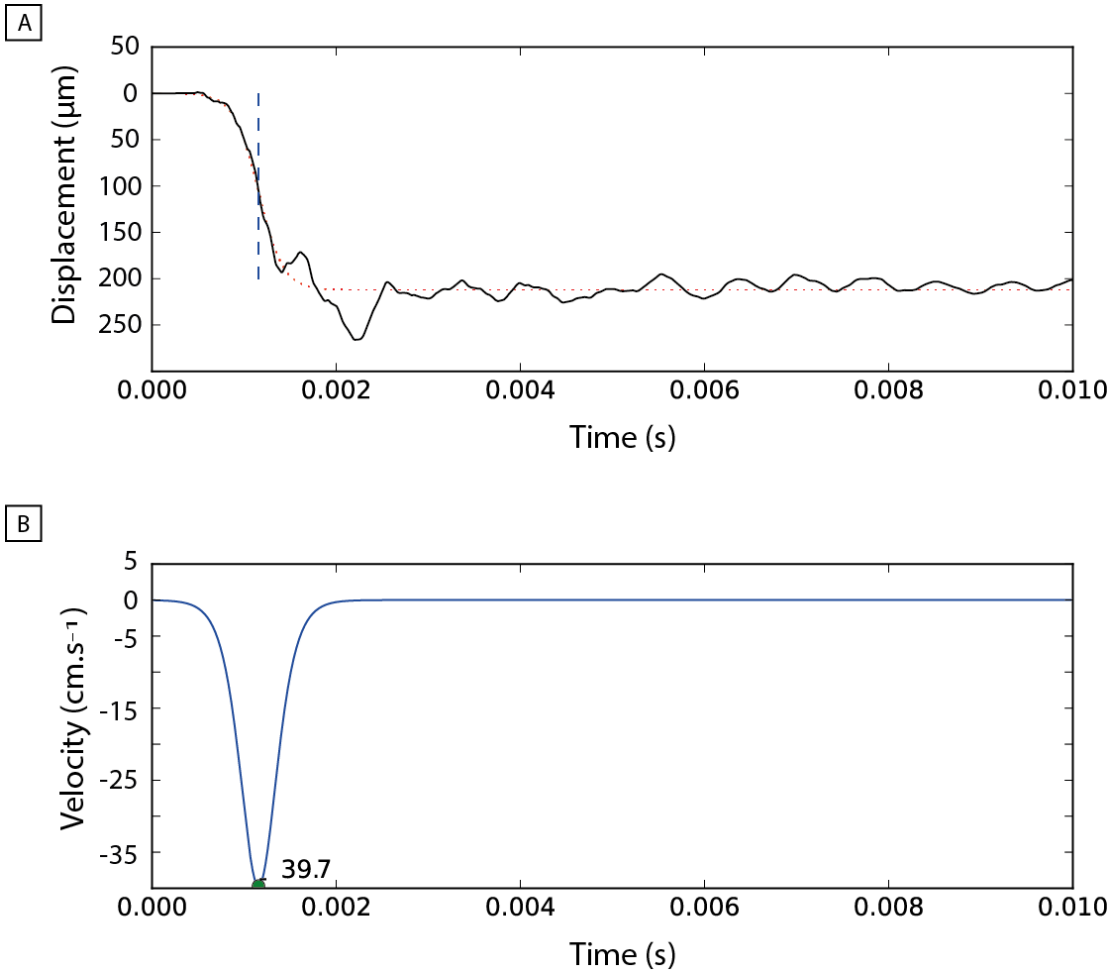

Figure 2: Modelled displacement and velocity as a function of time during slip.
(A) The raw displacement data is represented by the solid black line and has been scaled using the displacement data recorded from the LVDT. The red dashed line indicates the fitted curve assuming sigmoidal-type behaviour. The vertical dashed line marks the point of maximum velocity. (B) The solid blue line represents the corresponding modelled velocity, with a peak velocity at approximately 40cm.s^{-1}.

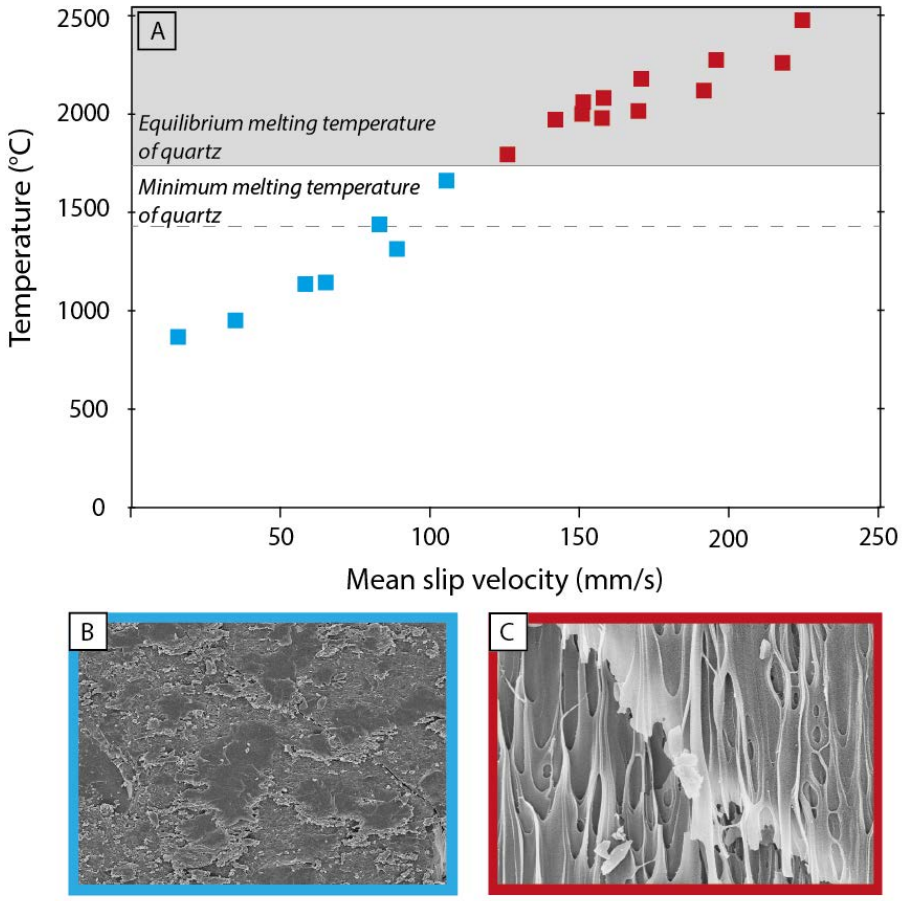

Figure 3: Estimated fault asperity temperatures.
(A) Asperity temperatures for faults experiencing stick-slip have been calculated using Equation 8 in Chapter 3. There is a strong correlation between the calculated asperity temperatures and the observed microstructures. Faults that produce small displacements, and consequently lower velocities, have reduced estimated asperity temperatures. All experiments indicated by the blue squares in (A) do not have sheared melt textures, but rather have gouge covered surfaces with the formation of the fractured glass patches indicated in (B). In contrast all experiments indicated by the red squares in (A) have larger displacements and higher velocities, producing the sheared melt textures as indicated in (C).

A key observation from the analysis of the preliminary interferometry data is the consistency of the modelled slip durations. While this suggests that the apparatus may play an important role in influencing slip rates and duration, it has allowed a first order estimation of the mean slip velocity in the existing experiments. If it is assumed that these experiments similarly slip over time intervals of approximately 1 millisecond, and that slip during this interval is approximately linear, fault asperity temperatures can be estimated and are shown in Figure 3. Although this data suggests a continuum of slip velocities from slow (< 10cm.s^{-1}) to fast (>10cm.s^{-1}) rather than the two distinct regions, as was qualitatively described in Chapter 2, there is a strong correlation between estimated slip velocities and observed microstructures. All 'high-velocity' slip events are characterised by the formation of drawn out glass filaments and the thermal modelling suggests that these events have the highest asperity temperatures. In contrast the 'low-velocity' slip experiments are microstructurally characterised by the formation of fractured glass patches and the calculated temperatures are uniformly lower.

Appendix 2

Corrections for jacket strength contribution and change in contact area of the sliding interface

1. Experimental methodology

When movement occurs along the experimental fault surfaces, both the annealed copper sleeve and outer jacket must deform, shearing along a narrow zone adjacent to the inclined fault surfaces. Consequently the sleeve and jacket contribute to the strength of the assembly and this additional strength must be calculated and corrected by subtracting the force required to deform the jackets from the total force recorded by the load cell. The methodology adopted for the calculation of the jacket correction uses a low strength sliding assembly to simulate the sliding fault surfaces and identify the strength contribution of a single metal sleeve. This was achieved by first calculating the strength of a double-jacket assembly (comprising of an outer jacket and inner sleeve) and then a single-jacket assembly (Fig. 1B). The subtraction of the strength of the single-jacketed assembly from the double-jacketed assembly allows an estimation to be made of the strength of the inner metal sleeve, which in turn, can be used to estimate the total jacket strength. Jacket strength calibration experiments (Table 1), have been undertaken over a range of confining pressures, axial displacement rates and temperatures, reflecting experimental conditions of the deformation experiments.

1.1 Room temperature experiments

The room temperature jacket strength experiments used a test assembly comprising of two alumina forcing blocks ground on a 30º incline relative to the maximum shortening direction, between which a 0.5mm thick graphite foil was placed (Fig. 1A). As a suite of

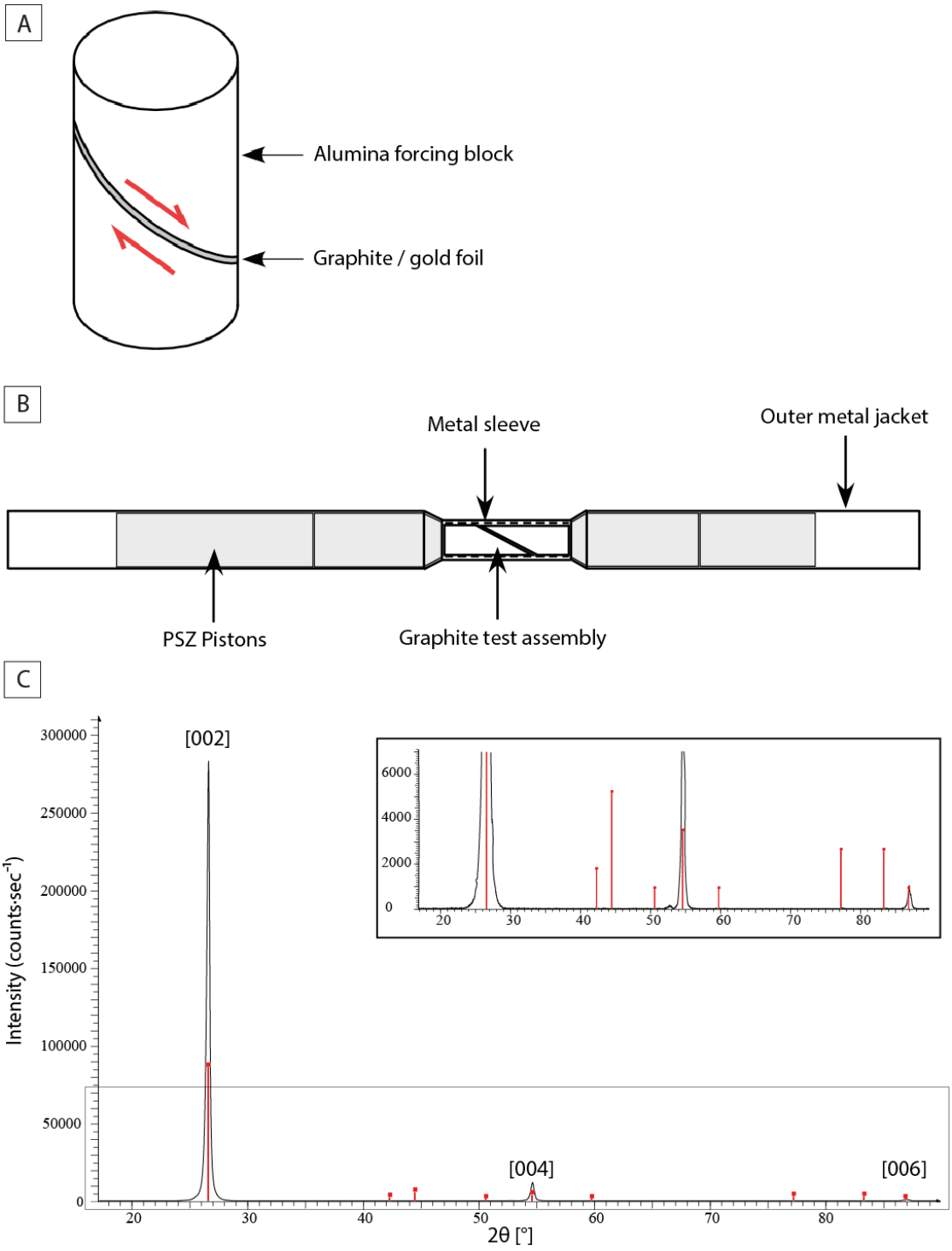

Figure 1: Jacket strength calibration assembly.
(A) Jacket strength calibration assembly comprising of two alumina forcing blocks between which is placed a single layer of graphite foil. During the high temperature jacket calibration experiments the graphite layer is replaced with annealed gold. (B) Jacket arrangement for strength correction experiments showing the location of the second metal sleeve – refer to text for details. (C) X-Ray diffractogram for the graphite foil used for jacket strength calibrations. The diffraction profile shows a very sharp (002) reflection, with minor (004) and (006) peaks also present. The graphite peaks associated with the 010, 011, 012, 013, 110 and 112 planes are absent indicating that the graphite crystals in the foil contain a very strong crystallographic orientation. Inset shows magnified diffraction profile to highlight background levels. An unexplained minor peak is distinguishable from the background at 53°, however, the peak intensity indicates only a trace concentration.

Table 1: Details of jacket strength calibration experiments.

Experiment	Temp (°C)	$P_{(c)}$ (MPa)	No. of Jackets	Material at Fault Interface	Type of Jacket (sleeve/jacket)	Axial Displacement Rate ($mm \cdot s^{-1}$)
JSC021	25	1	1	Graphite	Cu	$3.6x10^{-4}$, $1.78x10^{-3}$
JSC022	25	5	1	Graphite	Cu	$3.6x10^{-4}$, $1.78x10^{-3}$
JSC014	25	10	1	Graphite	Cu	$3.6x10^{-4}$, $1.78x10^{-3}$
JSC018	25	10	2	Graphite	Cu/Cu	$3.6x10^{-4}$, $1.78x10^{-3}$
JSC013	25	20	1	Graphite	Cu	$3.6x10^{-4}$, $1.78x10^{-3}$
JSC016	25	20	2	Graphite	Cu/Cu	$3.6x10^{-4}$, $1.78x10^{-3}$
JSC012	25	30	1	Graphite	Cu	$3.6x10^{-4}$, $1.78x10^{-3}$
JSC015	25	30	2	Graphite	Cu/Cu	$3.6x10^{-4}$, $1.78x10^{-3}$
JSC011	25	30	1	Graphite	Cu	$3.6x10^{-4}$, $1.78x10^{-3}$
JSC020	25	30	1	Graphite	Cu♦	$3.6x10^{-4}$, $1.78x10^{-3}$
JSC019	25	30	1	Graphite	Cu	$3.6x10^{-4}$, $1.78x10^{-3}$
JSC004	25	50	1	Graphite	Cu	$3.6x10^{-4}$, $1.78x10^{-3}$
JSC005	25	50	2	Graphite	Cu/Cu	$3.6x10^{-4}$, $1.78x10^{-3}$
JSC027	25	50	2	Graphite	Cu/Cu‡	$3.6x10^{-4}$
JSC028	25	50	1	Graphite	Cu‡	$3.6x10^{-4}$
JSC006	25	100	1	Graphite	Cu	$3.6x10^{-4}$, $1.78x10^{-3}$
JSC007	25	100	2	Graphite	Cu/Cu	$3.6x10^{-4}$, $1.78x10^{-3}$
JSC008	25	100	1	Graphite	Cu	$3.63x10^{-3}$
JSC009	25	100	2	Graphite	Cu/Cu	$3.63x10^{-3}$
JSC010	25	100	2	Graphite	Cu/Cu	$3.63x10^{-3}$
JSC023	25	200	1	Graphite	Cu	$3.6x10^{-4}$, $1.78x10^{-3}$
JSC024	25	200	2	Graphite	Cu/Cu	$3.6x10^{-4}$, $1.78x10^{-3}$
JSC038	900	100	2	Gold	Fe/Fe	$3.6x10^{-4}$
JSC039	900	100	1	Gold	Fe	$3.6x10^{-4}$
JSC044	850	100	2	Gold	Fe/Fe	$1.8x10^{-4} \rightarrow 7.2x10^{-4}$
JSC046	850	100	1	Gold	Fe	$1.8x10^{-4} \rightarrow 7.2x10^{-4}$
JSC034	800	100	2	Gold	Fe/Fe	$1.8x10^{-4} \rightarrow 7.2x10^{-4}$
JSC048	800	100	2	Gold	Fe/Fe†	$1.8x10^{-4} \rightarrow 7.2x10^{-4}$
JSC032	800	100	1	Gold	Fe	$1.8x10^{-4} \rightarrow 7.2x10^{-4}$
JSC043	750	100	2	Gold	Fe/Fe	$1.8x10^{-4} \rightarrow 7.2x10^{-4}$
JSC042	750	100	1	Gold	Fe	$1.8x10^{-4} \rightarrow 7.2x10^{-4}$
JSC033	700	100	2	Gold	Fe/Fe	$1.8x10^{-4} \rightarrow 7.2x10^{-4}$
JSC031	700	100	1	Gold	Fe	$1.8x10^{-4} \rightarrow 7.2x10^{-4}$
JSC049	700	100	2	Gold	Cu/Fe	$1.8x10^{-4} \rightarrow 7.2x10^{-4}$
JSC045	650	100	2	Gold	Fe/Fe	$1.8x10^{-4} \rightarrow 7.2x10^{-4}$
JSC047	650	100	1	Gold	Fe	$1.8x10^{-4} \rightarrow 7.2x10^{-4}$
JSC029	600	100	2	Gold	Fe/Fe	$1.8x10^{-4} \rightarrow 7.2x10^{-4}$
JSC030	600	100	1	Gold	Fe	$1.8x10^{-4} \rightarrow 7.2x10^{-4}$
JSC036	600	100	2	Gold	Fe/Fe	$1.8x10^{-4} \rightarrow 7.2x10^{-4}$
JSC035	600	100	1	Gold	Fe	$1.8x10^{-4} \rightarrow 7.2x10^{-4}$
JSC037	600	100	2	Gold	Fe/Fe	$1.8x10^{-4} \rightarrow 7.2x10^{-4}$
JSC040	600	100	2	Gold	Fe/Fe	$1.8x10^{-4} \rightarrow 7.2x10^{-4}$
JSC041	600	100	1	Gold	Fe	$1.8x10^{-4} \rightarrow 7.2x10^{-4}$
JSC050	400	100	2	Gold	Cu/Cu	$1.8x10^{-4} \rightarrow 7.2x10^{-4}$
JSC051	400	100	1	Gold	Cu	$1.8x10^{-4} \rightarrow 7.2x10^{-4}$
JSC052	500	100	2	Gold	Cu/Cu	$1.8x10^{-4} \rightarrow 7.2x10^{-4}$
JSC053	500	100	1	Gold	Cu	$1.8x10^{-4} \rightarrow 7.2x10^{-4}$
JSC054	600	100	2	Gold	Cu/Cu	$1.8x10^{-4} \rightarrow 7.2x10^{-4}$
JSC055	600	100	1	Gold	Cu	$1.8x10^{-4} \rightarrow 7.2x10^{-4}$

♦ Experiment to test the effect of annealing the copper jacket prior to the experiment.

‡ Forcing block oriented at 50° to the maximum principal stress.

† Sleeve made from the wasting down of the jacket material.

experiments was undertaken on misoriented faults (Chapter 3), potential differences in jacket strength resulting from changes in the jacket shear zone geometry also were tested using forcing blocks oriented at 50º to the maximum shortening direction.

Graphite foil was selected as the room temperature interfacial material owing to its low friction properties (as shown by its use as a solid state lubricant [*Savage*, 1948]) and its uniform and repeatable mechanical behaviour during the sliding experiments. The composition, structure and crystallographic orientation of the graphite foil were confirmed using XRD (Fig. 1C). The results indicate a strong crystallographic alignment, with the surface of the graphite foil aligned parallel with the basal plane of the graphite crystal structure.

Each calibration assembly was slipped for ~1mm at a nominal axial shortening rate of $0.36\mu m.s^{-1}$. To estimate the magnitude of the velocity dependence of the assembly strength, the assemblies were subjected to a velocity step after ~1mm of slip, at which point the axial displacement rate was increased to $1.78\mu m.s^{-1}$ for further ~0.2mm displacement. A number of experiments were also undertaken at an axial shortening rate of $3.63\mu m.s^{-1}$.

1.2 High temperature experiments

The jacket correction experiments undertaken at elevated temperatures used a similar test assembly to that described above. However, rather than using the graphite foil, which has the potential to oxidise at high temperatures, a thin layer (0.1mm) of annealed gold was placed at the interface between the alumina forcing blocks. Previous experiments [*Giger*, 2007] had shown that the gold has a very low shear strength when used in this application at temperatures above 600°C. Each assembly was then subjected to a velocity stepping regime, using nominal axial displacement rates of between 0.18 – 0.72 $\mu m.s^{-1}$ over a total maximum axial displacement of 1mm.

The experiments were undertaken on both double and single-jacketed assemblies at temperatures between 400-600°C for copper jackets and between 600-900°C for iron jackets. The copper tubing used for experimental jacketing is a commercial purity, thin-walled (0.25mm) tube, and the iron tubing was supplied by Uniform Tubes Inc. of Collegeville, Pennsylvania, and contains between 0.07-0.10% carbon and a number of other trace level impurities.

2. Results

2.1 Room temperature jacket corrections

The room temperature stress-displacement curves of the alumina-graphite assemblies are characterised by a poorly-defined yield point, followed by slip-hardening behaviour. Although the experimental assembly exhibits work hardening during slip, the strength differences between the single and double-sleeved assemblies does not significantly or consistently change with displacement (and are consistent with the observations of *Chester* [1994]). The dominant cause of the slip hardening is attributed to the graphite-alumina interface and/or the graphite, rather than the jacket. Although copper is well known for cold-working behaviour at low temperature, it is suggested that the most rapid formation of dislocations, may occur within the initial stages of slip [*Thompson*, 1934]. The absence of measurable strain hardening simplifies the application of the jacket correction as constant jacket strength can be assumed after yield.

The strength of the graphite assembly increases with increasing confining pressure (Fig. 2C). The pressure dependence (which suggests frictional behaviour) is attributed to the graphite-forcing block interface, rather than the metal sleeve and jacket, as the latter deforms by pressure insensitive, intracrystalline plastic deformation mechanisms. Deformation within the graphite foil layer is also possible, but examination of the deformed specimen and the location of the graphite foil relative to the alumina forcing blocks indicate that the majority of the strain is accommodated on one of the graphite-alumina interfaces.

Minor velocity strengthening was observed during the velocity stepping experiments. Results of experiments JSC008-JSC010, undertaken at nominal axial displacement rates of 3.63μm.s^{-1}, show a minor (approximately 3MPa) increase in the shear strength of the double-jacketed assemblies when compared with the experiments undertaken at an axial displacement rate of 0.36-1.78μm.s^{-1} (Fig. 2B). For the purposes of the calculation of jacket strength, the velocity effects at room temperature are too small to be accurately isolated and calculated. The essentially immaterial effect of velocity on the room temperature experiments is supported by the limited effect that velocity has on the rates of flow of copper at low temperatures [*Frost and Ashby*, 1982].

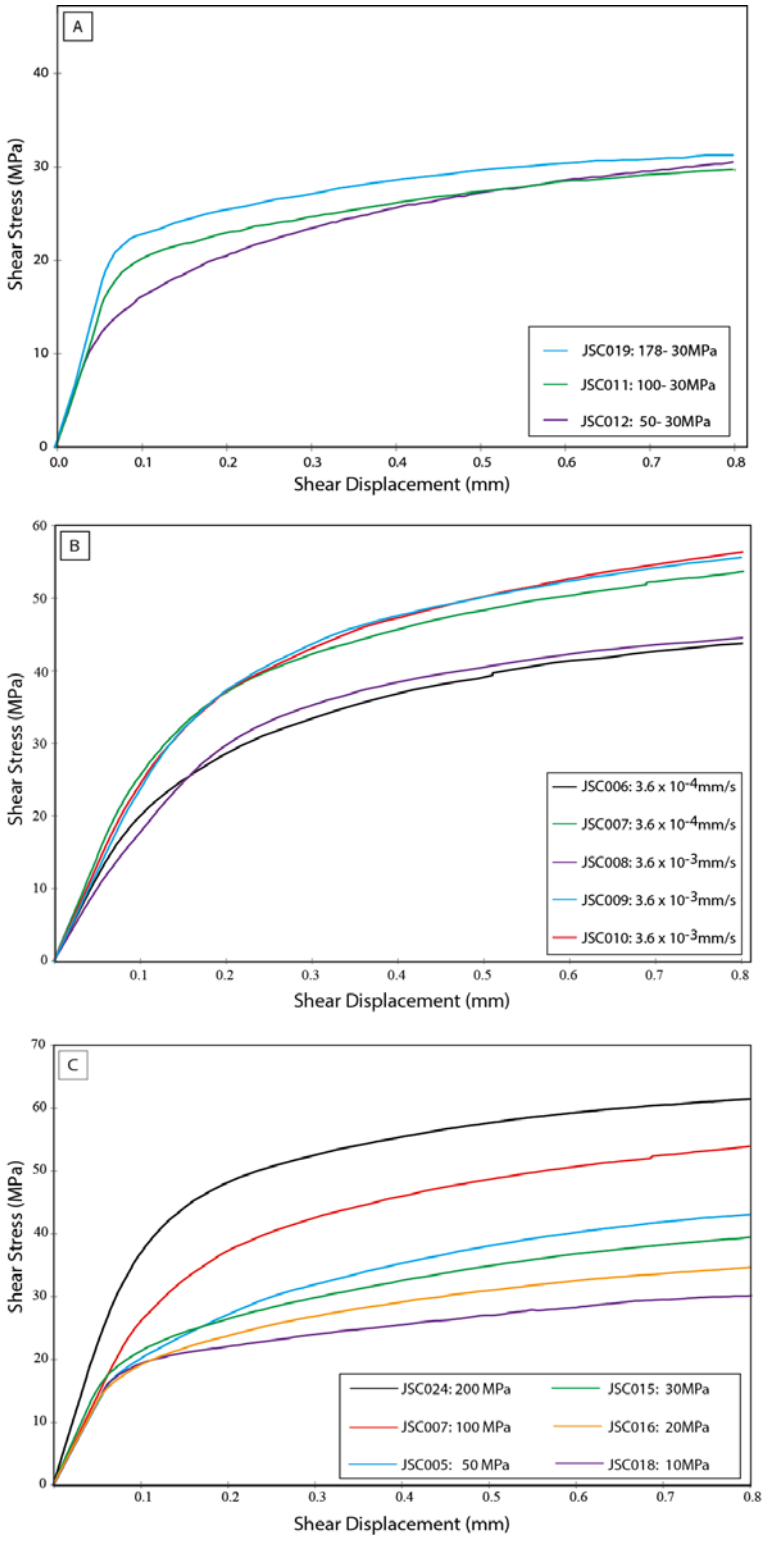

Figure 2: Room temperature jacket strength calibration experiments.
(A) The effect of jacket collapse at different confining pressures on jacket strength during the initial 0.8mm of shear displacement. When the initial collapse was undertaken at higher confining pressures it resulted in a high yield point and a lower rate of strain hardening during slip. (B) The effect of velocity on strength. Higher velocities resulted in a minor (~3MPa) increase in shear strength over the 0.8mm of shear displacement. (C) The effect of increasing confining pressure on the shear strength of the double jacketed assemblies.

In low confining pressure (< 50MPa) experiments, the yield strength was significantly reduced with decreasing confining pressure and there was a longer period of more intense strain hardening. It is suggested this phenomena is the result of permanent deformation being activated earlier on the samples deformed at lower confining pressures and is interpreted as resulting from incomplete jacket collapse onto the sample. The impact of potentially altering the extent of jacket collapse is indicated by the shape of the initial loading curve and the recorded strength during the first 1mm of displacement (Fig. 2A). As pore fluid experiments commonly involve low effective confining pressures, this observation resulted in modification of loading procedures to ensure full jacket collapse occurs prior to the commencement of deformation. Full jacket collapse is achieved by maintaining > 50MPa effective confining pressure for at least 1 hour prior to loading.

2.1.1 Calculation of jacket strength

Failure envelopes have been constructed using data from room temperature experiments undertaken at various confining pressures (Fig. 3). Best-fit values were determined for assembly strength at various displacements commencing at an initial displacement of 0.5mm. This approach was adopted to reduce the potential uncertainty arising from both the identification of the yield point (given its poor definition in the experimental results) and potential jacket collapse effects. Curves have been plotted at 0.1mm increments of axial displacement up to 0.9mm (Fig. 3A).

The results have been plotted assuming the empirical failure criterion that follows Mohr's hypothesis:

$$\sigma_1 = g(\sigma_3) \qquad 1$$

where σ_1 is a function of σ_3, although not necessarily a linear function (Fig. 3). The intercept between the failure envelope and the y-axis provides an estimate of the strength of the assembly at zero confining pressure, where it is assumed that the dominant strength of the assembly arises from the confining pressure-insensitive jacket contribution. Each of the corresponding double- and single-jacketed strength estimates are then subtracted to provide the strength of the metal sleeve.

To apply the corrections to the experimental data, the sleeve strength is considered in terms of the load (*F*) that it supports. Assuming that the total load on the double jacket assembly can be expressed as:

$$F_{J,Sl,S} = \sigma_{J,Sl,S} \cdot A_{J,Sl,S} \qquad 2$$

where $F_{J,Sl,S}$ is the load supported by the jacket (*J*), sleeve (*Sl*) and sample (*S*), $\sigma_{J,Sl,S}$ is the strength of the double jacketed assembly at zero confining pressure (as described above) and $A_{J,Sl,S}$ is the total area of the jacket, sleeve and sample. Similarly, the load supported by the single jacketed assembly is:

$$F_{J,S} = \sigma_{J,S} \cdot A_{J,S} \qquad 3$$

Thus, the load supported by the sleeve can be expressed as:

$$F_{Sl} = \sigma_{J,Sl,S} \cdot A_{J,Sl,S} - \sigma_{J,S} \cdot A_{J,S} \qquad 4$$

Assuming that the load borne by the copper jacket is proportional by area to that of the copper sleeve, the total jacket strength can be estimated as:

$$F_{J,Sl} = \frac{A_J}{A_{Sl}} F_{Sl} + F_{Sl} \qquad 5$$

For room temperature results refer to Table 3.

2.2 High temperature jacket corrections

The high-temperature jacket strength calibration experiments were undertaken assuming that the metal jackets deformed by pressure insensitive intracrystalline deformation mechanisms. Therefore experiments for both copper and iron jacket assemblies were undertaken at a constant confining pressure of 100MPa. The jacket material referred to as ‘iron’ is a low carbon (0.1%) steel and its behaviour is complicated by two crystallographic phase transitions (Ferrite + Cementite / Ferrite + Austenite / Austenite). The experimental results show a sharp strength discontinuity between 850º and 900º, which is consistent with the discontinuity observed at the Ferrite – Austenite phase boundary, and results from distinctive changes in the physical properties of the steel (such as lattice parameter, Burger’s vector, modulus and diffusion coefficients at this transition).

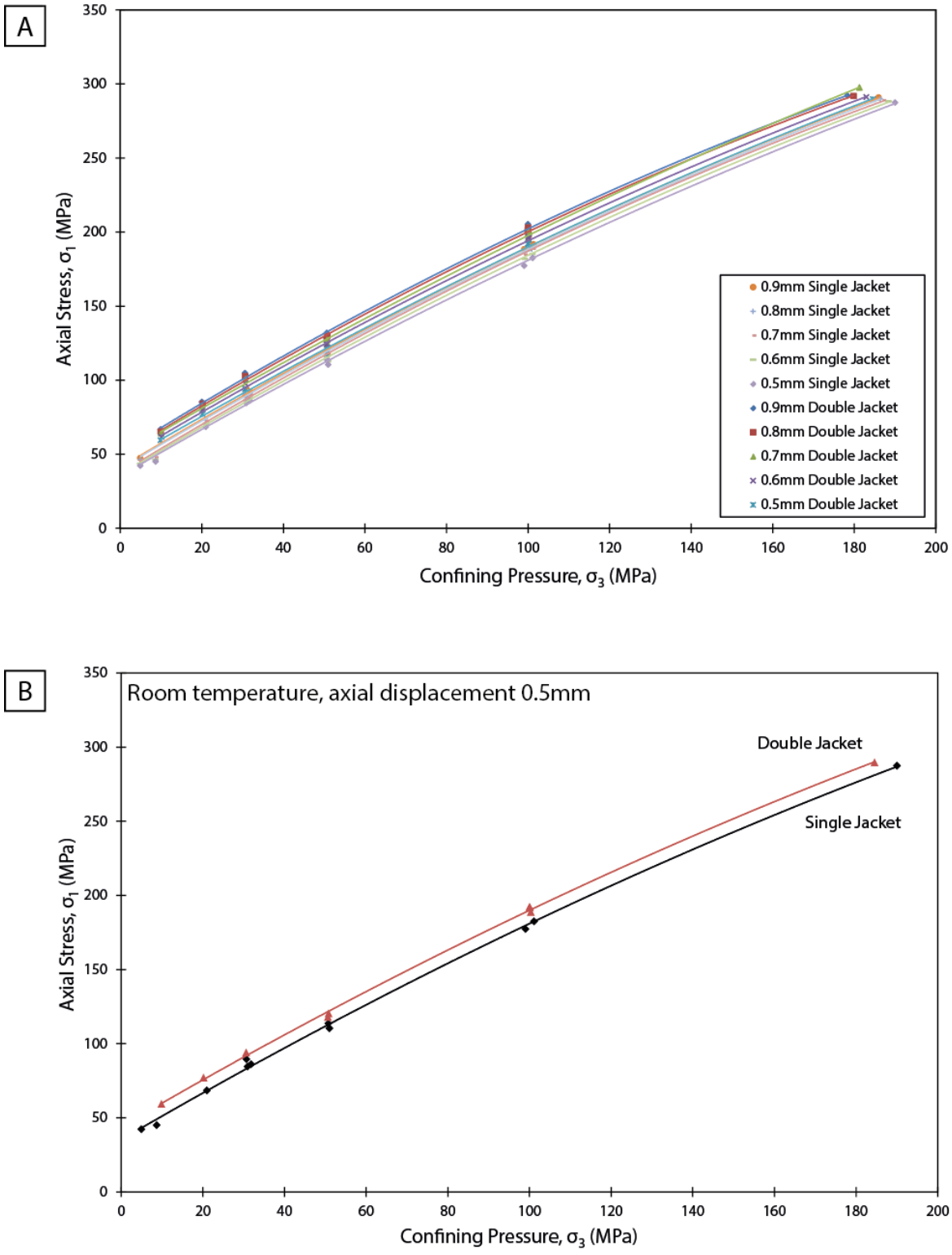

Figure 3: Results of room temperature copper jacket strength experiments
(A) Estimated failure envelopes for the graphite foil assemblies over a range of displacements with shear stress plotted as a function of normal stress. The results indicate either (1) that the failure strength of the assembly does not follow a linear Coulomb relationship or (2) that the experiments have reached the brittle-ductile transition of the graphite or graphite-alumina interface. (B) Construction of a failure envelope with axial stress plotted as a function of confining pressure. The upper group of results indicates the double-jacketed specimens while the lower group represents the results of the single jacket experiments.

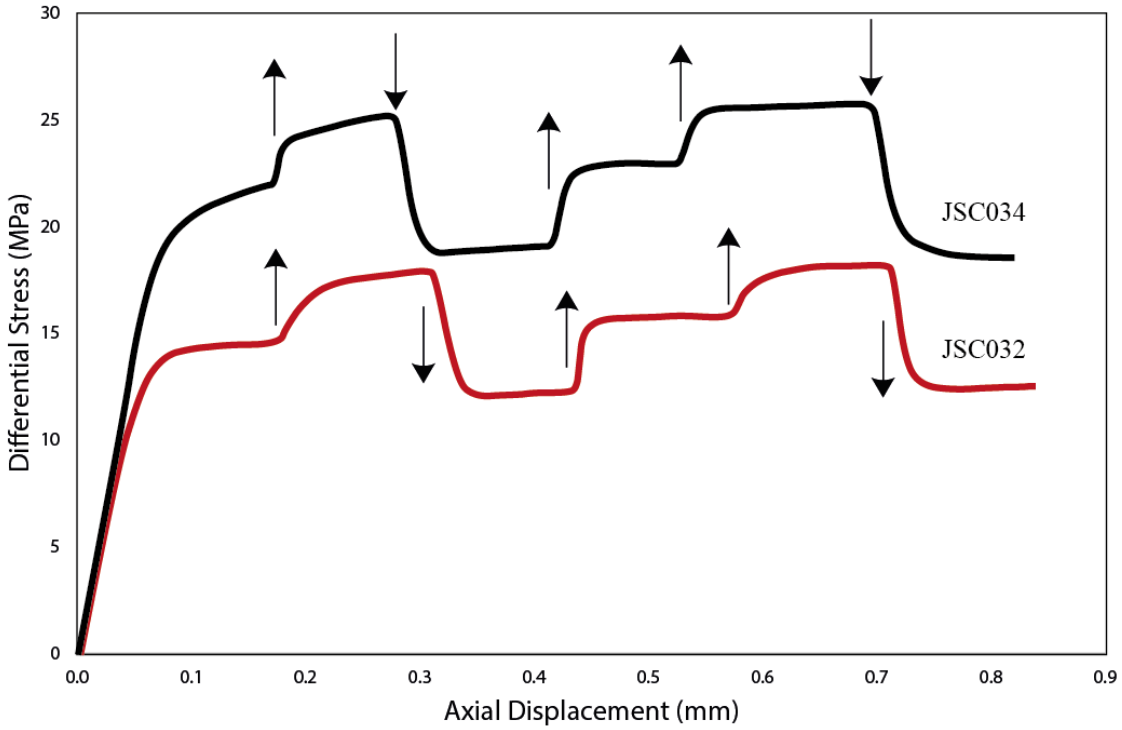

Figure 4: High temperature iron jacket strength calibration experiments
Representative experimental data showing differential stress plotted as a function of axial displacement for high temperature (800°) jacket strength experiments. The data is from JSC034 and JSC032, a double and single jacketed assembly respectively. These two curves show the effect of the velocity stepping at a single confining pressure. Arrows indicate a change in velocity (arrow pointing up indicates an increase in velocity and downwards pointing arrow indicates a velocity decrease) with experiments commencing at 0.36μm.s^{-1} before being stepped up to 0.72μm.s^{-1}, and down to 0.18μm.s^{-1}. This sequence has been repeated twice per experiment.

Published deformation mechanism maps for both copper and iron [e.g. *Frost and Ashby*, 1982] indicate an increase in deformation rate sensitivity with increasing temperatures. A velocity dependence of assembly strength was observed with the strength of the assembly increasing with increasing velocity. Although the high temperature copper experiments revealed a velocity dependence during the rate-stepping experiments, the subtraction of the single and double jacketed loads indicates that the between 400-600ºC the strain rate dependence is not large enough in the copper to be experimentally determined.

Where experiments are repeated using iron jacket material cut from different lengths, the resulting strength estimations show some variability in strength which is attributed to heterogeneity in structure and composition among the lengths of iron tubing. To overcome this issue a number of the experiments were repeated using jacketing material from different lengths of tubing to establish a representative strength.

2.2.1 Calculation of jacket strength

In high temperature experiments there is a rapid transition from elastic loading into an approximately steady-state stable sliding regime (Fig. 4). This allowed a simpler treatment of the results than could be achieved for room temperature calibrations. However, a slow leak in the hydraulics of the axial displacement system resulted in variability in nominal axial displacement rates relative to the predetermined estimated value. To allow a comparison of the data, the actual axial displacement rate was calculated from the experimental data and the stress-axial displacement rate for each experiment was plotted in log-log space. This provided a linear relationship and allowed the strength information from the desired axial displacement rates to be recovered.

The estimated strength contribution of the single and double iron-jacketed assemblies were calculated over temperatures between 600°-900°C using 50°C increments and axial displacement rates of 0.18μm.s^{-1}, 0.36μm.s^{-1} and 0.72μm.s^{-1}. The heterogeneity of the strength of the iron tubing can be seen in the distribution of the data points in Figure 5. The estimated load supported by of the single jacketed assembly was then subtracted from the corresponding double jacketed assembly to provide an estimation of the load supported by the iron sleeve.

Assuming that the load borne by the iron jacket is proportional by area to that of the iron sleeve, the estimated load supported by the iron jacketed is calculated as:

$$F_J = \frac{A_J}{A_{Sl}} F_{Sl} \qquad 6$$

where F_J is the load supported by the jacket, A_J is the area of the jacket, A_{Sl} is the area of the sleeve and F_{Sl} is the load supported by the sleeve.

To calculate the strength of the copper sleeve at high temperatures, an assembly consisting of a copper sleeve and an iron jacket was compared with the strength of an assembly consisting only of a single iron jacket. At 600°C the strength of copper jacket is negligible and by 700° it is below experimental resolution. Final calculated strength contributions of the iron jacket and copper sleeve assemblies are shown in Table 3.

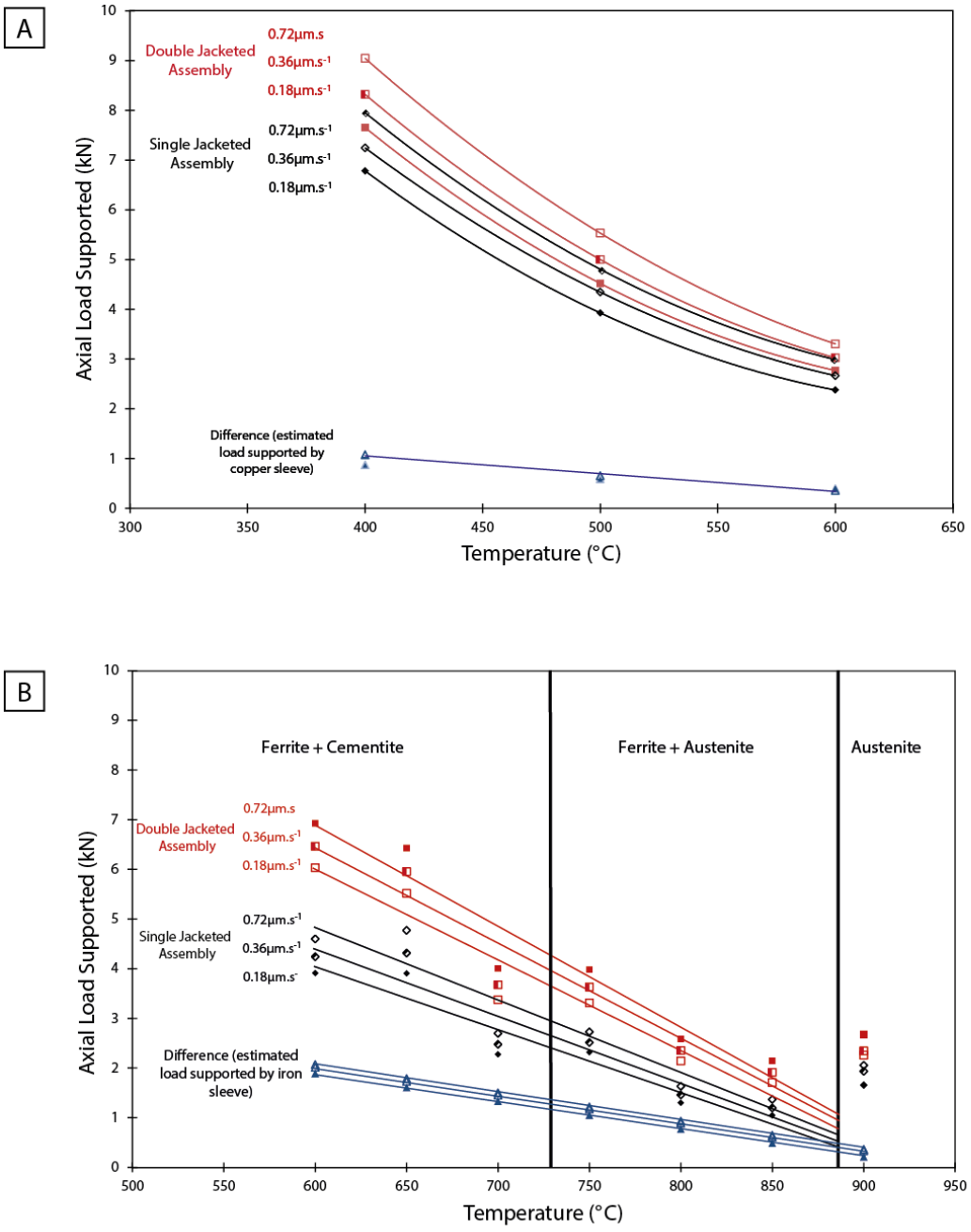

Figure 5: Results of high temperature jacket strength calibration experiments
(A) Axial load supported by a copper jacket assembly is plotted as a function of temperature. Red and black curves indicate double and single jacketed assemblies respectively over a range of axial displacement rates. The difference between the two curves is indicated by small blue triangles. Note that the influence of velocity on the strength of the assemblies is less than can be experimentally determined. (B) Graph estimating the axial load supported by an iron jacketed assembly over a range of temperatures and axial displacement rates. As in (A) the load supported by a double and single assembly is indicated along with the estimated load supported by an iron sleeve. Note the spread in jacket strength values resulting from heterogeneity in the starting material. The strengthening observed at the Ferrite + Austenite → Austenite transition is consistent with previously observed behaviour (e.g. *Frost and Ashby* [1982]). However the significant strength of the single jacketed experiment (possibly as a result of material heterogeneity) results in the estimated total strength of the iron sleeve being an approximately linear relationship across all phases.

Table 2: Estimation of strength contribution of copper jackets

Load supported by copper sleeve (kN)					
25°	**400°**	**500°**	**600°**	***650°***	***700°***
1.3	1.0	0.7	0.4	*0.2*	*0.0*

Load supported by copper jacket + sleeve (kN)			
25°	**400°**	**500°**	**600°**
3.3	2.6	1.7	0.9

Estimation of stress reduction on experiment (MPa)			
25°	**400°**	**500°**	**600°**
42.2	32.6	21.2	11.5

Table 3: Estimation of strength contribution of iron jacket

Load supported by iron sleeve (kN)							
Axial Displacement Rate (µm.s^{-1})	**600°**	**650°**	**700°**	**750°**	**800°**	**850°**	**900°**
7.2	2.1	1.8	1.5	1.2	0.9	0.6	0.4
3.6	2.0	1.7	1.5	1.2	0.9	0.6	0.3
1.8	1.9	1.6	1.3	1.0	0.8	0.5	0.2

Load supported by iron jacket and copper sleeve (kN)							
Axial Displacement Rate (µm.s^{-1})	**600°**	**650°**	**700°**	**750°**	**800°**	**850°**	**900°**
7.2	3.6	2.9	2.3	1.9	1.4	1.0	0.6
3.6	3.5	2.9	2.2	1.8	1.4	0.9	0.5
1.8	3.3	2.7	2.0	1.6	1.2	0.7	0.3

Estimation of stress reduction on experiment (MPa)							
Axial Displacement Rate (µm.s^{-1})	**600°**	**650°**	**700°**	**750°**	**800°**	**850°**	**900°**
7.2	45.6	37.4	29.3	23.7	18.2	12.6	7.0
3.6	44.5	36.4	28.4	22.9	17.4	12.0	6.5
1.8	42.0	34.0	26.0	20.5	15.0	9.5	4.1

3. Application of jacket correction to experimental data

To apply the jacket strength correction to the experimental data it is assumed that the yield point of the fault controls the yield of the jacket assembly. For simplicity, at the experimental yield point, the jacket and sleeve are assumed to simultaneously achieve both the calculated strength ($\sigma_{Sl,J}$) and a state of perfect plasticity. Prior to yield the load that the jackets support is assumed to increase linearly with displacement and thus the following two-stage approach to the jacket correction has been adopted.

Sample strength $\left(\sigma_S(t)\right)$ as a function of time is given by:

$$\sigma_s(t) = \frac{F_T - \left(\frac{t - t_0}{t_Y - t_0} \cdot F_{J,Sl}\right)}{A_S}, \qquad t < t_y$$

$$\sigma_s(t) = \frac{F_T - F_{J,Sl}}{A_S}, \qquad \text{otherwise} \qquad 6$$

where F_T is the total force recorded by the load cell, t is the sample time, t_0 is the recorded time that the experiment commenced, t_Y is the time recorded at yield and A_S is the cross-sectional area of the sample perpendicular to the direction which the axial force is applied.

4. Correcting for change in contact area of the sliding interface

The sliding interface of the sample has an elliptical shape formed when the cylindrical specimen is ground at an angle of between 30° - 70° to the cylindrical axis. During experiments force is applied to the sample through the cylinder ends. Axial stress is calculated as force acting on the sample area perpendicular to the direction of shortening. The shear stress and normal stress acting on the slip surface are then determined based on the inclination of the fault surface to the bulk maximum principal stress.

During the experiment the apparent contact area of the elliptical sliding surfaces is reduced as the fault blocks become offset with increasing shear displacement. The change in contact area results in the axial load being distributed over a reduced area, increasing the stress for any given load. The change in fault contact area can be

calculated in terms of the change in area perpendicular to the axial stress, allowing a corrected value to be calculated for the axial stress, shear stress and normal stress.

The vertical component of the shear displacement is given by the displacement measurements of the LVDT and knowing the angle of inclination of the fault surface, simple trigonometry can be used to calculate the horizontal component:

$$d_h = d_v \tan\theta \qquad 8$$

where d_h is the horizontal displacement, d_v is the vertical displacement of the fault and θ is the incline of the fault surface relative to the maximum shortening direction. However, the contact area of the sliding surface is already reduced by a chamfer which is ground on the leading edge of the fault to prevent the forcing block rupturing the jacket during slip. As such, area over which the axial stress is distributed can then be calculated using the equation:

$$A = \pi r \cdot (r - (2d_c + d_h) \qquad 9$$

where r is the radius of Fontainebleau cylinder d_c is the horizontal width of the chamfer. A certain amount of horizontal displacement can occur on the slip surface prior to there being any change in fault contact area. Further it can be assumed that no slip occurs on the fault during elastic loading, so accordingly the horizontal displacement can be expressed as:

$$d_h = d_{h(t)} - (d_y + d_c) \qquad 10$$

where, $d_{h(t)}$ is the horizontal displacement calculated by (8) at any point in time during the experiment, d_y is the horizontal component of displacement recorded at the yield point. Substituting (10) into (9) the area can be calculated as:

$$A = \pi r \cdot (r + d_y - \left(d_c + d_{h(t)}\right)) \qquad 9$$

Appendix 3

Starting Material

Fontainebleau sandstone is a well-sorted quartz sandstone that formed during the early Oligocene in the Paris Basin of northern France [*Haddad et al.*, 2006]. Its nearly pure, quartz composition, equigranular grain shapes, and porous properties make this sandstone eminently suitable for rock deformation experiments and it has previously been used in a number of different studies [e.g. *Kanagawa et al.*, 2000; *El Bied et al.*, 2002; *Giger et al.*, 2008]

1. Grain Properties

Optical and SEM analysis of the Fontainebleau sandstone revealed that it is composed dominantly of equigranular grains with subangular to rounded interfaces. Where the grains abut pore spaces the quartz shows the development of euhedral faceted surfaces (Fig. 1A-B). Dusty inclusion trails decorate the primary detrital grain surfaces indicating initially highly rounded grains that are now overgrown by authigenic quartz. Most detrital grains are monocrystalline, although a small proportion are polycrystalline and show signs of being recrystallised prior to erosion and deposition. The equigranular nature of the Fontainebleau sandstone indicates a high level of grain size sorting prior to deposition. The starting material has a narrow grain size distribution of approximately 200-250μm.

The grains show the consistent presence of euhedral quartz overgrowths beyond their original grain boundaries (Fig. 1C-D) and many of the detrital grains show planar bands of inclusions that appear consistent with being healed micro-cracks. Occasional grains exhibit undulose extinction and rare grains show presence of deformation lamellae, both of which suggest deformation of the source rock prior to erosion. No lattice preferred orientation was observed which is consistent with a shallowly buried (<100m) sandstone that has undergone limited diagenesis and no significant deformation [*Thiry et al.*, 1998; *Haddad et al.*, 2006].

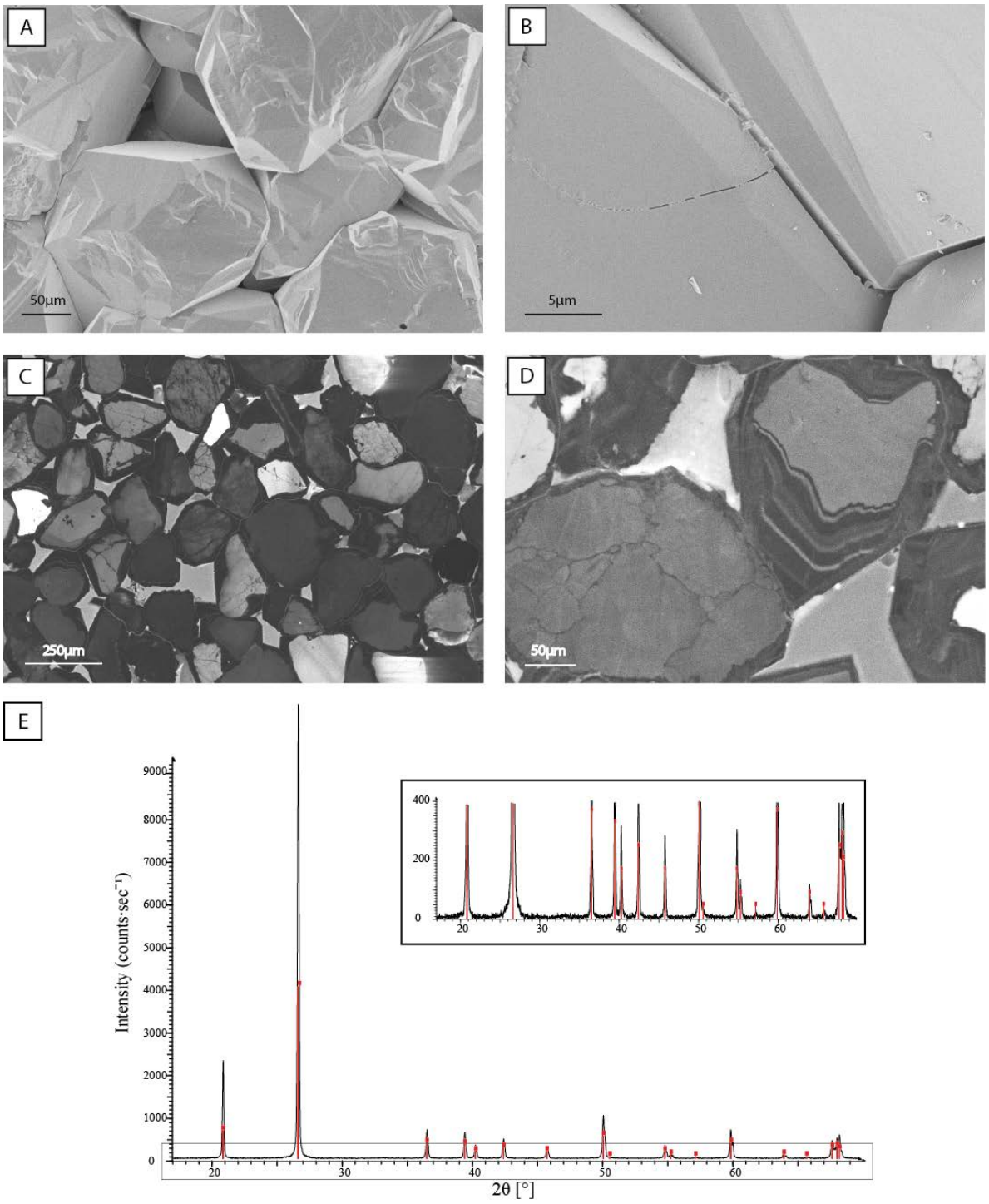

Figure 1: Microstructure and composition of the Fontainebleau sandstone starting material
(A) - (B) SE-SEM images of a broken surface of the Fontainebleau sandstone. Note the euhedral quartz overgrowths which form the angular structure of the pore network. Micro-cracks within the Fontainebleau grains are evident in (B). (C)-(D) Panchromatic cathodoluminescence SEM images of the Fontainebleau sandstone. Evidence of the original detrital grains and the darker overgrowth rims are clearly visible. A number of phases of overgrowth are evident by the banding in image D, and possibly represents different episodes of ground water saturation and quartz precipitation. (E) X-Ray diffractogram for the Fontainebleau sandstone sample. Inset shows magnified diffraction profile to highlight background levels.

SE-SEM analysis of a broken surface of the sandstone revealed the presence of rare intragranular micro-cracks (Fig. 1B) – a phenomena that is usually regarded as being unusual in Fontainebleau sandstone [*Tenthorey et al.*, 2003]. However, the occurrence of these micro-cracks is sufficiently rare that they do not pose a problem either in the post-experimental microstructural analysis or by altering porosity and fluid flow within the sample.

2 Composition

XRD analysis indicated that the sample was essentially pure quartz with only possible trace impurities (Fig. 1E) that were largely indeterminate from the background. Using Diffrac*plus* Eva 10 (2003) software it was found that these impurities were most likely trace muscovite, hematite and clays, however, their concentration was too low to allow accurate identification or quantification. Optical microscopy on thin sections of the starting material also revealed rare tourmaline.

3. Porosity and Pore Structure

Porosity was measured in six Fontainebleau sandstone samples obtained from disperse locations in the starting material block using the methodologies described in Section 4 (below). Results indicate that the sample has a total porosity of between 5.7% - 8.3% ± 0.3%. In contrast the accessible porosity, calculated using the imbibition method, is estimated to be between 4.3% - 5.6% ± 0.2% (Fig. 2C).

Microscopic analysis of the Fontainebleau sandstone starting material (Fig. 2A-B) reveals that all the pore structures are connected along grain boundaries and that there is negligible intragranular porosity. The difference, therefore, between the measurements for total porosity and accessible porosity is attributed to a percolation threshold phenomenon. It is suggested that, at the relatively low measured total porosities, the average pore entry radius is too small to allow all the pore spaces to be completely filled during imbibition at atmospheric pressure. A difference between the total and accessible porosity for low porosities (<10%) in Fontainebleau sandstone is in agreement with the data presented by *Bourbié and Zinszner* [1985]. A critical porosity (the point at which all pore connectivity is lost and permeability ceases) has been identified as being between 2.5-5% [*Lockner and Evans*, 1995; *Mavko and Nur*, 1997].

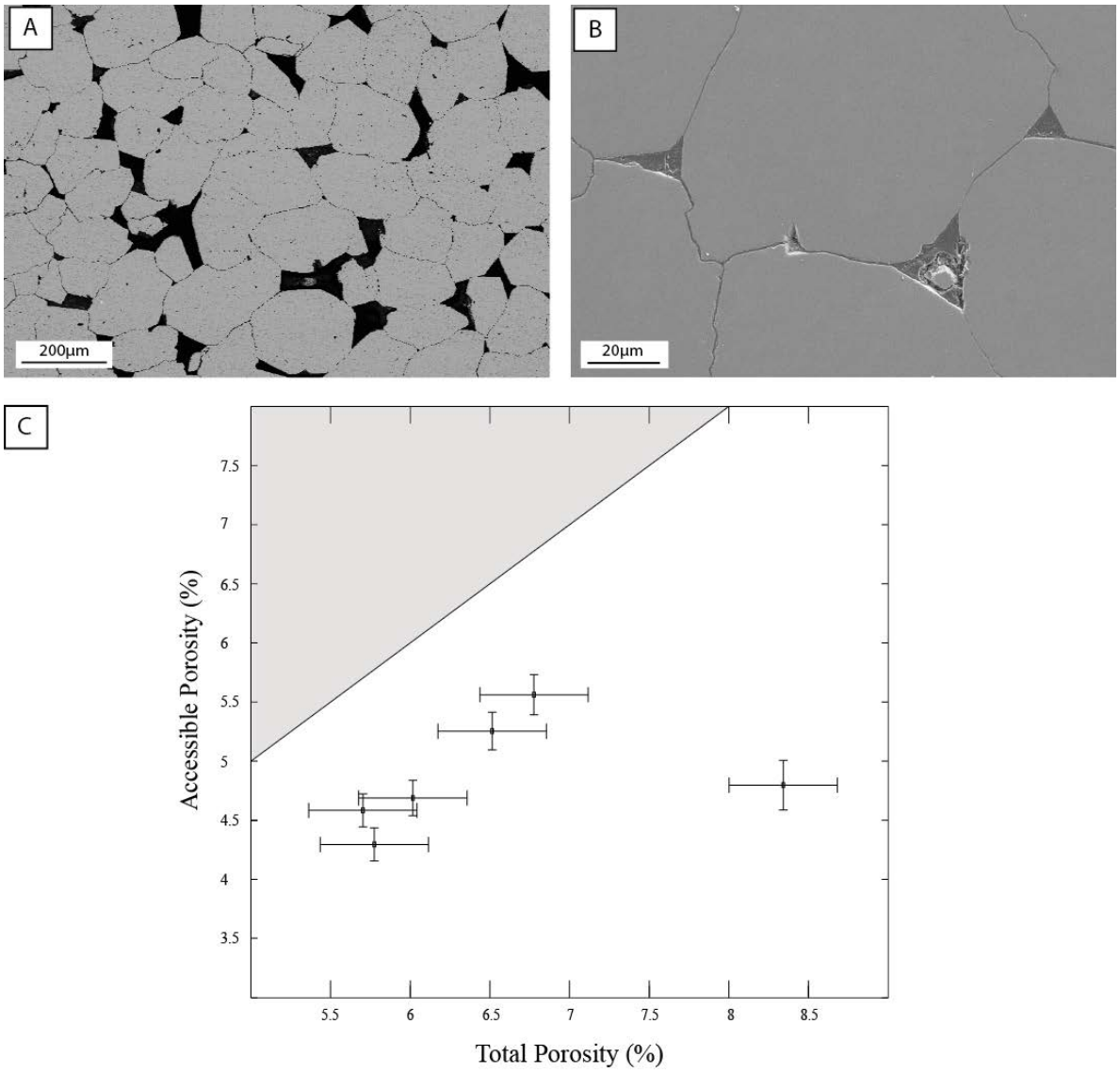

Figure 2: Initial pore structure and porosity of the Fontainebleau sandstone starting material
(A) BSE-SEM image of an epoxy impregnated sample of the Fontainebleau sandstone. The epoxy filled pores and pore throats (at the grain interfaces) image as the dark areas in the micrograph. The intragranular spots represent surface damage / plucking which occurred during sample preparation. Note the large size and angular shapes of many of the nodal pores (up to 100µm in diameter) and comparatively narrow apertures of the sheet like pore throats. (B) SE-SEM image detailing the cross section of three pore triple junctions (3-grain interfaces) and the sheet-like throats at two-grain interfaces. (C) Results of porosity tests undertaken on the Fontainebleau sandstone starting material. Accessible porosity is plotted against total porosity for each of the samples. The solid line indicates full pore accessibility ($\phi = \phi_a$).

SEM analysis of the pore structure reveals that the porosity is dominated by large angular nodal pores with diameters of up to 100μm (Fig. 2A). These nodal pores provide the majority of the storage capacity or porosity of the rock and are connected by narrow sheet-like pore throats that dominantly control the pore fluid transport properties [*Bernabé*, 1991]. In terms of experimental properties, the accessible porosity of the Fontainebleau sandstone readily facilitates access of pore fluid to the fault interface.

4. Methods for Calculating Porosity

Two different methods were employed for calculating porosity. The first method, or density method, provides an estimate of the total porosity of the rock, while the second technique, referred to as the imbibition method, measures accessible porosity.

4.1 Density Method

Total porosity can be defined as the fraction of the bulk rock (*V*) that is not occupied by solid matter [*Dullien*, 1992]. As the starting material to be used in the current suite of experiments is essentially monomineralic, the pore volume and porosity ϕ, can be calculated directly from the mineral density and the dry weight of the sample, by the equation:

$$\phi = 1 - \frac{\rho_s}{\rho_g} \qquad 1$$

where, ρ_s is sample density calculated by the ratio of sample mass to sample volume, and ρ_g is the grain density calculated from the average mineral density of quartz as provided in literature [e.g. *Fredrich et al.*, 1993].

4.2 Imbibition Method

The dry rock sample is immersed and vacuum-saturated in water. To obtain the saturated submerged weight, the sample is weighed suspended in a bath of the immersion fluid using a platinum basket attached to the stirrup of the measuring balance. In order to reduce the potential for error, the basket is suspended from the balance by a fine platinum wire so that only the diameter of the wire intersects the water surface. Next, the saturated weight in air is measured by removing the sample from the immersion bath, drying the excess surface water and weighing the sample.

Using the density of the immersion fluid, the differences in weight between the saturated (M_{sat}) and saturated submerged (M_{sub}) sample are be used to calculate the bulk volume (V):

$$V = \frac{M_{sat} - M_{sub}}{\rho_f} \qquad 2$$

The accessible pore volume (V_{ap}) is then calculated as the difference in weight between the water-saturated sample and the oven-dried sample (measured in Method 1):

$$V_{ap} = \frac{M_{sat} - M_{dry}}{\rho_f} \qquad 3$$

Finally the accessible porosity (ϕ_a) is calculated as the ratio between pore volume and total volume, which can be expressed as:

$$\phi_a = \frac{V_{ap}}{V} \qquad 4$$

Appendix 4

Summary of Experiments

Glossary of abbreviations used in this appendix:

P_c	Confining pressure
P_c'	Effective confining pressure
τ_p	Peak shear stress
σ_{nP}	Peak normal stress
μ*	Coefficient of friction prior to the stress drop associated with stick-slip
μ_{ss}	Coefficient of friction during stable sliding
D_{rs}	Shear displacement during rapid-slip event
t_{rs}	Time taken for stress drop during rapid-slip event
v_{rs}	Estimated velocity during rapid-slip event
A_{rs}	Estimated peak acceleration during rapid-slip event

1. Frictional melt experiments

Table 1: Summary of nominally dry frictional sliding experiments undertaken on bare interface faults

No.	Temp. (°C)	Jacket Config.	P_c (MPa)	Piston Velocity ($\mu m.s^{-1}$)	τ_P (MPa)	Stress Drop (MPa)	μ*	μ_{ss}	D_{ss} (μm)	t_{rs} (sec)	v_{rs} ($mm.s^{-1}$)	A_{rs} ($m.s^{-2}$)	Melt	Stick-slip
BIS007	400	Cu/Cu	100	0.36	132	-	-	0.69	-	-	-	-	No	No
BIS009	500	Cu/Fe	100	0.36	144	-	-	0.74	-	-	-	-	No	No
BIS010	900	Cu/Fe	100	0.36	170	79	0.78	-	142	-	-	-	Yes	Yes
BIS011	650	Cu/Fe	100	0.36	151	48	0.80	-	89	-	-	-	No	Yes
BIS019	927	Cu/Fe	100	0.36	167	87	0.83	-	151	-	-	-	Yes	Yes
BIS020	650	Cu/Fe	100	0.36	141	37	0.76	-	65	-	-	-	No	Yes
BIS026	900	Fe/Fe	100	0.36	134	36	0.75	-	61	-	-	-	Yes	Yes
BIS027	800	Cu/Fe	100	0.36	110	49	0.64	-	83	-	-	-	No	Yes
BIS029	800	Cu/Fe	100	0.36	165	111	0.85	-	196	-	-	-	Yes	Yes
BIS030	700	Cu/Fe	100	0.36	137	33	0.76	-	58	-	-	-	No	Yes
BIS032	850	Cu/Fe	100	0.36	159	73	0.83	-	126	-	-	-	Yes	Yes
BIS033	900	Cu/Fe	100	0.36	187	94	0.88	-	171	-	-	-	Yes	Yes
BIS034	900	Cu/Fe	100	0.36	166	85	0.84	-	150	-	-	-	Yes	Yes
BIS035	900	Cu/Fe	100	0.36	168	90	0.85	-	158	-	-	0.95	Yes	Yes
BIS036	800	Cu/Fe	100	0.36	147	79	0.79	-	158	0.015	10.5	0.42	Yes	Yes
BIS037	800	Cu/Fe	150	0.36	204	-	-	-	-	-	-	-	No	No
BIS038	800	Cu/Fe	150	0.72	207	112	0.72	-	225	0.0115	19.6	0.99	Yes	Yes
BIS039	750	Cu/Fe	100	0.36	145	75	0.90	-	15	0.011	13.6	0.11	No	Yes
BIS040	750	Cu/Fe	150	0.72	191	84	0.73	-	170	0.012	14.2	0.90	Yes	Yes
BIS041	900	Cu/Fe	50	0.36	93	53	0.89	-	106	0.011	9.6	0.16	No	Yes
BIS042	700	Cu/Fe	150	0.72	187	96	0.76	-	192	0.0123	15.7	0.77	Yes	Yes
BIS043	650	Cu/Fe	150	0.72	190	127	0.73	-	218	0.012	18.2	0.97	Yes	Yes
BIS044	600	Cu/Fe	150	0.72	178	-	-	0.69	-	-	-	-	No	No

BIS045	600	Cu/Fe	200	0.72	219	-	-	0.64	-	-	-	-	No	No
BIS046	600	Cu/Cu	200	0.72	228	-	-	0.66	-	-	-	-	No	No
BIS048	700	Fe/Cu	50	0.36	71	19	0.76	-	35	0.0145	2.4	0.05	No	Yes
BIS049	800	Fe/Cu	150	0.72	188	-	-	0.71	-	-	-	-	No	No

Table 2: Summary of experiments undertaken with subsequent hydrothermal pressing or slipped in the in the presence of fluids

No.	**Temp. (°C)**	**Jacket Config.**	**P_c (MPa)**	**P_f (MPa)**	**P_c' (MPa)**	**Time of Hot Pressing**	**Axial Disp. Rate ($\mu m.s^{-1}$)**	**τ_P (MPa)**	**Stress Drop (MPa)**	**μ^***	**μ_{ss}**	**D_{rs} (µm)**	**Melt**	**Stick-slip**
BIS024	900	Cu/Fe	100	0	100	-	0.36	162	82	0.83	-	143	Yes	Yes
	900	Cu/Fe	250	150	100	1hr	-	-	-	-	-	-	-	
BIS028	900	Cu/Fe	100	0	100	-	0.36	156	77	0.81	-	133	Yes	Yes
	500	Cu/Fe	250	150	100	1hr	-	-	-	-	-	-	-	
BIS050	700	Fe/Cu	200	Drained	?		0.72	229	-	-	0.67	-	No	No

2. Misoriented fault experiments

Table 3: Stress-driven fault-reactivation experiments undertaken on bare interface faults at 100MPa confining pressure

No.	Angle θ (°)	P_c (MPa)	Piston Velocity ($\mu m.s^{-1}$)	Peak Diff. Stress (MPa)	τ_P (MPa)	σ_{nP} (MPa)	Stick-slip / Failure	No. of rapid slip events	Stress drop of largest slip event (MPa)	Shear disp. of largest slip event (mm)	Total exp. disp. (mm)	Comments
MIS005	25	100	3.63	425	163	176	Low amplitude stick-slip	-	-	-	1.69	
BIS008	30	100	3.63	438	190	208	Yes	7	35	0.075	1.66	
MIS001	35	100	3.63	495	233	262	Yes	7	67	0.125	1.44	
MIS002	40	100	3.63	545	268	323	Yes	12	63	0.144	1.99	
MIS037	45	100	3.63	499	250	349	Yes	1	84	0.183	0.67	Halted after first major slip
MIS007	45	100	3.63	654	327	428	Yes	6	208	0.463	2.63	
MIS003	50	100	3.63	770	379	548	Yes	3	340	0.149	2.25	
MIS006	55	100	3.63	1037	487	796	Yes	2	623	0.878	1.81†	
MIS038	60	100	3.63	934	404	804	Yes	1	227	0.177	1.37†	
MIS004	60	100	3.63	933	430	845	Yes	2	529	0.846	1.91†	

† Total experimental displacement is given as axial displacement rather than shear displacement due to the formation of a new optimally oriented fault.

Table 4: Stress-driven fault-reactivation experiments undertaken on bare interface faults at 50MPa confining pressure

No.	Angle θ (°)	P_c (MPa)	Piston Velocity ($\mu m.s^{-1}$)	Peak Diff. Stress (MPa)	τ_P (MPa)	σ_{nP} (MPa)	Stick-slip / Failure	No. of rapid slip events	Stress drop of largest slip event (MPa)	Shear disp. of largest slip event (mm)	Total exp. disp. (mm)	Comments
MIS013	25	50	3.63	298	114	104	No	-	-	-	1.69	
BIS012	30	50	3.63	302	131	127	Low amplitude stick-slip	-	-	-	1.82	
MIS008	40	50	3.63	397	196	216	Yes	12	30	0.063	2.03	
MIS009	45	50	3.63	439	219	270	Low amplitude stick-slip	17	17	0.036	1.89	
MIS035	50	50	3.63	375	185	272	Low amplitude stick-slip	-	-	-	0.84	Halted prior to first major slip
MIS010	50	50	3.63	649	319	432	Yes	5	191	0.436	2.37	
MIS036	55	50	3.63	755	355	558	Yes	1‡	302	0.794	1.44	Halted after first major slip
MIS011	55	50	3.63	776	365	572	Yes	3	466	0.611	1.86†	
MIS031	55	50	3.63	787	370	579	Yes	3	391	0.715	1.98†	Sample prepared for microCT scanning
MIS012	60	50	3.63	823	356	669	Yes	2	418	1.265	1.68†	
MIS017	60	50	3.63	591	256	494	Yes	1	152	0.297	0.53	Halted after first major slip
MIS018	60	50	3.63	827	358	671	Yes	1	309	0.561	1.09	Halted just prior to failure on new optimally oriented fault
MIS028	65	50	3.63	788	394	445	Yes	1	505	0.638	1.27†	
MIS029	70	50	3.63	802	401	452	Yes	1	540	0.834	1.48†	

† Total experimental displacement is given as axial displacement rather than shear displacement due to the formation of a new optimally oriented fault.

Table 5: Stress-driven fault-reactivation experiments undertaken in the presence of pore fluids

No.	Angle θ (°)	P_c (MPa)	P_f (MPa)	P_c' (MPa)	Piston Velocity ($\mu m.s^{-1}$)	Peak Diff. Stress (MPa)	τ_P (MPa)	σ_{nP} (MPa)	Stick-slip / Failure	No. of rapid slip events	Stress drop of largest slip event	Shear disp. of largest slip event	Total exp. disp. (mm)
MIS022	60	80	30	50	3.63	755	327	620	Yes	2	421	0.726	1.938
MIS023	55	80	55	25	3.63	596	280	427	Yes	11	277	0.484	2.04

Table 6: Fluid-driven fault-reactivation experiments

No.	Angle θ (°)	P_c (MPa)	P_f (MPa)	P_c' (MPa)	Piston Velocity ($\mu m.s^{-1}$)	Peak Diff. Stress (MPa)	τ_P (MPa)	σ_{nP} (MPa)	Stick-slip / Failure	No. of rapid slip events	Stress drop of largest slip event	Disp. of largest slip event	Total exp. disp. (mm)
MIS024	40	80-100	30-80	15-50	3.63	230	113	159	Yes	28	33	0.059	1.33
MIS026	50	80	30-65	15-50	3.63	333	164	246	Yes	14	62	0.123	1.20
MIS041	55	80	30-65	15-50	3.63	575	270	437	Yes	10	157	0.280	2.02
MIS027	60	80	30-65	15-50	3.63	612	265	539	Yes	2	396	0.664	1.41

Table 7: Stress-driven failure of intact rock

No.	Angle θ (°)	P_c (MPa)	Piston Velocity ($\mu m.s^{-1}$)	Peak Diff. Stress (MPa)	τ_P (MPa)	σ_{nP} (MPa)	Stress drop during slip event (MPa)	Shear disp. during slip event (mm)	Total exp. disp. (mm)
IRF006	16	15	3.63	588	**165**	**61**	406	0.694	1.28
IRF005	17	30	3.63	664	**186**	**88**	480	0.796	1.66
IRF018	23	50	3.63	811	**302**	**186**	502	0.850	1.35
IRF004	25	70	3.63	964	**342**	**230**	588	0.970	1.89

Table 8: Fluid-driven failure of intact rock

No.	Angle θ (°)	P_c (MPa)	P_f (MPa)	P_c' (MPa)	Piston Velocity ($\mu m.s^{-1}$)	Peak Diff. Stress (MPa)	τ_P (MPa)	σ_{nP} (MPa)	Stress drop of largest slip event	Shear disp. of largest slip event	Total exp. disp. (mm)
IRF015	23	80	30-65	15-50	3.63	613	**220**	**109**	335	0.600	1.02
IRF017	24	80	30-60	20-50	3.63	650	**249**	**139**	390	0.697	1.10

Appendix 5
Supplementary Information

FIB milling and the correlation of SEM and TEM microstructures

One of the most powerful tools for understanding fault-surface microstructure used in this study was the preparation of TEM foils using focused ion beam (FIB) milling. This technique provides an ability to correlate detailed topographical and microstructural information from SEM imaging with subsurface compositional and structural information using the TEM [*Giannuzzi and Stevie*, 2005].

The images depicted in Figure 1 show the process of FIB milling, starting with the identification of a target site as indicated by the red line. A 1.5µm think layer of platinum is deposited over the full length of the intended section to protect it from ion beam damage during milling. Then, using a high beam current to allow fast ion milling, two stepped trenches are milled on either side of the platinum strip, leaving a wall of sample material that is typically one to two microns thick. Features such as cracks, pores and clasts present in the substrate are now visible and can be imaged using the electron beam to provide a reference for correlation once the sample preparation is finished (see fractures indicated by white arrows in Fig. 1). Relative slip sense of the FIB foils is also recovered.

The beam current is reduced and the sample is thinned on both sides, using the ion beam, to a nominal thickness of approximately 0.3µm. At this point the base of the sample is cut, but the ends are left intact to provide structural integrity to the foil. During final thinning the beam current is progressively reduced and thinning is carefully and slowly undertaken until the foil has a thickness of approximately 100nm, making it electron transparent. Once thinning and cleaning is complete, the ends of the sample are milled to separate the foil from the bulk substrate. The sample is lifted from its milled position using a glass needle and a micromanipulator and transferred onto a copper TEM grid with a carbon support film. The foil is then imaged using the TEM.

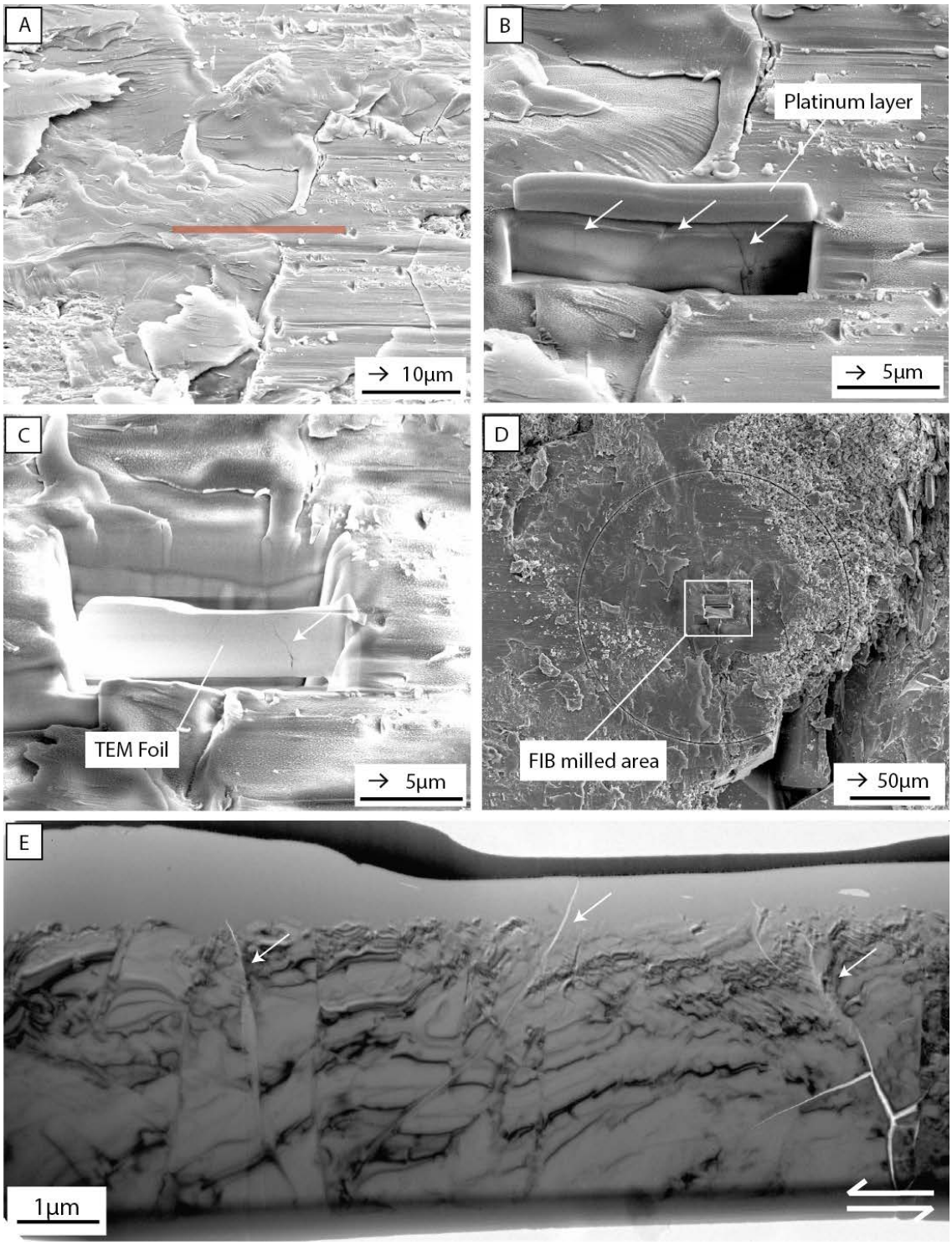

Figure 1: Correlation between SEM microstructures and FIB section
Images show the selection of a location on the fault surface (A), followed by various stages in the milling process. (B) Shows deposition of platinum layer and the milling of an initial trench adjacent to the sample location. (C) Depicts final TEM foil prior to the ends being cut. The wafer thickness is approximately 100nm. (D) Low magnification view of the milled TEM foil on the sample surface. (E) Final sample imaged using TEM. White arrows in images B,C and E indicate pre-existing cracks in the sample and show that fracturing is not the result of the milling process. The geometry and features preserved in the FIB section can be related to the SEM imaged fault surface, allowing microstructures and the slip sense to be recovered.

TEM Energy Dispersive Spectroscopy (Chapter 2)

A Amorphous Layer - Location 1

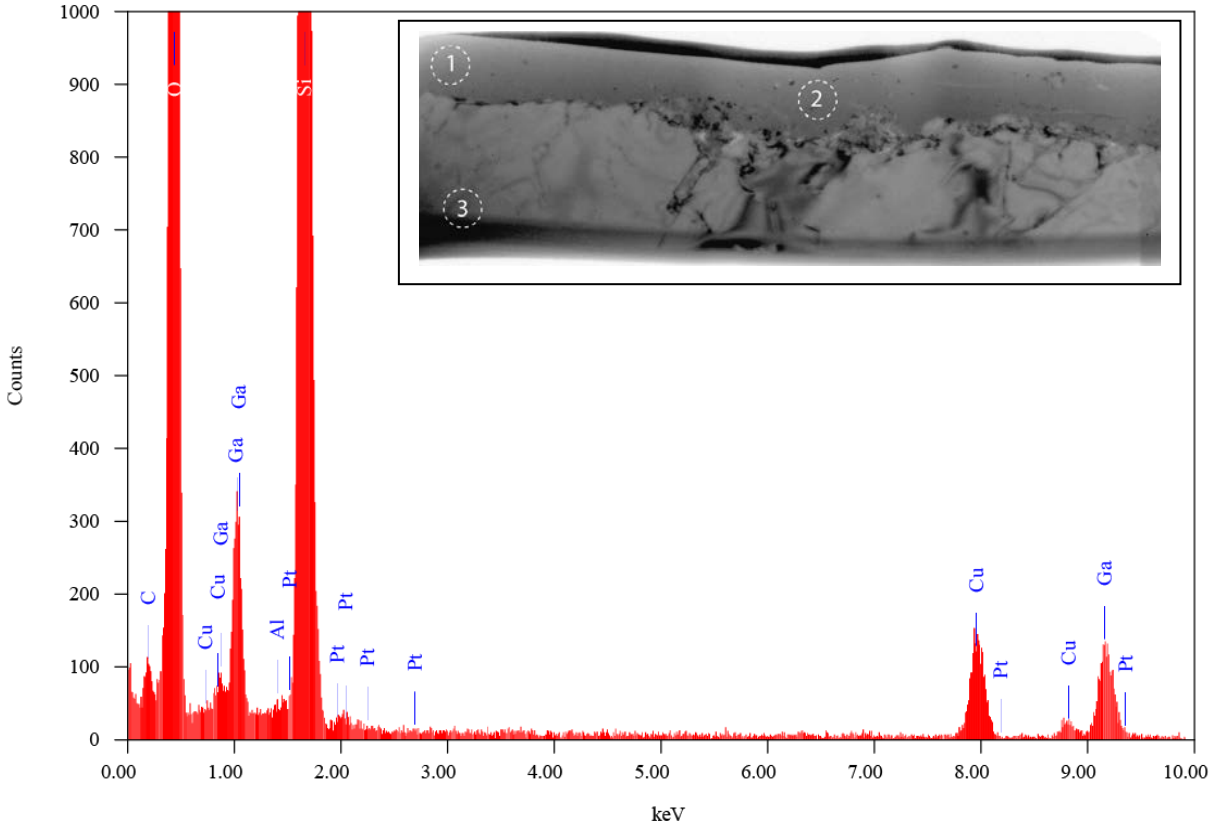

Date: 24/02/2015 12:00:57

Acquisition Parameter

Acc. Voltage	:	200.0 kV	Probe Current	:	1.00000 nA
Real Time	:	30.83 sec	Dead Time	:	2 %
Live Time	:	30.00 sec	Counting Rate	:	3292 Counts/sec
Preset	:	Live Time 30 sec			
Energy Range	:	0 - 40 keV	PHA Mode	:	T3

Thin Film Standardless Quantitative Analysis
Fitting Coefficient : 0.0675

Element	(keV)	Mass%	Counts	Sigma	Atom%
C	0.277	2.23	895.53	0.04	4.49
O	0.525	30.69	24122.13	0.20	46.40
Al					
Si (Ref.)	1.739	50.28	42140.34	0.32	43.31
Cu	8.040	3.03	2328.11	0.07	1.15
Ga	1.098	13.16	2337.60	0.32	4.57
Pt	2.048	0.61	133.30	0.12	0.08
Total	100.00	100.00			

B Amorphous Layer - Location 2

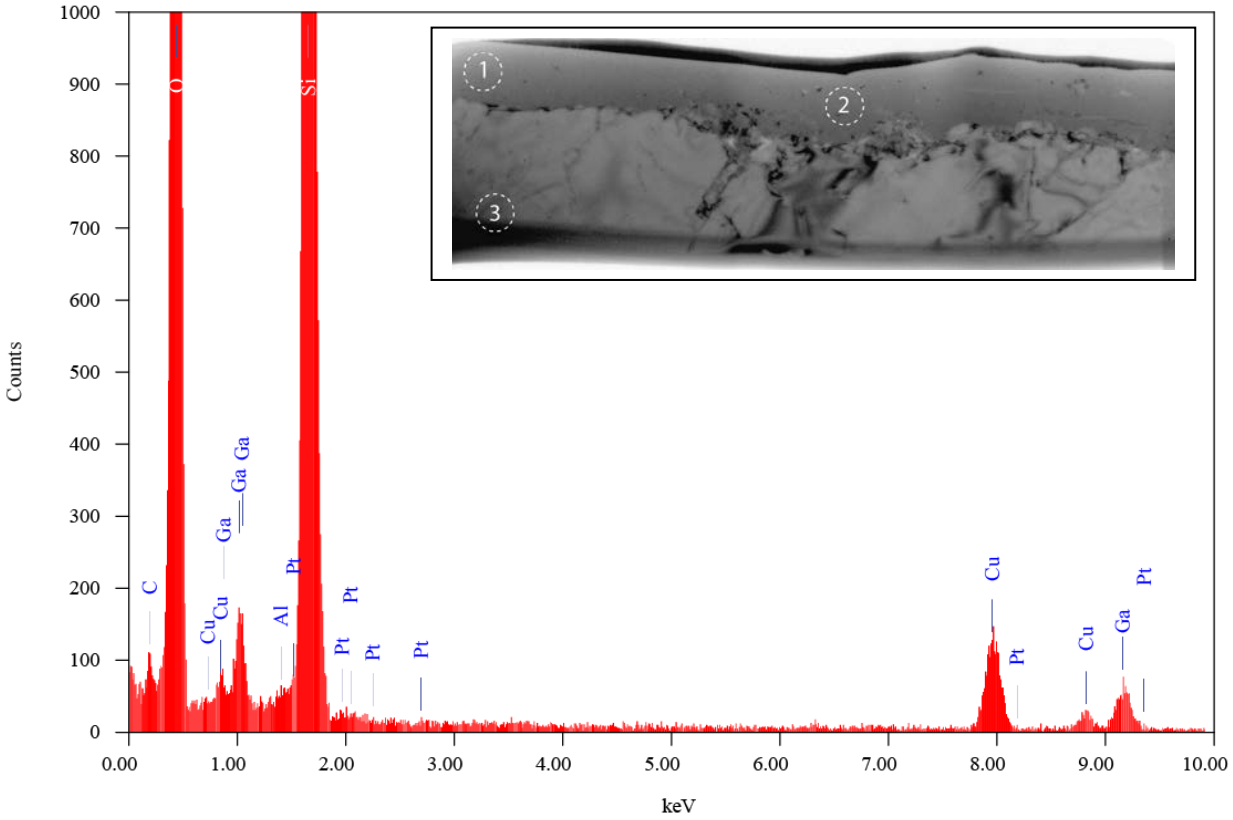

Date: 24/02/2015 12:05:33

Acquisition Parameter

Acc. Voltage	:	200.0 kV	Probe Current	:	1.00000 nA
Real Time	:	30.94 sec	Dead Time	:	3 %
Live Time	:	30.00 sec	Counting Rate	:	3604 Counts/sec
Preset	:	Live Time 30 sec			
Energy Range	:	0 - 40 keV	PHA Mode	:	T3

Thin Film Standardless Quantitative Analysis

Fitting Coefficient : 0.0675

Element	(keV)	Mass%	Counts	Sigma	Atom%
C	0.277	1.85	778.20	0.04	3.53
O	0.525	32.78	27021.92	0.20	47.03
Al					
Si (Ref.)	1.739	57.10	50187.13	0.33	46.67
Cu	8.040	2.70	2173.70	0.06	0.98
Ga	1.098	5.39	1004.06	0.22	1.77
Pt	2.048	0.18	40.60	0.10	0.02
Total	100.00	100.00			

C Quartz Substrate - Location 3

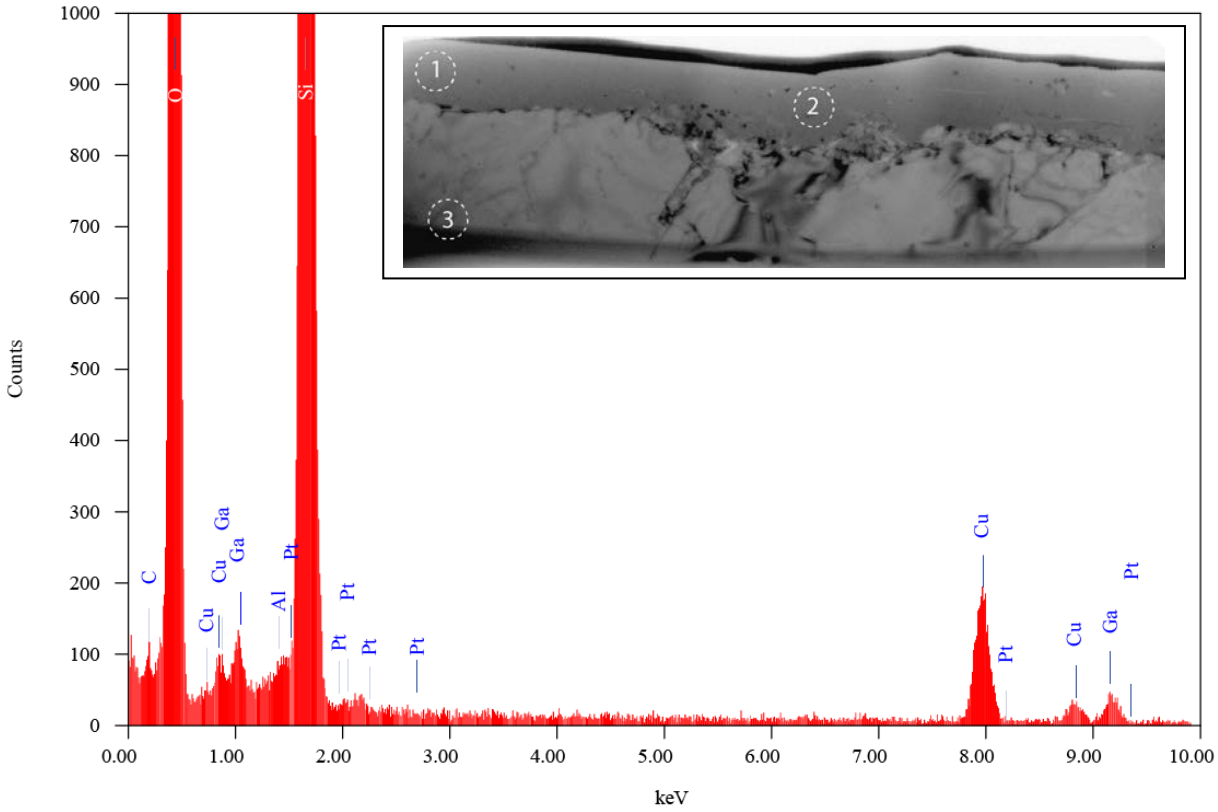

Date: 24/02/2015 12:09:53

Acquisition Parameter

Acc. Voltage	:	200.0 kV	Probe Current	:	1.00000 nA
Real Time	:	31.24 sec	Dead Time	:	3 %
Live Time	:	30.00 sec	Counting Rate	:	4891 Counts/sec
Preset	:	Live Time 30 sec			
Energy Range	:	0 - 40 keV	PHA Mode	:	T3

Thin Film Standardless Quantitative Analysis
Fitting Coefficient : 0.0675

Element	(keV)	Mass%	Counts	Sigma	Atom%
C	0.277	0.93	528.81	0.02	1.79
O	0.525	30.77	34156.10	0.17	44.39
Al					
Si (Ref.)	1.739	63.39	75033.95	0.30	52.10
Cu	8.040	2.80	3030.41	0.06	1.02
Ga	1.098	2.11	530.34	0.14	0.70
Pt					
Total	100.00	100.00			

Figure 2(A-C): TEM-EDS spectra
Identified peaks can be correlated with either the sample or sample preparation techniques. Silicon and oxygen form the elemental constituents of silica glass and it is notable that aluminium is below detection limits. Carbon is derived from the carbon film that the FIB sample is mounted on; platinum is deposited during the FIB milling to protect the sample and the gallium is associated with the gallium ion beam used during sample milling.

Indexed Diffraction Patterns (Chapter 2)

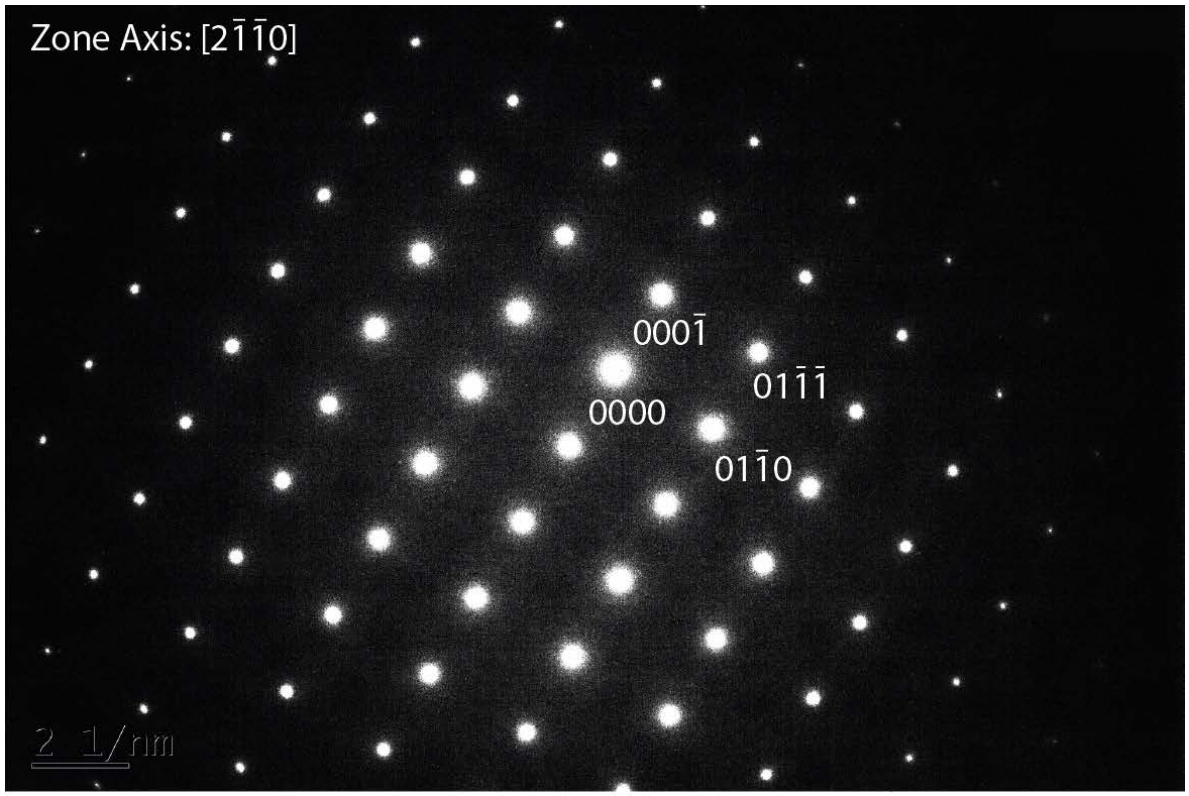

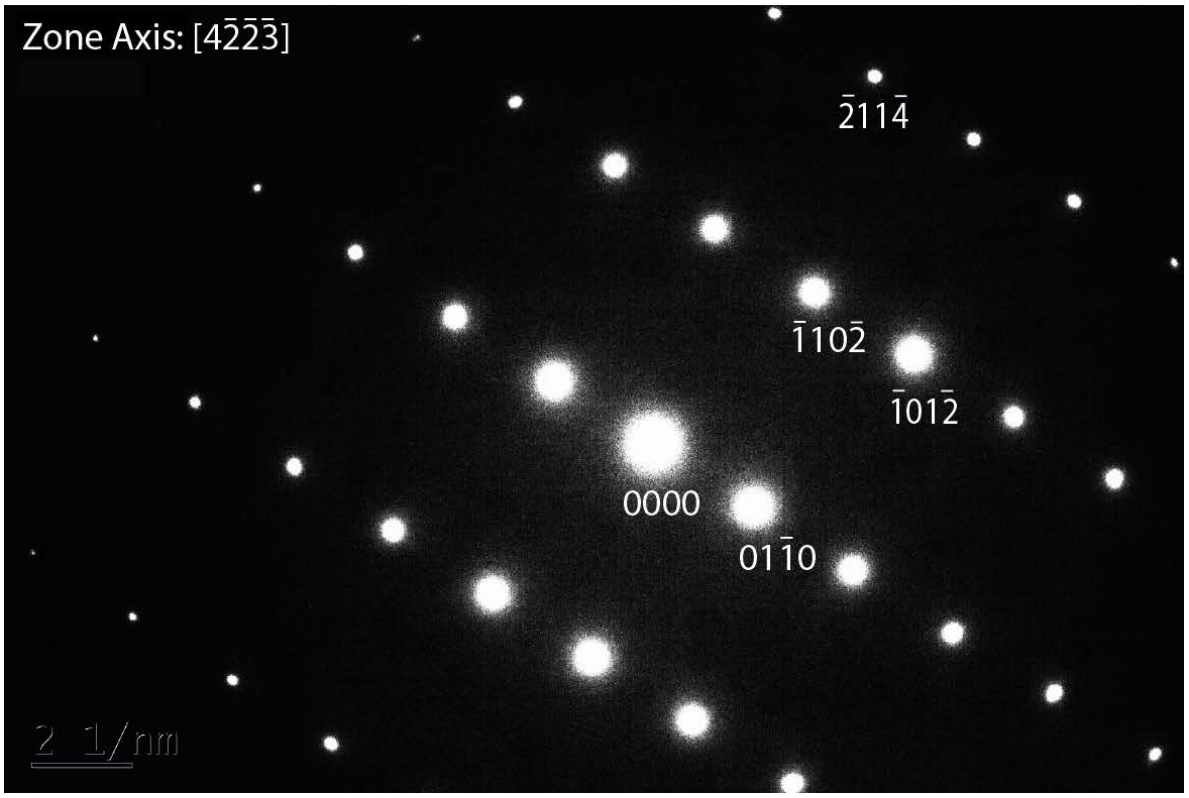

Figure 3: Indexed diffraction patterns from FIB section 4, BIS043.

XRD data for high temperature experimental fault surfaces (Chapter 2)

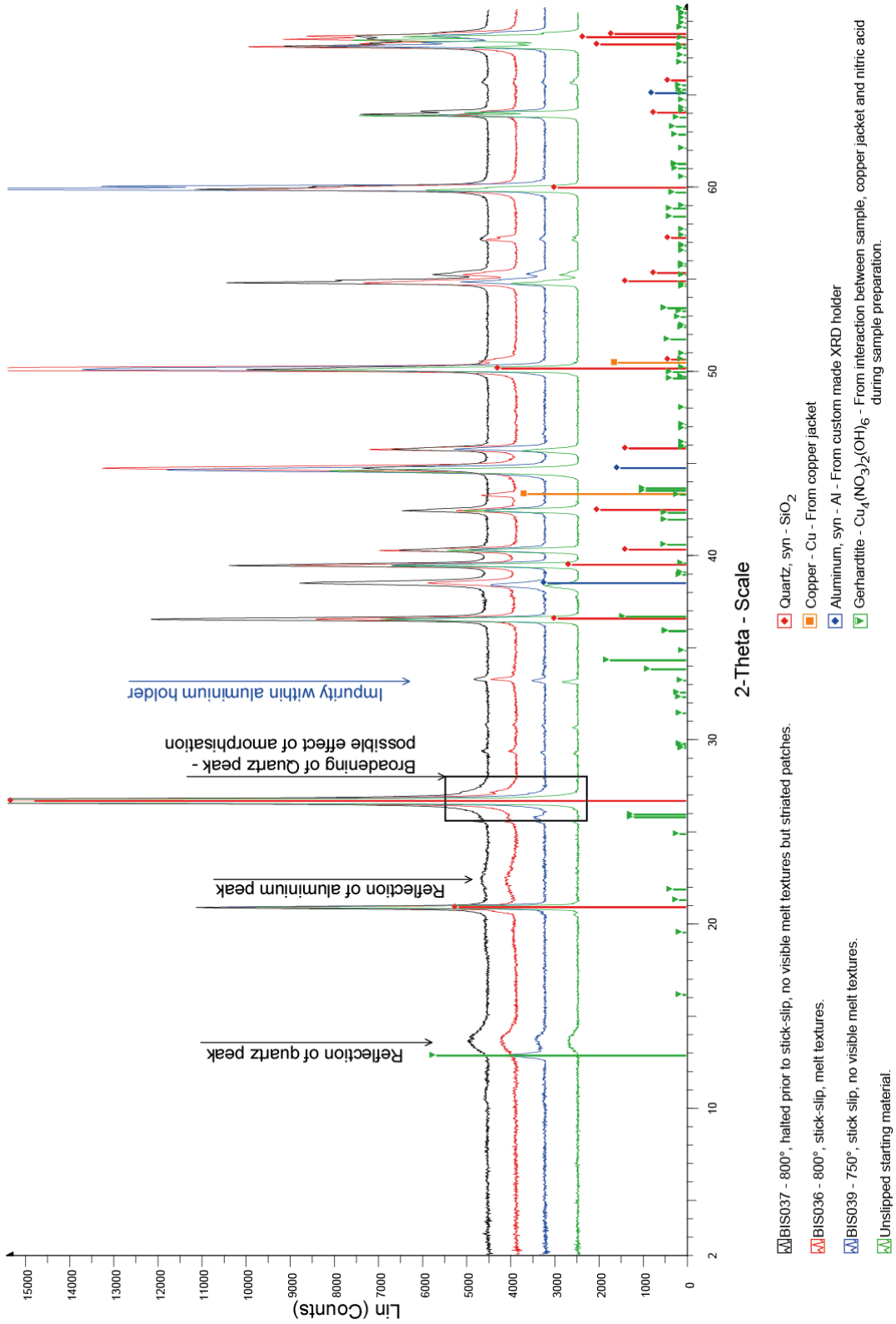

Figure 4: X-ray diffraction patterns for experimentally slipped and control sample surfaces
All peaks can be identified to be related to the sample, sample processing (assembly jacketing, acid dissolution etc.), or the holder that was custom built to allow XRD analysis of the slip surface *in situ*. Note that a broadening of the main quartz peak at $2\theta \approx 26.7$ on samples where amorphous material is evident in microstructural analysis.

Estimating the area of real contact (Chapter 2)

The microstructures formed during frictional sliding reveal a heterogeneous sliding surface with melt flow textures, fused patches, gouge and open voids, indicating that the two sliding surfaces only touch over a small fraction of their nominal contact area, on areas referred to as asperities. The reduced contact area results in a dramatic concentration of normal stress at the points of contact [*Bowden and Tabor*, 1950, 1964; *Logan and Teufel*, 1986; *Dieterich and Kilgore*, 1994]. As the load supported by the asperity forms an integral component of the frictional work that is done on a fault, being able to estimate the area of real contact is important for understanding temperature increases, the formation of melt and the potential for other solid state/mechanical amorphisation processes to occur.

The fault surfaces can be assumed to be analogous to a framework of Hertzian contacts between two rough elastic planes, with an increase in applied normal stress resulting in an increase in the total asperity contact area [*Greenwood and Williamson*, 1966; *Nielsen et al.*, 2010]. In an purely elastic model this results from an increase in the number of contacts rather than an increase in the individual size of the contacts [*Logan and Teufel*, 1986; *Dieterich and Kilgore*, 1994]. For quartz surfaces, previous investigations [e.g., *Logan and Teufel*, 1986; *Stesky and Hannan*, 1987] suggest, that to a first order, the relationship between real contact area and the applied normal stress is linear, and in the form:

$$A_R = \frac{\sigma_n}{\sigma_Q} \tag{1}$$

where A_R is the real contact area of the fault, σ_n is the apparent macroscopic normal stress acting on the fault plane and σ_Q is the shear strength of quartz during unconfined compressive failure. Based on the frictional contact theory of Bowden and Tabor [1950, 1964], it can be assumed that an asperity on the fault surface can support a load equivalent its compressive failure strength. Consequently many flash heating models [e.g. *Greenwood*, 1991; *Rice*, 2006; *Goldsby and Tullis*, 2011] assume that normal load supported by any individual contact is independent of the load being applied the fault. However, the strong positive correlation between normal stress and melt production on experimental fault interfaces outlined in Chapter 2, Section 3.1 suggests that this

assumption does not hold for the current suite of experiments, and is explored further during the thermal calculations in Chapter 2, Section 4.1.4.

The shear strength of quartz during unconfined compressive failure has been experimentally determined to be within the range of 2.2 to 10GPa at temperatures <600°C [*Brace*, 1963; *Logan and Teufel*, 1986; *Stesky and Hannan*, 1987; *Masuda et al.*, 2000]. Indentation hardness tests [*Brace*, 1963; *Evans*, 1984] suggest that the strength of quartz is temperature dependent, and therefore the estimated real contact area may change with increasing temperature. However, for the purpose of the first-order thermal calculations presented in Chapter 2 this possibility has been ignored and real contact area is calculated assuming an unconfined compressive failure strength between 2.2-10GPa.

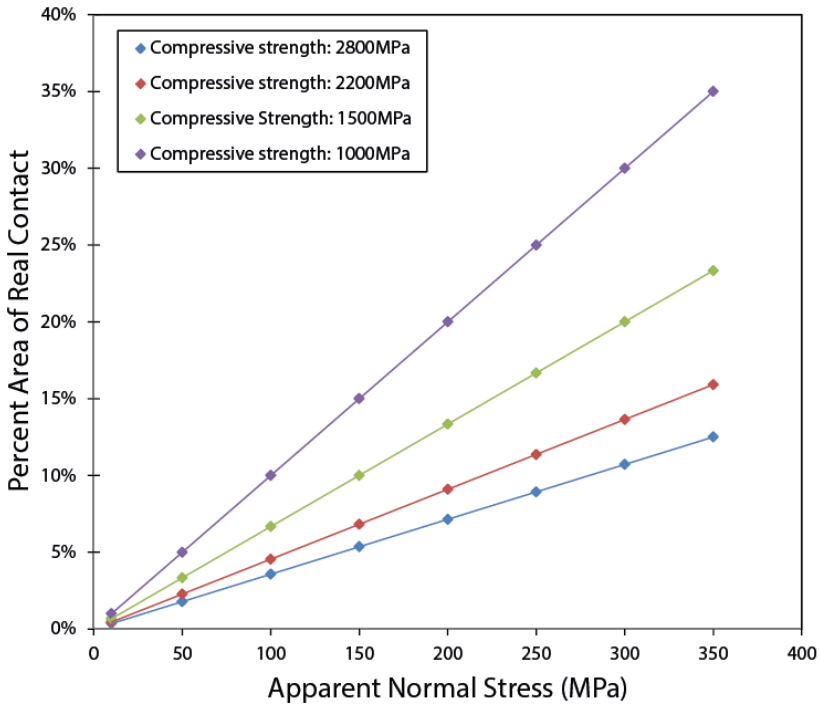

Figure 5: Relationship between area of real contact and apparent normal stress, assuming different compressive strengths for the quartz asperities.

Melting temperature of quartz (Chapter 2)

To be able to interpret the values calculated during the thermal modelling, an estimation of the anticipated melting temperature is needed. The thermodynamic melting point is defined as the temperature where the free energies of the crystalline and liquid phases are equal [*Wolf et al.*, 1990]. In quartz this can be difficult to determine with only subtle

differences in free energy between crystalline and amorphous states, suggesting that the structural reorganisation upon the destruction of crystalline order (lattice periodicity) is not significant [*Navrotsky*, 1994]. Further, numerous factors such as pressure, temperature, rate of temperature increase and differential stress states all potentially influence the conditions under which melting occurs. Previous research [e.g. *Navrotsky*, 1994; *Hudon et al.*, 2002] suggests that under ambient pressures the melting temperature for quartz ranges from 1470 – 1723ºC.

In the context of pseudotachylite research, where heating and melting occurs within a fraction of a second, a particularly pertinent issue is the influence of high temperature phase transitions on melting temperatures. When β-quartz is heated rapidly, it can by-pass the sluggish reconstructive β-quartz - β-cristobalite phase transition, melting directly into a metastable state at temperatures between 1400 - 1550°C [*Navrotsky*, 1994; *Hudon et al.*, 2002; *Bourova and Richet*, 2012]. Conversely increases in pressure potentially may result in significant increases in melting temperatures with experiments suggesting that melting occurs at ~1900ºC at 1GPa and at ~2150 at 2GPa under isostatic conditions [*Hudon et al.*, 2002]. It is not known how the complex stress states on the fault surface may influence the melting properties, nor how the evolution of stress states during sliding may enhance or impede melting.

Trace contaminants and/or fluid within the SiO_2 system may act as a flux, lowering the melting temperature relative to equilibrium melting conditions of a pure quartz system. Experimental studies of equilibrium melting of quartz + water system show that the liquidus is 1250ºC at P_c=100MPa and 1160ºC at P_c=150MPa [*Kennedy et al.*, 1962]. As discussed in Chapter 2, the small quantity of melt produced during the current suite of experiments makes compositional analysis difficult because the concentration of contaminants is beyond the limits of detection of conventional techniques such as energy dispersive X-ray spectroscopy (EDS). However, given the lack of detectable incorporated water during IR spectroscopy of the starting material, the levels of structurally bound water within the grains (in the form of OH defects) is estimated to be negligible. Therefore any fluid within the sample would likely be restricted to fluid inclusions, interfacial films and trapped pore fluids.

Physical properties of quartz used for thermal calculations (Chapter 2)

	Density $\rho\ (kg.m^{-3})$	**Specific heat** $c_p(J.kg^{-1}.K^{-1})$	**Thermal conductivity** $k(W.m^{-1}K^{-1})$	**Thermal diffusivity** $\kappa(10^{-6}m^2s^{-1})$
Quartz	2650	1186	7	2.23

Data obtained from Di Toro and Pennacchiono [2004] and references contained therein.

Mechanical data from experiments used for frictional heating calculations

Sample	**Melt Textures**	**Displacement (mm)**	**Velocity (mm/s)**	**Shear Stress (MPa)**	**Normal Stress (MPa)**	**Friction**
BIS043	Melt	0.218	18.17	190	261	0.727
BIS042	Melt	0.192	15.67	187	245	0.763
BIS041	No Melt	0.106	9.64	93	105	0.887
BIS040	Melt	0.17	14.17	191	262	0.73
BIS039	No Melt	0.15	13.64	145	161	0.899
BIS038	Melt	0.225	19.57	207	287	0.721
BIS036	Melt	0.158	10.53	147	187	0.787
BIS048	No Melt	0.0350	2.41	71	93	0.764

Thermal modelling: effect of varying parameters (Chapter 2)

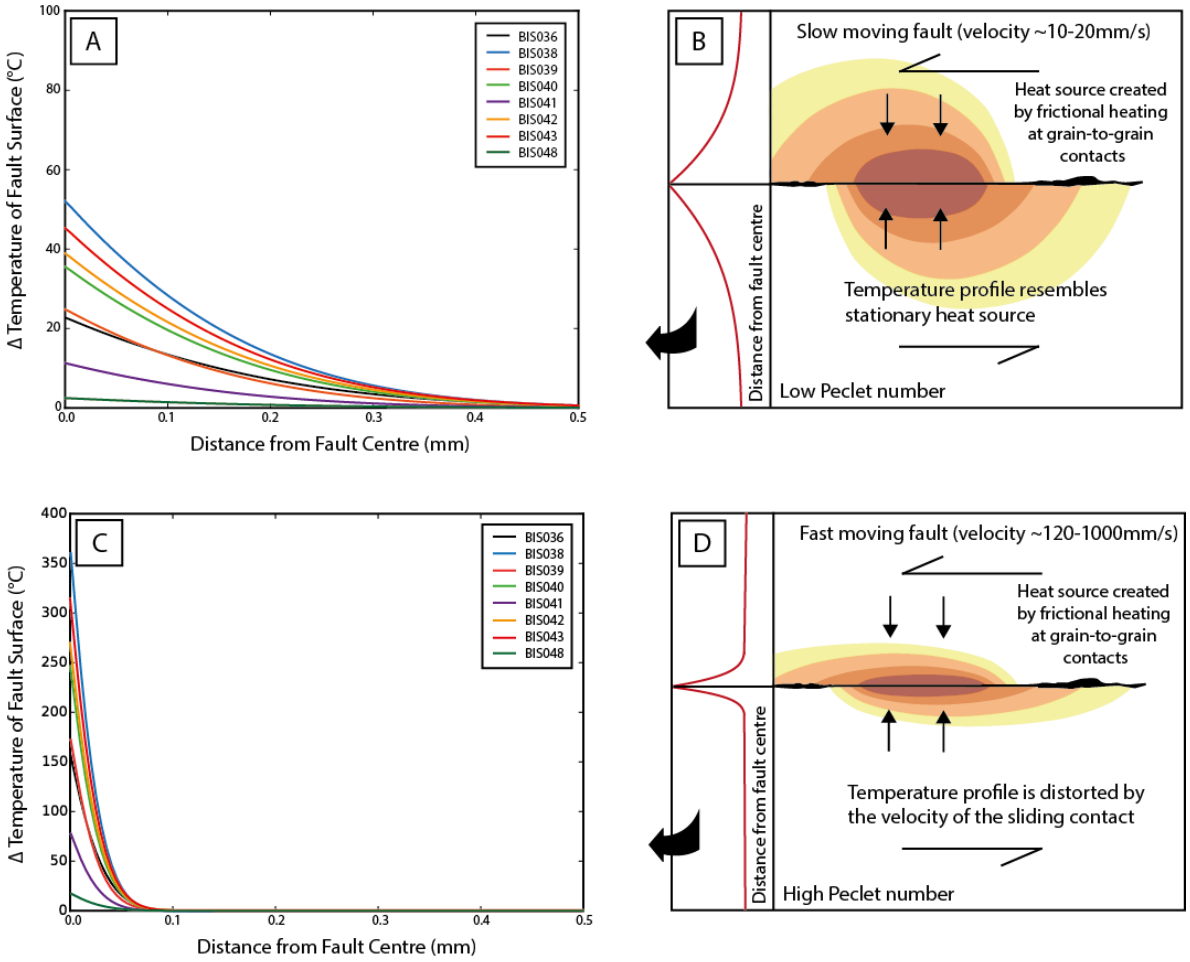

Figure 6: Calculations estimating the average increase in temperature on the fault surface showing the effect of sliding velocity.
(A) Graph showing frictional heating of the fault zone as a function of increasing distance perpendicular to the fault core. These calculations are based on the slip times estimated from the seismic data. (B) Results of A show a temperature profile resembling a stationary heat source with a largely even diffusion of heat from the asperity contact. (C) Frictional heating of the fault zone as a function of increasing distance perpendicular to the fault core, assuming the slip times estimated from the seismic data is underestimated by a factor of 50. The velocities used in these calculations approach seismic slip rates. (D) Results of C show the severe distortion of the temperature profile by the velocity of the sliding contact and suggest the majority of heating is confined to the region immediately adjacent to the slip zone.

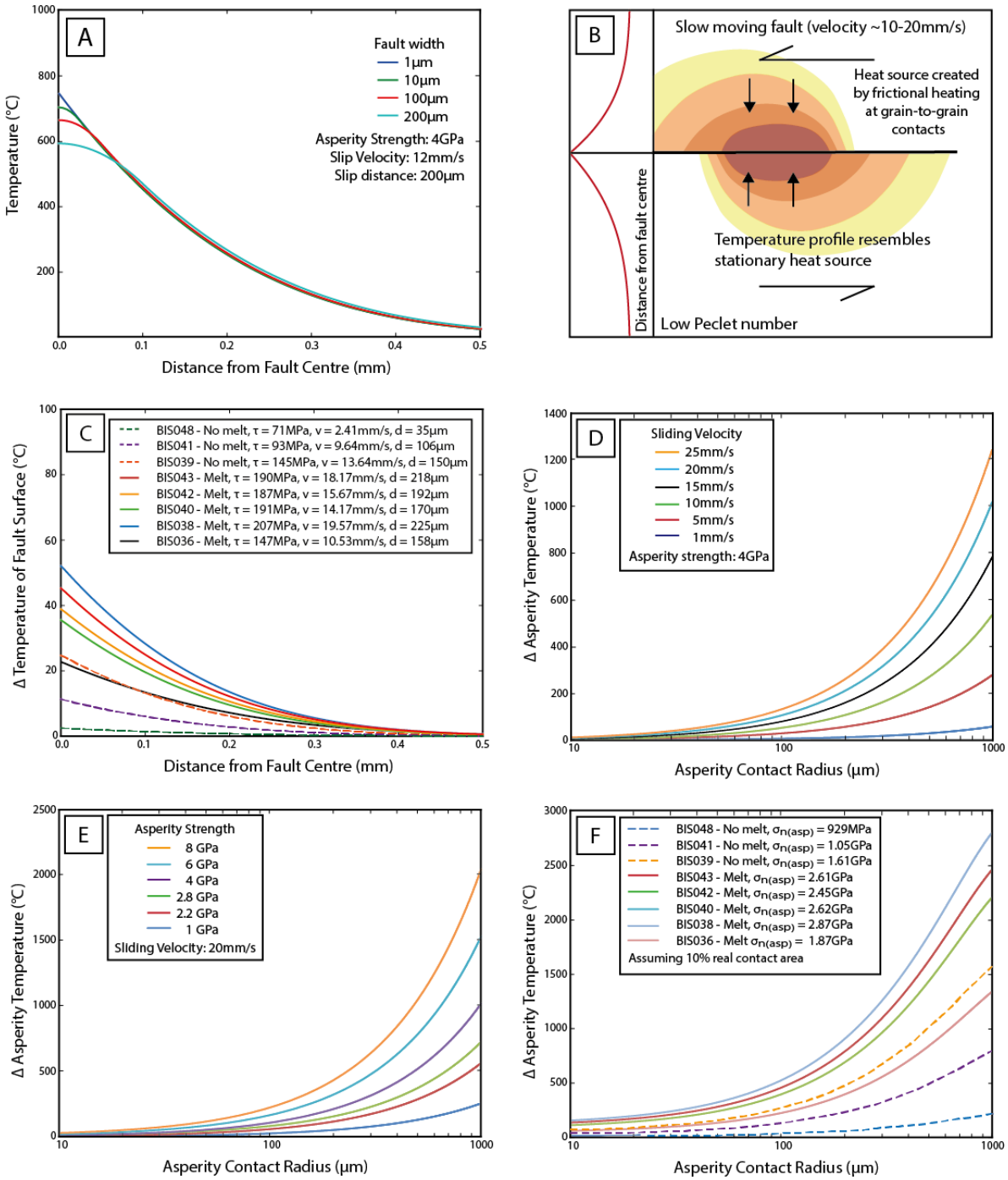

Figure 7: Effect of varying parameters on the production of heat on the fault surfaces
(A) Sensitivity of the model 1 (used to calculate frictional heating of the fault surfaces) to changes in fault width. When fault widths <5µm, there is essentially no impact of calculated fault temperatures. Faults in the current suite of experiments have a fault width of approximately 1-2µm. (B) Schematic illustration of the effect of a slow moving heat source (low Péclet number) [after *Stachowiak and Batchelor*, 1993]. (C) Estimated increase in fault surface temperature using data acquired from experiments. The change in estimated temperature with increasing displacement from the interface suggests a low Péclet number. (D) Change in asperity temperatures as a function of asperity radius in response to flash heating. Graph shows the effect of different sliding velocities. (E) The effect of different asperity strengths and diameters on the change in asperity temperature. (F) Change in asperity temperature using experimental data (see Appendix 5) and assuming a real fault contact area of 10% [*Logan and Teufel*, 1986]. Estimated normal stress acting on asperities (real contact area) is indicated and range from 0.9-2.9GPa.

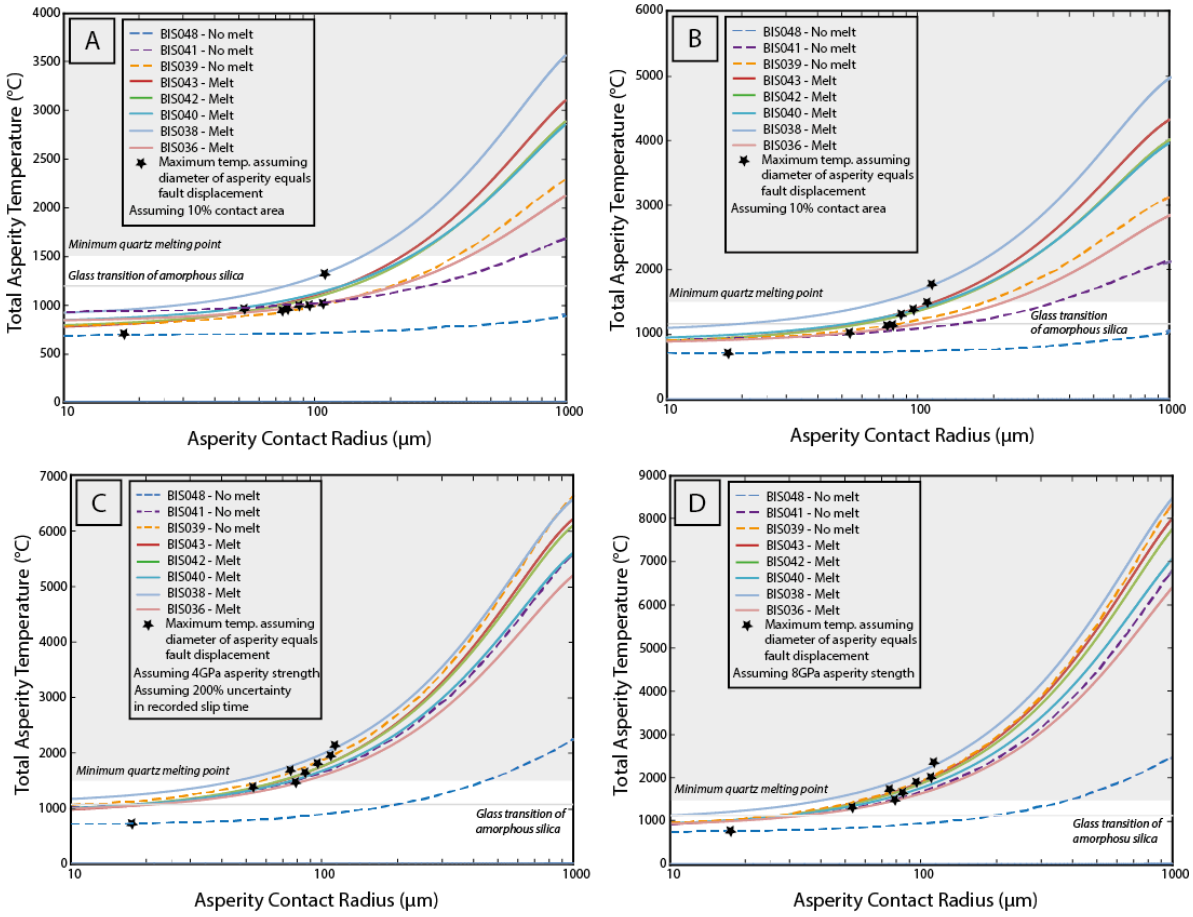

Figure 8: Effect of parameter uncertainty on the calculated total asperity temperature
(A) Graph showing estimated maximum asperity temperature using experimental data and assuming a asperity contacts account for 10% of the fault area. (B) Graph depicting estimated maximum asperity temperature assuming that the slip interface has a 10% real contact area and that the slip duration has been overestimated by 200% (C) Shows the effect of an asperity strength of 4GPa and an overestimated slip time. (D) Visualises the effect on total asperity temperature for a very high (8GPa) asperity strength. For C-D, it is assumed that the maximum normal stress of the interface is given by the compressive failure strength of the asperity, which is assumed as to be the same as for the material (i.e. quartz). Note that changing asperity normal stress to being equivalent to estimated values for the compressive strength of quartz results in convergence of the estimated maximum temperatures at large asperity contact radii compared with the results form experimental data (A). Further, the results are no longer consistent with the experimental observations of melt production.

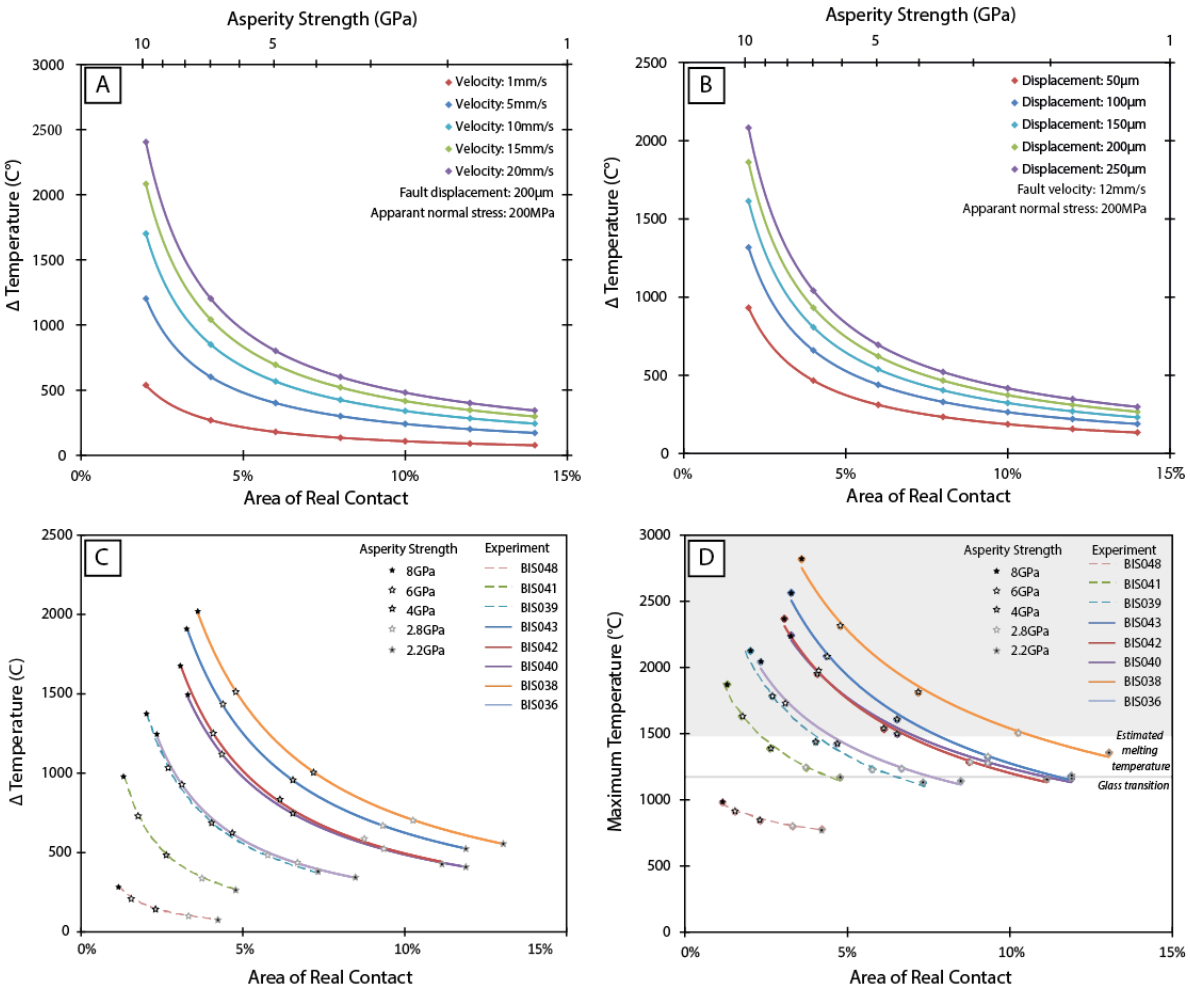

Figure 9: Change in asperity temperature as a function of real contact area and asperity strength
(A) Estimated change in asperity temperature as a function of real contact area/asperity strength over a range of sliding velocities and assuming a fault displacement of 200µm and apparent normal stress of 200MPa. (B) Estimated change in asperity temperature plotted as a function of real contact area assuming varying displacement and a constant velocity. (C) Graph showing the estimated change in asperity temperature as a function of real contact area using experimental data for apparent normal stress, velocity and displacement. (D) Visualises the estimated total asperity temperature including ambient experimental conditions for experimental data. Note the good correlation between observed melt and estimated maximum temperatures.

Loading curves of intact rock and misoriented fault experiments (Chapter 3)

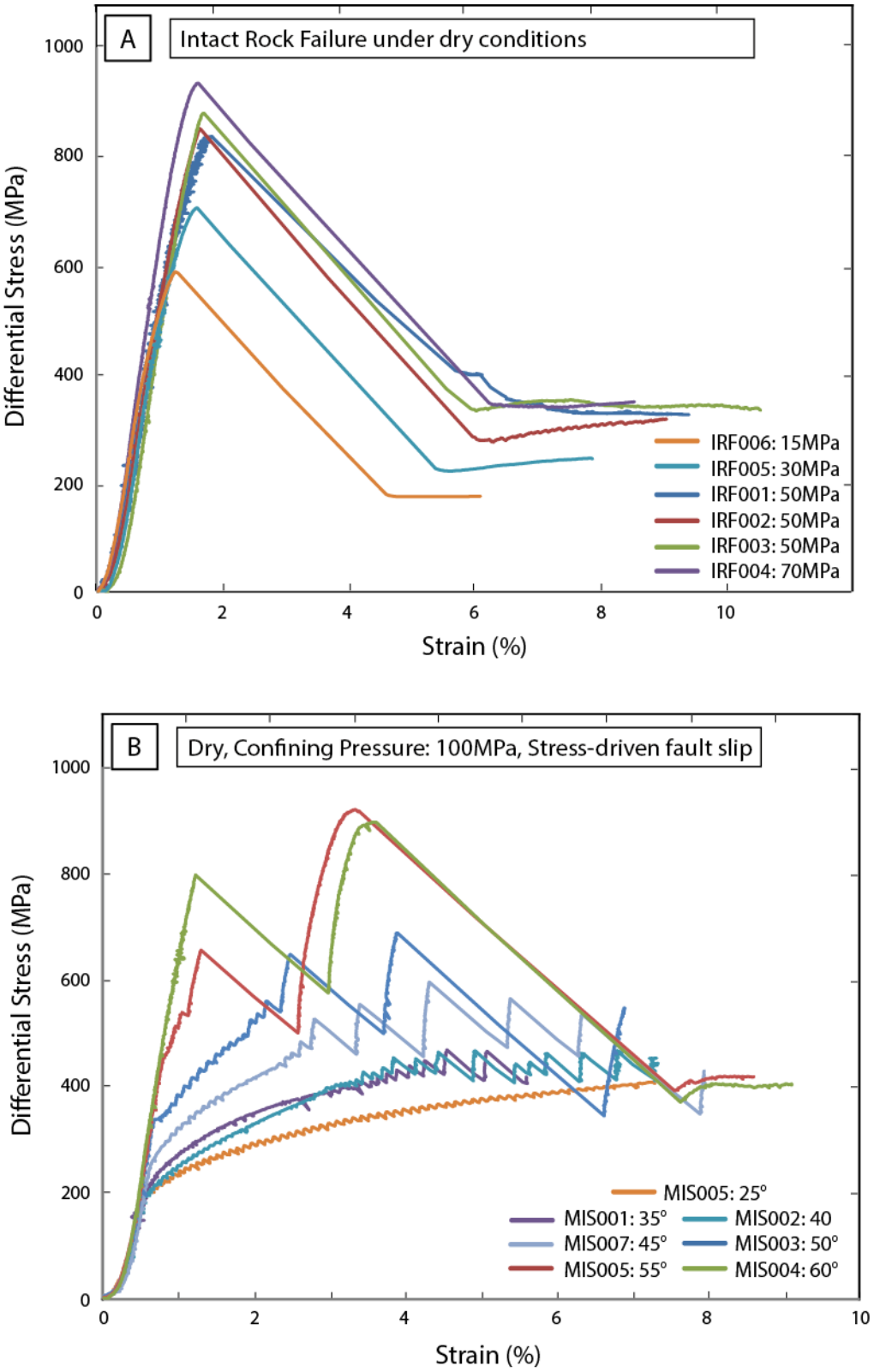

Figure 10: Comparison of stress-strain curves for intact rock failure and misoriented fault experiments.

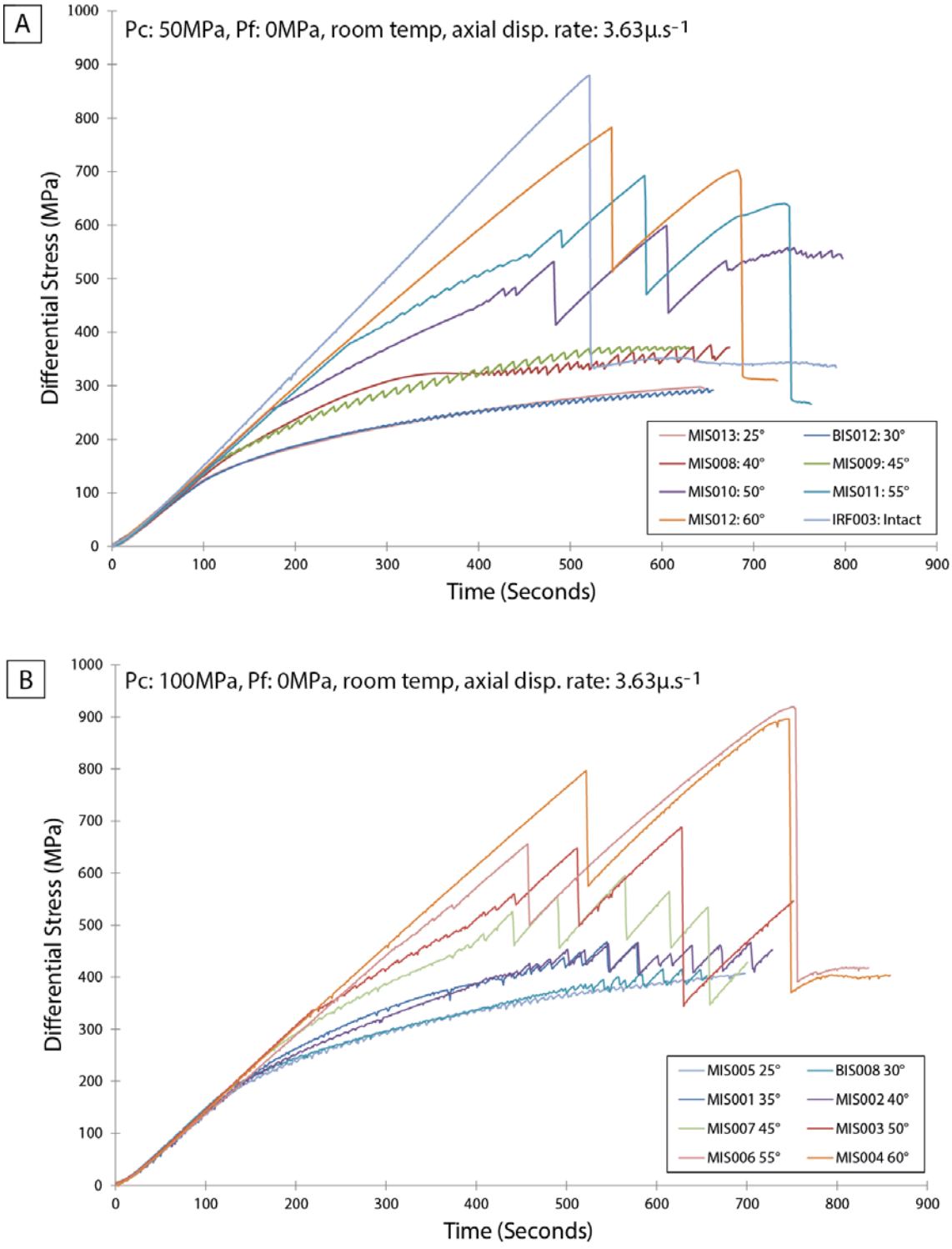

Figure 11: Comparison of loading curves for misoriented fault experiments between 50MPa and 100MPa confining pressure.

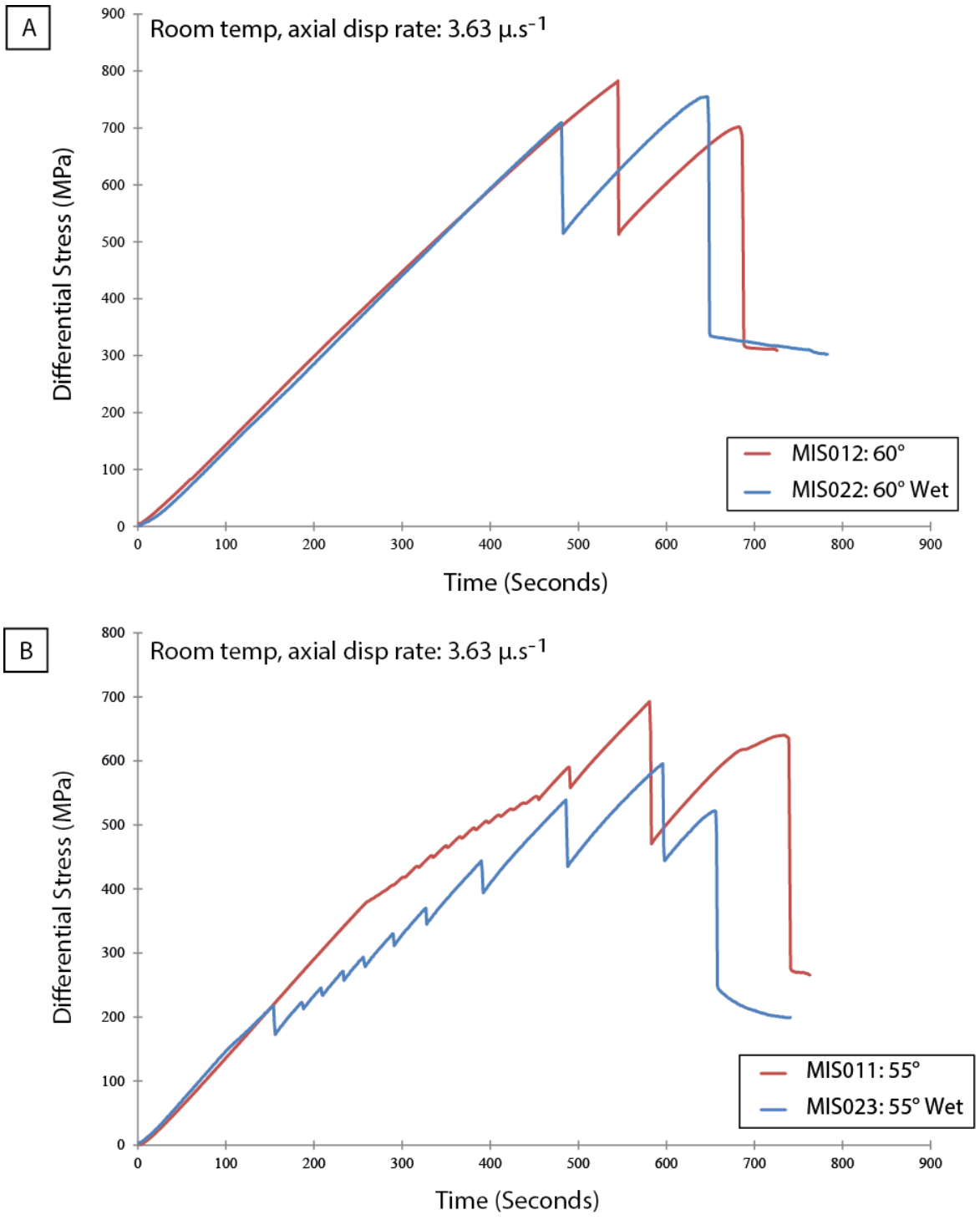

Figure 12: Loading curves for misoriented fault experiments. Comparison made between experiments undertaken at nominally dry conditions and water saturated conditions.

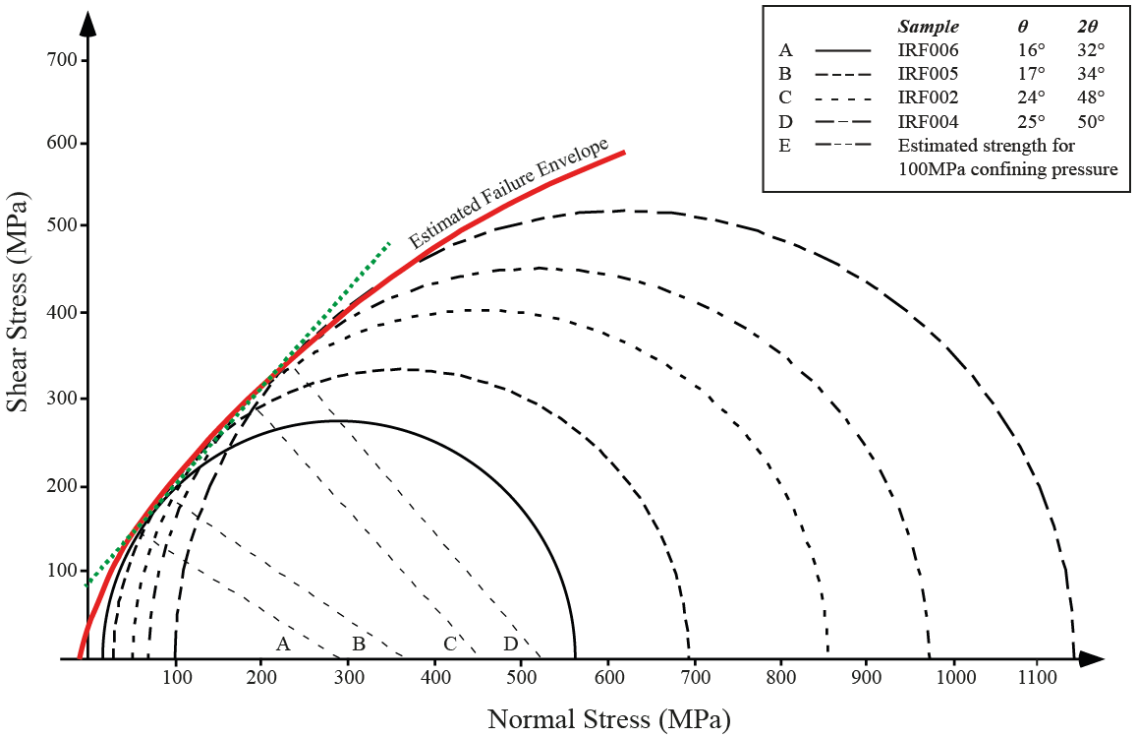

Figure 13: Morh Diagram showing the construction of failure envelopes for Fontainebleau sandstone

The failure envelope has been constructed using experimental data with the diameter of the circle representing differential stress at failure. The green dashed failure envelope assumes a linear relationship and estimates a high value of cohesive strength and large value of internal friction. The solid red failure has been estimated assuming a non-linear relationship between shear and normal stress at failure.

Spectral analysis using cathodoluminescence (Chapter 3)

Misoriented Fault Experiments: MIS017 θ_r = 60°, nominally dry conditions

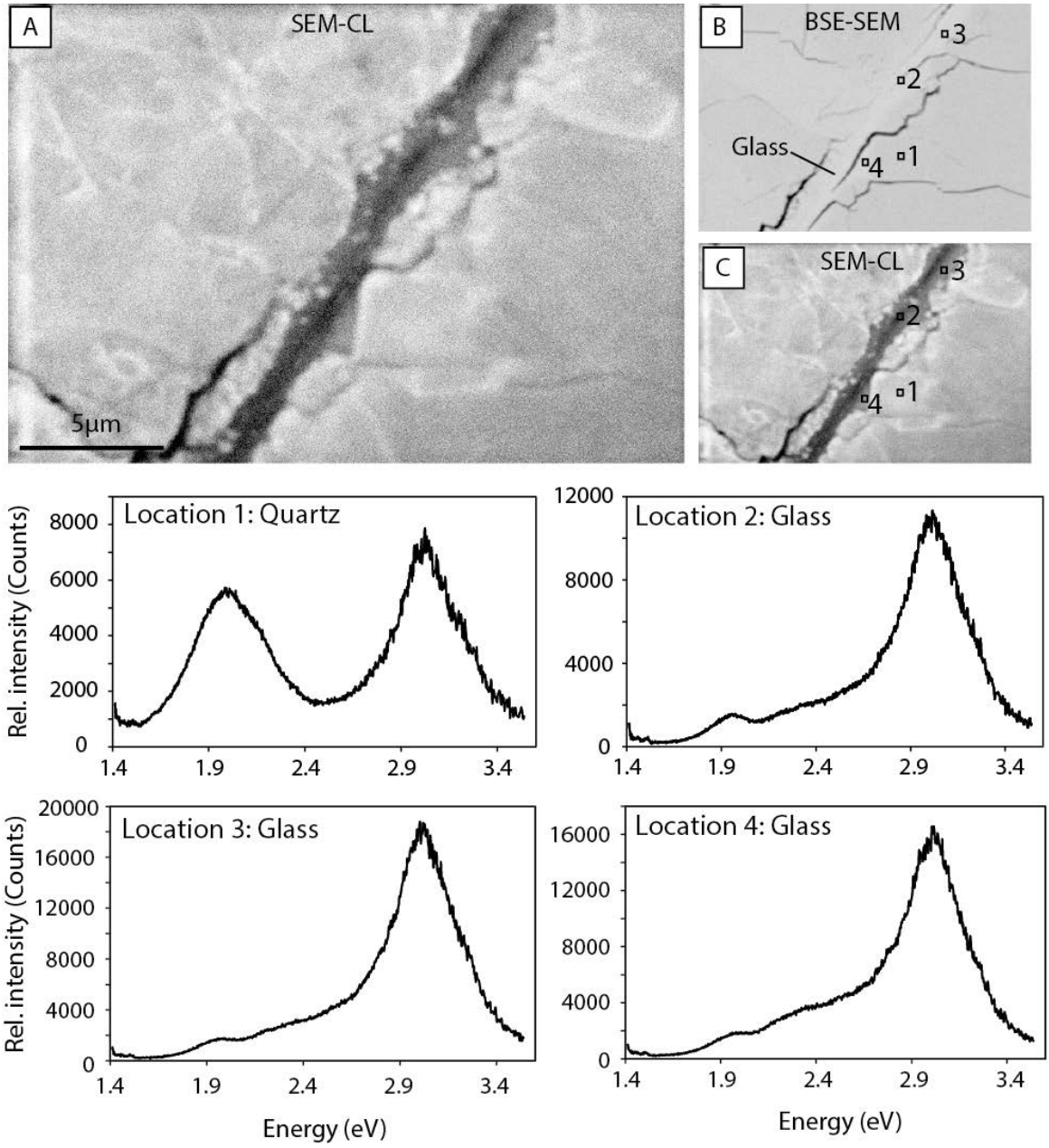

Figure 14: Cathodoluminescence analysis of a melt-welded interface created by the stress-driven reactivation of a θ_r=60° fault under nominally dry conditions.
Images and spectra acquired from MIS017, reactivated at P_c = 50MPa. (A) Panchromatic CL image of a melt-welded section of the fault. Melt can be seen as the dark band in the centre of the image. (B-C) BSE-SEM, panchromatic CL images (respectively) showing the location of spectral analyses. Spectra are shown, identified by location.

Misoriented Fault Experiments: MIS017 θ_r = 60°, nominally dry conditions

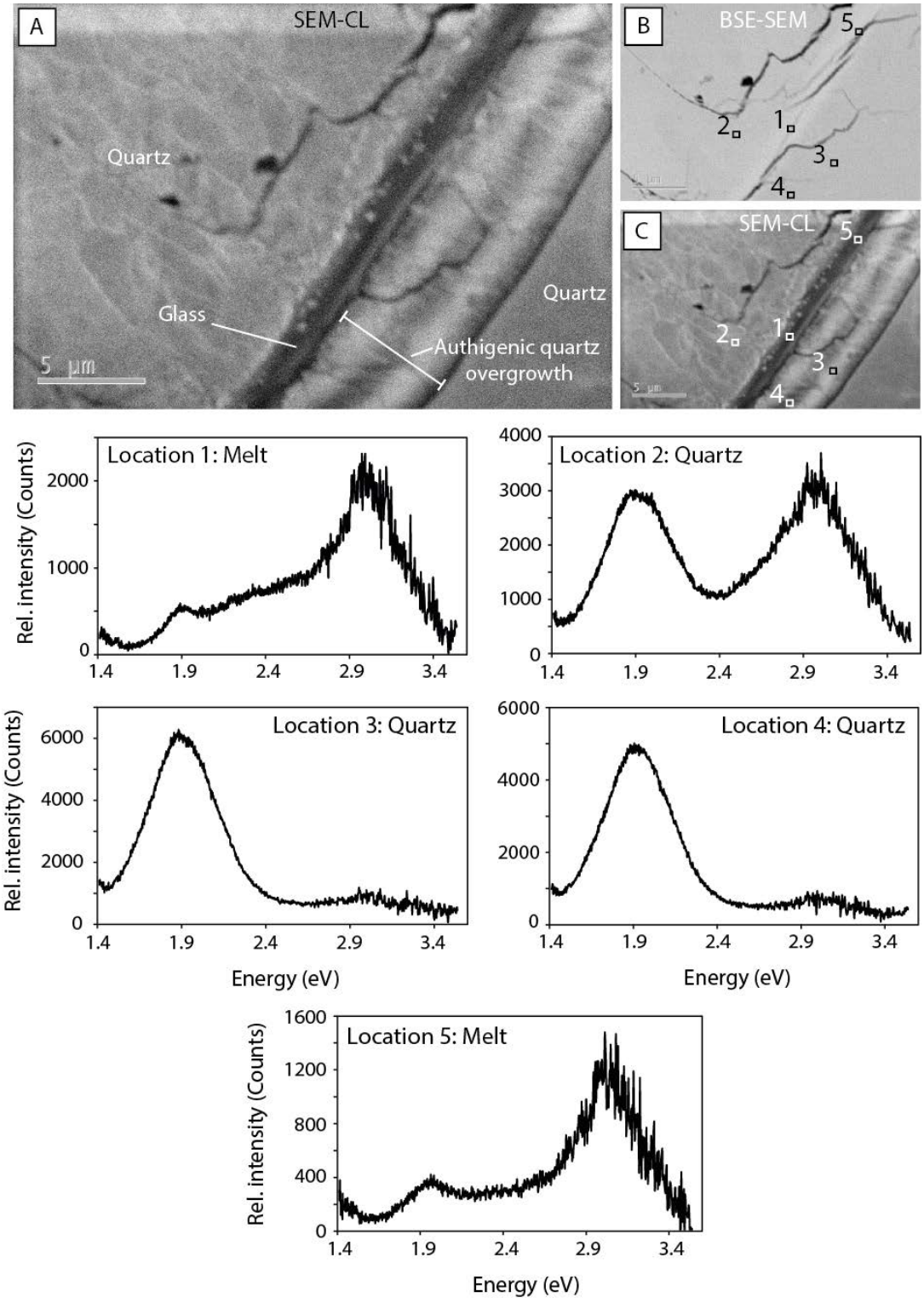

Figure 15: Cathodoluminescence analysis of a melt-welded interface created by the stress-driven reactivation of a θ_r=60º fault under nominally dry conditions.
Images and spectra acquired from MIS017, reactivated at P_c = 50MPa. (A) Panchromatic CL image of a melt-welded section of the fault. Melt can be seen as the dark band in the centre of the image. Note the banding of an authigenic quartz overgrowth which is approximately parallel to the melt. Clasts can be seen within the melt layer, as well as material that varies in luminescence intensity. (B-C) BSE-SEM, panchromatic CL images (respectively) showing the location of spectral analyses. Spectra are shown, identified by location.

Misoriented Fault Experiments: MIS017 θ_r = 60°, nominally dry conditions

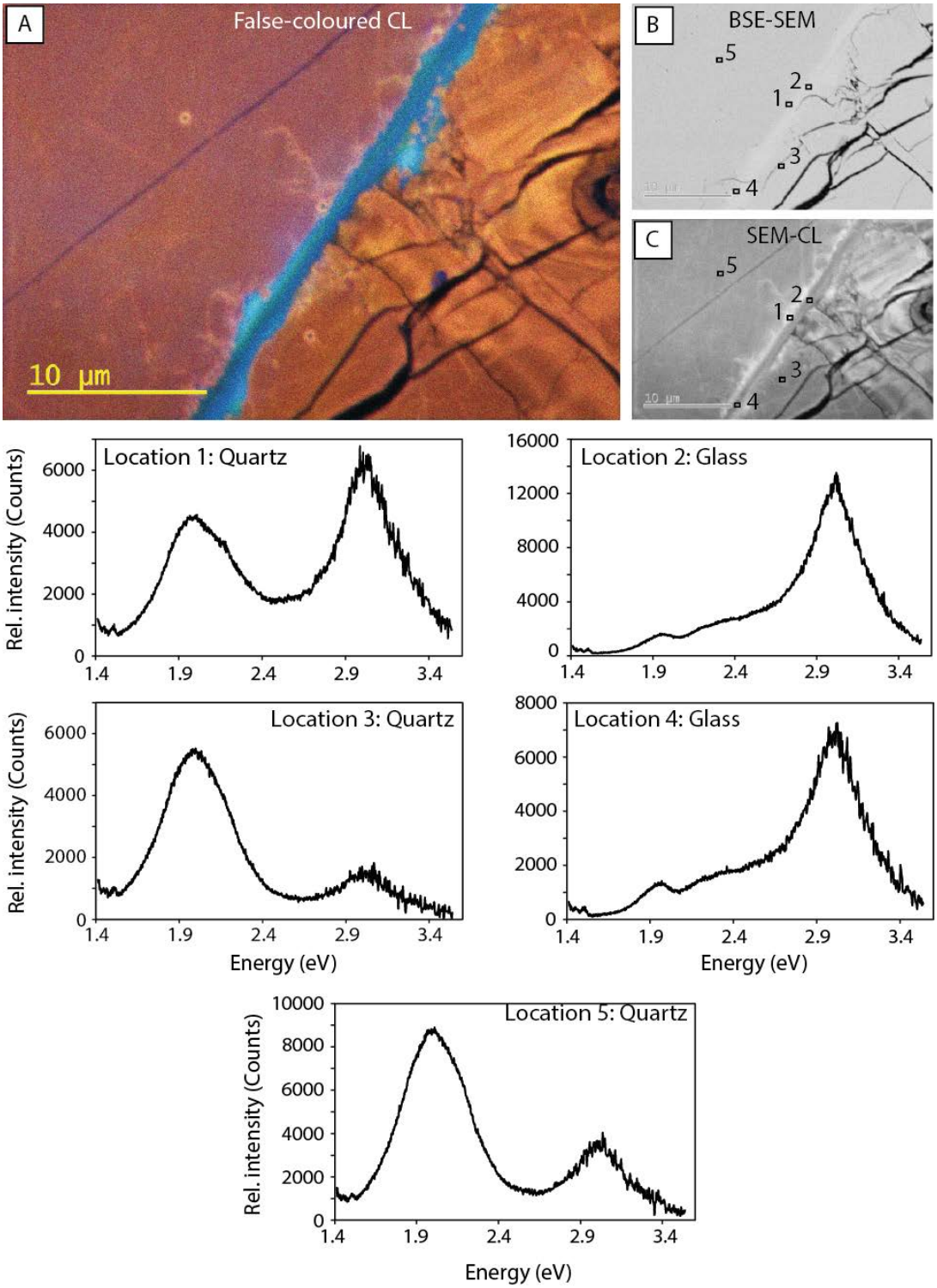

Figure 16: Cathodoluminescence analysis of a melt-welded interface created by the stress-driven reactivation of a θ_r=60° fault under nominally dry conditions.
Images and spectra acquired from MIS017, reactivated at P_c = 50MPa. (A) False coloured CL image of a melt-welded section of the fault. Melt can be seen as the blue band in the centre of the image (B-C) BSE-SEM, panchromatic CL images (respectively) showing the location of spectral analyses. Spectra are shown, identified by location.

Misoriented Fault Experiments: BIS004 θ_r = 30°, aseismic slip

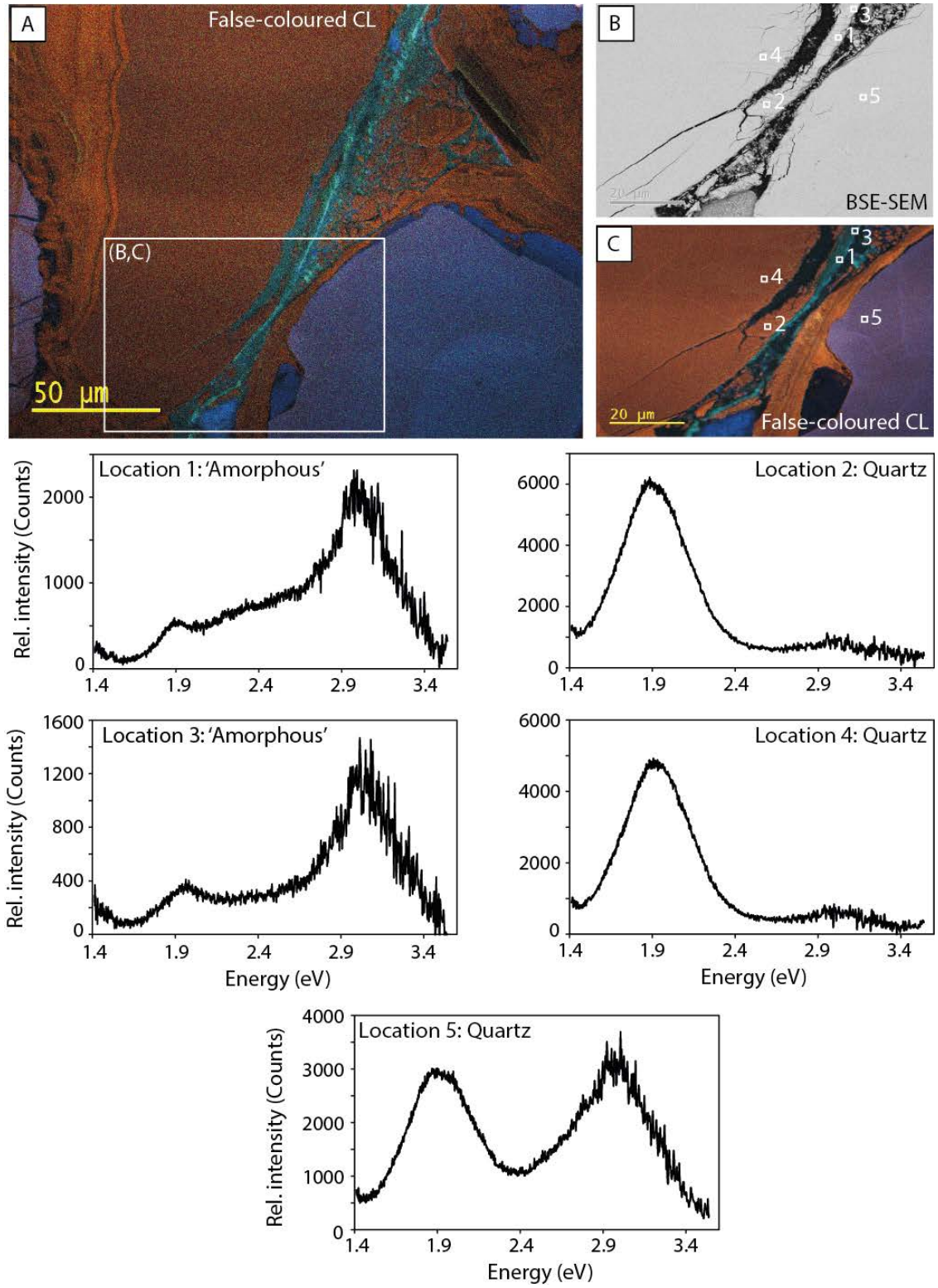

Figure 17: Cathodoluminescence analysis of an optimally-oriented, aseismically slipped fault under nominally dry conditions.
Images and spectra acquired from BIS004, reactivated at P_c = 100MPa. (A) False coloured CL image of the fault core of a mature, optimally oriented fault. Damaged/potentially amorphous material can be seen as the green-blue zones at the centre of the image. Inset shows the location of B and C. (B-C) BSE-SEM, false coloured CL images (respectively) showing the location of spectral analyses. Spectra are shown, identified by location.

Misoriented Fault Experiments: BIS004 θ_r = 30°, aseismic slip

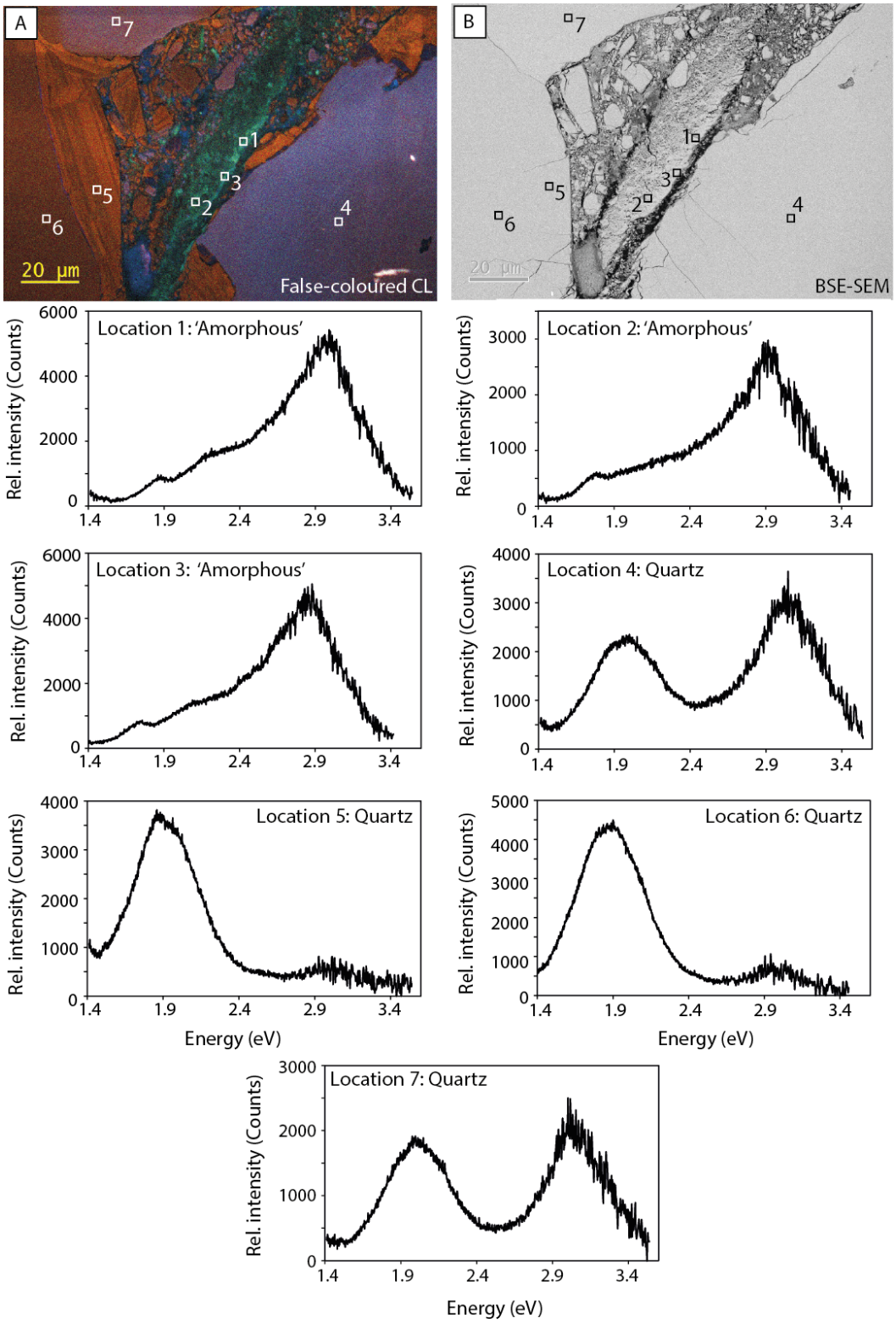

Figure 18: Cathodoluminescence analysis of an optimally-oriented, aseismically slipped fault under nominally dry conditions.
Images and spectra acquired from BIS004, reactivated at P_c = 100MPa. (A) False coloured CL image of the fault core of a mature aseismically slipped fault. Damaged/potentially amorphous material can be seen as the green luminescent zones at the centre of the image. (B) BSE-SEM showing the location of spectral analyses. Spectra are shown, identified by location.

Misoriented Fault Experiments: BIS001 θ_r = 30°, aseismic slip

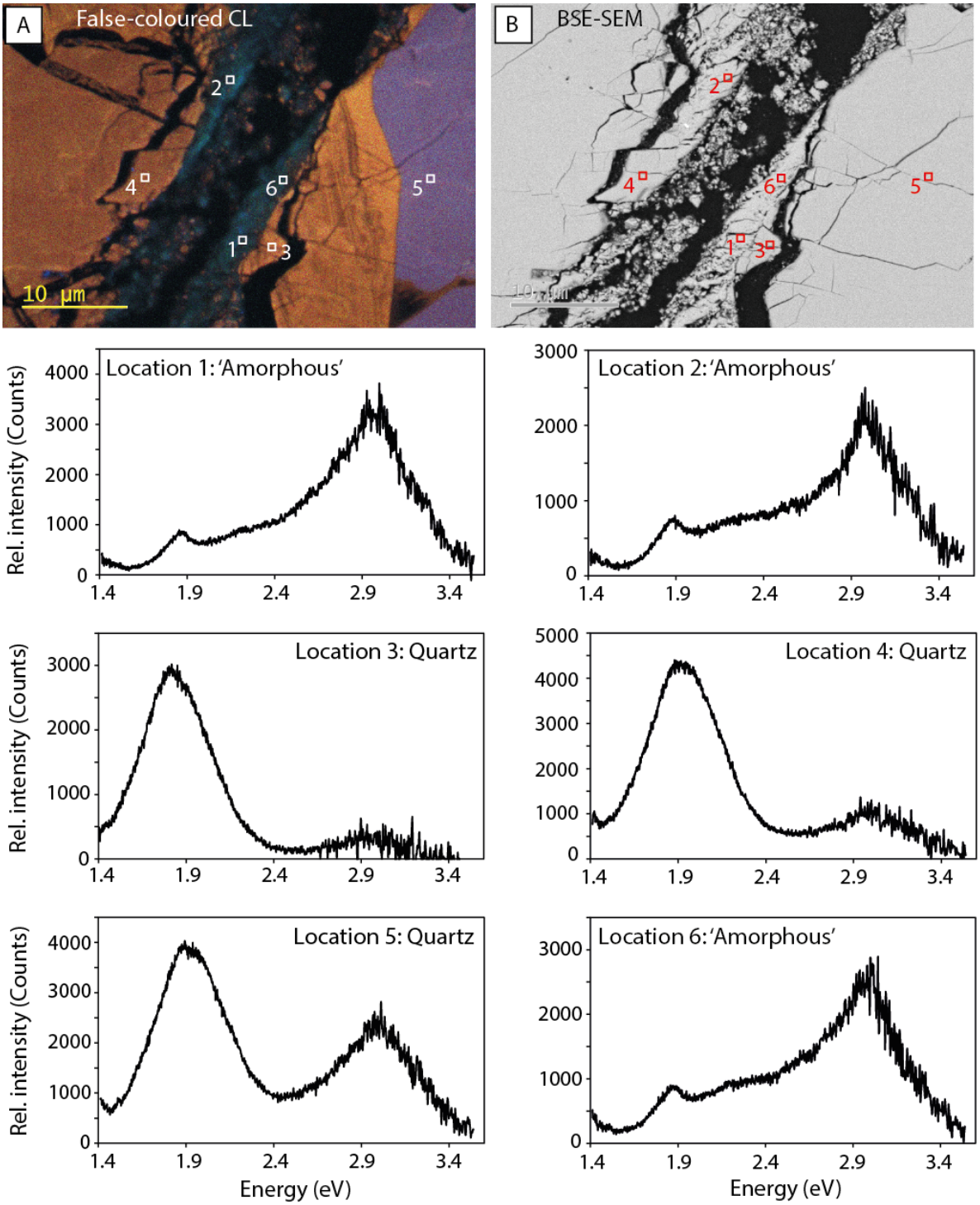

Figure 19: Cathodoluminescence analysis of an optimally-oriented, aseismically slipped fault under nominally dry conditions.
Images and spectra acquired from BIS001, reactivated at P_c = 100MPa. (A) False coloured CL image of a melt-welded section of the fault. Damaged/potentially amorphous material can be seen as the green-blue zones at the centre of the image. (B) BSE-SEM image showing the location of spectral analyses. Spectra are shown, identified by location.

Misoriented Fault Experiments: MIS027 θ_r = 60°, elevated pore fluids

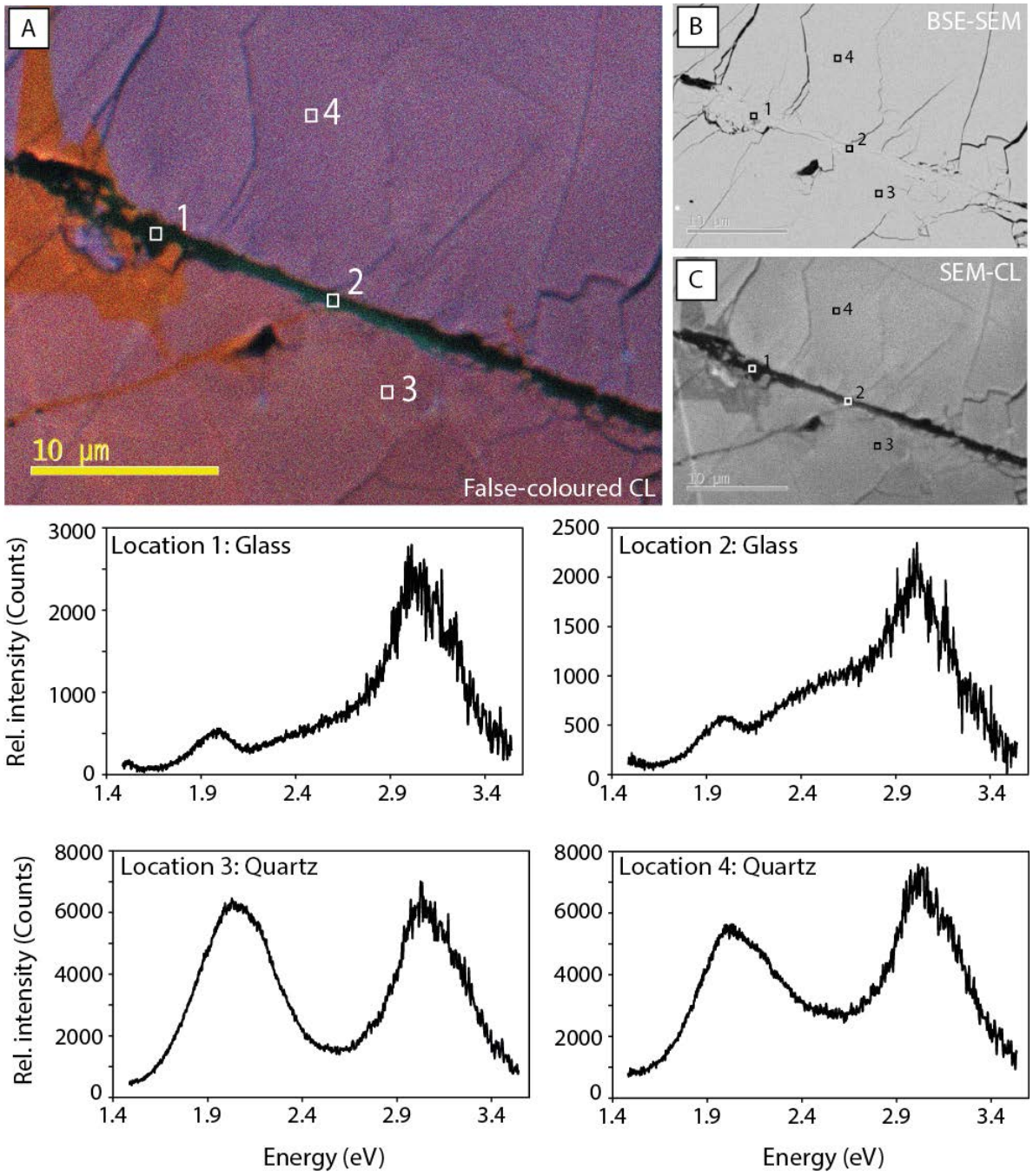

Figure 20: Cathodoluminescence analysis of a melt-welded interface created by the fluid-driven reactivation of a θ_r=60° fault under water saturated dry conditions.
Images and spectra acquired from MIS027, reactivated at P_c' = 15-50MPa. (A) False coloured CL image of a melt-welded section of the fault. Melt zone can be seen by the dark-green band with very low luminescence running across the sample. (B-C) BSE-SEM, panchromatic CL images (respectively) showing the location of spectral analyses. Spectra are shown, identified by location.

Misoriented Fault Experiments: MIS027 θ_r = 60°, elevated pore fluids

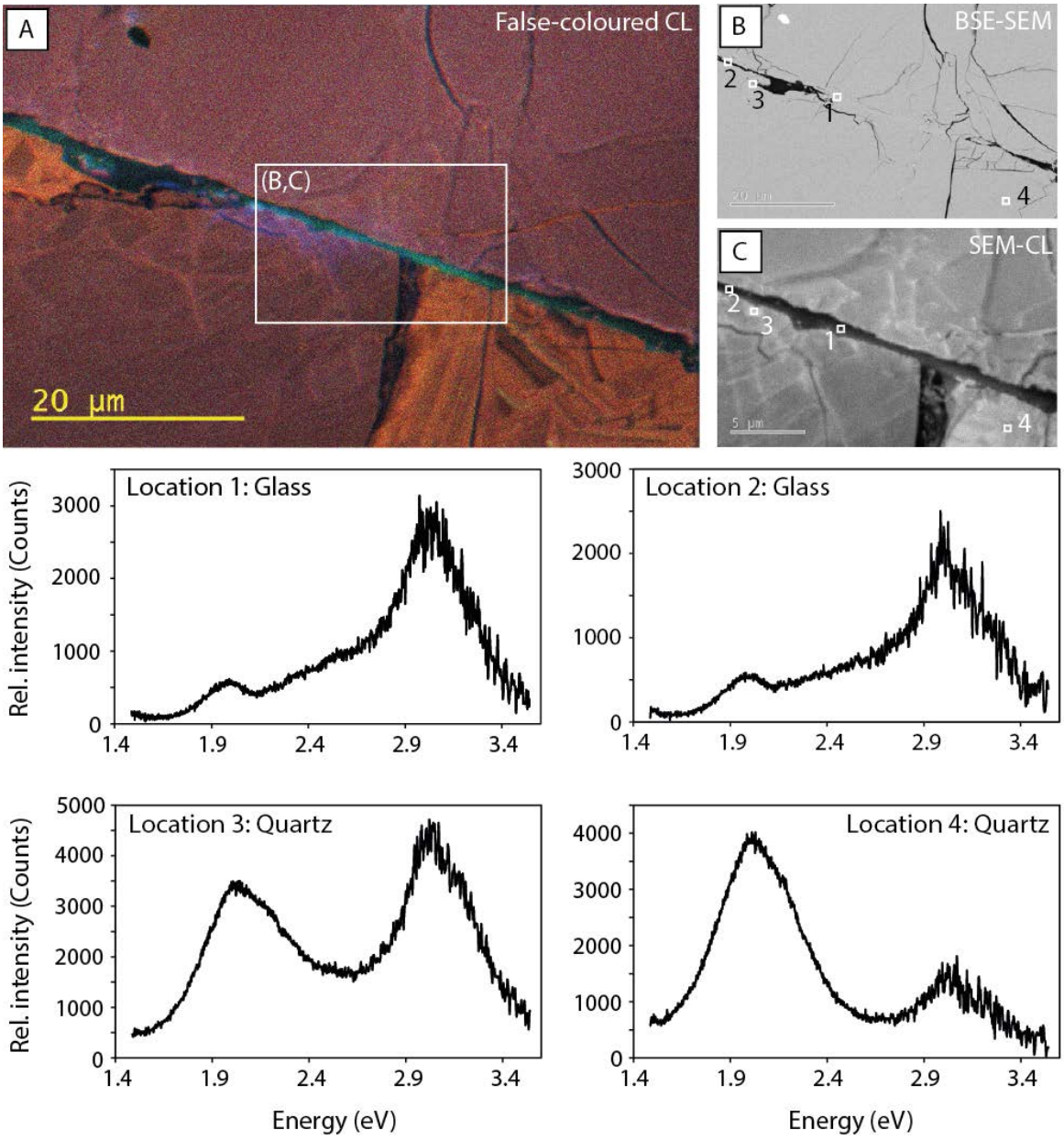

Figure 21: Cathodoluminescence analysis of a melt-welded interface created by the fluid-driven reactivation of a θ_r=60º fault under water saturated dry conditions.
Images and spectra acquired from MIS027, reactivated at P_c' = 15-50MPa. (A) False coloured CL image of a melt-welded section of the fault. Melt zone can be seen by the dark green-blue band running across the sample. Note the variation in intensity of the luminescence within the melt band. (B-C) BSE-SEM, panchromatic CL images (respectively) showing the location of spectral analyses. Spectra are shown, identified by location.

Misoriented Fault Experiments: MIS038 θ_r = 60°, hydrothermally treated for 6 hours at 900°C following slip

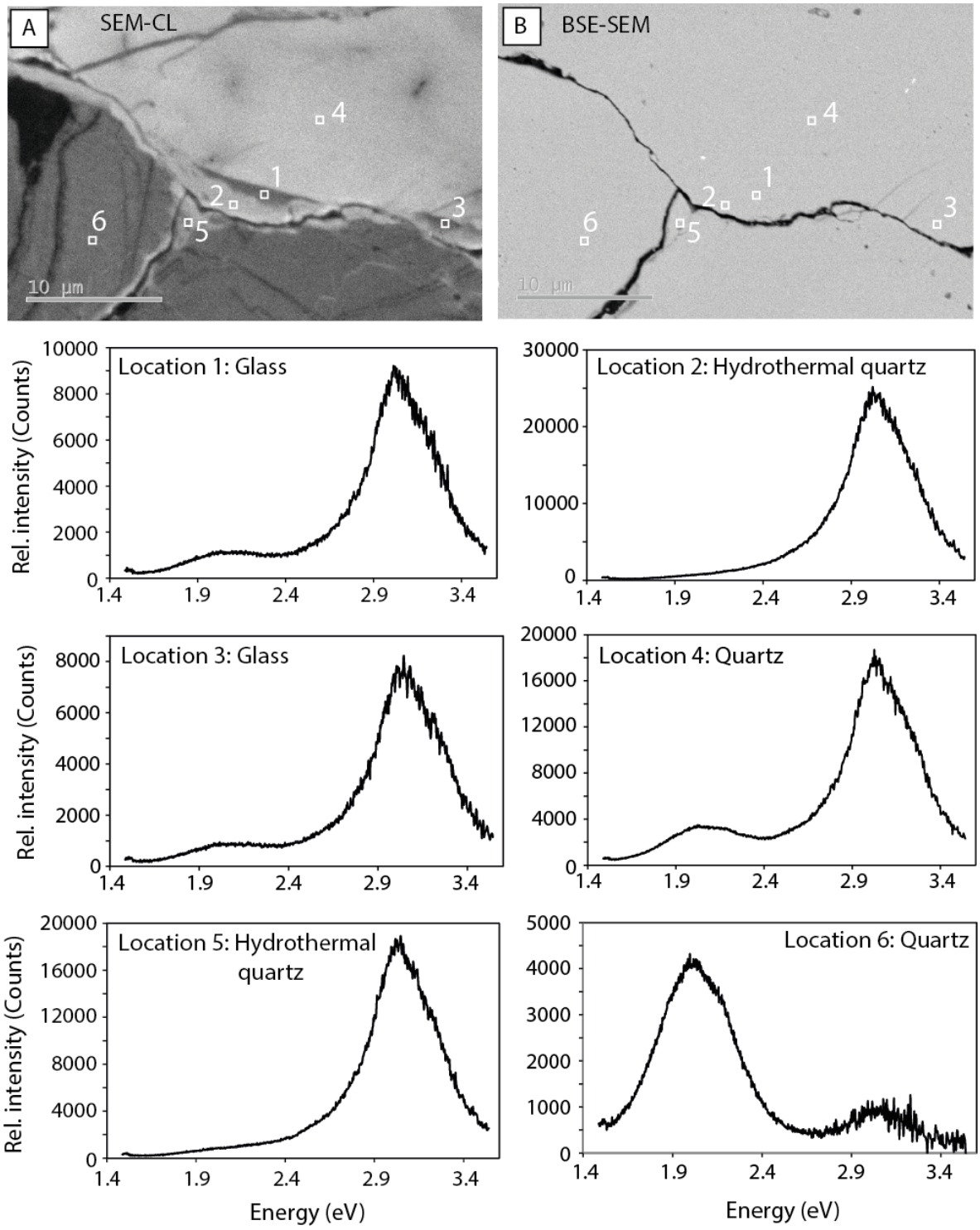

Figure 22: Cathodoluminescence analysis of a melt-welded interface that has been hydrothermally treated for 6 hours following slip.
Images and spectra acquired from MIS038, reactivated at P_c = 100MPa and then hydrothermally treated for 6 hours at P_c = 250MPa, P_f = 150MPa and T = 900MPa. (A-B) Panchromatic CL and BSE-SEM images (respectively) showing the location of spectral analyses. Note the presence of relict melt within the core of the fault that is surrounded by a hydrothermal quartz rim. Spectra are shown, identified by location.

Misoriented Fault Experiments: MIS038 θ_r = 60°, hydrothermally treated for 6 hours at 900°C following slip

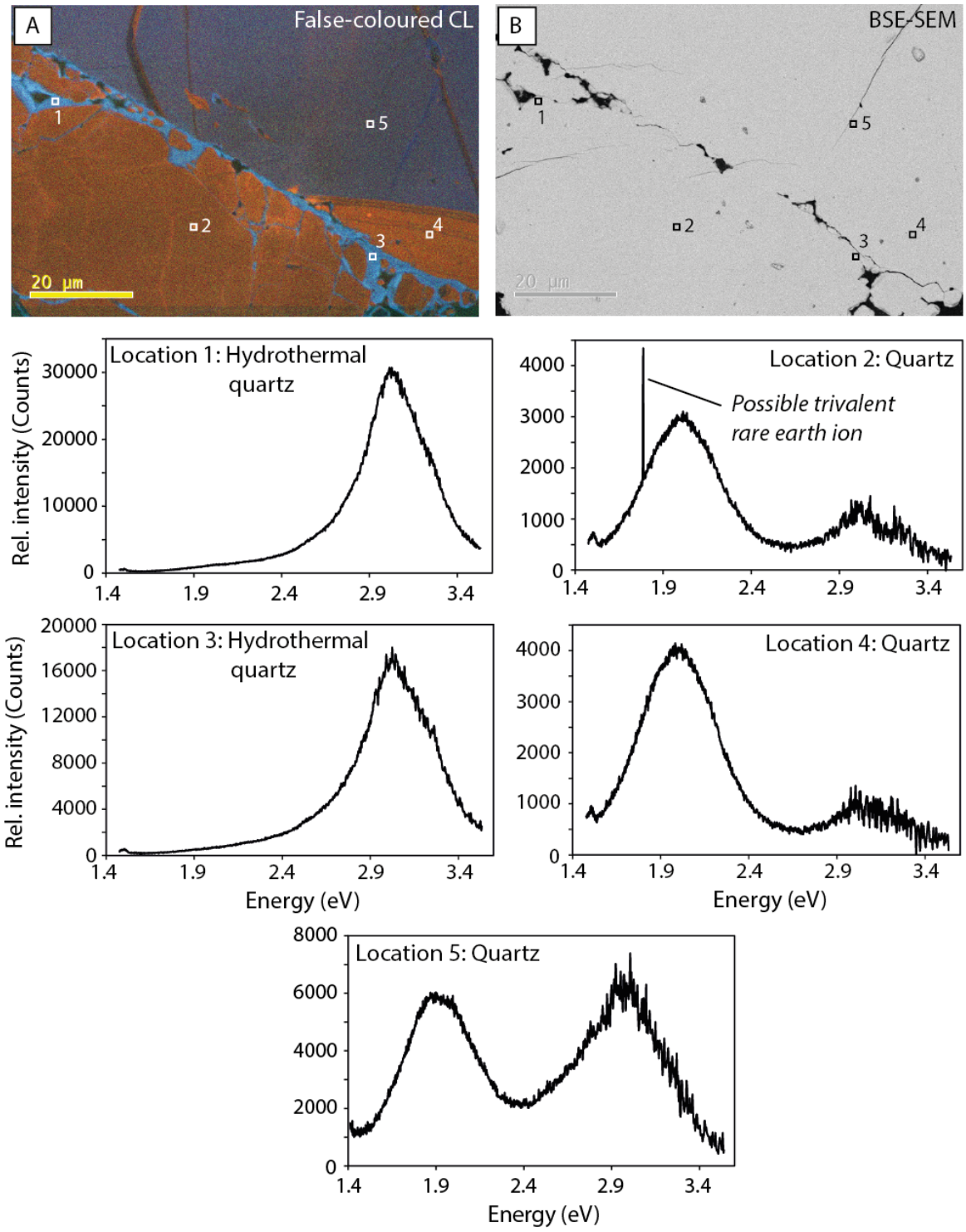

Figure 23: Cathodoluminescence analysis of a melt-welded interface that has been hydrothermally treated for 6 hours following slip.
Images and spectra acquired from MIS038, reactivated at P_c = 100MPa and then hydrothermally treated for 6 hours at P_c = 250MPa, P_f = 150MPa and T = 900MPa. (A-B) Panchromatic CL and BSE-SEM images (respectively) showing the location of spectral analyses. Note the cementation of the gouge particles by precipitated hydrothermal quartz (pale blue in the false coloured CL image). Spectra are shown, identified by location.